Understanding Valanginian continental climate using $\delta^{18}O$ from sphaerosiderites as a proxy for precipitation

A thesis submitted to the University of Oxford for the degree of Doctor of Philosophy

Ritwika Sengupta

Department of Earth Sciences, University of Oxford

and

St Edmund Hall, University of Oxford



Supervisors: Dr. Stuart Robinson and Dr. Nicholas Tosca

Submitted in Michaelmas, 2019

Declaration

I declare that the work presented in this thesis is wholly my own work, except where otherwise stated. The views and interpretations expressed herein are mine, and do not represent those of any other person or group.

Ritwika Sengupta

Additional material associated with this thesis

- **Data files** associated with this thesis have been uploaded digitally within a separate folder (**'Additional Materials_RitwikaSengupta'**) and references to those files are given in relevant sections of the Appendices.
- **Individual high-resolution pdf files of the four results chapters (Chapters 2, 3, 4, 5)** are also included in the additional materials. The combined thesis pdf file was produced for high quality print and is suitable for digital viewing or print. The high-resolution original individual pdf files are provided should the reader require them.

Contents

DECLARATION II
ADDITIONAL MATERIAL ASSOCIATED WITH THIS THESIS II
ACKNOWLEDGEMENTS IV
ABSTRACT V
EXTENDED ABSTRACT VI
TABLE OF CONTENTS XIII
LIST OF TABLES XVIII
LIST OF FIGURES XIX

Acknowledgements

This thesis would not have been possible without the help and encouragement of my two supervisors, Stuart Robinson and Nicholas Tosca. They have been incredibly patient, understanding, and kind mentors, and I couldn't have asked for better supervisors to guide me through this project. I want to thank them for the opportunity to conduct this research, and for all their support over the last four years.

I thank Alex Farnsworth (Bristol) for the climate-model data he kindly provided for this thesis. I also thank Joep van Dijk and Stefano Bernasconi (ETH) for giving me the opportunity to work on clumped isotopes. I am grateful to Joep for spending countless hours troubleshooting, and helping me patiently, to get to grips with a difficult method and some highly temperamental siderites. I am also hugely grateful to Madalina Jaggi and Stuart Bishop for their assistance in the lab at ETH. I thank all those at Oxford who have helped with lab work – Kat Clayton, Alice Barroll, Chris Day, Jon Wells, Steve Wyatt, Owen Green, Jon Wade, and Phil Gopon. John McArthur (UCL) and Gillian Mackinnon (SUERC) are also thanked for their help with solution analyses.

The last four years would have been difficult without the two supportive lab groups I have worked with. I thank everyone in the Tosca Lab (past and present!), and particularly huge thanks to Rosalie Tostevin, Clancy Jiang, Brooke Johnson, and Sascha Holland for all their help with experimental setup and interesting discussions. I am also hugely grateful for the past and present members of the self-proclaimed Mesozoic Mayhem group – Ronnie Guthrie, Will Hartz, Sietske Batenburg, Lawrence Percival, Lauren O'Connor, Tintin Naing, Danielle Kondla, and Jamie Lucas, and all their cake-based hilarity. Thanks also to Harry Taylor for help with the last stages of lab work, and whose ability to identify animal shaped siderites in SEM is yet unsurpassed.

My time at Oxford has been made all the richer by the wonderful people I have met at Teddy Hall, the Earth Sciences department, DTP, and at 61A St Clements. I am sorry I can't mention you all by name! I am incredibly grateful for the presence of William Glass, Violaine Andre, Melissa Bedard, Evie Foster, and Jack Evans in my life; they have all collectively kept me going in the last few years and provided incredible support and friendship. I want to particularly thank William Glass, for proofreading so many of my chapters, and for making me appreciate Oxford commas. A shout-out to Clancy Jiang and Gwen Antell who also proofread, calmed me down, and sent me lovely messages throughout write-up. I am thankful for the great bunch of people I met in office 30.18, and particularly want to thank Luke Jenkins for not making fun of me for having so many rocks, and Amber Madden-Nadeau for helping normalise the number of rocks its ok to have. I also hugely appreciated the baked goods from Isabelle Taylor and Ally Bryan that pretty much solely fuelled the last two weeks of write-up. I also want to thank Rebecca Smith for her calm and cool advice, and her faith in me. I am grateful to Naomi Saunders and Sietske Batenburg for always being there for tea, skype chats, and reminding me to take breaks. I also thank Harriet Allen, Chloe Kirkpatrick, and Bob Webb, who have been in my life for a long time and have cheered me on throughout.

My partner Jack Campbell has given me unwavering love, support, and understanding over the last four years. I am very lucky to have him in my life, and hope that I can support him in return, when he embarks on his PhD.

Being a woman in science, and particularly, a woman of colour in science can be difficult. I want to thank all the incredible women, trans and non-binary folk, and people of colour that I have met through conferences and workshops, who have reinstalled faith in me that the future of science will be compassionate. In particular, I want to thank the inspirational Nuzhat Tabassum, Rehemat Bhatia, Jazmin Scarlett, and Divya M. Persaud, for their patience, understanding, and useful advice.

Lastly, I want to thank my parents, Arumita and Nandan Sengupta, who have been so incredibly supportive and loving for not just the last four, but the last twenty-seven years. Without their adventurous decision-making and sacrifices I would not be here today. I also want to thank my grandmothers, Tapati Bose and Juthika Sengupta, and my late great-grandmother, Shefali Bose, who are all trailblazers and continue to inspire me. Collectively, my parents, my grandmothers, and my great-grandmother have lived through incredible social and political upheavals, civil war, injustice, and oppression, but somehow managed to build such joyous, weird, and wonderful lives for themselves. This thesis is dedicated to them and their *joie de vivre*.

Abstract

Terrestrial and marine carbon isotopes record a significant perturbation of the global carbon cycle during the Valanginian: the Valanginian positive Carbon Isotope Event (CIE). The CIE was associated with warm, invariant, low-latitude sea surface temperatures, increased humidity, and ocean fertilization. Although marine changes are well documented, terrestrial temperatures and hydrological response during the CIE are not yet fully understood. The non-marine Wealden Supergroup of Southern England (Berriasian–Hauterivian) provides an ideal record for reconstructing low-latitude continental palaeoclimate during the CIE. These strata contain abundant sphaerosiderites, spherical iron carbonate concretions ($FeCO_3$), which formed mainly in wetland environments and are thought to record meteoric $\delta^{18}O_{groundwater}$ reflective of regional hydrology. Wealden $\delta^{18}O_{siderite}$ varies between –3.5‰ and 0.6‰ VPDB, Δ_{47} temperatures are 33–39°C, and reconstructed groundwater values are isotopically heavy (–3.7‰ to 2.6‰ VSMOW). Compositional and morphological heterogeneity of the sphaerosiderites, comparison to experimental siderite syntheses, isotope transects of individual spheres, high Δ_{47} temperatures, and comparisons to climate models suggest that the sphaerosiderites are a seasonally, summer-biased palaeohydrological record. The $\delta^{18}O_{siderite}$ values from sphaerosiderite horizons alternate between isotopically heavy and light values, interpreted as drier (less precipitation/higher evaporation) and wetter (higher precipitation/less evaporation) conditions, respectively. Correlation to marine records using carbon isotope stratigraphy suggests synchronous relatively arid periods at the onset of the CIE, and just proceeding the peak of the CIE. A peak in humidity observed in the Tethyan realm during the peak of the CIE cannot be assessed conclusively in the Weald basin, due to poor siderite and organic matter preservation in the Wadhurst Clay. A facies-specific $\delta^{13}C_{org}$ shift and these poorly-preserved sphaerosiderites suggest a significant palaeoenvironmental change during deposition of the Wadhurst Clay, which needs further assessment. The geochemical records from the Weald Basin indicate that low-latitude terrestrial temperatures continued to be warm during the Valanginian CIE, supporting evidence from sea surface temperature reconstructions, and that there was periodic enhancement of the hydrological cycle during the Valanginian.

Extended Abstract

The Early Cretaceous geological record contains several notable perturbations of the global carbon cycle in marine and terrestrial organic matter and carbonates, observable as changes in ^{12}C to ^{13}C ratios ($\delta^{13}C$). Of these, the Ocean Anoxic Events (OAE's), characterised by globally correlated, widespread and synchronous deposition of black shales, have been most studied. However, a suite of smaller events are also recorded in the Early Cretaceous, which do not contain all the characteristics of OAE's but have the potential to provide important insight into Cretaceous climate mechanisms and long-term climatic trends. The focus of this thesis is on one such event, the Valanginian positive Carbon Isotope Excursion (CIE), a global carbon cycle perturbation expressed as a 1–2‰ $\delta^{13}C$ excursion in marine carbonates and a 3–5‰ $\delta^{13}C$ excursion in terrestrial organic matter. The CIE lacks the associated widespread black shale deposition typical of other OAE's, but is of similar amplitude to $\delta^{13}C$ excursions associated with OAE's. Therefore, to account for the $\delta^{13}C$ excursion during the Valanginian, platform drowning and/or increased terrestrial carbon sequestration have been suggested as possible mechanisms. The CIE is also associated with environmental perturbations, such as an enhanced hydrological cycle in the Tethyan realm (based on spore-pollen and clay assemblages), ocean fertilization, and a biocalcification crisis. Furthermore, there is evidence that beginnings of palaeoenvironmental changes predate the CIE, for instance both phosphorus accumulation rates and nannoconid abundances start changing prior to the CIE. Sea surface temperatures reconstructed using TEX_{86} suggest no temperature changes, with warm temperatures persisting at both high and low latitudes during the CIE. By contrast, evidence from glendonites, dropstones, and belemnite clumped isotopes has been used to suggest cooling, particularly in the high latitudes. Consequently, the palaeoclimatic and palaeoenvironmental changes associated with the Valanginian CIE are not yet fully understood, and little attention has been paid to terrestrial temperature changes and hydrology. Hence, this thesis aims to provide an Early

Cretaceous hydrological and temperature reconstruction using samples from a low-latitude non-marine deposit, the Wealden Supergroup of the UK, which spans Berriasian–Aptian stages (145–126 million years ago), encompassing the Valanginian CIE.

The Wealden Supergroup consists of non-marine strata predominantly deposited in fluvio-lacustrine settings within floodplain, channel, and lagoonal environments. The four main stratigraphic units of importance to this thesis are the Ashdown Formation, Wadhurst Clay Formation, Tunbridge Wells Sand Formation, and Weald Clay Group. These strata contain abundant palaeosol horizons with sphaerosiderites, iron carbonate ($FeCO_3$) concretions thought to have formed in waterlogged, reducing wetland soils. Due to their mode of growth, sphaerosiderites are thought to record the oxygen isotope composition of meteoric groundwater, and by extension, regional hydrology. The elemental composition of sphaerosiderites is also thought to reflect palaeoenvironmental conditions; increased Mg and Ca substitution is typically interpreted as reflecting marine influence, while comparative enrichment in Mn reflects formation in freshwater conditions. The elemental compositions and their reflection of palaeoenvironmental conditions are, however, poorly unconstrained as they have not been reproduced by laboratory syntheses of siderite. As freshwater sphaerosiderites are necessary for hydrological reconstructions, constraining the palaeoenvironmental conditions during siderite growth remains imperative for terrestrial hydrological reconstructions.

New experimental constraints on elemental uptake during siderite growth provided in this thesis suggest cation concentrations in pore waters are not the strongest determinants of minor element composition in siderite. Rather, elemental uptake is influenced by a complex set of parameters including pH, pCO_2, cation concentrations, siderite saturation, and growth rates. Mn uptake during siderite growth was found to be preferential to Ca and Mg, while Ca and/or Mg uptake was not discernible at ambient temperatures. In addition, comparison to modern siderite nodules forming in coastal wetlands suggests the presence of other

carbonate phases and/or pyrite to be a clearer indication of marine influences on pore water chemistry. Considering this result, a thorough mineralogical, petrographic, and geochemical analysis of Wealden sphaerosiderites was undertaken to allow a better understanding of palaeoenvironmental conditions and assess their suitability for palaeoclimate reconstructions.

Sphaerosiderites were sampled from more than 50 horizons at 3 boreholes: Fairlight, Westfield, and Cooden. The Wealden sphaerosiderites are generally well preserved in the Ashdown and Tunbridge Wells formations. The matrix was found to be soft and friable throughout the stratigraphy, and evidence of secondary cementation was lacking. By contrast, in the Wadhurst Clay, sphaerosiderite horizons are poorly preserved, and sphaerosiderites are partially or wholly recrystallised. The well-preserved sphaerosiderites in the Ashdown and Tunbridge Wells Sand appear to have grown in soils that were waterlogged and reducing but contain subtle compositional and morphological heterogeneities that implies the spheres were likely growing in dynamic conditions. The elemental heterogeneity includes concentric zones of increased minor element concentration (e.g. Mn, Ca, or Mg), elemental differences between cores and rims, and enhanced minor element concentrations associated with select bladed/spherulitic crystals and/or angular zones within spheres. Considering the new constraints from abiotic growth derived from experiments presented here, it is suggested that elemental heterogeneity likely reflects variability of pH, cation concentrations, DIC, and siderite saturation in groundwaters. The spheres may have been growing close enough to the soil surface for the pore waters to be affected by periodic recharging, consistent with sedimentological evidence (e.g. channels, flash flood deposits, and storm coquinas). Overall, the good preservation of primary fabrics, lack of post-burial cements, and lack of extensive alteration suggests the sphaerosiderites were recording a primary signal and are suitable for palaeoclimatic reconstructions.

To allow for correlation with other Early Cretaceous records, a bulk organic carbon isotope ($\delta^{13}C_{org}$) record through the Wealden Supergroup was produced from 5 boreholes. The use of carbon isotope stratigraphy as a tool for correlation between dispersed localities is well established, and the $\delta^{13}C$ of terrestrial organic matter has been shown to record the same carbon cycle perturbations and long-term changes as marine carbonate and marine organic matter $\delta^{13}C$ records. The $\delta^{13}C_{org}$ record from the Wealden Supergroup in the Weald basin confirms the Berriasian–Aptian age suggested by biostratigraphy, with the onset of the Valanginian CIE identifiable in the top of the Ashdown Formation and regionally correlated from multiple boreholes. A broad Valanginian CIE is recorded, and tentatively correlated to the Early Cretaceous marine composite $\delta^{13}C$ record. However, the Wadhurst Clay Formation spans part of the peak of the CIE and contains poorly preserved organic matter with a facies-specific shift in $\delta^{13}C_{org}$ values. This facies-specific $\delta^{13}C_{org}$ shift is interpreted to be due to a change in organic matter source and/or palaeoenvironmental changes such as marine incursions; thus, the shift is discarded from the record. The evidence of marine incursions is inconclusive in the literature and in the results of this study, and further work is necessary to assess the palaeoenvironmental conditions associated with the Wadhurst Clay.

The stable isotopic compositions of sphaerosiderites from well preserved strata (Ashdown and Tunbridge Wells Sand) show invariant $\delta^{18}O_{siderite}$ (–3.5‰ to 0.6‰ VPDB) and variant $\delta^{13}C_{siderite}$ (–40‰ to 5‰ VPDB). The invariant $\delta^{18}O_{siderite}$ is interpreted to be reflective of meteoric groundwater, and the variant $\delta^{13}C_{siderite}$ is interpreted as an expression of a mixture of reactive pathways converting organic matter to DIC, as expected in a low-latitude wetland. Clumped isotope (Δ_{47}) temperatures of representative sphaerosiderites suggest the temperatures in the Weald Basin were high (33–39°C), which correlate well with summer temperatures from climate models of the Weald Basin during the Early Cretaceous. The reconstructed $\delta^{18}O_{groudnwater}$ (–3.7‰ to +2.6‰ VSMOW) based on Δ_{47} temperatures and average $\delta^{18}O_{siderite}$ is isotopically heavier than in other datasets from the Cretaceous.

However, previous sphaerosiderite studies have assumed growth in Mean Annual Temperatures (MAT) and a constancy of groundwater conditions. Using the same sphaerosiderite samples as published in Robinson et al., (2010), it was demonstrated that the Δ_{47} temperature of those samples were 10°C higher than assumed MAT, and recalculated groundwaters aligned with those from this thesis. This example stresses the importance of evaluating the local controls on siderite growth before drawing palaeoclimatic conclusions.

Comparison with General Circulation Models (GCM's) suggests the main moisture source for the Weald Basin was likely the Proto-Atlantic and/or Tethys, a saline and restricted basin with a $\delta^{18}O_{seawater}$ composition of 0.5–1‰. However, this alone cannot explain the heavy groundwaters of up to 2‰ reconstructed from the sphaerosiderites. SIMS transects of limited individual spheres suggest a decreasing $\delta^{18}O_{siderite}$ and increasing $\delta^{13}C_{siderite}$ from core to rim, interpreted to be reflecting increased evaporation in groundwaters during the earlier part of growth. The latter part of the growth (i.e. sphere rims) may have occurred deeper in the soil profile, as suggested by a trend towards more methanogenic $\delta^{13}C_{siderite}$ values. This trend is coupled with mixing lines from bulk samples suggesting evaporation may have affected the sphaerosiderites. An Early Cretaceous GCM simulation by Farnsworth *pers. comm.,* (2019) at 4 times pre industrial CO_2 levels shows highest precipitation occurred during colder months in the Weald Basin during the Valanginian and Hauterivian, when most of the sphaerosiderites analysed were forming. As the siderite Δ_{47} temperatures align well with summer temperatures in the GCM's, it is argued that the groundwaters may have been recharged seasonally, perhaps in colder months, and then were modified by evaporation during Spring as temperatures increased. Therefore, during the summer months when siderite growth was predominant, sphaerosiderites would have recorded groundwaters with higher $\delta^{18}O$, due to evaporation over Spring. Furthermore, it has been demonstrated that some modern siderite nodules form during the summer, and that modern wetlands exhibit variable ground water stable isotope compositions seasonally.

Considering these observations, the high Δ_{47} temperatures from the Wealden sphaerosiderites, and isotopically heavy reconstructed groundwaters, it is suggested here that these sphaerosiderites, at least, are likely recording summer-biased groundwater signals in the Early Cretaceous.

The stratigraphic trend of $\delta^{18}O_{siderite}$ through the Wealden Supergroup alternates between isotopically heavy and isotopically light values. This is interpreted as reflective of periods of relatively more arid (less precipitation/more evaporation) and more humid (more precipitation/less evaporation) conditions. The Wealden record shows a period of aridity at the base of the Ashdown Formation, followed by a shift towards more humid conditions in the middle of the Ashdown Formation, and then a shift towards more arid conditions towards the top of the Ashdown Formation. In the Wadhurst Clay, the sphaerosiderites are recrystallised and so no interpretations are made from them. Above the Wadhurst Clay, at the base of the Tunbridge Wells Sand, $\delta^{18}O_{siderite}$ suggests arid periods and then a shift towards more humid periods up-section towards the top of the formation. The variability through the Wealden Supergroup record mostly correlates well to Tethyan records of aridity and humidity based on palynology. During the onset of the CIE (as $\delta^{13}C_{org}$ shifts to heavier values), both the Vocontian and Weald basins preserve evidence of arid periods. During the CIE as $\delta^{13}C_{org}$ values gradually start to decrease, both basins record a period of aridity and then a period of humidity up-section towards the Valanginian-Hauterivian boundary. The peak of the CIE and associated humidity in the Tethyan record cannot be assessed in the Weald Basin due to the presence of the Wadhurst Clay with recrystallised sphaerosiderites. Sedimentological, palaeontological, and facies-specific shift in $\delta^{13}C_{org}$ from the Wadhurst Clay does suggest a palaeoenvironmental change, previously interpreted as a more oxidised transgressive facies, but evidence of salinity changes are inconclusive. However, the Wadhurst Clay needs further evaluation to clarify whether the conditions preserved are in fact, evidence of wetter conditions, similar to those preserved in Tethyan records.

Overall, the Weald Basin sphaerosiderites provide novel terrestrial temperature data to suggest continued warmth in low latitudes during the Valanginian CIE, in line with existing sea surface temperature reconstructions of the Early Cretaceous. The sphaerosiderite record presented in this thesis is also unique in that, it charts changes in stable isotope composition of sphaerosiderites through stratigraphy, covering Berriasian–Hauterivian. The stable isotope compositions of the siderite record also align well with the inferred changes in humidity associated with intensification of the hydrological cycle in the Tethyan deposits. The changes in humidity have been attributed to movements of climate belts (e.g. the Northern Hemisphere arid belt) and the Inter-Tropical Convergence Zone (ITCZ), modulated by astronomical forcing. It is probable that the same controls were applicable in the Weald Basin, which was located at similar palaeolatitude as the Vocontian Basin.

Table of Contents

Chapter 1: Introduction

1 Introduction and motivation 1

2 The climates of the Early Cretaceous 2

2.1 Atmospheric pCO_2 2

2.2 High global marine and terrestrial temperatures 3

2.3 Climatic drivers 6

2.4 Early Cretaceous transient climate perturbations 9

3 The Valanginian positive Carbon Isotope Excursion ('Weissert Event') 11

3.1 Volcanic trigger 12

3.2 Environmental change associated with Valanginian CIE 13

3.2.1 Complex palaeoenvironmental changes 13

3.2.2 Inconclusive evidence of cooling 16

3.3 Objectives of this thesis 18

4 Geological Setting: The Wealden Supergroup of the Weald Basin 19

4.1 The Weald-Wessex basins 19

4.2 Stratigraphy in the Weald Basin and Sampling 21

4.2.1 The Purbeck Group (Tithonian to Berriasian) 25

4.2.2 The Ashdown Formation (Berriasian to Valanginian) 25

4.2.3 The Wadhurst Clay Formation (Valanginian) 26

4.2.4 The Tunbridge Wells Sand Formation (Valanginian) 27

4.2.5 The Weald Clay Group (Hauterivian – Aptian) 28

4.2.6 Lower Greensand Group (Aptian – Albian) 28

4.3 Paleoclimate in the Weald-Wessex basins 29

4.4 Tectonic or climate driven lithological changes? 31

5 Proxy background 33

5.1 Carbon Isotope ($\delta^{13}C$) stratigraphy from terrestrial organic matter 33

5.1.1 A chemostratigraphic tool 33

5.1.2 Proxy Caveats 33

5.2 Sphaerosiderites as a proxy for palaeohydrology and palaeoenvironment 35

5.2.1 Elemental composition of Sphaerosiderites as a proxy for palaeoenvironment 36

5.2.2 $\delta^{18}O$ of siderite as a proxy for precipitation 37

5.2.3 Proxy caveats 39

6 Aims 41

6.1 Chapter 2: Experimental synthesis of siderite to constrain trace element uptake 42

6.2 Chapter 3: The Valanginian CIE in the Weald Basin 42

6.3 Chapter 4: Petrography and Geochemical composition of sphaerosiderites from the Weald Basin 42
6.4 Chapter 5: Palaeohydrology in the Weald Basin during the Early Cretaceous 43
6.5 Chapter 6: Conclusions and Future Work 43

Chapter 2: Geochemical controls on elemental composition of siderite; Implications for palaeo-environmental reconstructions

1 Introduction 44
2 Methods 46
3 Results 50
3.1 Fe(II)-carbonate precipitation pathways 50
3.2 Cation uptake in siderite 53
3.2.1 Mn uptake 53
3.2.2 Ca uptake in siderite 55
3.2.3 Mg uptake in siderite 56
3.3 Rates of growth 58
3.4 Effect of salinity changes 60
4 Discussion 61
4.1 Comparison to previous studies 61
4.1.1 Trace element uptake in siderite 61
4.2 Mechanisms of cation uptake in siderite 62
4.2.1 Cation hydration characteristics 62
4.2.2 Crystal structure 63
4.2.3 Surface structural control 64
4.2.4 Transport / boundary layer control 65
4.2.5 Non-Traditional Precipitation Pathways 66
4.2.6 The role of temperature 67
4.3 Elemental composition of siderite as an indicator for palaeoenvironment 68
5 Conclusions 71

Chapter 3: An Early Cretaceous terrestrial carbon isotope record of the Wealden Supergroup from the Weald Basin, UK

1 Introduction 72
2 Materials and Methods 73
3 Results 75

3.1 $\delta^{13}C_{bulk}$, $\delta^{13}C_{wood}$, Hydrogen Index (HI), Oxygen Index (OI) and Total Organic Content (TOC) from individual boreholes 76
3.1.1 Fairlight borehole (Ashdown Formation) 76
3.1.2 Westfield borehole (Ashdown Formation , Wadhurst Clay Formation) 77
3.1.3 Cooden borehole (Wadhurst Clay Formation, Tunbridge Wells Sand Formation, Weald Clay Group) 79
3.1.4 Cuckfield borehole (Wadhurst Clay Formation, Tunbridge Wells Sand Formation, Weald Clay Group) 80
3.1.5 Warlingham borehole (Tunbridge Wells Sand Formation, Weald Clay Formation) 81
4 Discussion 82
4.1 Sampling and preservation of organic matter 82
4.2 Correlation of Wealden basin strata 85
4.2.1 Inter basinal correlation 85
4.2.2 A Composite Early Cretaceous terrestrial $\delta^{13}C$ record 88
4.2.3 Correlation to the Wessex Basin 92
4.2.4 Correlation to a composite marine carbon-isotope record 96
4.3 Implications for Wealden stratigraphy and climate 97
5 Conclusions 100

Chapter 4: Petrography and elemental characterisation of sphaerosiderites from the Wealden Supergroup

1 Introduction 102
2 Materials and methods 103
2.1 Sampling from boreholes 103
2.2 Sample Preparation and Analytical Techniques 105
3 Results 106
3.1 Hand Specimen petrography 106
3.2 Thin Section and SEM 107
3.2.1 Sphaerosiderite mineralogy and morphology 107
3.2.2 Dissolution textures 113
3.2.3 Recrystallisation textures in the Wadhurst Clay Formation 114
3.3 XRD 117
3.4 Element mapping and transects 120
3.4.1 Mapping zones of minor element uptake 120
3.4.2 Quantitative elemental transects 125
3.4.3 Elemental mapping of recrystallized sphaerosiderites (Wadhurst Clay) 130
3.5 Comparison of petrography and elemental geochemistry 132

3.5.1 Siderite and Pyrite 132
3.5.2 Multiple carbonate phases 134
4 Discussion 137
4.1 Variable physiochemical conditions during the growth of Wealden sphaerosiderites 137
4.1.1 Morphological and compositional heterogeneity 137
4.1.2 Origin of pyrite inclusions in sphaerosiderites 140
4.1.3 Minor calcite precipitation 141
4.1.4 Diagenetic alteration 142
4.2 The Wealden palaeoenvironment 143
4.2.1 A dynamic palaeoenvironment 143
4.2.2 Brackish or marine influence in a freshwater wetland? 145
4.3 Implications for understanding sphaerosiderite formation in wetlands through the Phanerozoic 148
5 Conclusions 150

Chapter 5: Palaeohydrology of the Early Cretaceous Wealden Supergroup in the Weald Basin

1 Introduction 152
2 Methods 153
2.1 Sample selection and stable-isotope analyses 153
2.2 SIMS (Secondary Ion Mass Spectrometry) transects 157
2.3 Clumped isotope thermometry (Δ_{47}) 158
3 Results 159
3.1 Stable Isotopes 159
3.2 $\delta^{18}O_{siderite}$ transects (SIMS) 168
3.3 Measured clumped isotope temperatures (Δ_{47}) 171
4 Discussion 172
4.1 Standardization in siderite measurements 172
4.1.1 Stable isotope measurements 172
4.1.2 SIMS measurements 173
4.2 Wealden palaeoenvironment 176
4.3 Palaeohydrology in the Wealden 180
4.3.1 Local hydrology of the Wealden wetland 180
4.3.2 Local temperature of the Wealden wetland 183
4.3.3 Changes in hydrology: wetter and drier periods? 186
4.3.4 $\delta^{18}O_{groundwater}$ values in the Wealden Wetland 188

4.3.5 Enriched $\delta^{18}O_{groundwater}$ values: A reflection of moisture source or evaporation? 191
4.3.6 Comparison with temperature data from other Early Cretaceous studies 198
4.4 Implications for Early Cretaceous climate 199
5 Conclusions 205

Chapter 6: Conclusions and Future work

1 Conclusions 207
1.1 Sphaerosiderites As A Proxy For Palaeoenvironment 207
1.2 An Early Cretaceous Terrestrial Carbon Isotope Record From The Weald Basin 209
1.3 Early Cretaceous Palaeohydrology Of The Weald Basin 210
2 Future Work 214
2.1 Sphaerosiderites As A Proxy For Palaeoenvironment 214
2.2 Age Constraints And Sampling Resolution In The Carbon Isotope Record From The Weald Basin 214
2.3 Sphaerosiderites And Palaeohydrology 215

References Cited 218
Appendices 237

List of Tables

Chapter 2: Geochemical controls on elemental composition of siderite; Implications for palaeo-environmental reconstructions

Table 2.1: Summary of experimental variables employed in this study.....49

Chapter 5: Palaeohydrology of the Early Cretaceous Wealden Supergroup in the Weald Basin

Table 5.1: $\delta^{18}O_{siderite}$ from ETH and Oxford for four natural siderite samples used as internal standards at ETH and reported in Fernandez et al., (2016). Conversion from VPDB to VSMOW of values reported in Fernandez et al., (2016) are based on equations in Sharp (2017). 157

Table 5.2: Mean δ18Osiderite and δ13Csiderite value of the average of each sphaerosiderite horizons assessed in each formation within the Wealden Supergroup. Standard deviation is of the means of horizons from each formation. Data generated by GasBench IRMS in Oxford. 160

Table 5.3: $\delta^{18}O_{siderite}$ of representative Wealden sphaerosiderites analysed at ETH and Oxford using respective sample powder preparation methods discussed in Section 2.1 (Depths in stratigraphy shown in Figure 5.1). Most of the samples have a $\delta^{18}O_{siderite}$ offset within natural variability of $\delta^{18}O_{siderite}$ observed in natural siderites. The samples which are not within error of $\delta^{18}O_{siderite}$ values (from different methods) of each other are highlighted in grey. 165

Table 5.4: Average stable isotope compositions from SIMS transects of FC5, FC9, and FC11 (Fairlight Clays samples from Robinson et al., 2010). Data generated by SIMS, Edinburgh. 169

Table 5.5: Δ_{47} values and calculated temperatures from representative sphaerosiderite horizons through the Wealden Supergroup. Data generated at ETH. 171

Table 5.6: Comparison of FC5, FC9, and FC11 (Fairlight Clays, Robinson et al., 2010) stable isotope values between analytical techniques (SIMS, IRMS), and sample powder preparation (spheres, small and large batches of powder). SIMS data are presented as mean of the averages of each transect (and standard deviation between the averages of the transects to avoid weighting transects higher due to more analysis points). This shows significant differences between methods, particularly between SIMS and IRMS, suggesting SIMS matrix effects need to be quantified. Differences between $\delta^{18}O_{siderite}$ with small and large batches of powder arise due to averaging over different number of spheres from horizons, suggesting some sphere horizons have a higher natural variability than is noted in smaller batches of powder. 175

Table 5.7: Compilation of $\delta^{13}C_{siderite}$ from published sphaerosiderite studies (modified from table in Weibel et al., 2016). 179

Table 5.8: Comparison of low-latitude proxy-based temperatures (Littler et al., 2011) and model temperatures (Farnsworth, *pers. comm.,* 2019). 198

List of Figures

Chapter 1: Introduction

Figure 1.1: Atmospheric pCO_2 reconstructions based on palaeosols, alkenones, and stomatal records for the Cretaceous, and the loess best fit (based on full dataset from Foster et al., 2017). 3

Figure 1.2: Long-term marine temperature trends during the Cretaceous based on temperature reconstructions from TEX_{86} and $\delta^{18}O$ of foraminifera (Figure from O'Brien et al, 2017). 4

Figure 1.3: Berriasian and Aptian palaeogeography, climate indicators and zones (figure modified from Hay and Floegel (2012), based on Chumakov et al (1995)). 5

Figure 1.4: Latitudinal change in precipitation flux for the Mid Cretaceous (Figure from Suarez et al., 2011). The temperature estimates correspond to leaf physiognomy based estimates from Wolfe and Upchurch (1987) and Spicer and Corfield (1992), Genesis-MOM from Zhou et al (2008), and warm and cool Cretaceous estimates from Barron et al (1983). 8

Figure 1.5: Short- and intermediate-term carbon cycle (modified from Skelton, 2003, based on Berner, 1999). 9

Figure 1.6: Box model for the long-term carbon cycle where grey boxes are reservoirs, green boxes are processes, and estimated fluxes of carbon are in black arrows (modified from Skelton, 2003). 10

Figure 1.7: The Valanginian positive Carbon Isotope Excursion (CIE) expressed in a Tethyan composite and in wood fragments from Crimea (Figure from Grocke et al, 2005). 12

Figure 1.8: A synthesis of palaeoenvironmental change during the Valanginian CIE from Follmi et al., (2012). The time scale is tuned to Gradstein et al., (2004). 14

Figure 1.9: Extent of deposition in the Weald-Wessex basins, palaeo-coastlines and source massifs. Dotted lines are current coastlines. Figure modified from Radley and Allen, (2012). 19

Figure 1.10: Stratigraphy of the Weald Basin with the main groups and formations of interest to this thesis. Age assigned based upon the biostratigraphy of Horne, (1995). Figure modified from Robinson et al., (2010). 21

Figure 1.11: Lithostratigraphy and location of boreholes from the British Geological Survey used to sample the main stratigraphic units in the Weald Basin based on core sheets. Depth values(metres) shown against each borehole and depths at which rootlets and sphaerosiderite horizons are noted in the core sheets. 24

Figure 1.12: Schematic of siderite growing in a wetland system, modified by Stuart Robinson from Ludvigson et al. (1998). 35

Figure 1.13: Schematic of Meteoric Sphaerosiderite Lines (MSL) and mixing lines in sphaerosiderites based on Ludvigson et al. (1998) (from Stuart Robinson). 38

Chapter 2: Geochemical controls on elemental composition of siderite; Implications for palaeo-environmental reconstructions

Figure 2.1: SEM micrographs of experimental precipitates showing representative morphological end-members. A to C) Fe concentration 1 mmol/kg, D to F) Fe concentration 10 mmol/kg. Morphological diversity is attributed to the range of siderite saturation states investigated, which in turn controls the rates of nucleation and growth. As shown from A to C and D to F, increasing pH causes precipitates to change from pure siderite to a mixture of siderite and chukanovite, to pure chukanovite. E shows a spherical particle with no apparent crystalline morphology at the resolution limit of the SEM (10s of nm), and is interpreted to be amorphous iron carbonate (AFC), which recrystallized to form the spherical clusters of rhombs, similar to polycrystalline particles shown in D. 51

Figure 2.2: Selection of growth experiments displaying cation concentration in solution with time. Pure siderite seed (0.5g) was added at the start of all experiments. Fe and Mn uptake are notable. The differences in Fe uptake reflect differences in starting pH and pCO_2, and therefore saturation state, between the experiments. Fe/Mn of the solution increases with decreasing siderite saturation, indicating that Mn is incorporated into the precipitate in preference to Fe with decreasing reaction rate of siderite. Ca and Mg concentrations are generally invariable, and uptake is not discernible. The final concentrations of Ca and Mg in all experiments are within error of the initial concentration. 54

Figure 2.3: Fe/Mn of precipitate and initial solution in growth and nucleation experiments. Fe/Mn of final precipitate was calculated from the initial and final Fe/Mn ratios from solutions. 55

Figure 2.4: Control growth experiments with only Fe and Ca in starting solution showed decrease in Ca, but within error. Therefore, no discernible uptake can be noted from the control experiments. 56

Figure 2.5: Control experiments with Fe and Mg as the only available cations to monitor Mg uptake in siderite at elevated temperatures, and in the absence of competing cations. Mg uptake was only discernible at 55°C. 58

Figure 2.6: Calculated K_{sp} = -10.28 at Mn substitution of 11 mol% into the carbonate phase formed on average during seeded growth experiments. 59

Figure 2.7: Experimental rates (mol//m^2/hr) from seeded growth experiments. Dashed lines indicate 95% confidence intervals. 60

Figure 2.8: Comparisons of apparent distribution coefficients (Kd') from Romanek et al (2009), Rimstidt et al (1998) and calculated Log K (Rimstidt et al., 1998). Kd is positively correlated to the solubility quotient of siderite with respect to trace cation, displaying a clear preference of Mn uptake over Ca and Mg. 61

Chapter 3: An Early Cretaceous terrestrial carbon isotope record of the Wealden Supergroup from the Weald Basin, UK

Figure 3.1: $\delta^{13}C_{bulk}$, $\delta^{13}C_{wood}$, Hydrogen Index (HI), Oxygen Index (OI,) and Total Organic Content (TOC) with depth in the Fairlight borehole (HC in units is Hydrocarbon, Wad. Clay = Wadhurst Clay). A moving average (span of 3) is fitted through all $\delta^{13}C_{org}$ data. 6 samples with low S2 peaks were discarded from the HI and OI figures. 76

Figure 3.2: $\delta^{13}C_{bulk}$, Hydrogen Index (HI), Oxygen Index (OI), and Total Organic Content (TOC) with depth within the Westfield borehole. A moving average (span of 3) is fitted through all $\delta^{13}C_{org}$ data (Stratigraphy Key: TWS = Tunbridge Wells Sand). 4 samples with low S2 peaks were discarded from the HI and OI figures. 77

Figure 3.3: $\delta^{13}C_{wood}$, $\delta^{13}C_{bulk}$, Hydrogen Index (HI), Oxygen Index (OI), and Total Organic Content (TOC) with depth within the Cooden borehole. A moving average (span of 3) is fitted through all $\delta^{13}C_{org}$ data. 4 samples with low S2 peaks were discarded from the OI and HI plots. 79

Figure 3.4: $\delta^{13}C_{bulk}$, $\delta^{13}C_{wood}$, Hydrogen Index (HI), Oxygen Index (OI) and Total Organic Content (TOC) with depth within the Cuckfield borehole. A moving average (span of 3) is fitted through all $\delta^{13}C_{org}$ data. 10 samples with low S2 peaks were discarded from the HI and OI plots. 80

Figure 3.5: $\delta^{13}C_{bulk}$, Hydrogen Index (HI), Oxygen Index (OI), and Total Organic Content (TOC) with depth within the Warlingham borehole. A moving average (span of 3) is fitted through all $\delta^{13}C_{org}$ data. 11 samples with low S2 peaks were discarded from the HI and OI plots. 82

Figure 3.6: HI versus OI within formation of the Wealden Supergroup. HI values are mostly < 200 mg HC/g TOC and OI values are usually < 200 mg CO2/g TOC. There is some scatter in HI values, particularly in the Ashdown Formation and the Wadhurst Clay. The Wadhurst Clay values also cluster along the HI axis more than the other formations, although the trend cannot be conclusively determined due to the limited sampling resolution. 84

Figure 3.7: Regional correlation using carbon isotope composition in the Weald Basin using 5 boreholes with moving average best fit line through individual boreholes. Regional correlation suggests the long-term trends between the boreholes corroborate. 87

Figure 3.8: Composite carbon isotope record of the Wealden Supergroup from the Wealden Basin, based on 5 boreholes; Fairlight, Westfield, Cuckfield, Cooden, and Warlingham. . 89

Figure 3.9: a) Composite carbon isotope record of the Weald Basin with a moving average with a span of 3. b) Composite $\delta^{13}C_{org}$ record of the Weald Basin with moving average fit once Wadhurst Clay data is removed. 90

Figure 3.10: Comparison between the composite carbon isotope records from the Weald and Wessex Basins. The Wessex Basin composite record (Robinson and Hesselbo, 2004) and the Weald Basin composite are plotted with a moving average with span of 3. Tentative correlations between the two basins are drawn in grey. 95

Figure 3.11: Comparison of the marine carbon isotope composite record (Ogg et al., 2016) with composite carbon isotope record of the Wealden Basin. Shaded areas are tentative correlations between the marine and terrestrial record. 97

Chapter 4: Petrography and elemental characterisation of sphaerosiderites from the Wealden Supergroup

Figure 4.1: Lithostratigraphy and location of the sampled boreholes (Detailed in Chapter 1). Depth in metres within individual boreholes. Sphaerosiderite horizons samples are marked at depth within relevant boreholes, those in blue were found to be suitable for palaeoclimate reconstructions (based on geochemical and isotopic characterisation in Chapter 4 and 5), those in red were not used in palaeoclimate reconstructions. 104

Figure 4.2: Representative hand specimen from the Ashdown Formation containing sphaerosiderites in a fine sandstone matrix. 107

Figure 4.3: Thin Section photomicrographs in cross polarised light of sphaerosiderites from A) sample CX1 (Tunbridge Wells Sand) with characteristic maltese cross extinction in the central part of the sphere and an oxidised rim and B) sample F13 (Ashdown) which lacks internal zonations but overall colour is red/brown indicating oxidation. The matrix consists mainly of quartz and clays, although the yellowish hue of quartz crystals suggests the thin section was > 30 μm in thickness. C) Sample CX1 thin section from A in Backscatter Imaging (SEM) showing compositional differences through contrast changes and spherulitic texture. D) BSE image of a sphere from sample W2 showing compositional differences in the outer rim compared to core, and clay and quartz inclusions. The depths and locations of the sphaerosiderite horizons can be found in Figure 4.1. 108

Figure 4.4: Representative sphaerosiderite morphologies. A) Spheres from F11 (Ashdown Formation, Fairlight borehole) with distinct central and outer zone with radial edges. B) Sphere from FX5 (Ashdown Formation, Fairlight borehole) which is homogenous and contains pyrite inclusions. C) Sample C9o (Tunbridge Wells Sand, Cooden borehole) containing a sphere with quartz inclusions and a blocky outer rim. D) Sphere from 67096 (Wadhurst Clay, Cooden Borehole) which is recrystallised but preserves the primary radial edges. E) Sphere from W3 (Ashdown Formation, Westfield borehole) with a microcrystalline core and radial spherulitic crystals on outer rim which are compositionally different to the core. D) Sphere from 67209F (Ashdown Formation, Fairlight borehole) with mottled contrast changes indicating subtle compositional differences. The depths and locations of the sphaerosiderite horizons can be found in Figure 4.1..... 110

Figure 4.5: Examples of variation in quartz and clay inclusions in sphaerosiderites from a) Wadhurst Clay b) Tunbridge Wells Sand, c) Ashdown Formation, and d) Tunbridge Wells Sand. Quartz inclusions vary in size and quantity, and clays are usually smaller than quartz inclusions. The depths and locations of the sphaerosiderite horizons can be found in Figure 4.1. 111

Figure 4.6: a) Example of sulphide inclusions (clusters of bright white contrast) in a sphaerosiderite from sample F10 (Ashdown Formation). b) Close up of a pyrite inclusion containing within it inclusions of siderite (light grey) and quartz and clays (dark grey). The depths and locations of the sphaerosiderite horizons can be found in Figure 4.1. 112

Figure 4.7: Dissolution textures (gaps or holes within spheres) from a range of stratigraphic horizons within the Wealden Supergroup A) FX6, Ashdown Formation B) F19, Ashdown Formation, C) 67237Cuc, Weald Clay, D) 67241Cuc, Tunbridge Wells Sand, which may be

due to the core falling out during sample preparation. The depths and locations of the sphaerosiderite horizons can be found in Figure 4.1. 114

Figure 4.8: Recrystallisation in A) C11, Wadhurst Clay, B) C12 Wadhurst Clay, from Cooden borehole, and C) W1 Wadhurst Clay from Westfield borehole. The depths and locations of the sphaerosiderite horizons can be found in Figure 4.1.....116

Figure 4.9: XRD spectra containing siderite from representative examples (F2, F12 and FC11 [Sample from Robinson et al., (2010)] from Ashdown, C1 and CX2 from Tunbridge Wells Sand,). Dotted line signifies siderite, abbreviations: qtz=quartz, kln=kaolinite, ill=illite. The depths and locations of the sphaerosiderite horizons can be found in Figure 4.1. 117

Figure 4.10: Siderite, Quartz, and Clay components within a composite depth produced with the assumption that sedimentation rates were similar in Fairlight, Westfield, and Cooden boreholes due to proximity. 118

Figure 4.11: Compositional changes across a sphere from C9 with an Mn rich core and a rim enriched comparatively in Ca and Mg (Sample C9, Tunbridge Wells Sand). Average substitution of Mn within this single sphere was 3.3 (± 0.3) ox%, Ca was 1.2 (± 0.2) ox% and Mg was 0.2 (± 0.1) ox%. The depths and locations of the sphaerosiderite horizons can be found in Figure 4.1.....121

Figure 4.12: Element Map of C1 (Tunbridge Wells Sand) showing concentric zones of Fe and Mn enrichment, with concentrations anti-correlated to each other. This is a particularly oxidised sample (1:2 ratio of siderite to hematite) but preserves fine scale elemental variations in Fe and Mn concentrations. See text for compositional details. The depths and locations of the sphaerosiderite horizons can be found in Figure 4.1.....122

Figure 4.13: Sphere from sample W2(Ashdown Formation) showing evidence of some parts of the nodule enriched in Ca corresponding to lower Fe content (less bright areas in Fe map – dotted white line), as well as evidence of Mn and Ca zoning in rim (arrows). The depths and locations of the sphaerosiderite horizons can be found in Figure 4.1.....124

Figure 4.14: Elemental transect from C1 (Tunbridge Wells Sand), showing higher concentration of Mn in core, and higher concentration of Mg and Ca in rim. Fe and Mn show a negative correlation. Correlations between other cations are weak. The depths and locations of the sphaerosiderite horizons can be found in Figure 4.1.....125

Figure 4.15: Elemental transect from F6 (Ashdown), showing higher concentration of Ca and Mg in core, negatively correlated to Fe. Mn concentrations remain low throughout the transect. The depths and locations of the sphaerosiderite horizons can be found in Figure 4.1. 126

Figure 4.16: Elemental transect from W2 (Ashdown), showing higher concentrations of Mn and Ca, and decrease in Mg concentration along a 150 µm length of the transect while concentrations of minor elements elsewhere in the transetc vary. Strong negative correlation is notable between Fe and Ca, and Fe and Mn. The depths and locations of the sphaerosiderite horizons can be found in Figure 4.1. 128

Figure 4.17: Correlations between all elemental transect data shows a large scatter. None of the correlations are statistically significant, apart from between Fe and Ca. These data comprise of 19 spheres from the Ashdown Formation, 2 from the Wadhurst Clay Formation, and 8 from the Tunbridge Wells Sand Formation. 129

Figure 4.18: Sample C11 from the Wadhurst Clay shows internal recrystallisation in core and primary fabric preserved in outer rim. Elemental map shows dispersed uptake of Mn and Ca, and primary Mn concentric zoned uptake preserved at rims (white arrow). The depths and locations of the sphaerosiderite horizons can be found in Figure 4.1. 131

Figure 4.19: Sulphide inclusions within a sphaerosiderite. The sulphide inclusions are rounded with blocky edges, randomly orientated, and dispersed through the core of the sphere. Mapping the inclusion shows siderite inclusions within, and minor quartz and clays. The depths and locations of the sphaerosiderite horizons can be found in Figure 4.1. 133

Figure 4.20: Sample F19 from the Fairlight Borehole and the Ashdown Formation showing a pseudo sphaerosiderite, consisting of a calcite block with siderite growing on the rim and layers of intergrowth in between. The depths and locations of the sphaerosiderite horizons can be found in Figure 4.1. 135

Figure 4.21: Sample 67241Cuc from the Tunbridge Wells Sand. A siderite sphere with uniform crystal sizes (cryptocrystalline centre) and evidence of calcite rhombs growing in the matrix surrounding the spheres, as well as incorporated into the sphere. The core of the sphere is 136

Chapter 5: Palaeohydrology of the Early Cretaceous Wealden Supergroup in the Weald Basin

Figure 5.1: Sphaerosiderites sampled for stable isotope analyses. In blue are the sphaerosiderite samples deemed suitable for palaeoclimatic analyses. In red are the sphaerosiderites samples deemed unsuitable for palaeoclimatic reconstruction based on preservation (Figure presented first in Chapter 4, Figure 4.1).....154

Figure 5.2: Invariant $\delta^{18}O_{siderite}$ and variant $\delta^{13}C_{siderite}$ of sphaerosiderites from the Wealden Supergroup. Spheres from the same horizon plot along these linear trends known as Meteoric Sphaerosiderite Lines (MSL's), suggesting they are recording a local $\delta^{18}O_{groundwater}$ signal, thought to be reflective of the meteoric groundwater in the waterlogged soils in which they are growing. Data generated by GasBench IRMS in Oxford. 161

Figure 5.3: Stable isotope data from sphaerosiderite horizons that do not exhibit Meteoric Sphaerosiderite Lines. Data generated by GasBench IRMS in Oxford.....162

Figure 5.4: Average $\delta^{18}O_{siderite}$ values of MSL horizons in the Ashdown, Wadhurst Clay and Tunbridge Wells Sand Formations. $\delta^{18}O_{siderite}$ values alternate between isotopically heavy and light values and are decoupled from lithological changes. 164

Figure 5.5: Carbon-Oxygen plot of siderite samples from this thesis (C5, C9, F5, F11) and from Robinson et al., (2010) (FC5,9 and 11) analysed at ETH and Oxford.....166

Figure 5.6: Average value from measurements at ETH, Oxford, and ETH-Oxford combined for samples from this thesis (C5, C9, F5, F11) and from Robinson et al., (2010) (FC5,9 and 11). 167

Figure 5.7: Stable isotope transects and representative backscatter images of two sphaerosiderite nodules (5-2 and 5-3) from FC5, one of three sphaerosiderite horizons

sampled from the Fairlight Clays (Ashdown Formation) from Robinson et al., (2010). Data generated by SIMS, Edinburgh. 168

Figure 5.8: Stable isotope transects and representative backscatter images of two sphaerosiderite nodules (11-1 and 11-2) from FC11 (Robinson et al., 2010) showing a noisy $\delta^{18}O$ transect, but the $\delta^{13}C$ transect trends are similar to those noted in FC5 and FC9. Data generated by SIMS, Edinburgh. 169

Figure 5.9: Representative elemental composition transects from sphaerosiderite horizons FC5, FC9, and FC11 showing changes in Fe, Mn, Mg, and Ca across spheres. 170

Figure 5.10: $\delta^{13}C_{siderite}$ values from each sphaerosiderite horizon with composite depth (composite depth based on assumption that due to the proximity of the Fairlight, Cooden, and Westfield boreholes, and that the sedimentation rates were similar between them). . 178

Figure 5.11: Mean $\delta^{18}O_{siderite}$ of sphaerosiderite horizons plotted with 1σ on a composite depth scale and a moving average (span of 3). Sphaerosiderites show a long-term $\delta^{18}O_{siderite}$ trend of alternating isotopically heavier and isotopically lighter values over the Berriasian–Valanginian, likely reflecting changes in local hydrology. 182

Figure 5.12: Average $\delta^{18}O_{siderite}$ of sphaerosiderite horizons plotted with 1σ on a composite depth scale, and a moving average best fit of each borehole with a span of 3. Δ_{47} temperatures from representative sphaerosiderite horizons through the stratigraphy are within error of each other and show the Weald Basin to have been consistently warm. 185

Figure 5.13: Fluctuating $\delta^{18}O_{siderite}$ could reflect wetter and drier periods in the Weald Basin due to regional changes in climate. Mean $\delta^{18}O_{siderite}$ of sphaerosiderite horizons plotted with 1σ and a moving average with a span of 3. The samples FC5, FC9, and FC11 (Robinson et al, 2010) are correlated to these boreholes by their depth in relation to the Lee Ness Sandstone, which is identified in the Fairlight borehole. 187

Figure 5.14: $\delta^{18}O_{groundwater}$ calculated using the maximum, mean, and minimum $\delta^{18}O_{siderite}$ on assumed MAT of 20-25°C (Slade and Batten, 1984) using the siderite-water fractionation equation of Carrothers et al., (1988). 189

Figure 5.15: $\delta^{18}O_{groundwater}$ calculated from the Wealden sphaerosiderites (using the minimum and maximum Δ_{47} siderite formation temperatures) are more isotopically heavy than the Albian gradient (Ufnar et al , 2004a) predicts for the palaeolatitude of the Weald Basin during the Early Cretaceous. 190

Figure 5.16: Early Cretaceous global annual average $\delta^{18}O_{seawater}$ from the Berriasian, Valanginian, and Hauterivian (Farnsworth, *pers. comm.*, 2019). The white star is approximate location of Weald Basin. 192

Figure 5.17: Average monthly changes from Berriasian-Hauterivian using data from Farnsworth, *pers. comm.,* 2019. The range of $\delta^{18}O_{groundwater}$ values are plotted for reference. 194

Figure 5.18: Valanginian model parameters: Monthly temperature (°C), precipitation (mm/day), evaporation (mm/day), and $\delta^{18}O_{precipitation}$. 196

Figure 5.19: Comparison between the Wealden carbon isotope composite record and the siderite composite record. Periods of humidity and aridity are at times decoupled from the carbon cycle changes. However, at other times like the onset of the Valanginian CIE, the

siderites record synchronous climatic changes. Timescale of the Tethyan record is GTS16 (Ogg et al., 2016). 200

Figure 5.20: Comparison of the Wealden sphaerosiderite record to spore-pollen assemblages from Kujau et al., 2013. At the onset of the Valanginian CIE, the siderite record matches the aridity in the Vocontian Basin. The siderite record correlated well to the humid/arid periods noted in the Upper Valanginian in the Vocation Basin. 204

Chapter 1
Introduction

1 Introduction and motivation

As water is a key resource for life on our planet, understanding the impact of anthropogenic climate change on the hydrological cycle is imperative. The operation of past greenhouse climates documented in the geological record (like the Cretaceous, 145–66 Ma) can provide important insight into the key processes regulating the hydrological cycle on Earth under elevated global temperatures. Understanding these past climates and climate mechanisms can provide a means to understand the response of the hydrological cycle to future climate change.

The Cretaceous world is perceived as warm, equable, and with high atmospheric pCO_2 (Barron, 1983; Barron and Peterson, 1989; Tarduno et al., 1998; Berner and Kothavala, 2001; Wallmann, 2001; Robinson et al., 2002; Friedrich et al., 2012; Jenkyns et al., 2012; Foster et al., 2017; O'Brien et al., 2017), and has been the focus of much interest as it hosts a number of global transient carbon cycle perturbations (Schlanger and Jenkyns, 1976; Arthur et al., 1985; Jenkyns, 2003; Jenkyns, 2010). In the warm greenhouse world of the Cretaceous, an intensified hydrological cycle is thought to have played a key role in maintaining increased latitudinal heat transport, supporting a more equable world (Barron, 1983; Barron and Peterson, 1989; Ufnar et al., 2002; Ufnar et al., 2004a; Suarez et al., 2011). However, evidence for an intensified hydrological cycle can be somewhat limited temporally and spatially, as well as, somewhat qualitative. Much of the research on Cretaceous climates has focused on the marine events of the Mid–Late Cretaceous (such as oceanic anoxic

events), but the Early Cretaceous hosts several of these global events, not all of which are as yet fully understood. Terrestrial datasets from the Cretaceous are also, generally sparse, but could provide crucial insights into Cretaceous hydrology and its responses during these global climate change events.

Soil carbonates from terrestrial deposits in the geological past can provide important insight into meteoric groundwater compositions in ancient wetlands, and by extension, provide information about the palaeohydrological cycle (Ludvigson et al., 1998; Ufnar et al., 2004b). Wetlands are also an important component of the modern hydrological cycle, and contribute to carbon storage, methane, and water vapour flux. Therefore, understanding ancient wetlands systems remains necessary to constrain responses of the hydrological cycle to climate change, and also to evaluate climate drivers in a greenhouse world. This thesis focuses on reconstructing hydrological changes using Early Cretaceous (Berriasian–Barremian) soil carbonates (specifically, siderite, $FeCO_3$) from the Wealden Supergroup, UK, in order to evaluate terrestrial climate, palaeoenvironment, and hydrology. Using a carbon isotope ($\delta^{13}C$) record from terrestrial organic matter within the Wealden Supergroup, this thesis evaluates the global implications of this Early Cretaceous terrestrial climate record and contextualises how local changes in hydrological cycling responded to a global carbon cycle perturbation.

2 The climates of the Early Cretaceous

2.1 Atmospheric pCO_2

It is generally accepted that the major control on climate over geological time is the changing concentration of atmospheric pCO_2 (Retallack, 2002; Royer, 2008; Beerling and Royer, 2011; Foster et al., 2017), and during past warm periods, proxy evidence suggests elevated CO_2 levels compared to the present day. During the Cretaceous, the atmospheric

pCO_2 reconstructions (Figure 1.1) indicate a range of 250–2985 ppm during the Cretaceous, (Retallack, 2002; Robinson et al., 2002; Haworth et al., 2005; Royer et al., 2012; Franks et al., 2014; Foster et al., 2017 and references therein). The scatter is attributed to artefacts of proxies or to natural variability in pCO_2 (Bice et al., 2006). Although a large scatter exists, the proxies reveal a general long-term trend (Ekart, 1999; Franks et al., 2014; Wang et al., 2014; Foster et al., 2017). The trend of the LOESS regression (Figure 1.1) implies an increase in pCO_2 is from Berriasian to Turonian, followed by pCO_2 decrease towards the Late Cretaceous (Foster et al., 2017). This trend also implies that climate during the Cretaceous may have seen an overall warming until the Mid Cretaceous before experiencing a long-term cooling towards the Late Cretaceous.

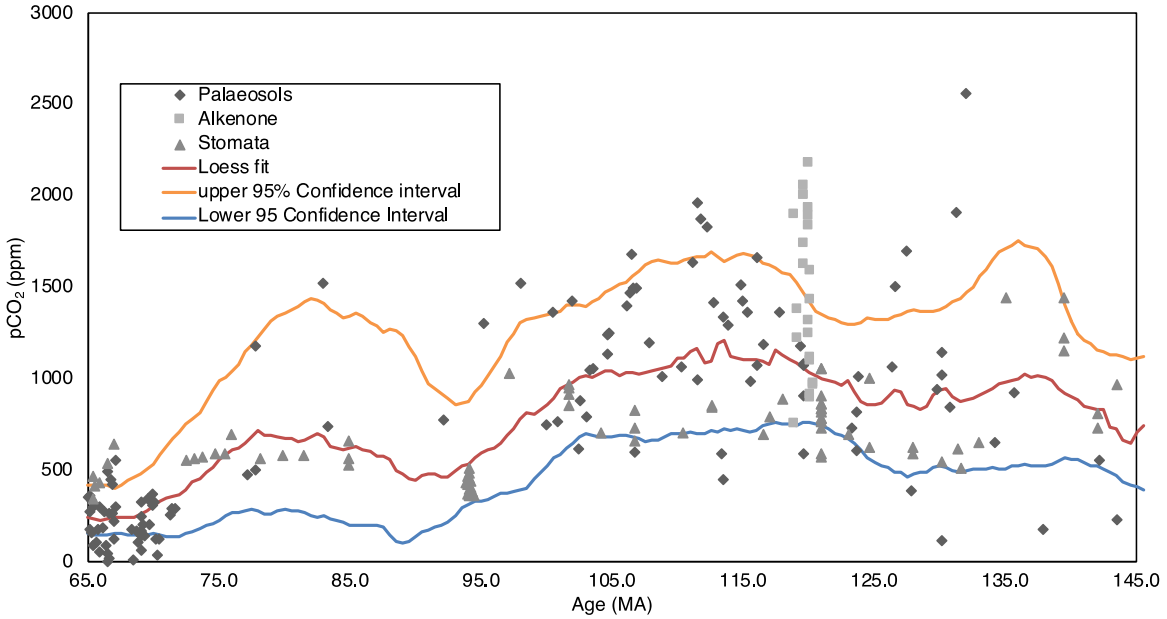


Figure 1.1: Atmospheric pCO_2 reconstructions based on palaeosols, alkenones, and stomatal records for the Cretaceous, and the loess best fit (based on full dataset from Foster et al., 2017).

2.2 High global marine and terrestrial temperatures

Sea surface temperature (SST) reconstructions from TEX_{86} (TetraEther indeX of tetraethers composed of 86 carbon atoms), and $\delta^{18}O$ of planktonic foraminifera suggest that Early Cretaceous oceans were warm, with high-latitude surface temperatures > 20 ºC and

low-latitude surface temperatures > 30 ºC (Huber et al., 1995; Schouten et al., 2003; Mutterlose et al., 2010; Littler et al., 2011; Jenkyns et al., 2012; Price and Passey, 2013; Meissner et al., 2015; O'Brien et al., 2017 and references therein; Vickers et al., 2019). Deep and intermediate waters during the Cretaceous were also significantly warmer than modern day (> 20 ºC based on $\delta^{18}O$ of benthic foraminifera) (Friedrich et al., 2012; O'Brien et al., 2017 and references therein). The sea surface temperatures suggest warm temperatures throughout the Cretaceous, but with a trend towards warming to the Mid-Cretaceous and then cooling in the Late Cretaceous (Figure 1.2).

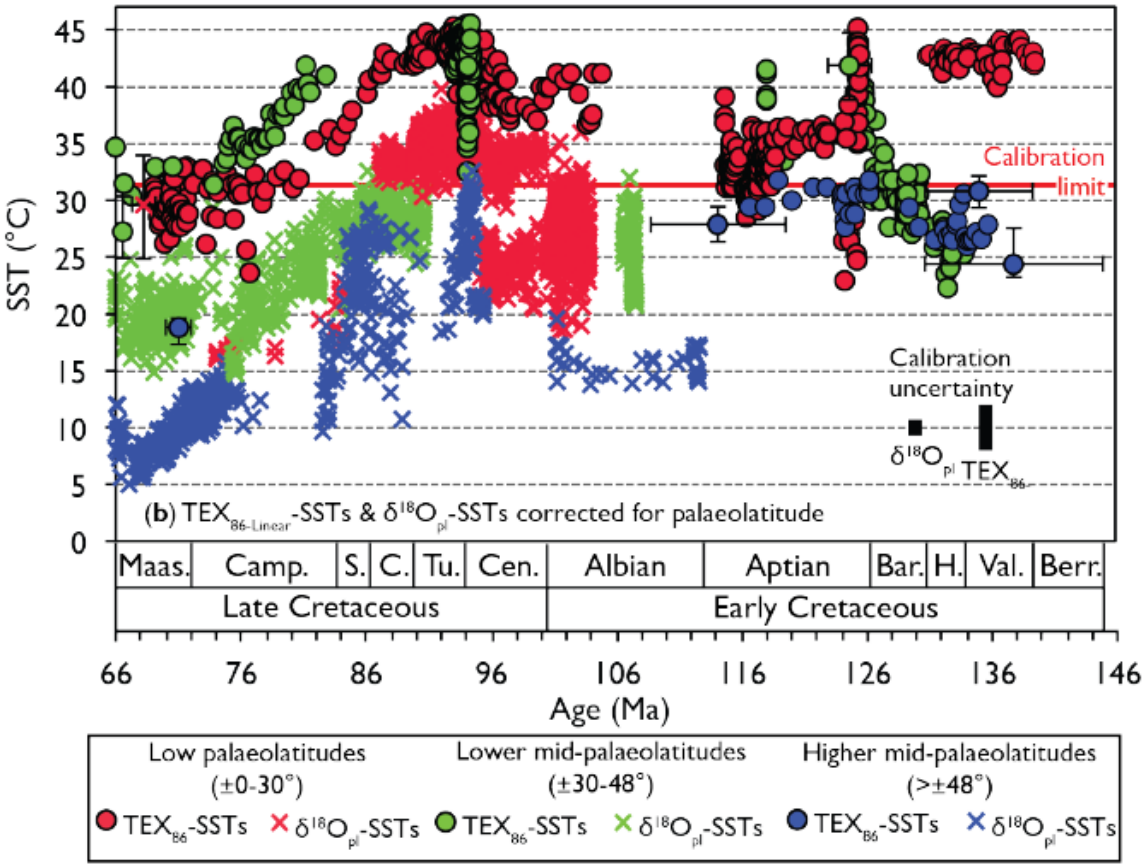


Figure 1.2: Long-term marine temperature trends during the Cretaceous based on temperature reconstructions from TEX_{86} and $\delta^{18}O$ of foraminifera (Figure from O'Brien et al, 2017).

Latitudinal temperature gradients in the oceans during the Cretaceous were also lower compared to present day, approximately 0.2–0.3 ºC per 1º latitude between 15º and 53º,

compared to the modern day 0.5 ºC in Northern Hemisphere and 0.6 ºC in Southern Hemisphere per 1º latitude (Barron, 1983; Barrera, & Savin, 1999; Huber et al., 2002; Bice et al., 2006; Littler et al., 2011; Upchurch et al., 2015; O'Brien et al., 2017).

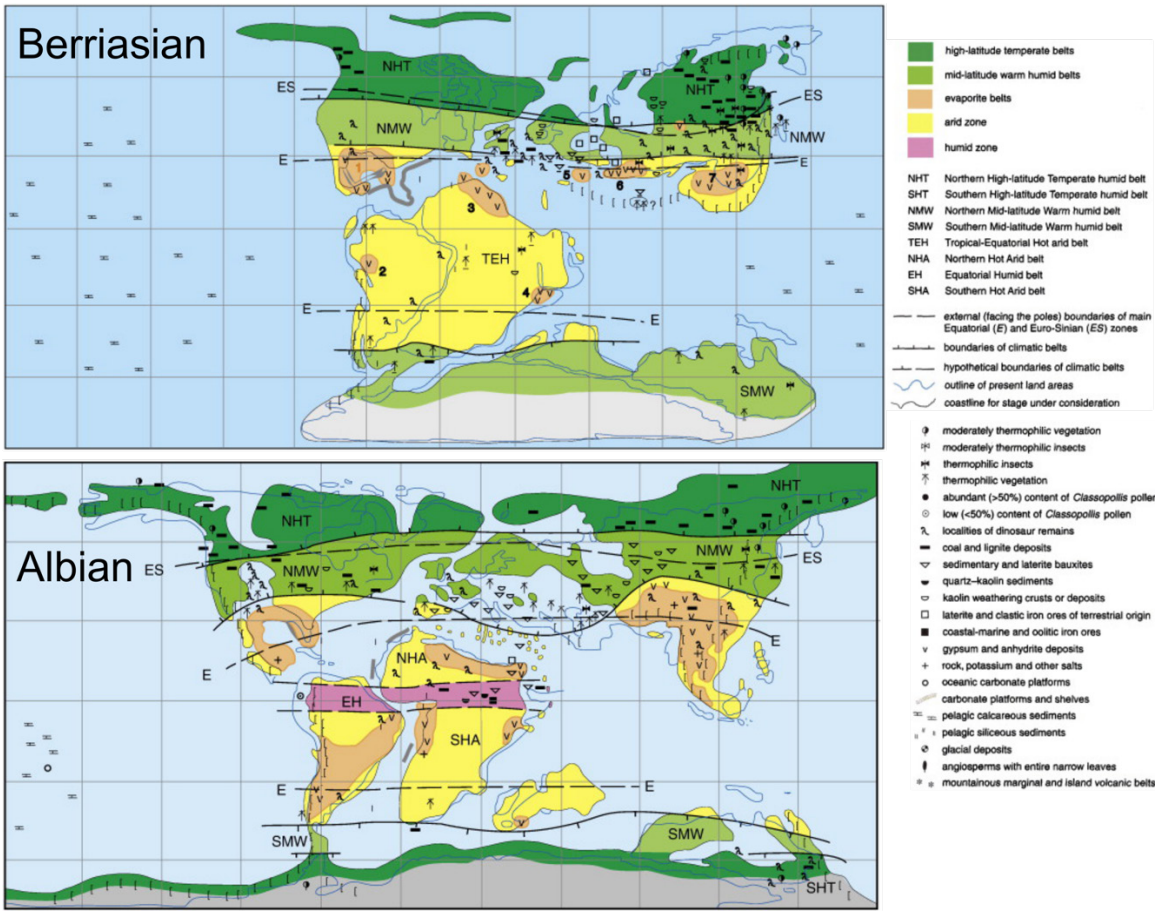


Figure 1.3: Berriasian and Aptian palaeogeography, climate indicators and zones (figure modified from Hay and Floegel (2012), based on Chumakov et al (1995)).

Continental temperature reconstructions from the Early Cretaceous are generally limited in temporal and spatial resolution, and suggest Mean Annual Temperatures at low latitudes of approximately 20–25 ºC (Sladen and Batten, 1984; Allen et al., 1998). Terrestrial temperatures of 10–19°C (dependent on proxy) are suggested at higher latitudes from Barremian–Turonian (Herman and Spicer, 1996; Herman and Spicer, 2010; Amiot et al., 2011). Early Cretaceous (Berriasian–Albian) climate belt reconstructions indicate widespread aridity in continental interiors at the equatorial region, with more humid and

temperate belts at > 30º latitudes (Chumakov et al., 1995; Hay and Floegel, 2012). Phosphate, clay, and spore-pollen assemblages from Tethyan deposits indicate fluctuating arid and humid periods occurred at mid-low latitudes (< 40ºN), with climate belt locations likely sensitive to astronomical forcing (Duchamp-Alphonse et al., 2011; Kujau et al., 2013; Westermann et al., 2013). During the Albian, rising sea levels (Huber et al., 2002; Miller et al., 2011; Haq, 2014; Sames et al., 2015) and the presence of continental seaways increased humidity in the continental interiors, leading to increased evidence of equatorial humid zones (Figure 1.3).

2.3 Climatic drivers

Atmospheric pCO_2 is considered the primary driver of Phanerozoic climate change (Royer et al., 2004; Royer, 2008; Royer, 2010; Beerling and Royer, 2011; Royer et al., 2012). For instance, sea surface temperatures increase from the Early Cretaceous (Berriasian–Valanginian) to the Mid-Cretaceous (Cenomanian–Turonian) and then decrease towards the Late Cretaceous, seemingly co-varying with atmospheric pCO_2 changes (Figure 1.1 and 1.2). However, large scatter and sparse resolution in the Early Cretaceous atmospheric pCO_2 record, and temporal and spatial biases in the temperature records (e.g. low resolution in Berriasian, Albian) can make intercomparisons difficult.

Furthermore, despite significant pCO_2 changes throughout the Cretaceous, there is clear evidence of sustained warmth (Friedrich et al., 2008; Littler et al., 2011; Jenkyns et al., 2012; O'Brien et al., 2017 and references therein). Coupled with model-data disparities, particularly in the high latitudes (DeConto et al., 1999; Zhou et al., 2012; Hay et al., 2019), parameters other than CO_2 are thought to have also played a role in maintaining greenhouse conditions. Increased atmospheric and oceanic heat transport may have contributed to reduced equator to pole temperature gradients in a warmer greenhouse world (Barron, 1983; Ufnar et al., 2004a; Hay et al., 2019). For instance, a weakening of subtropical and polar

fronts due to atmospheric circulation changes has been suggested as a possible method of increasing heat transport to poles (Hay, 2008; Hay and Floegel, 2012). Climate modelling and proxies suggest that palaeogeographic changes (Chumakov et al., 1995; Hay and Floegel, 2012; Lunt et al., 2016), other greenhouse gases like methane and water vapour (Jahren et al., 2001; Ufnar et al., 2004a; Beerling et al., 2009; Suarez et al., 2011), and cloud feedbacks (Kirk-Davidoff et al., 2002; Kump and Pollard, 2008) were also drivers of climate change in the Cretaceous.

The role of hydrology and terrestrial climate in sustaining warmth, and their response to climate change events has generated significant interest in recent decades. With increased global temperatures, the atmosphere's vapour-holding capacity increases, increasing latent heat transfer from equator to poles and contributing to a shallower latitudinal temperature gradient (Ufnar et al., 2002; Ufnar et al., 2004a; Suarez et al., 2011). Water vapour is also an important greenhouse gas and increased concentrations in the atmosphere reinforces greenhouse conditions (Hay and DeConto, 1999). Based on terrestrial precipitation reconstructions from the Early–Mid Cretaceous and mass balance calculations (Figure 1.4), an increase in global temperatures is thought to increase mid-latitude humidity and width of the humid belt (Ufnar et al., 2002; Ufnar et al., 2004a; Suarez et al., 2011; Hasegawa et al., 2012; Hay and Floegel, 2012). Evidence for this includes the distribution of deserts in the warmer Mid-Cretaceous, which suggests shrinking of the Hadley cell when pCO_2 is thought to have exceeded 1000 ppmv (Hasegawa et al., 2012). The shrinking of the Hadley cells allowed for a latitudinal expansion of humid conditions at mid-latitude in the Mid Cretaceous, while in the comparatively cooler Early and Late Cretaceous with lower pCO_2, a poleward shift of the subtropical belts and an expansion of the Hadley cell may have allowed a wider arid belt (Hasegawa et al., 2012). The increased humid conditions in the warmer Mid Cretaceous is suggested by Hasegawa et al (2012) to be reflected in the extent

of wetlands/waterlogged environment deposits in Northern Hemisphere mid-latitudes (White et al., 2001; Ufnar et al., 2004a).

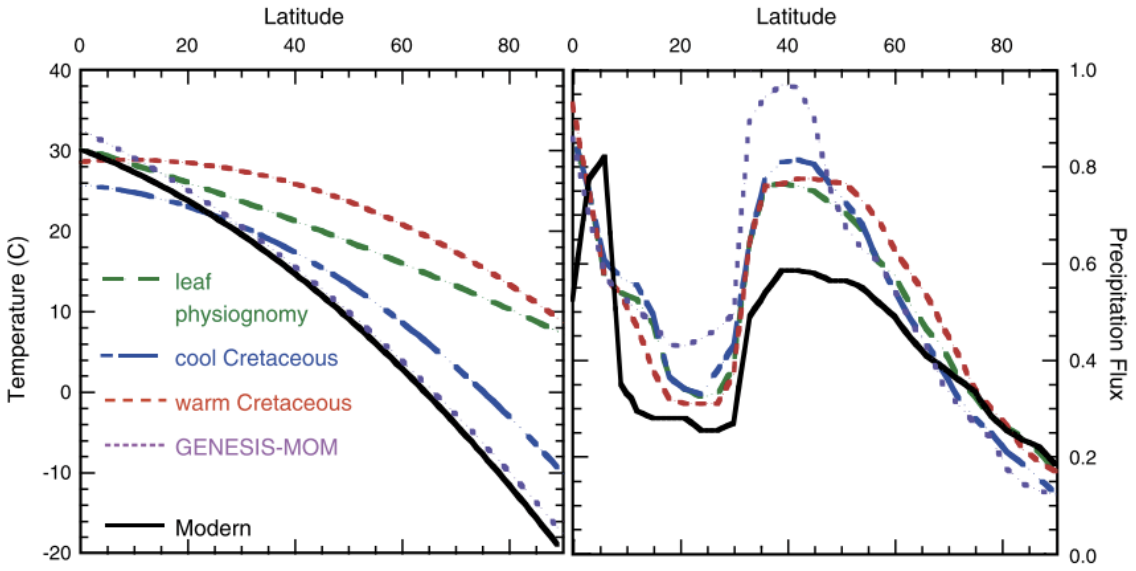


Figure 1.4: Latitudinal change in precipitation flux for the Mid Cretaceous (Figure from Suarez et al., 2011). The temperature estimates correspond to leaf physiognomy based estimates from Wolfe and Upchurch (1987) and Spicer and Corfield (1992), Genesis-MOM from Zhou et al (2008), and warm and cool Cretaceous estimates from Barron et al (1983).

Wetlands are an important component of water storage on our planet today (Skelton et al., 2003; Lal, 2009; Mitsch et al., 2010; Mitsch et al., 2013; Mitsch and Gosselink, 2015), are sources of methane and water vapour (Cao et al., 1998), and support an abundance of plant and animal life (Erwin, 2009; Mitsch and Gosselink, 2015). Methane is an important greenhouse gas and has a significantly higher radiative forcing than CO_2. The possibility of elevated methane concentrations, in combination with high CO_2, has already been suggested to explain Cretaceous warmth (Bice et al., 2006). Therefore, increased wetland extents in the Cretaceous may have contributed greenhouse gases into the atmosphere, and influenced the hydrological cycle, playing a role in reinforcing greenhouse conditions (Ufnar et al., 2004a; Suarez et al., 2011; Föllmi, 2012; Hay et al., 2019). Extensive wetlands may have also played an important role in vegetation feedbacks as increased C3 vegetation aids warming in climate

models (Zhou et al., 2012). Understanding Cretaceous wetland systems can thus provide important insight into the responses and roles of these components on global climate.

2.4 Early Cretaceous transient climate perturbations

The primary drivers of Early Cretaceous climate perturbations can be considered in the wider context of the Cretaceous carbon cycle. The pre-industrial carbon cycle exhibits characteristic behaviour on both short and long timescales. The short-term carbon cycle (Figure 1.5) involves the rapid exchange of carbon over times scales up to 1000 years between the ocean, soil and biota, and is predominantly responsible for short-term pCO_2 changes (Berner, 1999; Skelton et al., 2003).

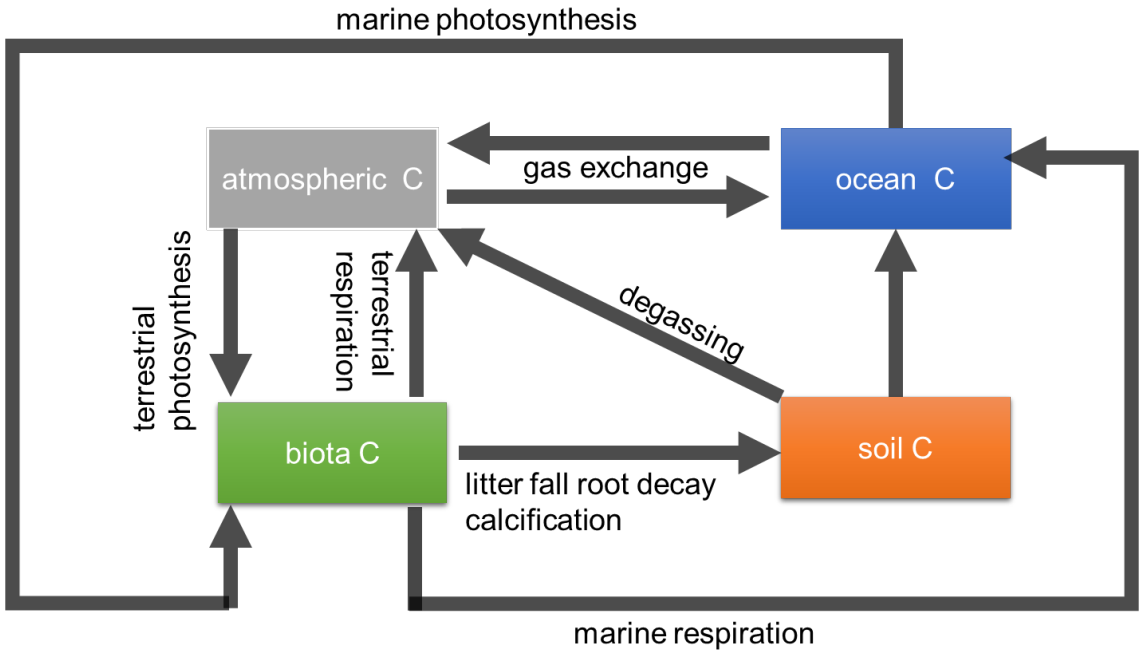


Figure 1.5: Short- and intermediate-term carbon cycle (modified from Skelton, 2003, based on Berner, 1999).

The long-term carbon cycle (Figure 1.6) controls pCO_2 changes on geological timescales (1000s to 1,000,000s of years.) and involves geological processes that release carbon into the atmosphere (e.g. seafloor spreading, rift and arc volcanism, Large Igneous Province (LIP) emplacement) and the processes driving carbon sequestration (e.g. organic

carbon burial, silicate weathering) (Pitman and Talwani, 1972; Arthur et al., 1985; Larson, 1991; Berner and Kothavala, 2001; Berner, 2003; Poulsen et al., 2003; Müller et al., 2008; Föllmi, 2012). The balance between these sources and sinks of carbon on long time scales drives the global carbon cycle changes, and in turn global climatic changes.

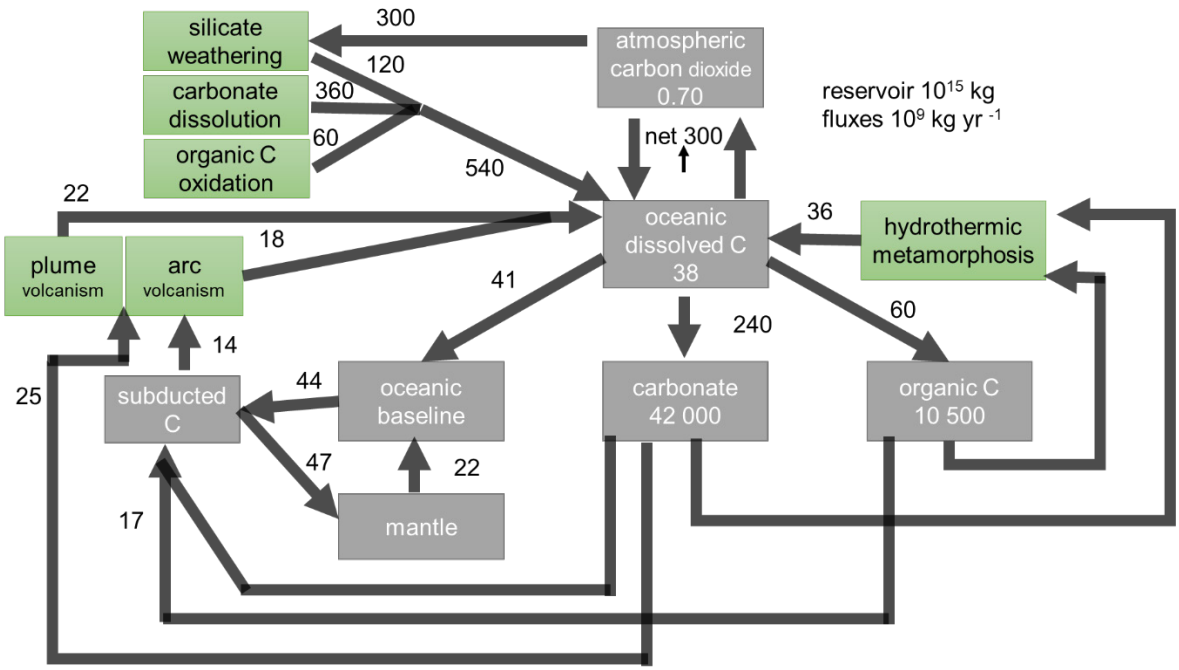


Figure 1.6: Box model for the long-term carbon cycle where grey boxes are reservoirs, green boxes are processes, and estimated fluxes of carbon are in black arrows (modified from Skelton, 2003).

During the Cretaceous, transient global carbon cycle perturbations due to changes in the fluxes and storage of carbon can be recognised by changes in the ratios of ^{12}C to ^{13}C ($\delta^{13}C$) measured in sedimentary archives. Examples of such global events include the Oceanic Anoxic Events (OAE's) (Schlanger and Jenkyns, 1976) which led to widespread deposition of organic-carbon-rich black shales due to high productivity and inferred widespread ocean anoxic conditions (Schlanger and Jenkyns, 1976; Jenkyns, 1997; Jenkyns, 2003; Emeis and Weissert, 2009; Jenkyns, 2010; Föllmi, 2012). The Early Cretaceous experienced several such global carbon cycle perturbations, such as the Valanginian 'Weissert' event, late Hauterivian 'Faraoni' event, the Early Aptian OAE 1a, Early Albian OAE 1b, and the Late

Albian OAE 1d (Lini et al., 1992; Jenkyns, 2003; Erba et al., 2004; Weissert and Erba, 2004a; Föllmi, 2012). Although the OAE's have generally been well studied, other climatic events (e.g. The Valanginian Weissert event) are yet to be fully explored and understood.

Evidence of continued warm conditions throughout the Early Cretaceous suggests greenhouse conditions persisted as the background climatic state (Littler et al., 2011; Jenkyns et al., 2012; O'Brien et al., 2017; Vickers et al., 2019a). However, cold snaps are also inferred during some intervals, notably in the Valanginian and Aptian (Frakes and Francis, 1988; Frakes et al., 1995; Stoll and Schrag, 1996; De Lurio and Frakes, 1999; Price, 1999; McArthur et al., 2004; McArthur et al., 2007; Amiot et al., 2011; Price and Passey, 2013; Grasby et al., 2017). Evaluating the lesser studied events remains crucial to understanding the context of climate perturbations and the long-term climatic trends during the Cretaceous era. To that end, this thesis focuses in part on one of these 'smaller' events of the Early Cretaceous; The Valanginian positive Carbon Isotope Excursion (CIE) or 'Weissert' event.

3 The Valanginian positive Carbon Isotope Excursion ('Weissert Event')

The Valanginian positive Carbon Isotope Excursion (CIE), also known as the 'Weissert event', is a distinct global chemo-stratigraphic marker (Weissert et al., 1985; Lini et al., 1992; Erba et al., 2004; Meissner et al., 2015). The positive carbon isotope excursion (Figure 1.7) varies between 1.5–2 ‰ in marine carbonates, and 3–5 ‰ in terrestrial organic matter (Weissert et al., 1985; Lini et al., 1992; Channell et al., 1993; Hennig et al., 1999; Erba et al., 2004; Weissert and Erba, 2004a; Gröcke et al., 2005; Nunn et al., 2010; Kujau et al., 2013; Meissner et al., 2015; Price and Mutterlose, 2015; Celestino et al., 2017).

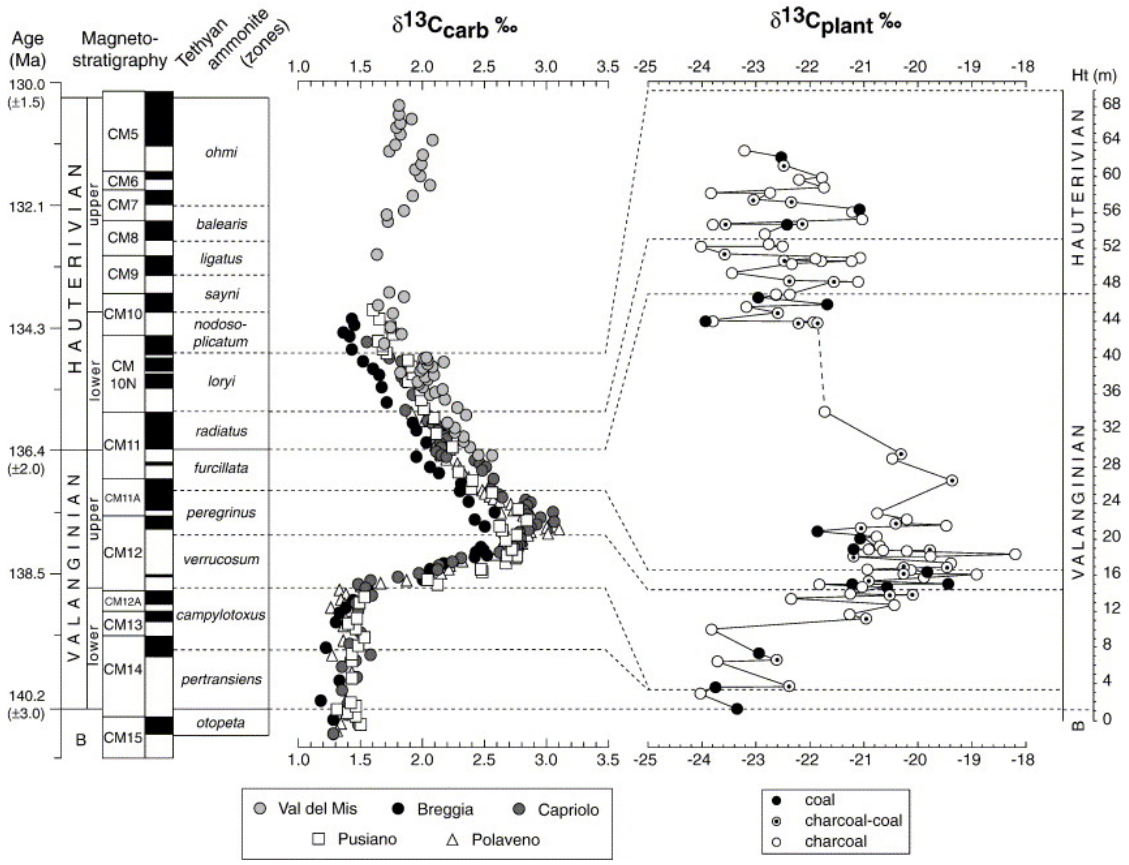


Figure 1.7: The Valanginian positive Carbon Isotope Excursion (CIE) expressed in a Tethyan composite and in wood fragments from Crimea (Figure from Grocke et al, 2005).

The Valanginian CIE is similar to OAE's in some ways, in that, there is evidence of increased ocean fertilization and biotic stress (Duchamp-Alphonse et al., 2007; Westermann et al., 2013), and is associated with increased volcanic activity (Weissert and Erba, 2004; Martinez et al., 2015). However, unlike OAE's, there is limited evidence of black shale deposition, and deep and intermediate waters are thought to have remained well oxygenated during the Valanginian (Westermann et al., 2010; Kujau et al., 2012).

3.1 Volcanic trigger

The emplacement of the Parana-Etendeka Large Igneous Province (P-E LIP) is generally invoked as a trigger for the Valanginian CIE (Erba et al., 2004; Weissert and Erba, 2004b; Duchamp-Alphonse et al., 2007; Duchamp-Alphonse et al., 2011). Recent astrochronological dating from the Vocontian Basin sets the Valanginian CIE onset at 135.22

±1 Ma, lasting for 5.85 Myr (Martinez et al., 2013; Martinez et al., 2015), coincident with emplacement dates of the P-E LIP at 134.6 ±0.6 Ma (Thiede and Vasconcelos, 2010). The emplacement of the P-E LIP is thought to have caused increased pCO_2, leading to increased weathering (Lini et al., 1992; Follmi et al., 1994; Erba et al., 2004; Weissert and Erba, 2004a; Föllmi, 2012).

It has been suggested that the CO_2 flux from volcanic activity may have been lower compared to other Cretaceous OAE's, leading to an absence of the characteristic widespread anoxia and organic matter deposition (Martinez et al., 2013). However, the amplitude of the $\delta^{13}C$ excursion is significant enough to warrant significant sequestration of ^{12}C and/or release of ^{13}C. A decrease in shallow marine carbonate production coupled with increased preservation of terrestrial organic matter has been proposed as a possible mechanism to explain the Valanginian CIE (Westermann et al., 2010; Kujau et al., 2012; Morales et al., 2015). Terrestrial systems like wetlands can be suitable areas for carbon sequestration due to their anoxic and waterlogged nature, and account for 20–30% of the modern soil carbon pool (Lal, 2009; Mitsch et al., 2013 and references therein). Evidence of enhanced terrestrial organic burial (such as coal and charcoal deposition) is known from the Berriasian to the Hauterivian (Ziegler et al., 1987; McCabe and Parrish, 1992) but poor age constraints mean that a conclusive link between increased terrestrial carbon storage and the CIE cannot yet be established. A better understanding of the dynamics of ancient wetland systems, and their response to climatic and hydrological change, is important for understanding whether they played a role during climate change events like the Valanginian CIE.

3.2 Environmental change associated with Valanginian CIE

3.2.1 Complex palaeoenvironmental changes

Palaeoenvironmental changes occurred during the Valanginian CIE, but are also notable before the onset of the CIE, which makes the link between the environmental changes and

the CIE difficult to evaluate (Figure 1.8) (Reboulet et al., 2003; Erba and Tremolada, 2004; Gréselle et al., 2011; Kujau et al., 2012; Kujau et al., 2013; Westermann et al., 2013; Mattioli et al., 2014; Morales et al., 2015).

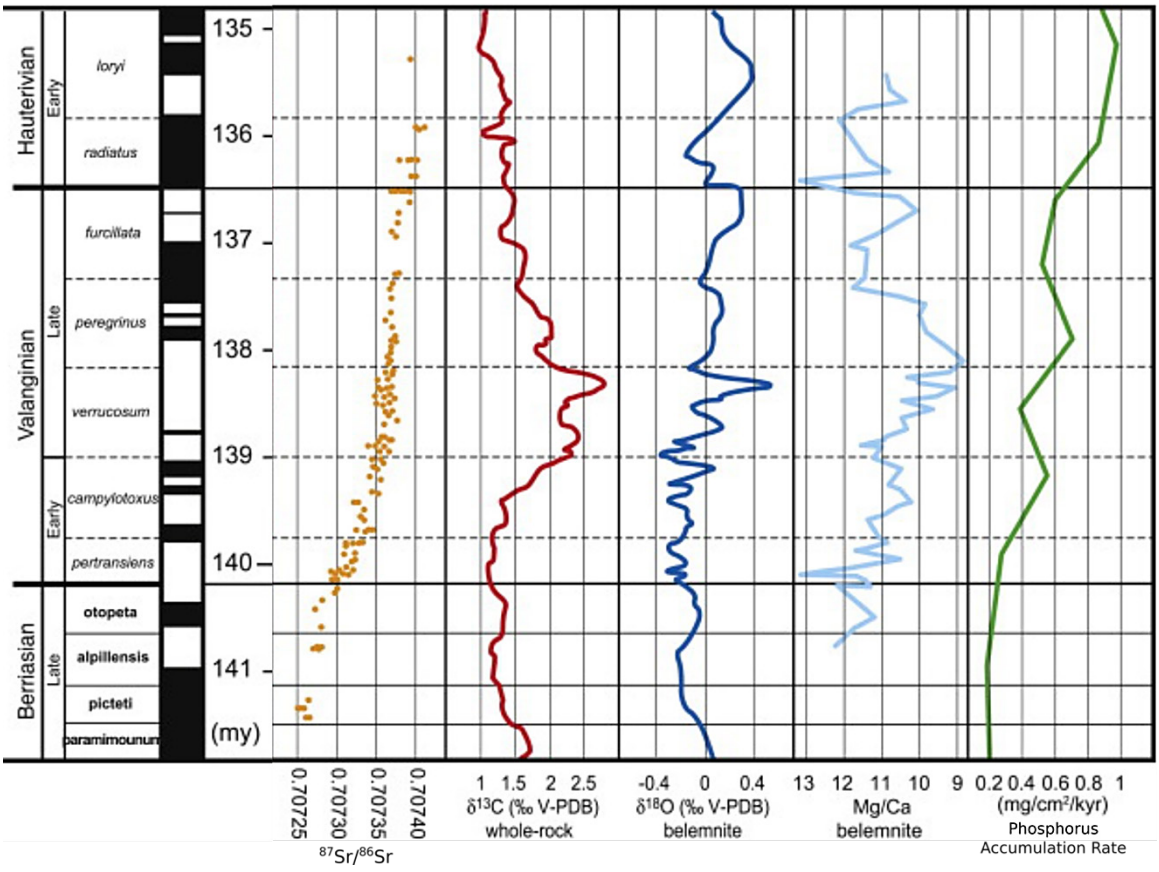


Figure 1.8: A synthesis of palaeoenvironmental change during the Valanginian CIE from Follmi et al., (2012). The time scale is tuned to Gradstein et al., (2004).

Temperatures from TEX_{86} show persisting warm sea surface temperatures (> 30ºC) during the Valanginian CIE in low latitudes (Littler et al., 2011). Evidence from nannofossils and phosphorus accumulation rates (Figure 1.8) suggests increased weathering and fertilization of ocean waters at low latitudes started before the onset of the Valanginian CIE, from the Berriasian-Valanginian boundary, and continued after the peak of the CIE (Duchamp-Alphonse et al., 2007; Föllmi, 2012). A decline in nanoconids is also notable before the onset of the Valanginian CIE, with continued decline after the CIE (Erba et al., 2004; Duchamp-Alphonse et al., 2007; Gréselle et al., 2011; Barbarin et al., 2012; Mattioli

et al., 2014). Platform drowning events are noted in the Tethyan Basin as unconformities and hiatuses, although the precise timing of drowning events and corresponding sea level variations are not constrained well in all sections (Wortmann and Weissert, 2000; Burla et al., 2008; Gréselle and Pittet, 2010; Morales et al., 2013 and references therein).

The palaeoenvironmental changes associated with the Valanginian CIE can also be regionally complex and disparate. For instance, nannofossil fluxes increase in the Vocontian basin during the peak of the CIE, while they decrease in pelagic settings such as the Lombardian basin (Erba and Tremolada, 2004; Gréselle et al., 2011). Gréselle et al., (2011) also acknowledges quantitative differences in counting nannofossil assemblages between studies, as well as likely regional palaeoceanographic differences at different palaeolatitudes. Barbarin et al., (2012) shows the nannofossil decline started before the Valanginian CIE in two sections in the Vocontian basin, but recovered partially during the peak of the CIE when $\delta^{18}O_{apatite}$ temperatures from fish teeth suggest up to 3 ºC cooling (Pucéat et al., 2003; Barbarin et al., 2012). However, calibration and standardization associated with $\delta^{18}O_{apatite}$ may bias it to cooler temperatures (Pucéat et al., 2010), although this does not explain the stratigraphic cooling trend notable in the record (Pucéat et al., 2003; Barbarin et al., 2012). However, TEX_{86} suggests sea surface temperatures remained warm (Littler et al., 2011), although this could potentially be explained by palaeoceanographic differences in regulating warming and/or cooling within different basins. The inferred cooling from fish teeth (Pucéat et al., 2003) is also at odds with the enhanced humidity and inferred warmth from other nannofossil work, clay indexes, and spore-pollen assemblages in the Vocontian basin during the peak of the CIE (Duchamp-Alphonse et al., 2007; Duchamp-Alphonse et al., 2011; Kujau et al., 2013; Westermann et al., 2013). Some of these regional variations could likely be attributed to secondary factors such as proxy artefacts and/or poorly constrained ages, and further work is required to fully understand the regional complexities in environmental changes associated with the CIE.

Currently, most evidence does suggest enhanced humidity in the Tethyan realm during the CIE peak, interpreted as warm conditions matching the warm reconstructed sea surface temperatures (Duchamp-Alphonse et al., 2011; Littler et al., 2011; Kujau et al., 2013; Mattioli et al., 2014; Morales et al., 2015; Charbonnier et al., 2016). The intensification of the hydrological cycle is also considered an important driver for the Valanginian CIE due to increased weathering and runoff, likely influencing carbon burial in both terrestrial and marine realms (Westermann et al., 2010; Charbonnier et al., 2016). Prior to the CIE onset, arid periods are notable from clay and spore-pollen assemblages in the Vocontian basin, and these periods are not found in comparatively more distal settings such as in the Lombardian basin, or at higher latitude sites such as the Mid Polish Basin (Kujau et al., 2013; Westermann et al., 2013). The disparity between sites has been attributed to the location of climate belts and the position of the Inter Tropical Convergence Zone (ITCZ) (Kujau et al., 2013; Westermann et al., 2013; Charbonnier et al., 2016). After the humid period associated with the Valanginian CIE in the Tethyan region, the climate is interpreted to have become more unstable, alternating between humid and/or arid periods (Westermann et al., 2013; Charbonnier et al., 2016). The dominant control on the variability from humid to arid conditions is attributed to Milankovitch forcing which affects monsoonal circulation, as well as movement of the ITCZ and climate belts (Hasegawa et al., 2012; Kujau et al., 2012). Humidity is postulated to have intensified in certain periods (such as the Valanginian CIE) due to external factors like vegetation feedbacks (Kujau et al., 2013).

3.2.2 Inconclusive evidence of cooling

Clumped isotope temperatures of sub-Arctic belemnites suggest up to 10 ºC cooling from Berriasian to Valanginian (Price et al., 2011; Price and Passey, 2013), but do not concur with TEX_{86} at low-mid latitudes which suggest continued warmth during much of the Early Cretaceous (Littler et al., 2011). Clumped isotopes from belemnites from the southern high

latitudes suggests a mean temperature of approximately 25°C during Hauterivian–Aptian (Vickers et al., 2019a), cooler than the TEX_{86} at high latitudes, but higher than sub-Arctic belemnites. In the Boreal Arctic realm, $\delta^{18}O$ and Mg/Ca of belemnites are interpreted as recording 7ºC cooling while only 1–4ºC cooling is interpreted in Tethyan deposits (McArthur et al., 2007; Price et al., 2011; Meissner et al., 2015). However, recent work has shown temperature estimates from Mg/Ca in belemnites is actually an unreliable palaeo-temperature proxy as Mg/Ca does not appear to correlate to changes in $\delta^{18}O_{belemnite}$ at species or genera level (Mutterlose et al., 2010; Li et al., 2013). Comparison between clumped isotope temperatures and $\delta^{18}O$ of belemnites also suggests the assumption of $\delta^{18}O_{seawater}$ of –1‰ in $\delta^{18}O_{belemnite}$ based temperature reconstructions may not apply (Zhou et al., 2008; Bernasconi et al., 2011; Price and Passey, 2013). Furthermore, ecological factors related to belemnite habitat and vital effects are also not fully understood (Mutterlose et al., 2010). Constraints on the onset of the Valanginian CIE in the Boreal records are also limited (Price et al., 2011; Meissner et al., 2015), and the inferred cooler periods may not necessarily relate to the CIE itself.

Additionally, the presence of dropstones and glendonites have been interpreted as evidence of high-latitude ice during the Valanginian (De Lurio and Frakes, 1999; Price, 1999; Rogov et al., 2017), but these observations do not relate to the presence of ice in a straight-forward way. For example, glendonites are indicative of bottom water temperatures up to 7 ºC (Greinert and Derkachev, 2004; Zhou et al., 2015; Vickers et al., 2019b and references therein), which may not necessarily indicate glacial conditions. Furthermore, rafted deposits (e.g. dropstones) can also be vegetation rafted and are not considered conclusive indicators of glaciation (Bennett et al., 1996). A more prolonged cooling period from the late Berriassian to early Barremian has been suggested by Vickers et al., 2019b based on evidence of glendonites in Artic locations throughout these periods (Grasby et al.,

2017; Rogov et al., 2017; Vickers et al., 2019b and references therein) suggesting cooling predated the Valanginian CIE and continued after.

It seems clear from the evidence available that palaeoenvironmental changes in the ocean were occurring before the onset of the Valanginian CIE and continued after. Low-latitude records generally agree that, during the CIE, the hydrological cycle would have intensified leading to increased terrigenous inputs into ocean basins. The evidence for cooling is inconclusive and constraining the disparities between high-latitude temperature proxies merits further work.

3.3 Objectives of this thesis

The hydrological cycle is thought to have played a crucial role in latitudinal heat transport and in maintaining warm equable conditions during past greenhouse intervals (Barron, 1983; Ufnar et al., 2004a; Suarez et al., 2011; Föllmi, 2012). Understanding the hydrological changes regionally and globally during a global carbon cycle perturbation like the Valanginian CIE is important to understanding the role of hydrological cycling in carbon cycle perturbations as a control on nutrient and clastic influx, freshwater stratification of lakes and/or marginal seas, and dynamicity of ancient terrestrial systems, as well as responses of the hydrological cycle to climate change. This thesis aims to reconstruct continental palaeohydrology from an Early Cretaceous non-marine sedimentary sequence (the Wealden Supergroup from the UK) using the stable isotopic composition of siderite concretions from palaeosol horizons. Additionally, a $\delta^{13}C_{org}$ record for the Wealden Supergroup will allow chemostratigraphic correlations to other Early Cretaceous deposits, and thereby allow the evaluation of regional hydrological changes in the context of the Valanginian CIE.

4 Geological Setting: The Wealden Supergroup of the Weald Basin

4.1 The Weald-Wessex basins

The non-marine Wealden Supergroup of Southern England was deposited during the Early Cretaceous (Berriasian to Aptian) within the Weald-Wessex basins at a palaeolatitude of 30–34ºN (Worssam and Morter, 1978; Morter, 1984; Allen and Wimbledon, 1991; Horne, 1995).

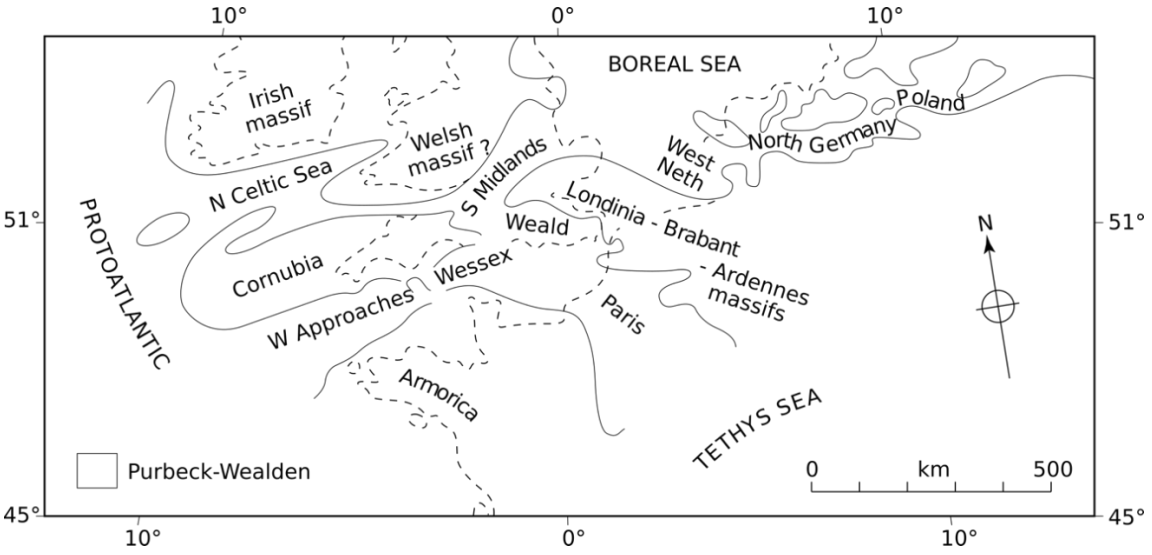


Figure 1.9: Extent of deposition in the Weald-Wessex basins, palaeo-coastlines and source massifs. Dotted lines are current coastlines. Figure modified from Radley and Allen, (2012).

The Weald-Wessex basins was surrounded by three active source massifs; Cornubia, Londinia, and Armorica (Figure 1.9) (Sladen and Batten, 1984; Allen et al., 1998).Provenance studies suggest a predominantly Cornubian source for the Wealden sediments in the Wessex Basin. In contrast, in the Weald Basin, the Wadhurst Clay Formation and Tunbridge Wells Sand Formation are thought to have been sourced predominantly from Londinia, with minor contributions from Armorica. In the Barremian, however, the Weald Clay records evidence of Cornubian sources, indicating a connection between the Wessex and Weald basins at that time (Sladen and Batten, 1984; Allen and

Wimbledon, 1991; Allen et al., 1998; Radley, 2006a; Radley, 2006b; Radley and Allen, 2012). In north-eastern England, coeval Lower Cretaceous deposit are marine, indicating a coastline with the Boreal Sea existed 50–100 km to the north of the Weald-Wessex basins (Figure 1.9). The Tethyan Sea was to the south east approximately 200 km away (Figure 1.9).

Two major lithological facies, one arenaceous and the other argillaceous, have been identified within the Wealden Supergroup. The arenaceous formations are often rich in kaolinite, consisting of mudstones, siltstones and fine to coarse grained sandstones interpreted as meanderplain, floodplain, and channel deposits (Allen, 1989; Allen et al., 1998; Radley and Allen, 2012). The argillaceous formations are dominated by mudstones and thought to be deposited in lower energy environments such as lakes, coastal lagoons, and mudflats (Allen, 1975; Allen, 1981; Allen, 1989; Allen et al., 1998). Fossils are sparse or locally clustered in the arenaceous formations, but remains of land plants, freshwater molluscs, fish, and dinosaurs have been found. The argillaceous formations generally have abundant ostracods, brackish to fresh water molluscs, fish, remains of aquatic and land plants, and reptiles (Austen and Batten, 2018 and references therein).

The Wealden Supergroup lithostratigraphy shows alternating changes between these argillaceous and arenaceous lithofacies, with regional differences in the timing of deposition of these lithofacies between the Weald and Wessex basins. These basinal differences have been interpreted as the consequence of local tectonics and/or climate (Allen et al., 1998; Allen, 2010; Radley and Allen, 2012). The Weald Basin consists of four main stratigraphic units; The Ashdown Formation (includes Fairlight Clays), Wadhurst Clay Formation, Tunbridge Wells Sand Formation (includes Grinstead Clay), and overlying them, the Weald Clay Group. In contrast, the Wessex Basin contains two formations, the alluvial arenaceous Wessex Formation overlain by the lacustrine-lagoonal argillaceous Vectis Formation

(Radley, 2006b; Radley and Allen, 2012). The data presented in this thesis is solely from samples within the Weald Basin, spanning the four main stratigraphic units within it, which are discussed in detail in Section 4.2. Further discussion regarding controls on lithofacies in the Weald-Wessex basins is presented in Section 4.4.

4.2 Stratigraphy in the Weald Basin and Sampling

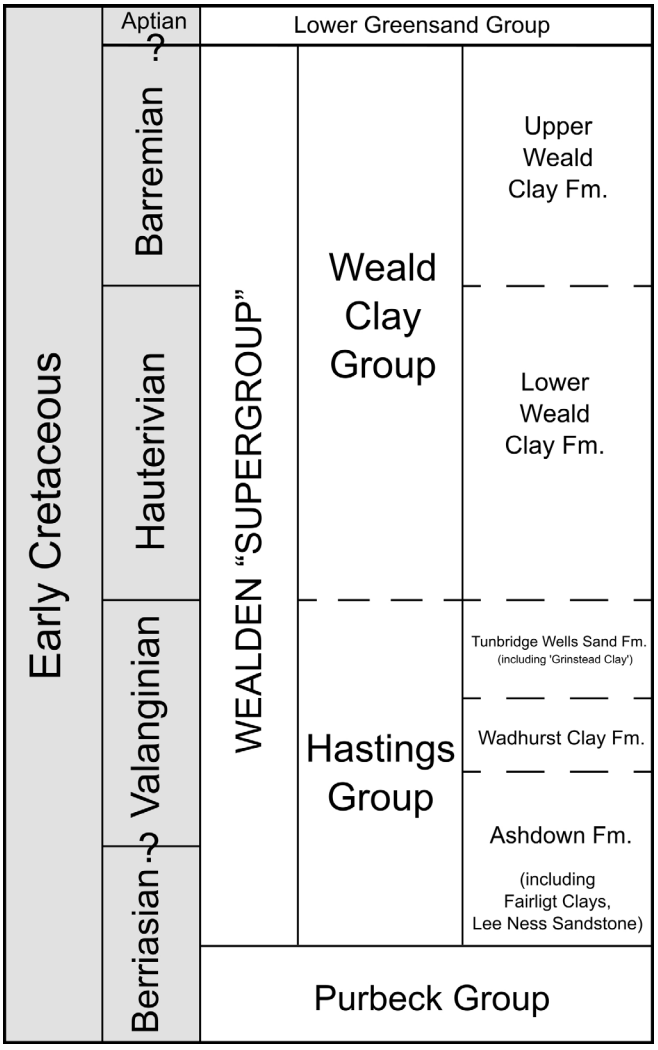


Figure 1.10: Stratigraphy of the Weald Basin with the main groups and formations of interest to this thesis. Age assigned based upon the biostratigraphy of Horne, (1995). Figure modified from Robinson et al., (2010).

The main stratigraphic units within the Weald Basin of importance to this thesis are shown in Figure 1.10 and described in detail below. The age model within the Weald Basin

is mainly based on ostracod biostratigraphy, with limited work on charophyte assemblages used to compare with marine successions(Allen and Wimbledon, 1991; Feist et al., 1995; Horne, 1995; Radley and Allen, 2012). The ostracod biostratigraphy and charophyte biostratigraphy are based on several boreholes across the Weald Basin, for example, Cooden, Warlingham, Hailsham, Ripe, and Guestling 1-3, to name a few (not all of which are named clearly in publications or currently have samples available or stored within BGS). The initial ostracod work by Anderson (1985) was revised by Horne (1995) to suggest the currently accepted age model for the Weald Basin shown in Figure 1.10. The ostracod biostratigraphy is an internal biostratigraphic framework for the Weald Basin and is tied with only a few points using other biostratigraphic work (e.g. charophytes) via species or zonal equivalents to other basins (Allen and Wimbledon, 1991; Feist et al., 1995). As the lithostratigraphy is considered synchronous across the Weald Basin, the age model based on biostratigraphic work to date on boreholes across the Weald Basin is considered to apply across the basin, and has been implemented in studies of the Wealden sediments (Radley and Allen, 2012).

The cores used in this study to collect samples from the Wealden Supergroup are stored at the British Geological Survey in Keyworth, UK, accessible through their administrative office for academic work. Suitable cores were identified based on published BGS reports and logs accessible through the BGS 'Geology of Britain' online database. Sampling was conducted by Ritwika Sengupta with initial help from Stuart Robinson. Graphic logs of each borehole are presented in Figure 1.11, reconstructed using the core sheets of each borehole as continuous cores were unavailable for most. Hence, the reconstruction presented in these logs is dependent on the initial record presented in the core sheets, however, this is deemed suitable in understanding the broad sedimentological changes at formation level through these cores. The five main cores used for sampling were from the Fairlight, Westfield, Cooden, Cuckfield, and Warlingham boreholes. Continuous cores were not available for most boreholes. Fairlight had continuous cores available for

most of the borehole as well as bulk samples every 1–2 m, but some gaps in the Ashdown Formation of up to 10 m exist. Westfield and Cooden contained only registered specimens every 2–5 m. Cuckfield contained bulk samples and registered specimens every 1-5 m. Warlingham contained registered specimens every 1–5 m. As the samples were limited often to registered specimens, only small (1 cm length pieces could be taken). To maximise sampling for organic matter through the stratigraphy, samples were taken every 2–5 m where possible (bearing in mind there is no continuous core, and therefore in some cases sample gaps of up to 10 m can exist). For sphaerosiderites, all horizons notable in the cores were sampled (approximately 70 in total including all cores) and decisions were made later in the project on which horizons were suitable based on preservation, time, and financial constraints.

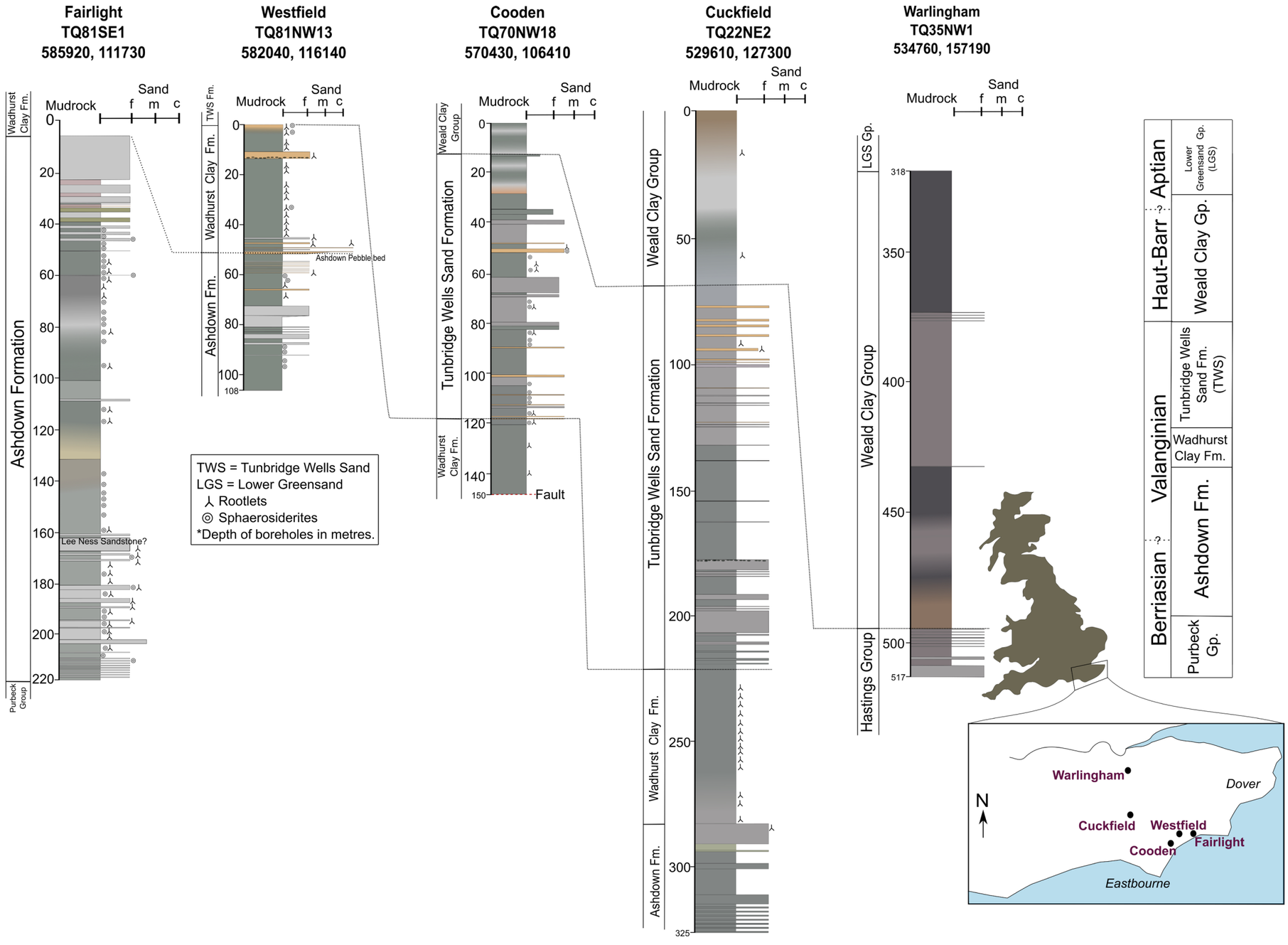


Figure 1.11: Lithostratigraphy and location of boreholes from the British Geological Survey used to sample the main stratigraphic units in the Weald Basin based on core sheets. Depth values(metres) shown against each borehole and depths at which rootlets and sphaerosiderite horizons are noted in the core sheets and during sampling. The colour changes in strata noted in the core sheets are also shown.

4.2.1 The Purbeck Group (Tithonian to Berriasian)

The Purbeck Group underlies the Wealden Supergroup and consists of marginal freshwater, brackish and marine interbedded limestones, mudstones, and evaporites with significant lateral variation (Westhead and Mathert, 1996; Allen et al., 1998). It can be up to 186 m thick in the Weald Basin, ranging from Late Jurassic (Tithonian) to Early Cretaceous (Berriasian) in age (Batten, 1982; Morter, 1984; Allen and Wimbledon, 1991; Horne, 1995; Radley and Allen, 2012). The boundary of the Purbeck Group and the Wealden Supergroup is conformable (Morter, 1984; Allen and Wimbledon, 1991; Horne, 1995; Allen et al., 1998). The Purbeck Group was not sampled in this study but the top of the unit provides an important lithostratigraphic tie-in point.

4.2.2 The Ashdown Formation (Berriasian to Valanginian)

The Ashdown Formation consists of fine sandstones, siltstones, and rare mudstones (Edmunds and Gallois., 1965). The overall thickness of this formation ranges from 100–250m, with thicker units to the west of the Weald Basin (Edmunds and Gallois., 1965; Allen and Wimbledon, 1991; Radley, 2006a). The Ashdown Formation is interpreted as recording floodplain deposits; the upper part contains evidence of scours and channels as well as interchannel lakes (Allen and Wimbledon, 1991; Allen et al., 1998; Radley, 2006a; Radley and Allen, 2012). The sandstones show evidence of cross bedding and can be massive and thickly bedded, with scour and channel marks. Sun-marks and casts of dinosaur footprints record intermittently subaerial exposure (P. Allen, 1981; Allen and Wimbledon, 1991; Allen et al., 1998; Radley, 2006a; Radley and Allen, 2012). The upper boundary is marked by the, locally pebbly, ‘Top Ashdown sandstone’ and a ‘widespread’ erosion surface, although the lateral continuity of the erosional surface has not been determined (Allen and Wimbledon, 1991; Allen et al., 1998; Radley, 2006a). Fossils within the Ashdown Formation include

plant fragments of ferns and conifers (Hughes, 1975), megafossils such as vertebrate bones and teeth (Austen and Batten, 2018), and ostracods (Horne, 1995; Austen and Batten, 2018).

The Ashdown Formation core sampled in this study (from the Fairlight and Westfield boreholes), consisted of a mixture of fine to medium sandstones interspersed with some mudstones. It contained several horizons with concentrations of sphaerosiderites (every 5–10 m), as well as plant organic matter, including fragments of fossil wood (> 1 cm length).

4.2.3 The Wadhurst Clay Formation (Valanginian)

The Wadhurst Clay Formation varies in thickness from 40–80 m and consists of fine mudstones or shales with less frequent beds of siltstones and rare limestones (Allen and Wimbledon, 1991; Allen et al., 1998; Radley, 2006a; Radley and Allen, 2012). The Wadhurst Clay Formation has been interpreted as representing a freshwater to slightly brackish lake or lakes within the Weald Basin; the presence of *Equisetites* soil beds suggests water levels remained shallow (< 2 m) throughout the period of deposition (Allen, 1975; Allen et al., 1998). The presence of sandstone scour fills and thicker sandstone units (e.g. the Cliff End Sandstone member, the Tilgate Stone) indicate periods of storm activity or fluvial runoff and that fan deltas prograded into these lakes. The mudstones are poorer in kaolinite compared to the formations stratigraphically above or below the Wadhurst Clay, and contain abundant Classopolis pollen which has been interpreted to indicate a drier climate (Batten, 1982; Batten, 1998). Fossils within the Wadhurst Clay include ostracods, conchostracans, snails and low salinity bivalves, and generally degraded palynormorphs (Batten, 1982; Batten, 1998; Austen and Batten, 2018). The upper boundary with the Tunbridge Wells Sand is conformable and indicative of continued shallow water environments.

The Wadhurst Clay Formation sampled in this study (from the Westfield, Cooden, and Cuckfield boreholes) consisted of mudstones, with occasional fine sandstones layers, and

sandstones at the top of the unit, transitioning to the bottom of the Tunbridge Wells Sand. A few horizons of sphaerosiderites were found but they were poorly preserved. The organic matter present was very fine (< 1 mm length) and concentrated in small horizons.

4.2.4 The Tunbridge Wells Sand Formation (Valanginian)

The Tunbridge Wells Sand Formation consists of fine to medium grade sandstones, coarsening up to the top of the formation, and ranges from 46–122 m in thickness. It has been divided into 'Lower' and 'Upper' sections, separated by thinly bedded siltstones known as the Grinstead Clay, and erosional surfaces at the top of the Grinstead Clay. The extent of the Grinstead Clay varies and it is not recognisable outside of the western High Weald (Radley, 2006a). Fish remains, charcoal fragments, dinosaurs and the clubmoss Lycopodites have been found. The Lower Tunbridge Wells Sand beds have been interpreted as shallow channels and fans on a braidplain built away from Londinia. The Grinstead Clay can be up to 30 m thick, overlying eroded sandstone layer (Ardingly Sandstone), and consists of shale, mudstone, siltstone, and thin shell beds (Allen et al., 1998; Radley, 2006a; Radley and Allen, 2012). It has yielded an abundance of molluscs and microfossils, and is interpreted as a lake/lagoon complex, although the presence of *Equisetites* soil beds confirms continuing shallow water conditions. There is also evidence of lateral variability within the Grinstead Clay and the existence of sandier horizons (such as the Cuckfield Stone Member). The Upper Tunbridge Wells Sand comprises fine grained sandstones and siltstones and is interpreted as being deposited in a meanderplain setting.

The Tunbridge Wells Sand sampled in this study (from the Cooden and Cuckfield borehole) was generally fine sandstones and mudstones with relatively abundant evidence of palaeosols with sphaerosiderites (on average every 5–10 m) and fragments of organic matter (< 1 cm in size). Sphaerosiderites used in this study were mainly from the Cooden borehole, as they had better preservation and were more abundant within Cooden than the

Cuckfield borehole. The Tunbridge Wells Sand Formation within the Cuckfield borehole was also thicker and contained the Grinstead Clay formation, a fine mudstone, which was not exposed within the Cooden borehole.

4.2.5 The Weald Clay Group (Hauterivian – Aptian)

The Weald Clay consists mainly of mudstones with occasional shelly limestones, sandstones and siltstones with occasional red mottling (Worssam and Morter, 1978). The fauna present are similar to the lithofacies stratigraphically below, but conditions in the Weald Clay are interpreted to become more saline towards the top of the group, as a result of the marine transgression into the overlying, marine Lower Greensand group (Worssam and Morter, 1978; Radley and Barker, 1998; Radley, 2006a; Radley and Allen, 2012). The variable lithologies within the Weald Clay are interpreted as changing conditions from deposition in a meanderplain to lacustrine-lagoonal settings. Provenance studies also show the presence of tourmaline rich sands indicating a change of source to the Cornubian massif, as the Londinian massif was likely deeply eroded by the Hauterivian (Allen et al., 1998).

The Weald Clay sampled in this study (using Warlingham and Cuckfield boreholes) consists mainly of mudstones with organic fragments (< 1 mm) and a few horizons containing poorly preserved sphaerosiderites.

4.2.6 Lower Greensand Group (Aptian – Albian)

The Lower Greensand Group (LGS) is mainly composed of poorly consolidated sands and sandstones with occasional siltstone intervals. It was deposited in shallow seas in marginal marine conditions and is a result of transgression during the Late Barremian (Ruffell and Batten, 1994). The boundary between the Weald Clay Group and LGS is unconformable (Ruffell and Batten, 1994). The LGS was not sampled in this study but provides a reference point for stratigraphic correlation.

4.3 Paleoclimate in the Weald-Wessex basins

Sedimentary fill within the Weald-Wessex basins is considered to record a warm, semi-arid climate featuring distinct wet and dry periods during the Early Cretaceous. Sedimentological evidence also supports heavy discharge and flash floods (Allen et al., 1998; Radley, 2006a; Radley, 2006b). The presence of sun cracks, calcrete nodules, and red vertisols with shrinkage features indicate dry periods (Allen et al., 1998). Charcoal is present in both Weald and Wessex basins, suggesting forest fires occurred, perhaps during dry periods in the source areas of the uplands, as well as on the flood plains (Allen et al., 1998). The evidence from insect assemblages suggests warm subtropical to temperate conditions, supporting the suggestions from sedimentological evidence (Jarzembowski, 1995). Molluscan shells contain thick regularly-spaced growth lines, indicative of alternating wet and dry phases, suggesting seasonality within their short life-span (Batten, 1998; Radley, 2006b; Austen and Batten, 2018).

In the Wessex Basin, there is evidence of vertisols with cracks and calcrete nodules suggesting dry periods (Allen et al., 1998) but the additional presence of gleys indicates that, in some areas, water tables were high for long periods of time (Allen et al., 1998; Wright et al., 2000). There is also evidence of fluctuating dynamic water tables, such as palaeosol types switching in a vertical sequence, and evidence of periodic floods and storms in poorly sorted bone, plant and organic debris, muddy conglomerates, and storm coquinas (Allen, 1981; Wright et al., 2000; Radley, 2006b). In contrast, there are no calcrete layers known in the Weald Basin but there are differentiated red mottled palaeosols that contain mudcracks indicating periods of desiccation (Allen et al., 1998). The Weald Basin palaeosols are thought to have developed under wetter conditions than in the Wessex Basin, interspersed with some drier, hotter periods (Allen et al., 1998). Mean Annual Temperatures (MAT) are thought to have been around 25°C during warm periods based on clay assemblages,

sedimentological evidence of wet or dry conditions (e.g. evaporites, flash flood debris), and palynology (Sladen and Batten, 1984; Allen, 1989; Allen and Wimbledon, 1991; Allen et al., 1998). Sladen and Batten (1984) also suggest the presence of cooler periods where mean temperatures may have been around 10ºC. However, these temperatures seem unrealistically low compared to other Early Cretaceous temperature estimates (e.g. Littler et al., 2011; Jenkyns et al., 2012; O'Brien et al., 2017, Vickers et al., 2019). The 25 ºC MAT estimate of Sladen and Batten (1984) is more in line with MAT from climate modelling of the Early Cretaceous (Haywood et al., 2004; Lunt et al., 2016).

Overall, the evidence suggests that the Weald-Wessex basins experienced a fluctuating humid/arid climate that created a dynamic environment with periodic groundwater recharging, flash floods, and droughts during the Early Cretaceous. The differences in lithofacies deposited spatially and temporally between the two basins suggests that climate may have been subtly different between the two basins; the Weald Basin being wetter and the Wessex Basin being more prone to aridity (Allen, 1975; Allen et al., 1998; Radley and Allen, 2012). However, uncertainty remains as to how far climate affected the variations, particularly at smaller than formation scale, as local factors like sea level and tectonics likely played crucial additional roles (Allen, 1975; Allen, 1989; Allen et al., 1998).

General Circulation Models (GCM) focusing on the Early Cretaceous Wealden (Haywood et al., 2004) yield model temperatures that agree well with the proxy evidence suggesting a warm climate. The surface temperatures in the models range from 32–36°C in summer to 8–12°C in winter (Haywood et al., 2004), which supports the Mediterranean-type climate invoked from sedimentological and palaeontological evidence (Allen et al., 1998). However, precipitation remains high throughout the year in the model (Haywood et al., 2004) which is not characteristic of a Mediterranean type climate, and is somewhat at odds with the seasonality and drier periods interpreted from the sedimentological data.

Evaporation almost always exceeds precipitation in the models of Haywood et al., (2004), partially due to the specified high sea surface temperatures they used. Haywood et al., (2004) suggest it is possible to generate an apparent dry season in proxy data if evaporation remains high during one season and exceeds precipitation, as the proxies available are recording a balance of precipitation minus evaporation. The wet conditions simulated in the models do however, support the proxy evidence of a dynamic climate with flash flooding and storms (J. Allen, 1981; Allen et al., 1998; Wright et al., 2000; Radley, 2006a; Radley, 2006b). It is also important to consider that there was likely temporal variability in the Wealden climate. During the Early Cretaceous (Berriasian to Barremian), there were shifts from humid to arid climates noted in both the Weald-Wessex, Vocontian, and Polish basins (Allen et al., 1998; Ruffell and Worden, 2000; Kujau et al., 2013; Westermann et al., 2013; Charbonnier et al., 2016). This temporal variability is not necessarily captured in modelling, particularly as models (such as Haywood et al., 2004) consider one palaeogeography and one CO_2 level, which may not be reflective of the conditions that existed in the Weald Basin during the Early Cretaceous. It is equally important to understand this temporal climate variability to better constrain the palaeoclimatic history of the Weald-Wessex basins.

4.4 Tectonic or climate driven lithological changes?

The lithologies within the Weald-Wessex basins are characterised by formation scale arenaceous-argillaceous couplets referred to as ‘megacycles’ (Allen, 1946; Allen and May, 1959; Allen, 1967; Allen, 1975; Allen, 1989; Allen et al., 1998). The cycles in the Weald Basin include the pairs Ashdown-Wadhurst Clay, Lower Tunbridge Wells Sand-Grinstead Clay (laterally discontinuous), and the Upper Tunbridge Wells Sand-Weald Clay. Based on the inferred shallow water levels (Allen et al., 1998), the lithological differences between the argillaceous and arenaceous formations are interpreted as changes in sediment type and supply based on tectonic changes in the source massifs, mainly in Londinia which was the

closest source (Allen, 1975; P. Allen, 1981; Allen and Wimbledon, 1991; Allen et al., 1998; Radley and Allen, 2012).

There are also notable regional differences in the arenaceous-argillaceous couplets. In contrast to the multiple megacycles within the Weald Basin, the Wessex Basin only contains one pair; the argillaceous Wessex formation overlain by the arenaceous Vectis formation (P. Allen, 1981; Allen and Wimbledon, 1991; Allen et al., 1998; Radley, 2006a; Radley, 2006b). These basinal differences are suggested to reflect regional climatic differences up until the Hauterivian, with wetter conditions persisting in the Weald Basin (Ruffell et al., 1996; Taylor, 1996; Allen et al., 1998). The Wessex Basin's semi aridity is attributed to an interplay of western rain shadows from massifs and distant catchments (Allen et al., 1998 and references therein). While in the Weald Basin, the water table was recharged from closer catchments creating a higher frequency of water bodies which lasted longer. During the Hauterivian, the clay mineralogy of the Vectis formation (Wessex Basin) and the Weald Clay Group (Weald Basin) are similar, suggesting a more homogeneized climate or better sediment routing connections between the two basins, perhaps related to subsidence of local barriers and/or a transgression (Allen et al., 1998 and references therein).

Therefore, the controls on regional lithofacies in the Weald-Wessex basins are not yet fully understood. Further evidence exploring the relation between climate and tectonics and the Weald-Wessex lithofacies is still necessary to assess the interplay of tectonics and climate on sediment deposition in these basins.

5 Proxy background

5.1 Carbon Isotope ($\delta^{13}C$) stratigraphy from terrestrial organic matter

5.1.1 A chemostratigraphic tool

As the shallow ocean and atmospheric carbon reservoirs are linked, changes in the carbon isotope composition of one should to be reflected in the other, providing an important tool for reconstructing past carbon cycle changes (Scholle and Arthur, 1980). The processes controlling CO_2 fluxes to and from the atmosphere, such as volcanism or carbon sequestration via weathering (discussed in Section 2.4), can change the ratios of ^{12}C to ^{13}C ($\delta^{13}C$) in the ocean and atmospheric reservoirs. As plants take up atmospheric CO_2 through photosynthesis, the carbon isotope composition of plant matter is thus controlled, at least partially, by the carbon isotope composition of atmospheric CO_2. Furthermore, the carbon isotope composition of terrestrial organic matter is shown over geological timescales to track that of the marine reservoir (Hasegawa, 1997; Gröcke, 1998; Gröcke et al., 2005; Hesselbo et al., 2007), suggesting that the dominant control on carbon isotope composition of terrestrial organic matter is the $\delta^{13}C$ of atmospheric CO_2. This provides an important means of chemostratigraphic correlation between dispersed global localities and marine and terrestrial sediments.

5.1.2 Proxy Caveats

In the modern world, plants exhibit three types of photosynthetic pathways which affect the carbon isotope compositional ranges in plant organic matter; C3 (Calvin-Benson cycle; $\delta^{13}C$ of –33‰ to –22‰), C4 (Hatch-Slack cycle; $\delta^{13}C$ of –10‰ to –20‰) and CAM (Crassulacean acid metabolism; intermediate $\delta^{13}C$ values between C3 and C4) (Bender, 1971; Smith and Epstein, 1971; Kohn, 2010). Carbon isotope stratigraphy using fossil plants requires an assumption that the palaeo-ecosystem in question did not contain a mixture of

photosynthetic pathways. Evidence suggests that C4 plants likely did not evolve until the Miocene (Cerling et al., 1993) and Mesozoic fossil plants are shown to have $\delta^{13}C$ values consistent with C_3 photosynthetic pathways (Bocherens et al., 1993; Hasegawa, 1997; Gröcke, 1998; Gröcke et al., 1999; Robinson and Hesselbo, 2004; Gröcke et al., 2005; Hesselbo et al., 2007; Yans et al., 2010). CAM plants are generally succulents, and therefore, unlikely to be present in the Cretaceous palaeoenvironments of interest to this thesis (Jacobs et al., 1999). Therefore, in the Mesozoic, the assumption of a singular photosynthetic pathway within the ecosystem is valid.

Modern plants also show variability in their carbon isotope compositions within constituent parts of the same plant. For instance, wood can vary by up to 4‰ within one tree, while leaves can be up to 3‰ lighter than wood, and variability also exists between branches, twigs, and between early and late wood (Leavitt and Long, 1982; Leavitt and Long, 1986). $\delta^{13}C$ values of plants are also affected by local pCO_2 as well as temperature variations, salinity and water supply, adding further complications (Gröcke, 1998).

Diagenesis also plays a role in altering $\delta^{13}C$ values from terrestrial organic matter. Lignins and lipids are most resistant to diagenesis, and have $\delta^{13}C$ values isotopically lower than the bulk plant. Thus, the preferential loss of carbohydrates over lignins and lipids during diagenesis would drive values to become isotopically lighter by 1–2‰ (Benner et al., 1987; Spiker and Hatcher, 1987; Gröcke, 1998; Opsahl and Benner, 1999). However, $\delta^{13}C$ values from fossil plants can be 2–3‰ heavier compared to a modern average C_3 plant value of –27‰, indicating enrichment in ^{13}C. This enrichment is thought to be due to post burial diagenesis, such as coalification, and charcoalification (Jones and Chaloner, 1991; Poole et al., 2002). However, studies on fossil coalified and charcoalified wood from the same stratigraphic sections show no significant differences in $\delta^{13}C$, and the trends noted in $\delta^{13}C$ in fossil wood appear to match those from co-eval marine carbonates suggesting that the

carbon isotope composition of terrestrial organic matter is dominantly controlled by the carbon cycle changes over relatively long-intervals of geological time (Hasegawa, 1997; Grocke, 2002; Hesselbo et al., 2002; Hesselbo et al., 2003; Gröcke et al., 2005; Hesselbo et al., 2007).

5.2 Sphaerosiderites as a proxy for palaeohydrology and palaeoenvironment

Sphaerosiderites are iron carbonate spheres ranging in size up to several hundred microns that are known to form in waterlogged and reducing soils in modern and ancient wetland environments (Figure 1.12) (Pye et al., 1990; Mozley and Wersin, 1992; Moore et al., 1992; Ludvigson et al., 1998; Driese et al., 2010; Ludvigson et al., 2013).

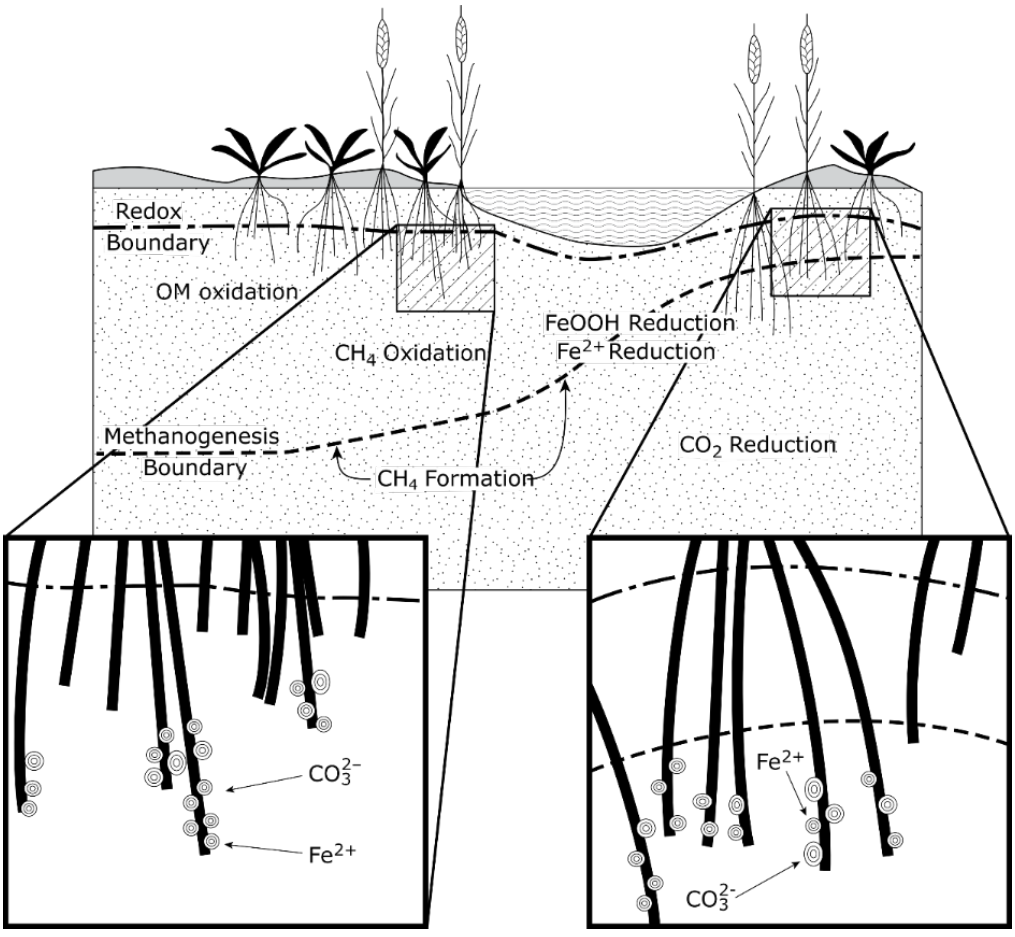


Figure 1.12: Schematic of siderite growing in a wetland system, modified by Stuart Robinson from Ludvigson et al. (1998).

Due to their mode of growth, they are thought to preserve the oxygen-isotopic composition ($\delta^{18}O$) of meteoric groundwater, and have been widely used throughout the Phanerozoic for palaeohydrological reconstructions (Ludvigson et al., 1998; Khim et al., 1999; Choi et al., 2003; Ufnar et al., 2004a; Suarez et al., 2009; Passey, 2014; Weibel et al., 2016). Siderite is formed from the oxidation of organic carbon coupled with the reduction of ferric oxide minerals, yielding Fe^{2+}, alkalinity, and dissolved inorganic carbon; together, this drives eventual supersaturation with respect to siderite (Ludvigson et al., 1998). In freshwater continental wetlands, the low sulphate concentration limits microbial sulphate reduction and therefore pyrite precipitation, which would otherwise consume iron (Berner, 1971; Pye et al., 1990).

5.2.1 Elemental composition of Sphaerosiderites as a proxy for palaeoenvironment

Siderite is known to form in both marine and terrestrial porewaters (Mozley, 1989; Ufnar et al., 2004b), and it is important to establish (particularly in marginal facies) whether marine incursions into meteoric groundwaters occurred. Based on early diagenetic formation of siderite, it has been implicitly assumed that the elemental composition of siderite should reflect the chemistry of the growth solution (i.e. palaeo pore waters) (Mozley, 1989). Extensive substitution of Mg or Ca in siderite has been interpreted as indicating growth in marine conditions while low Mg or Ca and higher Mn is thought to indicate growth in freshwaters (Mozley, 1989). These assumptions have been used to evaluate siderites throughout the Phanerozoic to assess their suitability for palaeoclimatic studies and for understanding palaeoenvironments during growth (Mozley, 1989; Choi et al., 2003; Ufnar et al., 2004b; Choi and Kim, 2006; Suarez et al., 2009; Robinson et al., 2010; Ludvigson et al., 2013; Weibel et al., 2016).

However, the assumption that elemental composition of siderite reflects chemistry of growth solution is not easily reconciled with laboratory syntheses, which have failed to

reproduce the compositional link between siderite and pore water chemistry (Thornber and Nickel, 1976; Carothers et al., 1988; Mortimer et al., 1997; Jimenez-Lopez and Romanek, 2004; Romanek et al., 2009). Previous studies have examined controls on siderite chemical composition particularly in reference to Ca and Mg. However, experimental conditions are typically associated with crystallisation rates that may be orders of magnitude higher than natural settings (Postma, 1980; Pye et al., 1990; Steinmann and Shotyk, 1997). In contrast, chemical controls on Mn uptake in siderite have not been well constrained, particularly for low supersaturation growth conditions. Mn is often a dominant component in siderite, but comparatively little is known about the palaeoenvironmental factors leading to Mn-rich siderites (Fisher et al., 1998; Choi et al., 2003; Lim et al., 2004; Weibel et al., 2016). Similarly, the significance of Mg-rich compositions, and associated changes in Ca, reported in ancient sphaerosiderites (Mozley and Wersin, 1992; Fisher et al., 1998; Khim et al., 1999; Khim et al., 2000; Choi et al., 2003; Lim et al., 2004), are poorly understood in the context of laboratory experiments (Thornber and Nickel, 1976; Mortimer et al., 1997; Romanek et al., 2009), which have been unable to reproduce natural concentrations of Mg in siderite. Although the latter observation has been intuitively ascribed to the influence of marine waters (Mozley, 1989; Choi et al., 2003; Ufnar et al., 2004b; Choi and Kim, 2006; Suarez et al., 2009; Robinson et al., 2010; Ludvigson et al., 2013; Weibel et al., 2016), the rates and mechanisms of element incorporation during siderite nucleation and growth are not fully understood.

5.2.2 $\delta^{18}O$ of siderite as a proxy for precipitation

Due to their mode of origin in waterlogged and reducing soils, the $\delta^{18}O$ values of sphaerosiderites are thought to be faithful recorders of the $\delta^{18}O_{groundwater}$ and soil temperature. The oxygen isotopic composition of waterlogged soils in humid climates is thought to be

minimally affected by evaporation, and therefore the sphaerosiderites growing in such environments should also be reflecting the regional $\delta^{18}O$ of precipitation.

Studies on multiple sphaerosiderites from the same location and stratigraphic horizon can produce Meteoric Sphaerosiderite Lines (MSL) showing an invariant $\delta^{18}O$, interpreted to reflect local meteoric groundwater, and variant $\delta^{13}C$. The variability in $\delta^{13}C$ is attributed to the Dissolved Inorganic Carbon (DIC) pool in pore waters reflecting spatial heterogeneity in a variety of processes such as bacterial degradation of organic matter, microbial methane oxidation, and methanogenesis (Whiticar et al., 1986; Whiticar and Faber, 1986; Mozley and Wersin, 1992; Mozley and Carothers, 1992; Ludvigson et al., 1998; Jimenez-Lopez and Romanek, 2004; Ufnar et al., 2004b). MSL's can also be used to identify if sphaerosiderite horizons are recording a mixture of pore water sources. A hypothetical example is shown in Figure 1.13, where the red data represent sphaerosiderites within a horizon which form a Meteroic Sphaerosiderite Line. By contrast, the blue data plot along a mixing line with positively correlated $\delta^{13}C$ and $\delta^{18}O$ positively, suggesting a mixing between marine and meteoric pore waters.

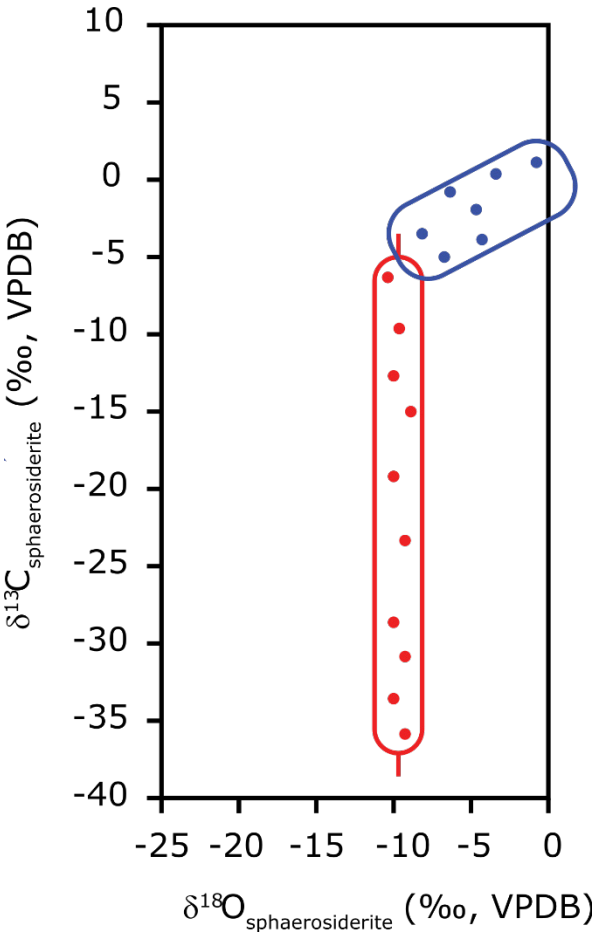


Figure 1.13: Schematic of Meteoric Sphaerosiderite Lines (MSL) and mixing lines in sphaerosiderites based on Ludvigson et al. (1998) (from Stuart Robinson).

MSL's have been widely used to reconstruct palaeo-groundwater $\delta^{18}O$, generally assuming siderite growth at Mean Annual Temperatures (MAT). As discussed above, the $\delta^{18}O_{groundwater}$ is interpreted as reflecting the $\delta^{18}O$ of regional precipitation. Studies on North American sphaerosiderites, mostly from the margins of the Western Interior Seaway, have produced a steep palaeolatitudinal gradient thought to reflect increased mid-latitude precipitation due to a stormier climate during the Cretaceous (White et al., 2001; Ufnar et al., 2004a). However, this conclusion has been disputed by climate modelling that has shown that the steep $\delta^{18}O$ gradient in siderites is also likely influenced by regional palaeotopography and sea level (Poulsen et al., 2007). Despite the likelihood of local effects, sphaerosiderites have provided an important record of continental palaeoclimates, and continue to be useful tools for reconstructing and refining our understanding of palaeohydrology in deep time. A detailed discussion of proxy caveats is presented in Section 5.2.3.

5.2.3 Proxy caveats

5.2.3.1 Heterogeneity within sphaerosiderites

Sphaerosiderites are known to exhibit elemental and morphological heterogeneity. In one study, the morphological changes are attributed to growth rates linked to siderite saturation in pore waters, with larger crystals linked to slower rates (Passey, 2014). However, this has not been fully constrained as sphaerosiderites vary in morphology through the geological record, and do not always conform to one particular pattern of morphological change within individual spheres. Compositional heterogeneity within spheres is usually attributed to varying palaeoenvironmental conditions during growth (Choi et al., 2003; Ufnar et al., 2004b; Weibel et al., 2016) leading to the inference that siderites record palaeo pore water composition (Mozley, 1989). However, as discussed in Section 5.2.1, this may be an oversimplification as laboratory syntheses are unable to produce elemental compositions

reflecting solution composition (Thornber and Nickel, 1976; Mortimer et al., 1997; Romanek et al., 2009). Isotopic heterogeneity within sphaerosiderites has not been explored, but the elemental and morphological heterogeneity recorded in sphaerosiderites suggests that isotopic composition within individual spheres is likely to be heterogeneous.

An additional issue arises from the growth period of sphaerosiderites which is not well constrained. Historical sphaerosiderites from Chattanooga, Tennessee are thought to grow for < 100 years (Driese et al., 2010) while nodules in Norfolk have formed around man-made nuclei in 6 months (Pye et al., 1990). Therefore, isotopic data from sphaerosiderites in deep time is an average of a generally unconstrained growth period. In light of this, it is important to evaluate the elemental and morphological heterogeneity in geological sphaerosiderites to provide a nuanced palaeoclimate and palaeoenvironmental interpretation.

5.2.3.2 Palaeoenvironmental assumptions

To calculate $\delta^{18}O_{groundwater,}$ from geological siderites, siderite-water fractionation equations from laboratory studies are used (Carothers et al., 1988; Zhang et al., 2001; van Dijk et al., 2018). This requires assumptions of the growth temperature of siderite and an assumed constancy of $\delta^{18}O_{groundwater}$ during growth.

Sphaerosiderites used in palaeoclimate reconstruction are usually assumed to be growing at Mean Annual Temperature (MAT) (Ludvigson et al., 1998; Ufnar et al., 2004a; Ufnar et al., 2004b; Ufnar et al., 2004c; Robinson et al., 2010; Weibel et al., 2016; Ross et al., 2017). However, recent work on modern siderite nodules suggests they can exhibit a temperature bias, dependent on the depth of growth within the soil profile (Van Dijk et al., 2019). Modern nodules growing in Norfolk, UK exhibited a summer bias in the temperatures reconstructed from clumped isotope measurements. In contrast, the clumped isotope temperature of siderite nodules from Houma, Louisiana were more akin to MAT. The siderites from Louisiana were growing at an undetermined depth within the soil profile,

while the Norfolk siderite nodules were growing just below the water table and close to surface. Van Dijk et al., (2019) suggest siderites growing closer to the surface record a summer biased signal, while deeper in the soil profile the seasonal temperature changes are dampened. This highlights that the assumption of sphaerosiderite growth at Mean Annual Temperature (MAT) is not universally applicable. Therefore, palaeoclimate reconstructions from siderites need an independent method of verifying temperature or depth of growth for calculating the isotopic composition of meteoric groundwater.

Studies on modern wetlands have also shown that the assumed $\delta^{18}O_{groundwater}$ constancy during growth may not be universally applicable (Driese et al., 2010; Ludvigson et al., 2013). High annual variation in modern $\delta^{18}O_{groundwater}$ at Chattanooga, Tennessee was linked to seasonally biased groundwater recharging, with variations of up to 6‰ recorded in one month. Sphaerosiderites growing in these porewaters were also shown to be 1–2‰ offset from the measured $\delta^{18}O_{groundwater}$ (Driese et al., 2004; Ludvigson et al., 2013). Although this may not be the case for all wetland systems, it highlights that pore waters may be far more variable than previously assumed.

6 Aims

The main aim of this thesis is to assess whether the Early Cretaceous continental hydrological cycle changed during the global Valanginian CIE (Lini et al., 1992; Stoll and Schrag, 1996; Erba et al., 2004; Weissert and Erba, 2004b; Littler et al., 2011; Föllmi, 2012; Price and Passey, 2013), using siderite as a proxy for palaeohydrology. This aim will be achieved by (1) laboratory synthesis of siderite to better constrain siderite as a proxy for palaeoclimate reconstruction, (2) using C-isotope stratigraphy to identify the Valanginian CIE in the Weald Basin, and (3) using the geochemistry of sphaerosiderite from the Berriasian–Hauterivian sediments of the Weald Basin, to reconstruct palaeohydrology across the Valanginian event. Specific details about each chapter are presented below.

6.1 Chapter 2: Experimental synthesis of siderite to constrain trace element uptake

The trace element composition of siderite has been used to identify marine influence (Mozley, 1989), as identifying freshwater siderites is essential when reconstructing the continental hydrological signal. Experimentally synthesised siderite from varying solution chemistries and saturation states will be used to constrain the dependence of siderite elemental chemistry on pore water chemistry. This study also evaluates siderite nucleation and growth at much lower saturation that previously reported, and at levels more analogous to natural wetland environments. In doing so, this chapter better constrains elemental uptake at low saturations and assesses the suitability of siderite as a proxy for paleoenvironmental conditions. This chapter has been published in *Geochimica et Cosmochimica Acta* (Sengupta et al., 2020, Geochemical Controls on elemental composition of siderite: Implications for palaeoenvironmental reconstructions, v. 271, p. 1–15).

6.2 Chapter 3: The Valanginian CIE in the Weald Basin

The Valanginian CIE is a global and synchronous event noted in both marine and terrestrial records (e.g. Weissert et al., 1998; Gröcke et al., 2006). This chapter describes the analysis of bulk organic $\delta^{13}C$ spanning the Berriasian–Hauterivian in order to identify the Valanginian CIE as expressed in the Weald Basin. In doing so, the chapter aims to correlate the Weald Basin sediments to the terrestrial $\delta^{13}C$ record from the Wessex Basin (Robinson and Hesselbo, 2004), and to Early Cretaceous marine records.

6.3 Chapter 4: Petrography and Geochemical composition of sphaerosiderites from the Weald Basin

This chapter aims to characterise Berriasian–Hauterivian sphaerosiderites from the Wealden Supergroup. It evaluates the morphology and mineralogical phases within

sphaerosiderites and surrounding matrix, the elemental composition, and suggests palaeoenvironmental and diagenetic interpretations to constrain the suitability of samples for palaeoclimate reconstruction.

6.4 Chapter 5: Palaeohydrology in the Weald Basin during the Early Cretaceous

This chapter is focused on $\delta^{18}O$ and clumped isotope palaeothermometry of sphaerosiderites, using these techniques to assess the hydrological cycle and climate in the Weald Basin during the Early Cretaceous. It also compares the $\delta^{18}O$ from sphaerosiderites with bulk organic $\delta^{13}C$ from Chapter 3 to understand climatic changes in the Weald Basin during the Valanginian CIE.

6.5 Chapter 6: Conclusions and Future Work

The last chapter presents the broad findings of this thesis, such as constraining siderite as a proxy for palaeoenvironment, its implications for the Wealden sphaerosiderites, and the implications of this Early Cretaceous palaeoclimate dataset from the Wealden in improving our understanding of the climatic effects of Valanginian CIE at low latitudes. This chapter also discusses suggestions for future work.

Chapter 2

Geochemical controls on the elemental composition of siderite: Implications for palaeoenvironmental reconstructions

The results and analysis presented in this chapter has been published in Sengupta et al, (2020) (*https://doi.org/10.1016/j.gca.2019.12.010*). This chapter constitutes a minor reformatting of that work to fit within the context of this thesis.

1 Introduction

Siderite ($FeCO_3$) is found in sedimentary rocks throughout geological time, notably as a constituent of Precambrian banded iron formations (BIFs), and in many sandstones, fine-grained siliciclastics, carbonates, and pedogenic nodules spanning the Precambrian and Phanerozoic (Bahrig, 1989; Choi et al., 2003; Johnson et al., 2008; Lim et al., 2004; Ludvigson et al., 1998; Pye et al., 1990; Robinson et al., 2010; Ufnar et al., 2004a, 2004b; Weibel et al., 2016). Of these deposits, early diagenetic siderite spheres (or "sphaerosiderites"), occurring within a range of strata deposited in dominantly non-marine environments (Ludvigson et al., 1998; Ufnar et al., 2004a; Ludvigson et al., 2013), are perhaps among the most studied examples of siderite precipitation of the Phanerozoic.

As sphaerosiderites are thought to grow in wetland soils, they are considered to be important archives of the continental hydrological system by providing a record of the $\delta^{18}O$ of meteoric groundwater (Mozley and Wersin, 1992; Ludvigson et al., 1998; Choi et al., 2003; Ufnar et al., 2004a; Choi and Kim, 2006; Suarez et al., 2009; Robinson et al., 2010; Ludvigson et al., 2013). Consequently, unravelling the precise nature of pore waters, from

which sphaerosiderites precipitated, has persisted as a major research goal. Indeed, the elemental composition of sphaerosiderites has been extensively used to infer freshwater, brackish or marine porewater conditions, in order to identify those samples likely to record a meteoric groundwater signal (Fisher et al., 1998; Choi et al., 2003; Lim et al., 2004; Ufnar et al., 2004a; Ufnar et al., 2004b; Driese et al., 2004; Robinson et al., 2010; Ludvigson et al., 2013; Weibel et al., 2016). For example, based on sedimentological studies of siderite-bearing strata, sphaerosiderites with more extensive Ca and Mg substitution are considered to reflect a marine influence, while higher concentrations of Mn compared to Ca or Mg are commonly interpreted to reflect freshwater conditions (Mozley, 1989; Ludvigson et al., 1998; Driese et al., 2010). However, laboratory synthesis has failed to produce Ca or Mg rich siderites, and little attention has been paid to Mn uptake (see Chapter 1 Section 5.2.1) (Thornber and Nickel, 1976; Carothers et al., 1988; Mortimer et al., 1997; Jimenez-Lopez and Romanek, 2004; Romanek et al., 2009).

The goal of this study is to address these issues through an experimental investigation of the controls on the chemical composition of inorganically precipitated siderite. In particular, the experiments presented here extend to relatively low saturation states and, hence, growth rates which may more closely represent wetland systems in which modern and ancient siderite growth has occurred. This chapter presents results from nucleation and growth experiments investigating a range of factors, such as pCO_2, salinity, cation concentration, temperature, and pH. In light of the results, the principal factors controlling the elemental composition of siderite in natural and synthetic systems are discussed. Finally, geological processes are reviewed that may further modify the elemental composition of sphaerosiderite in sedimentary systems, in order to provide a process-based framework to aid in their robust paleoenvironmental interpretation.

2 Methods

Two types of siderite precipitation experiments were conducted; homogeneous nucleation (where siderite was spontaneously precipitated directly from solution) and seeded growth (where siderite overgrowths were precipitated on to pre-existing seed material). These two experiment types can be distinguished based on saturation state, which is controlled by concentration of Fe^{2+}, pCO_2 (or total dissolved inorganic carbon, DIC), and pH. The saturation state of siderite can be expressed with the following relation:

$$FeCO_3(siderite) = Fe^{2+} + CO_3^{2-}$$

At solubility equilibrium:

$$K_{sp} = a_{Fe2+} * a_{CO32-} = 10^{-10.24} \text{ (Fosbøl et al., 2010)}$$

Under non-equilibrium conditions the ion activity product (IAP) and siderite saturation (SI) are:

$$IAP = a_{Fe2+} * a_{CO32^-}$$

$$\Omega = IAP/Ksp$$

$$SI = \log_{10}(\Omega)$$

Recent studies of the Fe(II)-carbonate system at ambient temperature (Dideriksen et al., 2015; Jiang and Tosca, 2019) have shown that homogeneous nucleation of Fe(II)-carbonate commonly involves the initial formation of a precursor phase (i.e., amorphous Fe carbonate or AFC) and that its apparent solubility corresponds approximately equal to a SI = 2.6. Thus, an operational definition is adopted for the threshold associated with homogeneous nucleation at this saturation state (Steefel and Van Cappellen, 1990; Van Cappellen, 1991). The conditions dominated by siderite growth (in the presence of seed material) should

therefore lie within a range of SI = 0 to 2.6 (Dideriksen et al., 2015), while at SI > 2.6, the homogeneous nucleation process is expected to dominate.

Precipitation experiments were conducted in 500 ml glass and LDPE bottles, covered in aluminium foil to prevent UV photolysis. The bottles were sealed with no headspace in order to achieve a closed system (and to prevent CO_2 degassing). All experiments were conducted in an anoxic glovebox, with 96% N_2 and 4% H_2 atmosphere. Palladium catalysts and anhydrous $CaSO_4$ desiccant ensured the oxygen concentration within the glovebox remained less than 1ppm, and the ambient atmosphere was kept at low relative humidity. All reactant stock solutions were prepared in the anoxic glovebox using 18 M-Ω deionized (DI) water. The water was purged with O_2 free-N_2 gas for 1 hour (Butler et al., 1994) and then left on a stir plate for 30 minutes in the glovebox to allow for the removal of residual oxygen.

Stock solutions prepared beforehand included 1M NaCl and 1M NaOH. 3-(*N*-morpholino)propanesulfonic acid (MOPS) and NaOH were together used to control the pH, while NaCl was used to produce a range of salinities and ionic strengths, approaching values corresponding to natural settings from fresh to marine pore waters. Because MOPS features significant steric hindrance of its acid-base functional groups, it does not exhibit appreciable complexation with transition metals such as Fe^{2+} in solution (Kandegedara and Rorabacher, 1999). After initial preparation (with $FeCl_2$), the 1 M Fe^{2+} stock solution was treated with Fe^0 powder (> 99%, Sigma-Aldrich) and HCl (1M) to reach a pH of 2 and left for 24 hours. This treatment reduced any Fe^{3+} in solution introduced from the reagent powder or from residual oxygen and stabilised the solution. After 24 hours, the solution was passed through a container with a Nd-magnet embedded in the bottom to remove the Fe^0 from solution. 1M $NaHCO_3$ solution, used to supply the carbonate in the reaction, was freshly prepared before each experiment to limit degassing.

Nucleation experiments were conducted at 20˚C (i.e., ambient temperature) and were started upon the delivery of $NaHCO_3$ stock solution with a syringe before being sealed with an opaque bottle cap. After delivery of the Fe stock solution, the experiments were left to run for 24 hours on an orbital shaker. The resulting precipitate was vacuum filtered in the glovebox and allowed to dry for 48 hours within the glovebox (covered in foil to avoid photo oxidation). The pH of each experiment was measured at the start (after addition of Fe^{2+}) and at the end (before filtration of precipitate). For growth experiments, the procedure was the same as stated above, except a premade pure (verified by X-ray diffraction) siderite seed was added to facilitate growth. The siderite seed (Appendix A.1.1) was imaged using FEI FEG Scanning Electron Microscope (SEM) at the Department of Earth Sciences, University of Oxford and the specific surface area was found to be $6 m^2/g$ as analysed using BET surface analysis (Micromeritics 3flex) at the Chemistry Research Laboratory, University of Oxford. Growth experiments were left for 25–30 days without stirring but were periodically shaken. Two elevated temperature growth experiments were also conducted at 40˚C and 55˚C respectively, under the same conditions. In these two cases, a stir plate with an integrated hotplate and temperature probe was used. The temperature probe was placed in the solution through the sealed septum placed in the bottle cap.

The conditions explored within these experiments are summarised in Table 2.1. Fe concentration was kept constant within batches of experiments, while Ca, Mn, and Mg were varied with reference to Fe. The Fe concentration was chosen based on reported pore waters from modern bogs (Postma, 1980; Pye et al., 1990), which vary from 0.2–1 mmol/kg with depth. It was necessary to conduct experiments at a higher concentration of Fe than reported from natural waters to produce enough solid precipitate for a range of analyses, and so that time-resolved changes in aqueous concentration could be observed with relatively high precision. The saturation states of the growth experiments are lower than previous experimental studies (Romanek et al., 2009; Thornber and Nickel, 1976).

	Nucleation	Growth	High Temperature
Cation concentrations	Fe, Mn, Ca:1–10 mmol/kg Mg: 0.25–52 mmol/kg	Fe, Mn, Ca: 0.1–1 mmol/kg Mg: 0.05- 5 mmol/kg	Fe: 1 mmol/kg Mg:0.5 mmol/kg
DIC	10 mmol/kg	2–5 mmol/kg	5 mmol/kg
pH	7–9	7–8	7.5
Ionic Strength	0.013–0.7	0.013–0.106	0.013
logΩ	2–3.6	0.5–1.975	2.38–2.65
Stirring	Orbital shaker	No	Hot plate with integrated stir plate
Siderite seed	No	Yes	Yes
Temperature	25˚C	25˚C	40˚C and 55˚C

Table 2.1: Summary of experimental variables employed in this study

Solution samples were taken at the beginning and end of the nucleation experiments, and every 2–4 days during growth experiments (depending on the length of the experiment). The solution samples were immediately acidified with 5% HNO_3 and analysed for major element chemistry using Inductively Coupled Plasma-Optical Emission Spectrometry (ICP-OES) at Scottish Universities Environmental Research Centre (SUERC) and Department of Earth Sciences, UCL. All analysis batches included matrix matched quality control standards. Rates of reactions were calculated by the difference in measured cation concentration (Fe and Mn) over a given time unit, and correcting the saturation state by subtracting DIC and recalculating for the next time step. Precipitates were analysed using a FEI FEG-SEM at Oxford to image the crystalline morphology at high resolution. An EDS detector was used to constrain elemental composition of experimental precipitates. The precipitates were also analysed using a PANalytical Empyrean Series 2 X-ray diffractometer at Oxford, which used a Co Kα source at 40 kV and 40 mA. Samples were prepared in the glovebox on zero-background single crystal silicon substrates and sealed with X-ray transparent Kapton film prior to analysis.

3 Results

3.1 Fe(II)-carbonate precipitation pathways

After removal of Al foil, precipitates were visibly identified in nearly all experiments. Once filtered, the precipitates ranged in colour from greenish-gray to dark brown, as is typical of $FeCO_3$ synthesis (Fosbol et al., 2010). The precipitates were dried at 25˚C, and also changed colour when drying, generally becoming darker. Powder X-Ray diffraction analyses confirmed that experimental precipitates were dominated by Fe(II)-carbonate minerals (Appendix A.1.2). XRD analysis of precipitates formed between pH 7 and 8 show the material to be mostly siderite. Exceptions to this included some of the higher pH experiments (pH 8 to 9) which also produced chukanovite ($Fe_2(OH)_2CO_3$). Precipitate morphology varied from siderite rhombohedra of various forms (~1–4 μm in length) to spherical particles composed of clusters of smaller rhombs (Figure 2.1). The spheres were on average 10 μm in diameter, while the constituent rhombs comprising the spheres were typically < 1 μm along single crystal edges.

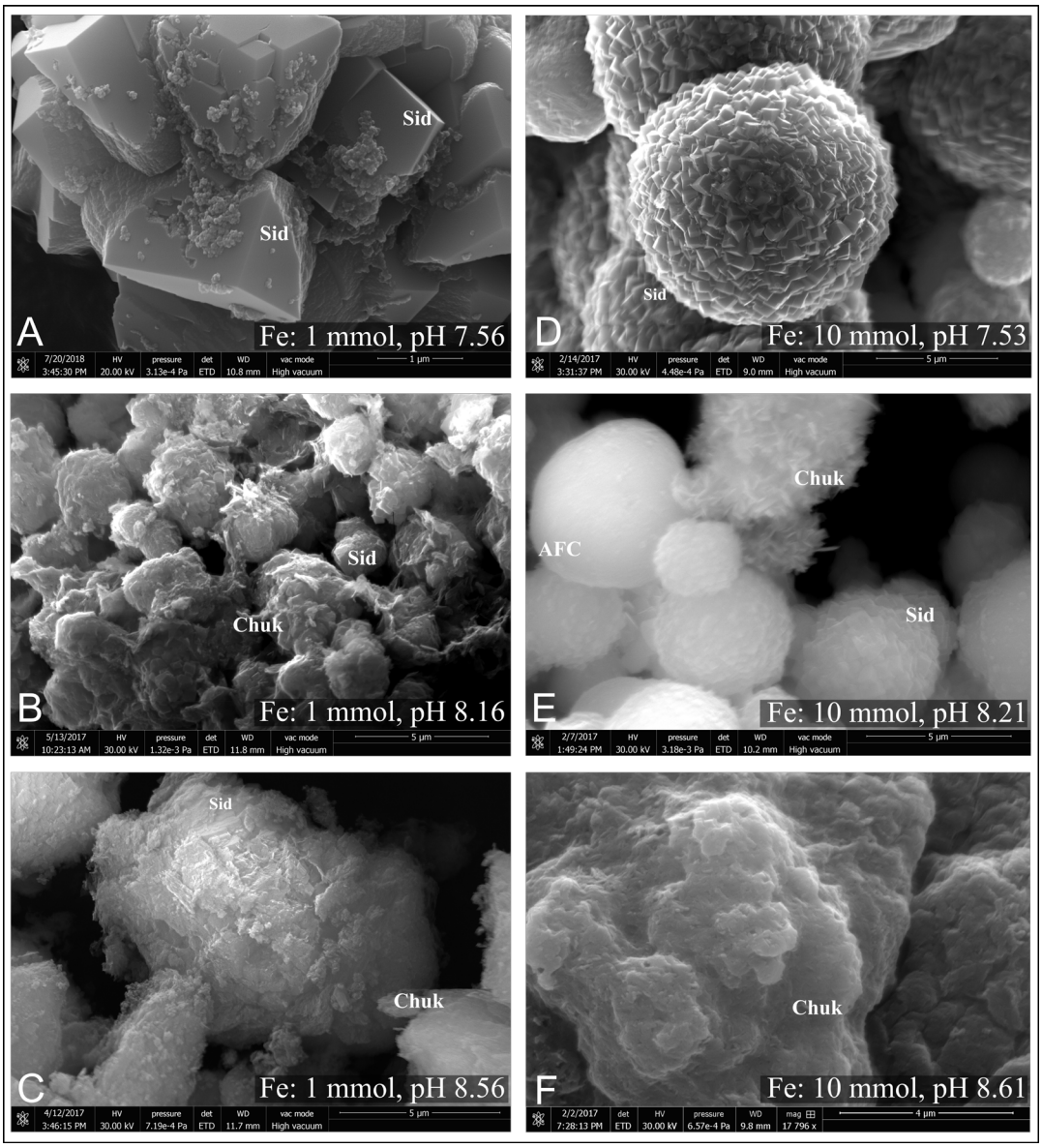


Figure 2.1: SEM micrographs of experimental precipitates showing representative morphological end-members. A to C) Fe concentration 1 mmol/kg, D to F) Fe concentration 10 mmol/kg. Morphological diversity is attributed to the range of siderite saturation states investigated, which in turn controls the rates of nucleation and growth. As shown from A to C and D to F, increasing pH causes precipitates to change from pure siderite to a mixture of siderite and chukanovite, to pure chukanovite. E shows a spherical particle with no apparent crystalline morphology at the resolution limit of the SEM (10s of nm), and is interpreted to be amorphous iron carbonate (AFC), which recrystallized to form the spherical clusters of rhombs, similar to polycrystalline particles shown in D.

Above pH 8, pure siderite could not be obtained. The precipitate was either a mixture of siderite and chukanovite or purely chukanovite. Between pH 8.5 and 9 the precipitates were nanocrystalline and often purely chukanovite (Figure 2.1c, f). Chukanovite [$Fe_2(CO_3)(OH)_2$] is an iron(II) carbonate hydroxide with acicular, platy or fibrous crystals. It is metastable with respect to siderite, and thus can transform to siderite with time (Azoulay et al., 2012). The presence of chukanovite and siderite mixed within the sample (Figure 2.1b, e) indicates more than one formation pathway for siderite, probably through competitive surface nucleation of the two phases on an amorphous precursor (Dideriksen et al., 2015).

The range in morphology (rhombs to spherical clusters of rhombs) is most likely influenced by the balance between nucleation and growth rates. Previous studies of Fe(II)-carbonate precursor structures and stability have shown that the amorphous precursor provides a low energy pathway to Fe(II)-carbonate mineralisation (Sel et al., 2012; Dideriksen et al., 2015). After its initial nucleation, the amorphous precursor provides a substrate for the subsequent heterogeneous nucleation of siderite (or chukanovite), as observed in other mineral systems (Van Cappellan, 1992; Nielsen et al., 2014). Rapid surface nucleation would therefore replace the initially spherical amorphous particle with a significant number of siderite rhombs encrusted on its surface (Van Cappellan, 1992; Nielsen et al., 2014). This process continues until the amorphous precursor is consumed and progressively replaced by siderite, yielding an overall morphology that Dideriksen et al. (2015) argued was a distinctive product of this mineralisation pathway. This morphology is identical to that observed in the experiments (Figure 2.1d, e) presented here. The clusters of rhombs in spherical polycrystalline aggregates were primarily noted in the nucleation experiments with Fe^{2+} concentration of 10 mmol, allowing a high saturation state and rapid nucleation. The rhombohedral crystal shape was observed in experiments with lower Fe^{2+} concentration of 1 mmol as well as lower pH, and therefore lower saturation, together promoting slower nucleation rates relative to growth rates.

3.2 Cation uptake in siderite

3.2.1 Mn uptake

Mn uptake was observed in all experiments with Mn2+ present in the initial solution (a range of such data from growth experiments is presented in Figure 2.2). Fe and Mn decreased in all growth experiments with time (Figure 2.2). In experiment 8 at pH 8 (Figure 2.2), Fe and Mn show a slight increase after 20 days; this pattern is observed across all cations analysed. As solution samples were analysed in groups and retained in the glovebox after acidification, this is interpreted to reflect gradual sample evaporation in the low-humidity glovebox atmosphere with increased experiment duration. During growth experiments Fe/Mn ratios increased as reactions progressed, coincident with decreasing siderite saturation, which in turn led to decreasing growth rates. Because experiments were conducted in closed vessels, the removal of Fe during precipitation leads to a progressive decrease in siderite saturation state and therefore lower reaction rates with time. The negative relationship between rate and Fe/Mn indicates (data not shown, see Appendix A.1.1) that Mn uptake is influenced by the siderite saturation state in solution.

Fe/Mn ratios of the initial solution and the final precipitate show a strong positive correlation for both nucleation and growth experiments as shown in Figure 2.3, but the evolution of Fe/Mn in solution over time (Figure 2.2) suggests cation ratios are not the sole factor in controlling Mn uptake. The correlation between Fe/Mn of the precipitate and initial solution appears to deviate from a 1:1 line (Figure 2.3), although this deviation is statistically insignificant. The relationship between calculated Fe/Mn in the precipitate and the initial Fe/Mn in nucleation experiments also varies with crystalline Fe(II)-carbonate phase (siderite and chukanovite). EDS spectra and ICP-OES data from pure chukanovite samples (Figure 2.3) shows Mn uptake in chukanovite to be less than in siderite. However, a positive

correlation is still present, regardless of the phase, as evidenced by a similar trend in the pure siderite growth experiments.

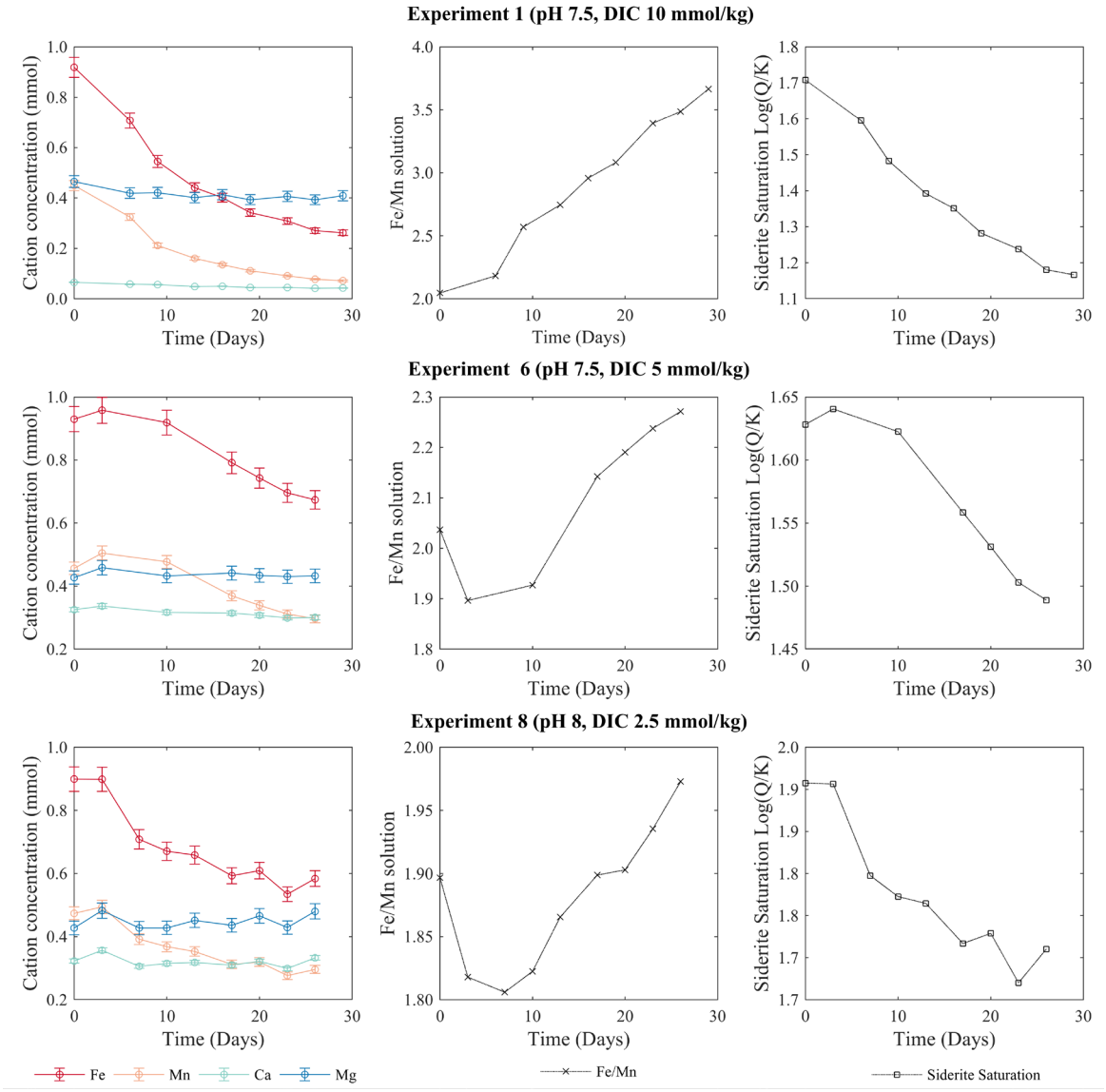


Figure 2.2: Selection of growth experiments displaying cation concentration in solution with time. Pure siderite seed (0.5g) was added at the start of all experiments. Fe and Mn uptake are notable. The differences in Fe uptake reflect differences in starting pH and pCO_2, and therefore saturation state, between the experiments. Fe/Mn of the solution increases with decreasing siderite saturation, indicating that Mn is incorporated into the precipitate in preference to Fe with decreasing reaction rate of siderite. Ca and Mg concentrations are generally invariable, and uptake is not discernible. The final concentrations of Ca and Mg in all experiments are within error of the initial concentration.

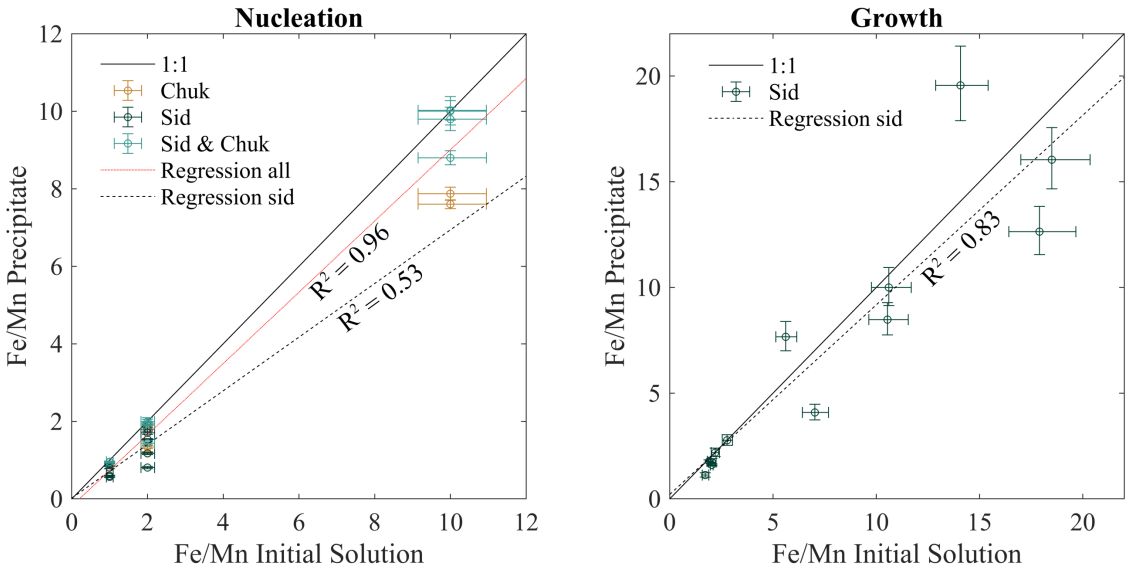


Figure 2.3: Fe/Mn of precipitate and initial solution in growth and nucleation experiments. Fe/Mn of final precipitate was calculated from the initial and final Fe/Mn ratios from solutions.

3.2.2 Ca uptake in siderite

For nucleation experiments, Ca was incorporated into siderite with less preference than for Mn. Ca uptake was between 10–30% of initial concentration in nucleation experiments, but correlations with factors such as pH, cation concentrations or pCO_2 were not statistically meaningful. At higher pH, Ca uptake appeared to increase, but the presence of multiple phases complicates the interpretation of data collected from these experiments (Appendix A.1.1).

In contrast, during growth experiments, Ca uptake was not discernible when Mn was present (Figure 2.2). Although there is some variation in Ca over time, mostly noticeable in experiment 8 (Figure 2.2), this is likely an artefact of dilution. The final concentration of Ca is still within error of the starting concentration, and therefore Ca uptake is not discernible using ICP-OES. EDS spectra of some of the growth experiments show a very minor amount of Ca present in the precipitate (0.5–1.6 wt%). The amount detected also increased when the

average rate of the experiment was generally higher. For instance, one experiment with an average rate of growth of 0.02 mmol/day showed 1–1.2 wt% uptake of Ca on EDS. In contrast, an experiment with a rate of a growth of 0.002 mmol/day, resulted in an EDS measurement of 0.2–0.6 wt % Ca. However, these quantities are very close to the detection limits of SEM-EDS and cannot be used for quantitative analyses. They are presented simply to support the solution chemistry data which suggests that Ca uptake was negligible during growth experiments.

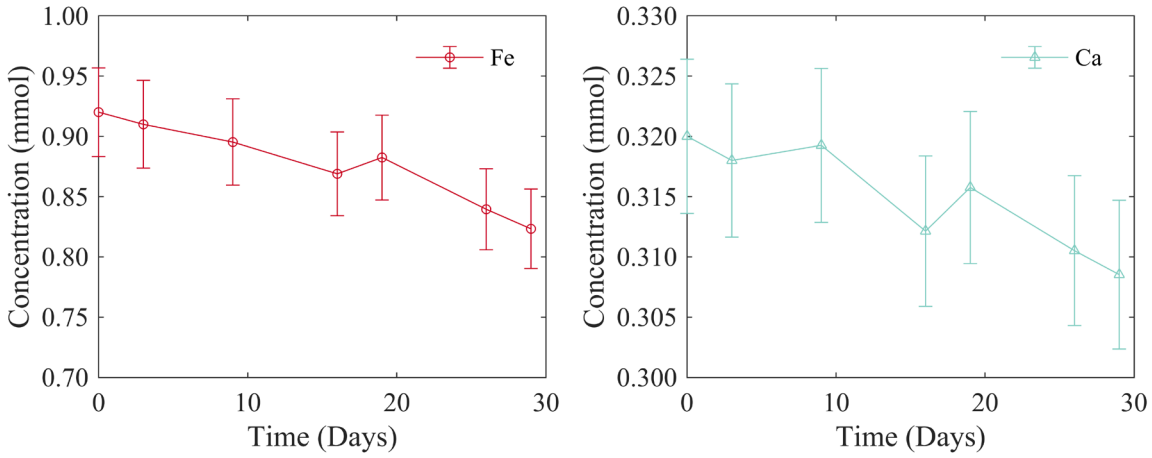


Figure 2.4: Control growth experiments with only Fe and Ca in starting solution showed decrease in Ca, but within error. Therefore, no discernible uptake can be noted from the control experiments.

Control growth experiments at low saturations were conducted with only Fe and Ca to investigate whether the presence of Mn was inhibiting Ca uptake. In these experiments there is no observable uptake of Ca under the conditions explored here, despite clear evidence for siderite growth (Figure 2.4). EDS spectra yielded 0.2–0.5 wt% Ca in these control experiments.

3.2.3 Mg uptake in siderite

ICP-OES data show no evidence for Mg uptake into siderite in either nucleation or growth experiments at ambient temperature. Some variation in Mg concentration is noted in

Figure 2.2, although this is mainly in Experiment 8. Similar to the Ca concentrations discussed above, the variations in Mg can be attributed here to inconsistencies in dilution between some samples. However, the end concentration and the starting concentration of Mg are within error of each other and therefore significant Mg uptake is not detectable by ICP-OES.

As mentioned previously, nucleation experiments above pH 8 produced a mixture of siderite and chukanovite. EDS-SEM point analysis on these samples detected a small Mg peak, although it was very close to the detection limit. As this peak was noted in 60% of samples above pH 8, it could be inferred that a very minor amount of Mg may have been taken up in the chukanovite structure, but not enough to be detectable by ICP-OES. This was the case irrespective of whether Mn and/or Ca were present in solution, including at modern marine concentrations of Mg (52 mmol). Mg is known to inhibit calcite growth at seawater concentrations (Zhang and Dawe, 2000; Davis et al., 2004; Chen et al., 2005) but, in contrast, Mg did not appear to have any effect on Mn or Ca uptake in siderite in the experimental temperature and pressure ranges used, even at modern seawater concentrations.

As previous studies have considered the effect of temperature on Mg uptake in siderite (Romanek et al., 2009), two higher temperature Mg control experiments were also conducted to explore this effect further. As expected, the rate of seeded siderite growth increases with temperature (Figure 2.5). The 40°C experiment yielded no evidence for Mg uptake, within analytical error. At 55˚C, Mg uptake was statistically significant, though minor, at 0.0099 mmol in total (< 2% of the initial concentration). SEM-EDS point analysis detected a small Mg peak, although it is bordering on the detection limit.

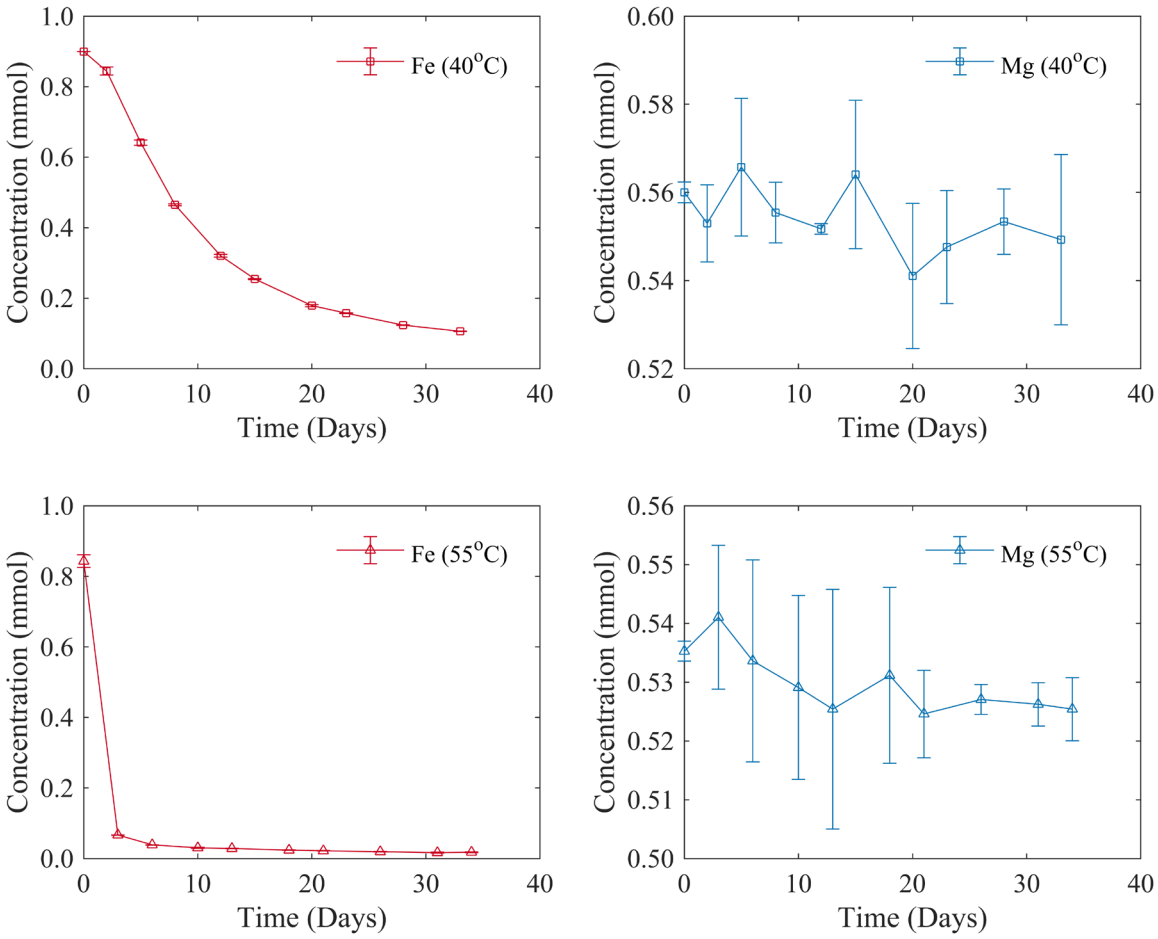


Figure 2.5: Control experiments with Fe and Mg as the only available cations to monitor Mg uptake in siderite at elevated temperatures, and in the absence of competing cations. Mg uptake was only discernible at 55°C.

3.3 Rates of growth

Solution chemistry data from seeded growth experiments indicate that each experiment is associated with significant Mn uptake, in addition to Fe, into overgrowths precipitated on siderite seed material. Thus, in order to calculate growth rates as a function of solution supersaturation, supersaturation was evaluated with respect to a Mn-bearing siderite with a composition equating to the average Mn coprecipitated in overgrowths (i.e., 11 mol% Mn in $FeCO_3$, or $Fe_{0.89}Mn_{0.11}CO_3$). In order to estimate the log K_{sp} for such a material, a complete binary solid solution between $MnCO_3$ and $FeCO_3$ was assumed and a regular solid solution model employed to estimate activity coefficients of solid phases (Glynn, 2000). This regular

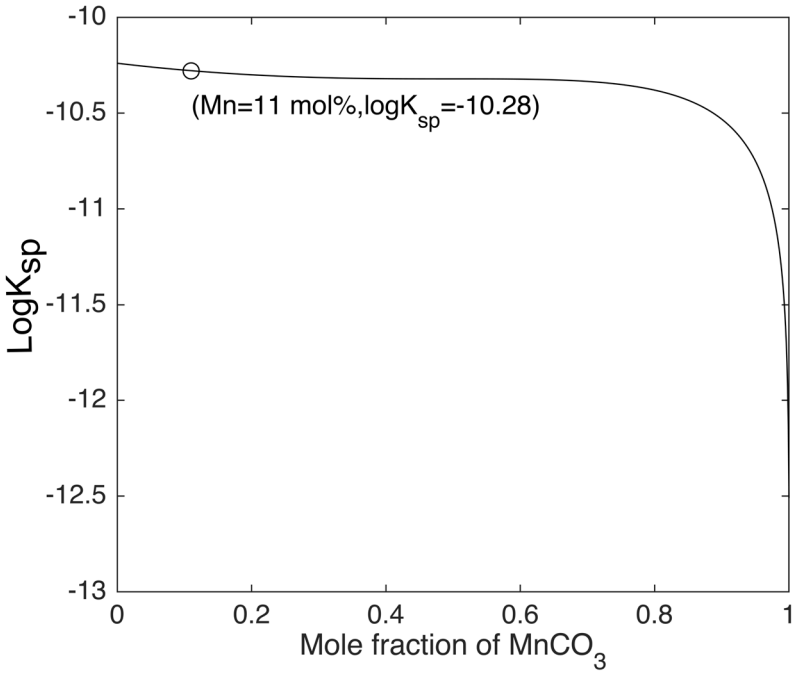


Figure 2.6: Calculated K_{sp} = -10.28 at Mn substitution of 11 mol% into the carbonate phase formed on average during seeded growth experiments.

solid solution model employs the dimensionless parameter, a_0, which is used in the expansion series to estimate the excess Gibbs free energy of mixing between two end-members (Glynn, 2000). For the $(Fe,Mn)CO_3$ system. This dimensionless parameter is constrained to a value < 2.0 based on experimental data (Glynn, 2000). The log K_{sp} value for $FeCO_3$ equal to –10.24 (Fosbøl et al., 2010) and, for $MnCO_3$, a log K_{sp} value equal to –12.51 (Jensen et al., 2002) is used. The resulting K_{sp} for $(Fe,Mn)CO_3$ as a function of composition is illustrated in Figure 2.6.s

Experimentally calculated surface area-normalised growth rates for seeded experiments are shown in Figure 2.7 as a function of supersaturation relative to $Fe_{0.89}Mn_{0.11}CO_3$. Although the data are highly scattered, a statistically significant relationship between growth rate and precipitation is evident within the 95% confidence interval. This relationship can be expressed with a general rate law for growth:

$$R = k(\Omega\text{-}1)^n$$

where R is rate (mol/m^2/hour) k is the rate constant, n is the empirical reaction order and (Ω–1) is the supersaturation with respect to $Fe_{0.89}Mn_{0.11}CO_3$. This data constrains n to

0.95 and k to 8.11E-8 mol/hr. The empirical reaction order is generally thought to contain information about the dominant growth mechanism (Teng et al., 2000). Kinetic studies of mineral growth typically attribute n values of 1 to reflect adsorption-controlled growth, values of 2 to reflect growth at screw dislocations via a spiral growth mechanism, and values > 2 to reflect growth at screw and edge dislocations (Teng et al., 2000). However, this general rate law does not take into account the structure and source of dislocations at the mineral surface and, because such empirical rate laws are typically derived from bulk solution chemistry measurements, do not reflect growth processes actually operating at mineral surfaces (Teng et al., 2000). From the experimental data it is not possible to resolve statistically significant crossover points in the empirical reaction order as a function of supersaturation which might be taken to reflect a change in the dominant mechanism. More data will be required to elucidate this dependence, in particular direct observations of the dominant surface growth mechanism under these conditions.

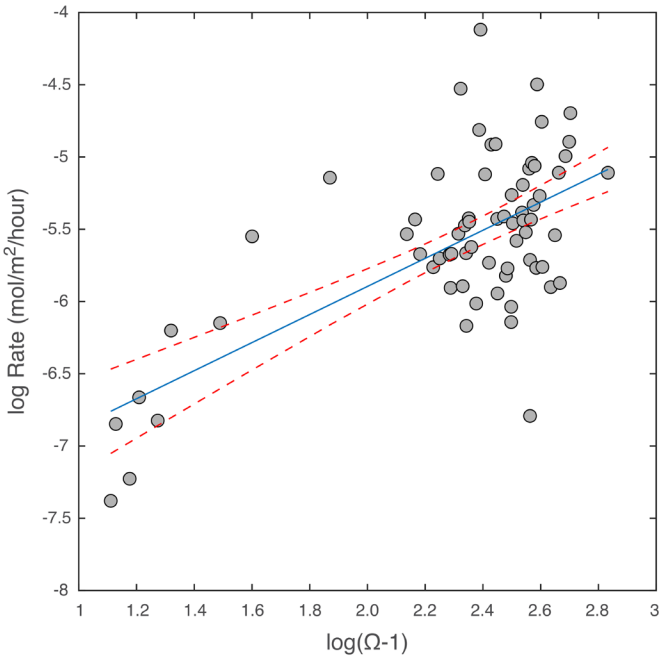


Figure 2.7: Experimental rates (mol//m^2/hr) from seeded growth experiments. Dashed lines indicate 95% confidence intervals.

3.4 Effect of salinity changes

As mentioned in Table 2.1, salinity changes were explored using NaCl concentrations analogous to fresh, brackish and marine waters, in the presence of Fe, Mg, Ca and Mn as

available cations. However, salinity changes were found to have no significant effect on the uptake behaviours described in the above sections (Appendix A.1.4).

4 Discussion

4.1 Comparison to previous studies

4.1.1 Trace element uptake in siderite

In their examination of the partitioning of trace elements between carbonate minerals and aqueous solutions, Rimstidt et al. (1998) observed that, for calcite, the apparent distribution coefficients derived from experimental work correlated with the quotient of the solubility product of the host carbonate to the trace element carbonate. The authors also extended this analysis to siderite, using an experimental dataset reported previously (Thornber and Nickel, 1976). To facilitate comparison to the experimental data presented in this chapter, the estimated apparent trace element distribution coefficients for siderite from Romanek et al. (2009) are plotted in Figure 2.8.

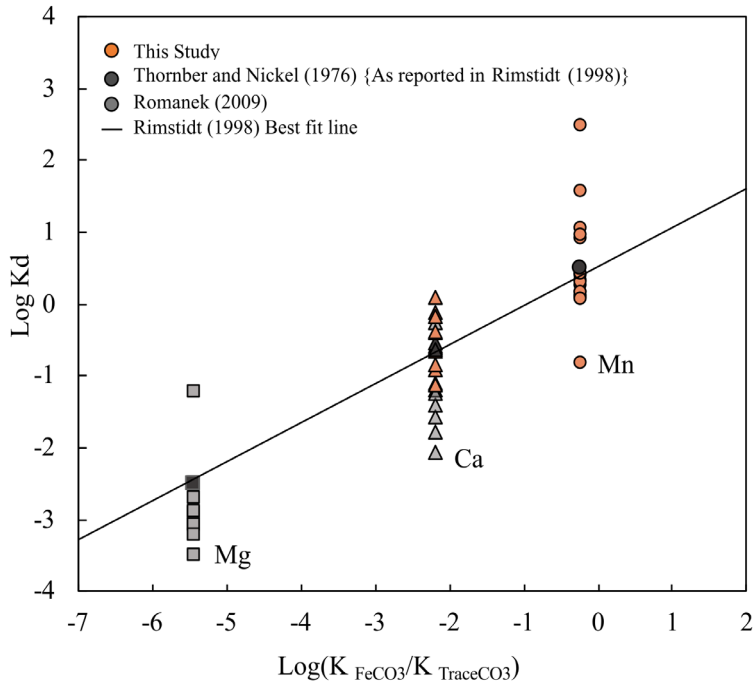


Figure 2.8: Comparisons of apparent distribution coefficients (Kd') from Romanek et al (2009), Rimstidt et al (1998) and calculated Log K (Rimstidt et al., 1998). Kd is positively correlated to the solubility quotient of siderite with respect to trace cation, displaying a clear preference of Mn uptake over Ca and Mg.

This data support the initial observation by Rimstidt et al. (1998) that, in addition to calcite, trace element incorporation into siderite correlates with the quotient of the siderite and trace element carbonate solubility products. Although available experimental data show significant variation about this trend, this general correlation leads to two conclusions. The first is that, as the experiments show, trace element uptake into siderite should occur with increasing preference in the following order: Mg << Ca < Mn; this finding is consistent with Rimstidt et al (1998). Romanek et al. (2009) have previously shown a linear relation between Ca:Fe(aq) and Ca:Fe(s) in the absence of Mn but presence of Mg. This, along with the low Kd of Ca compared to Mn, also implies that Ca uptake is hindered by the presence of the preferential trace cation Mn. The second conclusion, noted by Rimstidt et al. (1998), is that the slope of the correlation deviates from the equilibrium slope of 1, meaning that kinetic processes rather than equilibrium processes ultimately control trace element incorporation into siderite during nucleation and/or growth.

In the discussion that follows, a review of the factors behind these apparent trends in element uptake during siderite growth are provided, and these factors with respect to reported compositional data for ancient siderites, are discussed.

4.2 Mechanisms of cation uptake in siderite

4.2.1 Cation hydration characteristics

Free ions (such as Fe^{2+}, Mn^{2+} etc.) in aqueous solution are closely associated with H_2O molecules. Dehydration energies required for a cation to be extracted from these hydrating H_2O molecules, and become incorporated to a growing crystal surface, are dependent on cation size and charge. Romanek et al. (2009) attributed the lack of Mg uptake during siderite growth at ambient temperature to a higher dehydration energy required for Mg^{2+} as opposed to Ca^{2+} and Fe^{2+}. However, the hydration enthalpies of Mg^{2+} and Fe^{2+} are, in fact, very similar (Burgess, 1978). This data presented here show that observable Mg uptake does not

occur during nucleation or growth at ambient temperatures, regardless of solution chemistry. The presence of Mg also does not appear to affect the uptake of other cations, where the main trend was a preference for proportional Mn uptake. Finally, if dehydration was a main kinetic control, the relative hydration energies would predict preferential uptake of Ca over Mn, the opposite to what is observed in the data presented here and in previous studies (Figure 2.8). Together, this indicates that other factors must be primarily responsible for cation uptake during siderite growth.

4.2.2 Crystal structure

The preference for Mn^{2+} uptake over Ca^{2+} and Mg^{2+} during siderite growth could relate partly to structural differences between rhombohedral carbonates. Intuitively, it might be expected that cations with a similar radius to iron to be accommodated more readily in the siderite structure. Reeder (1983), based on experimental work summarised by Goldsmith (1983), suggested that the differences in ionic radius between cation pairs in rhombohedral carbonates could be divided into two classes: pairs that should exhibit complete miscibility (differences $\leq$ 0.11Å), and those that should exhibit limited miscibility (differences $\geq$ 0.11Å). On this basis, cation radius differences between Fe^{2+} and Mn^{2+}, and Fe^{2+} and Mg^{2+} predict complete miscibility, whereas Fe^{2+} and Ca^{2+} predict limited miscibility. To a first approximation, this suggests that there may be few structural barriers to extensive Mn incorporation in the siderite lattice, consistent with the Mn uptake data. In addition, these relationships suggest that structural factors may limit the amount of Ca incorporation in the siderite lattice, which may be one factor contributing to the observed low distribution coefficients for Ca. The prediction of full miscibility between Mg and Fe in siderite, however, suggests that the negligible uptake observed in the experiments and low apparent distribution coefficients (Thornber and Nickel, 1976; Rimstidt et al., 1998; Romanek et al., 2009) may be better explained by kinetic factors.

4.2.3 Surface structural control

Mineral growth mechanisms are strongly controlled by saturation state, implying that the structure of the siderite surface, as it grows in solution, may control trace element uptake. In general, with increasing supersaturation, mineral growth progresses from spiral growth triggered at surface kink sites, to 2D nucleation, and non-classical growth (possibly involving an amorphous precursor) above what is termed the roughening transition (Sunagawa, 2007; Rodriguez-Navarro et al., 2016). However, most natural systems are poised at saturation states that promote spiral growth, which features the advancement of structurally non-equivalent growth steps on growth hillocks (Paquette and Reeder, 1995; Rakovan and Reeder, 1996; Reeder and Rakovan, 1999; Sunagawa, 2007). Previous work on calcite has shown that during spiral growth, trace element uptake is strongly controlled by both the rates of growth step advancement and by structural characteristics of kink sites generated at non-equivalent growth faces (Paquette and Reeder, 1995; Reeder, 1996; Rakovan and Reeder, 1996). This process ultimately results in intra-sectoral zoning of trace elements on the calcite surface (Paquette and Reeder, 1990). This work also suggests that cation size may play a role in determining trace element incorporation at the growing interface, with sterically unconstrained kink sites favouring larger cations, and more constricted kink sites favouring smaller cations (Paquette and Reeder, 1995; Rakovan and Reeder, 1996). This work offers a conceptual framework to explain differential element incorporation and variations with growth rate, using the documented Mn incorporation. Specifically, increases in growth rate will translate to increases in the rate of growth step advancement (Gratz et al., 1993). However, different growth steps exposed on symmetrically non-equivalent faces will respond differently to saturation state. On this basis, one explanation for the observed decrease in Mn uptake with increases in growth rates may be that growth rate increases translate to more rapid advancement of growth steps at the siderite surface where Mn incorporation is less favoured, perhaps by surface structural constraints.

Another possibility is that if growth rates of siderite increase to the point where a different growth mechanism begins to dominate (i.e., 2D nucleation), then trace element incorporation may exhibit corresponding differences. However, the saturation state at which 2D nucleation might begin to dominate siderite growth is unconstrained, and the growth rate data cannot statistically resolve changes in the empirical reaction order, or the relationship between growth rate and saturation state which might signal a mechanism change.

4.2.4 Transport / boundary layer control

An additional kinetic control, discussed by Rimstidt et al. (1998), involves the transport of trace elements through solution to the surface of the growing crystal. Because trace elements are likely to be incorporated at rates that differ from the rate of Fe^{2+} incorporation into siderite, this may lead to the development of a solution boundary layer that is either depleted in the trace element (i.e., if Kd > 1) or enriched in the trace element (i.e., if Kd < 1). This will, in turn, influence the effective Kd, rate of cation diffusion to the growing surface, and/or influence the overall growth rate of the mineral (i.e., lead to oscillatory zoning; Reeder et al., 1990; Wang and Merino, 1992).This relationship predicts that trace elements where the apparent distribution coefficient is > 1 should exhibit an increase in element uptake with decreasing growth rate. Indeed, the observations of Mn uptake suggest that this process may be operating, analogous to Mn uptake in calcite (Dromgoole and Walter, 1990). However, as discussed above, because surface structural controls on element uptake may also be important in this system, it is not possible to uniquely identify which processes are most important. Indeed, both may be operating, leading to a network of complex kinetic controls on element uptake.

The boundary layer is likely to shrink with increasing temperature due to increased rates of diffusion. This would minimise the role of the diffusion layer in controlling cation uptake. However, despite these expectations, available data indicate a number of competing factors

as temperature increases. For example, Rimstidt et al. (1998) showed that modelled Kd values for numerous cations in calcite do not change significantly over 0–100˚C and attributed this to solubility products of carbonates changing similarly with temperature. In their model, however, the Kd of Mg in calcite increased with temperature. The influence of temperature on Mg uptake in siderite is further discussed in Section 4.2.6.

4.2.5 Non-Traditional Precipitation Pathways

As discussed above, there seem to be few structural constraints limiting the extent of Mg incorporation into the siderite structure, yet Mg uptake in siderite is characterised by very low distribution coefficients. This is analogous to the incorporation of Mg in calcite, which is characterised by similarly low distribution coefficients (Reeder, 1983; Rimstidt et al., 1998; Romanek et al, 2009). Yet, Mg-rich calcite is well known from modern and some ancient marine carbonate successions, and notably from biologically-mediated calcite precipitation (Weiss et al., 2002; Addadi et al., 2003; Politi et al., 2009). Recent studies of carbonate precipitation kinetics have shown that the formation of an amorphous calcium carbonate (ACC) precursor permits significant Mg-incorporation upon precipitation (Blue and Dove, 2015). The Mg content of the ACC depends strongly on pH and Mg concentration in solution. As ACC recrystallises, the resulting calcite is often characterised by relatively high Mg content (Blue et al., 2017). The precipitation of ACC itself requires very high supersaturation states in the $CaCO_3$ system (Brečević and Nielsen, 1989) which, as previous studies have shown, can be attained in biomineralizing systems through the specific roles of biomolecules (Weiner and Dove, 2003). Amorphous precursor phases also feature commonly in the Fe(II)-carbonate system, in particular during homogeneous nucleation (Dideriksen *et al.*, 2015; Jiang and Tosca*.,* 2019). Such a pathway might be common in systems that achieve rapid supersaturation with respect to siderite. One example is through dissimilatory Fe-reduction where Fe^{2+}, DIC, and total alkalinity are all simultaneously

increased as the reaction progresses. In fact, experimental studies of dissimilatory Fe-reduction show morphological evidence for precipitation of siderite through an amorphous iron carbonate (AFC) precursor (Mortimer et al., 1997; Johnson et al., 2005; Dideriksen et al., 2015).

Such precipitation pathways in the Fe(II)-carbonate system might be expected to influence element incorporation in to the siderite structure, given that amorphous $CaCO_3$ has been shown to be relatively indiscriminate toward trace element uptake (Littlewood et al., 2017). The homogeneous nucleation experiments producing siderite via an amorphous precursor phase, however, show no discernible increase in Mg. EDS-SEM detects only a small peak for Mg, barely above detection limit. This is in agreement with other studies showing low apparent Kd of Mg in siderite (Thornber and Nickel, 1976; Romanek et al., 2009). There is, however, one notable exception. Romanek et al (2009) reported that Mg was only incorporated in to siderite structure when Mg starting concentration was at modern seawater concentrations, along with increased temperature and/or very large increases in carbonate alkalinity. However, it is unclear from their data whether Mg uptake is uniquely confined to siderite or instead to a Mg-rich carbonate phase, as the precipitates reported include multiple carbonate phases (i.e., siderite, and magnesite or hydromagnesite).

4.2.6 The role of temperature

A number of studies have documented strong increases in the distribution coefficient describing Mg incorporation into calcite with temperature (Katz, 1973; Oomori et al., 1987; Mucci, 1987) Data for Mg^{2+} incorporation into siderite with temperature are far more limited. Data reported by Romanek et al. (2009) show uptake of Mg at 70˚C, consistent with analogous predictions from the $CaCO_3$ system (Romanek et al., 2009). However, the precipitate identified was magnesite or hydromagnesite, where Fe becomes a trace cation. The experiments presented here attempt to further investigate this. The 40˚C experiment did

not show Mg uptake above the margin of error, however the precipitate formed at 55˚C did co-precipitate Mg (consuming < 2% of the initial concentration of Mg). Mg concentrations used in the experiments were 40–50% lower than Fe concentrations, and siderite was verified through XRD. The limited data predict that Mg uptake into siderite may continue to increase with increasing temperature. Therefore, in the absence of other clear controls on Mg incorporation into siderite, temperature can be considered as one of the strongest controls on Mg concentrations in light of available data.

4.3 Elemental composition of siderite as an indicator for palaeoenvironment

One of the motivating scientific questions for this study is whether major element composition of siderite can be a reliable paleoenvironmental indicator of pore water conditions, applicable to continental siderite studies through the Phanerozoic. Elemental compositions of sphaerosiderites and other early diagenetic forms of siderite have been reported in many studies (Mozley, 1989; Baker et al., 1996; Choi et al., 2003; Lim et al., 2004; Ufnar et al., 2004a; Robinson et al., 2010; Ludvigson et al., 2013; Passey, 2014; Weibel et al., 2016). Some of these studies report similar compositional trends, notably the repeated observation of Mn rich cores, and Ca and Mg rich outer rims/overgrowths (Curtis et al., 1986; Baker et al., 1996; Choi et al., 2003; Lim et al., 2004; Passey, 2014; Weibel et al., 2016). Other examples show only minor Ca, Mg and Mn substitution, with Mn incorporated the least (Choi et al., 2003; Robinson et al., 2010). Generally, extensive Ca or Mg substitution, or extensive substitutions of cations other than Fe^{2+} have been considered to indicate marine alteration (Mozley, 1989; Choi et al., 2003; Lim et al., 2004; Ufnar et al., 2004a; Robinson et al., 2010; Weibel et al., 2016).

The results presented here indicate that the cation chemistry in solution alone has little bearing on elemental uptake in siderite. Instead, each trace cation (Mn, Ca, Mg) has a distinctly different uptake behaviour, affected by concentration, siderite saturation, presence

of other competing cations, crystal structural controls, and growth mechanisms. For example, the results indicate that Mn uptake from natural pore waters would be preferential even if Ca and Mg concentrations are high (i.e., marine). The results also indicate Fe/Mn ratios of the solution to be reflected in the Fe/Mn ratios of the precipitate, and so high Mn substitution in geological siderite could simply indicate a relatively high Mn content in the pore waters, and not impure siderites reflecting a marine influence as suggested in Choi and Kim (2006). Further to this, the results imply that observations of "Ca-rich siderite" are problematic and suffer from a lack of supporting evidence from the crystal growth literature. The most parsimonious explanation is that other factors must be at play in a natural system allowing Ca uptake into siderite. Comparison of experimental and geological examples of siderite also sheds light on the origins of Mg enrichment in geological siderites. Given current constraints on Mg incorporation and partition coefficients, rather than marine influences, Mg-enriched overgrowths on rims of sphaerosiderites could perhaps be explained as products of diagenesis at shallow burial temperatures (Curtis et al., 1986; Mozley and Wersin, 1992; Baker et al., 1996; Choi et al., 2003; Lim et al., 2004; Passey, 2014; Weibel et al., 2016).

Another origin of Mg-enriched compositions may be the presence of additional carbonate minerals. For instance, if Ca-Mg carbonate was present in the initial mineral assemblage, its recrystallisation to siderite is thermodynamically favoured if pore water Fe^{2+} concentrations are 5% of Ca^{2+} concentrations (Berner, 1971). Evidence of the growth of Ca-Mg carbonate and siderite in the same environment, including in the same concretion, can be found in wetland intertidal marsh sediments in Norfolk, UK, reported by Pye et al. (1990). The siderite cements from these concretions do not show Mg enrichment, instead Mg is enriched in the calcite cement growing in the same concretion. As most studies determine elemental compositions using electron microprobe, carbonate phases are typically not identified unambiguously (for instance, through XRD). Therefore, the reported Ca-Mg-

Mn substitutions could alternatively be interpreted as physical mixtures of zoned carbonates, such as those examined by Pye et al. (1990).

Finally, one puzzling feature of geological siderite relates to the low, but non-negligible, background concentrations of Mg in almost all natural siderites (0.5–2 mol% $MgCO_3$) (Choi et al., 2003; Ufnar et al., 2004a; Robinson et al., 2010; Weibel et al., 2016). The two mechanisms of Mg enrichment (temperature increases or Ca-Mg carbonate replacement) suggested here do not readily apply to all examples where this has been observed. One remaining consideration could be the role of organic macromolecules during siderite precipitation. For instance, in calcium carbonate, it has been shown that carboxylated proteins, and other biomolecules, influence the uptake of Mg (Stephenson et al., 2008; Wang et al., 2009). In one study, carboxylated proteins with more of an affinity for binding Ca allowed production of Mg-rich amorphous calcium carbonate similar to high-Mg calcite or dolomite. The ratios of Mg/Ca depended on the binding properties of the organic molecules involved (Wang et al., 2009). In a wetland system, rich in organic by-products, biological macromolecules could be similarly influencing the growth of siderite, allowing deviation in cation uptake behaviour from those observed in classical abiotic crystal growth. Assessing this is beyond the scope of this study and merits further work, and whether or not the background Mg values noted in siderite could perhaps be a signal of biological activity must await further experimental and observational evidence. Nonetheless, this study provides key abiotic constraints in elemental uptake for siderite growth in saturations more analogous to natural waters than previous studies, which can be used to better our understanding of the offsets between abiotic and biotic pathways.

The elemental composition of siderite clearly reflects a variety of growth conditions, and thus cannot be solely used to infer palaeoenvironment. Instead, siderites should be studied in the wider context of the sedimentology and stratigraphy of the units they grew

within, with detailed petrography and mineralogy of the spheres, as well as isotopic and elemental composition, to have a broad understanding of their growth conditions, and assess their suitability for palaeoclimate reconstruction.

5 Conclusions

The experimental results presented here provide new insight into the coprecipitation of Mn, Ca, and Mg during siderite nucleation and growth. This experimental dataset emphasises the role of kinetic factors in regulating trace element incorporation into siderite, in particular, surface structural controls during growth, transport phenomena, and temperature. In reality, because multiple factors regulate trace element incorporation, general and quantitative relationships between mineral chemistry and solution composition are difficult to ascertain, and thus, palaeoenvironmental interpretations should be made with these factors in mind.

Nevertheless, although experimental results provide valuable mechanistic information on the chemical controls on siderite composition, discrepancies between synthetic and natural systems still persist. Available data indicate that the apparent differences in the Mg and/or Ca concentration of both natural and synthetic siderite may in fact arise from incomplete mineralogical and geochemical characterisation. In order to address this issue more quantitatively, new and robust datasets, including complete characterisation of all crystalline carbonate phases within natural and synthetic samples, will be required. This should further illuminate the relationship between mineral chemistry and depositional environment and the potential for natural siderite specimens to reveal paleoclimatic information through their chemical and/or isotopic composition.

Chapter 3

An Early Cretaceous terrestrial carbon isotope record of the Wealden Supergroup from the Weald Basin, UK

1 Introduction

The Early Cretaceous contains several significant climate perturbations, but attention has mostly focused on those in Aptian age or younger strata. Among the pre-Aptian carbon cycle perturbations, the Valanginian positive Carbon Isotope Excursion (CIE), noted in both terrestrial and marine localities, has been of particular interest (Weissert et al., 1985; Lini et al., 1992; Gröcke et al., 1999; Erba et al., 2004; Robinson and Hesselbo, 2004; Duchamp-Alphonse et al., 2007; Nunn et al., 2010; Westermann et al., 2010; Kujau et al., 2012; Meissner et al., 2015; Morales et al., 2015; Celestino et al., 2017; Aguado et al., 2018). During the Valanginian CIE, there is some evidence of cooler conditions in the high latitudes. These include migration of Boreal fauna to lower latitudes, lower Mg/Ca temperatures from belemnites, a calcification crisis, glendonites, and dropstone deposits (Frakes et al., 1995; Price, 1999; Mutterlose and Kessels, 2000; McArthur et al., 2004; Price and Nunn, 2010; Price and Passey, 2013). However, evidence from low latitudes suggests continued warm conditions throughout the Valanginian CIE, including high sea surface temperatures (> 30°C) (Littler et al., 2011). Low-latitude Tethyan sites also suggest an intensified hydrological cycle during the CIE, interpreted to indicate warm conditions (Kujau et al., 2013; Westermann et al., 2013). However, little attention has been paid to terrestrial temperature or hydrological changes, and consequently, the palaeoenvironmental

changes associated with the Valanginian CIE are not yet fully understood. Further evidence, particularly from terrestrial records would be useful for evaluating the climate response to the Valanginian CIE, and provide insight into terrestrial processes during Cretaceous climate perturbations. A detailed discussion on the existing literature on the Valanginian is provided in Chapter 1 Section 3.

The Wealden Supergroup (Berriassian–Barremian) provides an ideal record of terrestrial deposits to aid our understanding of Valanginian climate. The presence of organic matter and fossil wood provides the means to document carbon cycle perturbations recorded in the Wealden Supergroup, and correlate these to the hydrological changes inferred from the sphaerosiderites (presented in Chapters 4 and 5). The carbon isotopic composition of terrestrial organic matter has been shown to record, over geological timescales, the same temporal trends noted in marine carbonates and marine organic matter (Hasegawa, 1997; Gröcke et al., 1999; Hesselbo et al., 2002; Heimhofer et al., 2003; Hesselbo et al., 2003; Robinson and Hesselbo, 2004; Gröcke et al., 2005; Hesselbo et al., 2007; Franks et al., 2014). Based on this approach, this chapter presents an Early Cretaceous terrestrial carbon isotope record from the Weald Basin and correlates it to existing Early Cretaceous terrestrial and marine carbon isotope records. This will allow the palaeohydrological and palaeoclimatic data from sphaerosiderites to be placed in the wider context of Early Cretaceous climate change.

2 Materials and Methods

Samples were collected from five boreholes that were also used to sample sphaerosiderites in Chapter 4 and 5; Cooden, Westfield, Fairlight, Cuckfield, and Warlingham. Cooden, Westfield, and Fairlight are all within 6 miles of Hastings, Sussex, UK. Cuckfield is approximately 60 miles west of Hastings, but on the same limb of the Weald anticline as Cooden, Westfield, and Fairlight. The Warlingham borehole is 116 miles

north-west of Hastings, on the opposite limb of the Wealden anticline. Further details of the boreholes can be found in Chapter 1 (Section 4). These boreholes span four main stratigraphic units; Ashdown Formation, Wadhurst Clay Formation, Tunbridge Wells Sand Formation, and Weald Clay Group, spanning the late Berriassian to Barremian. Samples were collected every 0.5–5 m, depending on availability of sampling material.

Organic matter ranges from < mm-sized specks to rare cm-sized pieces of fossil wood. The Ashdown Formation has a few horizons with fossil wood fragments along with smaller specks of organic matter. In contrast, the Wadhurst Clay samples appeared more oxidised and weathered, with poorly preserved organic matter. The Tunbridge Wells Sand has a few horizons with fossil wood fragments (1–2 cm length), with smaller clusters (< 0.5 cm diameter) preserved in muddier horizons. The Weald Clay generally preserved much finer pieces (< 0.1 cm) of organic matter.

In most cases, the organic matter present was too fine-grained and insufficiently concentrated to allow easy separation of individual pieces for analysis. Instead, bulk sediment samples were used for carbon isotope analyses, with analyses on fossil wood fragments where they were available in the stratigraphy. Samples (typically about 2–3 cm^3 pieces) were crushed using a Frisch Mortar-Grinder to produce a fine homogenised powder. When necessary, the samples were crushed further by hand with an agate mortar and pestle. In 10 samples, organic matter was visible and > 1 cm in diameter. In these cases, the area containing the piece of organic matter was scratched with a cleaned spatula into an agate mortar and pestle and crushed by hand to a homogenised powder. A representative subset of the powdered samples were analysed using a Rock-Eval 6 Standard Analyzer at University of Oxford to evaluate organic matter content and source rock characteristics (Hydrogen Index, Oxygen Index, T_{max}, S_2). Approximately 40 mg of sample was analysed in the oxidation and pyrolysis ovens, where they were incrementally heated from room temperature

to 850°C. The mineral carbon content was calculated from S3MINC and S5 peaks. The Total Organic Content (TOC) content was obtained from the combined CO and CO_2 fluxes representing the Pyrolyzable Carbon (S1 + S2 + S3CO + $S3CO_2$) and the Residual Carbon (S4CO + $S4CO_2$). Internal standard SAB134 was analysed every 6–8 samples and reproducibility calculated from 19 samples. The reproducibility of TOC was ±0.03% (1σ) and for Mineral Carbon Content ±0.07% (1σ), ±10 mg HC/g TOC (1σ) for Hydrogen Index (HI), ±3.2 mg CO_2/g TOC (1σ) for Oxygen Index (OI), and ±2.4°C (1σ) for T_{max}. The HI, OI, and T_{max} values are only presented from samples with S2 > 0.2 (Peters, 1986).

For $\delta^{13}C$ analyses, the powdered samples were first decarbonated. 1–3 g of each sample was digested in 50 ml of 5% Hydrochloric acid (HCl) within a sealed plastic tube and heated in a water bath at 60°C for 4 hours. Given the generally low carbonate contents of the samples (< 2%), one round of acid treatment was sufficient to remove all carbonate. Following the acid treatment, the samples were centrifuged to separate the acid from powder, and the acid removed. The sample was then washed and centrifuged with De-Ionised (DI) water several times until the pH tested as neutral, then dried at 60˚C overnight. For carbon isotope analyses, the powdered samples were weighed (5–40 mg) and packed in tin capsules to be analysed at the Open University's Stable Isotope Geochemistry facility. Carbon isotope ratios were measured against internal standards, calibrated to the Vienna Pee Dee Belemnite (VPDB) international scale. Standard deviation of repeat analyses of standards was < ±0.1‰. All results presented here are expressed as per mil (‰) deviation from VPDB.

3 Results

The geochemical results against depth within individual boreholes are presented in Figures 3.1–3.5. The stratigraphic boundaries are placed according to the previously established lithological framework for the Weald Basin (Edmunds and Gallois., 1965; Worssam and Morter, 1978; Allen et al., 1998; Radley and Allen, 2012). A moving average

with depth (span of 3) is applied to the $\delta^{13}C$ values to evaluate the trends within individual boreholes. The values for organic wood fragments are reported as $\delta^{13}C_{wood}$, for bulk organic samples as $\delta^{13}C_{bulk}$, and when discussing a combination of both ($\delta^{13}C_{wood}$ and $\delta^{13}C_{bulk}$), as $\delta^{13}C_{org}$.

3.1 $\delta^{13}C_{bulk}$, $\delta^{13}C_{wood}$, Hydrogen Index (HI), Oxygen Index (OI) and Total Organic Content (TOC) from individual boreholes

3.1.1 Fairlight borehole (Ashdown Formation)

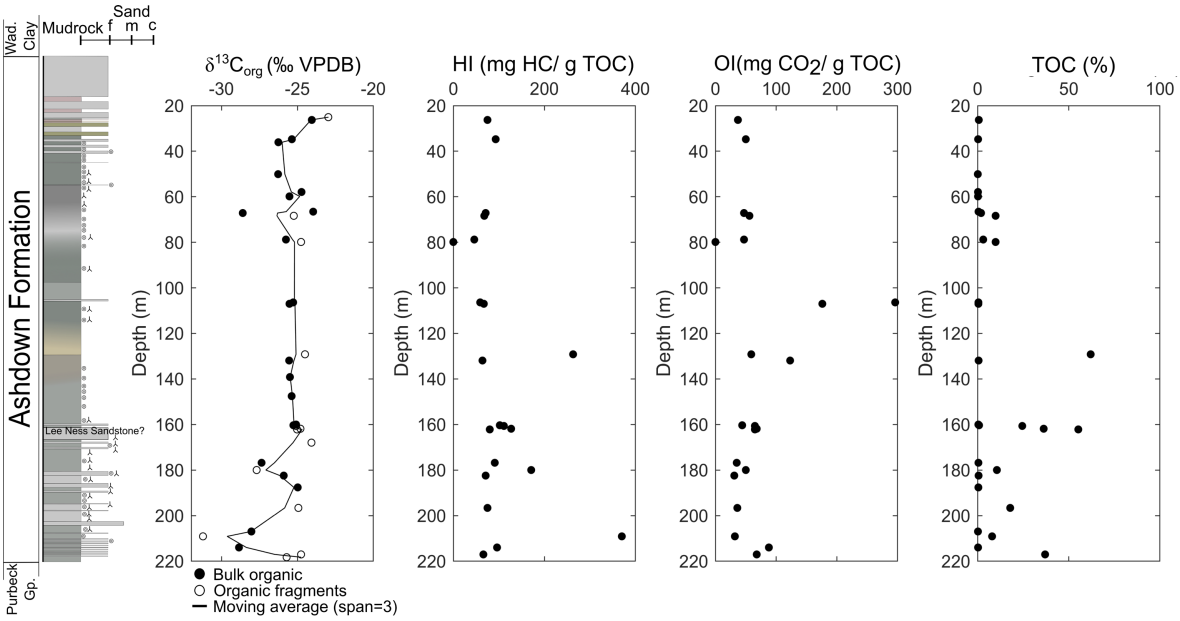


Figure 3.1: $\delta^{13}C_{bulk}$, $\delta^{13}C_{wood}$, Hydrogen Index (HI), Oxygen Index (OI,) and Total Organic Content (TOC) with depth in the Fairlight borehole (HC in units is Hydrocarbon, Wad. Clay = Wadhurst Clay). A moving average (span of 3) is fitted through all $\delta^{13}C_{org}$ data. 6 samples with low S2 peaks were discarded from the HI and OI figures.

The Fairlight borehole spans the entirety of the Ashdown Formation with a thickness of 200 m (Figure 3.1). This borehole has several horizons with large (> 1 cm length) pieces of organic matter, such as coalified fossil wood, which are plotted separately (unfilled circles) in Figure 3.1. The average $\delta^{13}C$ value from organic fragments and bulk organic matter ($\delta^{13}C_{org}$) in the Ashdown Formation is –25.71‰ ±1.61 (1σ), and ranges from –23‰ to

–31.22‰. This range of carbon isotopic composition falls within the expected values for Mesozoic C3 plants (Bocherens et al., 1993).

The $\delta^{13}C_{org}$ values within the Ashdown Formation fluctuates between c. –24 ‰ and c. –32‰ at 200 to 160 m depth, and then remains relatively stable at c. –25‰, from 160 m to 40 m depth. In the top 20 m of the Fairlight borehole, the $\delta^{13}C_{org}$ values gradually increase up-section to c. –23‰. HI values are mostly < 200 mg HC/g TOC, and OI values are mostly < 200 mg CO_2/g TOC from the representative samples. TOC values are generally < 2%, with an exception at 160 m where values increase to 50% due to the presence of fossil wood fragments. $\delta^{13}C_{wood}$ values do not show significant differences to the $\delta^{13}C_{bulk}$ values from bulk organic samples at the same stratigraphic level.

3.1.2 Westfield borehole (Ashdown Formation , Wadhurst Clay Formation)

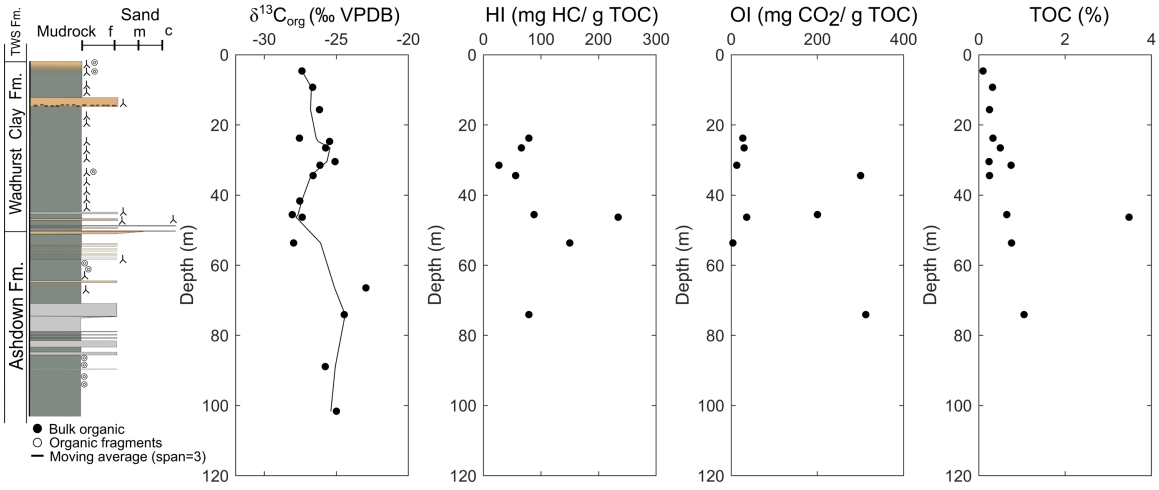


Figure 3.2: $\delta^{13}C_{bulk}$, Hydrogen Index (HI), Oxygen Index (OI), and Total Organic Content (TOC) with depth within the Westfield borehole. A moving average (span of 3) is fitted through all $\delta^{13}C_{org}$ data (Stratigraphy Key: TWS = Tunbridge Wells Sand). 4 samples with low S2 peaks were discarded from the HI and OI figures.

The Westfield borehole spans the top 40 m of the Ashdown Formation, and the entire Wadhurst Clay Formation (50 m thickness). This borehole had limited sample availability, and were mostly registered samples where only a small (< 5 cm) piece could be removed for

analyses. In the Wadhurst Clay, there were no visible large (> 1 cm) fossil wood fragments and the mudstones appeared oxidised. In contrast, the limited samples available from the Ashdown Formation contained mudstones with small (< 1 mm) flakes of organic matter visible to the eye. The $\delta^{13}C_{org}$ values at 100 m depth in the borehole, in the Ashdown Formation, are c. –25‰, increasing to c. –23‰ at the top of the Ashdown Formation. The average $\delta^{13}C_{org}$ value within the Ashdown Formation is –24.54‰ ±1.19 (1σ), within range of the expected values for Mesozoic plants. In the Wadhurst Clay, the $\delta^{13}C_{org}$ values abruptly decrease to –27‰ before gradually increasing up-section for the next 10 m to –25‰, and then decreasing again to –27‰ by the top of the Wadhurst Clay. The average $\delta^{13}C_{org}$ value of organic matter in the Wadhurst Clay is –26.76‰ ±0.98 (1σ). The $\delta^{13}C_{org}$ values are relatively higher in the Ashdown Formation than the Wadhurst Clay, and the means of the two formations are just outside of one standard deviation, differing by ~ 1‰. The $\delta^{13}C_{org}$ values within the Wadhurst Clay appear to show a positive excursion.

The HI values are generally < 100 mg HC/g TOC , and only two samples at 60 m depth have HI values > 200 mg HC/g TOC. OI values show more variation, with three samples > 200 mg CO_2/g TOC. TOC remains between 0.1% and 1% through most of the borehole, with one sample increasing to 3.7% at 46 m depth.

3.1.3 Cooden borehole (Wadhurst Clay Formation, Tunbridge Wells Sand Formation, Weald Clay Group)

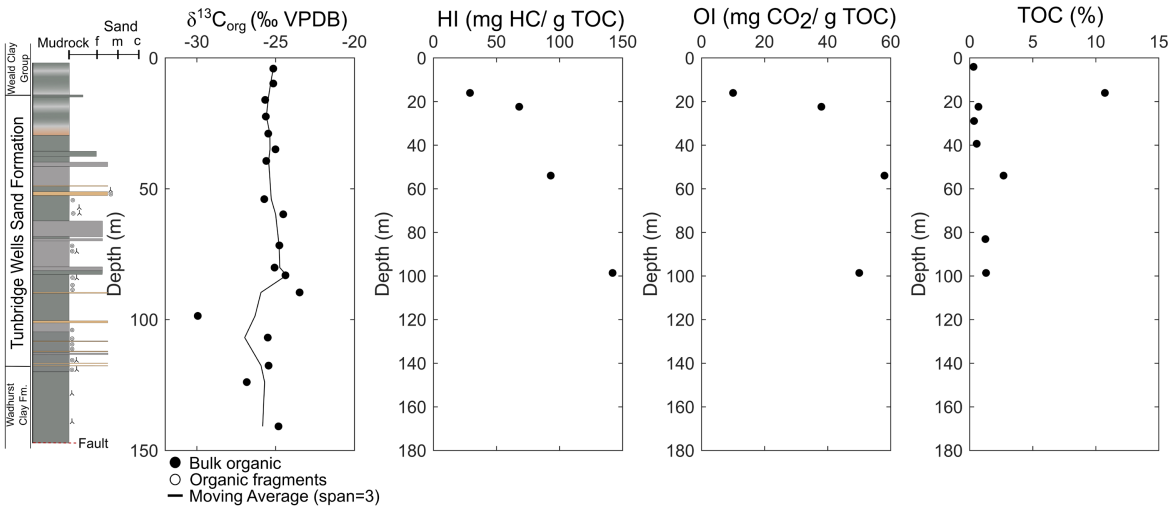


Figure 3.3: $\delta^{13}C_{wood}$, $\delta^{13}C_{bulk}$, Hydrogen Index (HI), Oxygen Index (OI), and Total Organic Content (TOC) with depth within the Cooden borehole. A moving average (span of 3) is fitted through all $\delta^{13}C_{org}$ data. 4 samples with low S2 peaks were discarded from the OI and HI plots.

The Cooden borehole spans the top 45 m of the Wadhurst Clay, the entire Tunbridge Wells Sand (120 m thickness), b and 10 m of the Weald Clay. Organic matter is dominated by small specks barely visible to the naked eye, and occasional fragments >1 cm. The larger fragments are generally concentrated in sandier horizons. The average $\delta^{13}C_{org}$ value from the Wadhurst Clay is –25.62‰ ±1.24 (1σ). In the Tunbridge Wells Sand, the average $\delta^{13}C_{org}$ value is similar to the Wadhurst Clay at –25.41‰ ±1.28 (1σ). These $\delta^{13}C_{org}$ values in both formations are consistent with values expected for Mesozoic plants (Bocherens et al., 1993).

The $\delta^{13}C_{org}$ values in the Wadhurst Clay fluctuate between c. –27‰ and c. –24‰. In the Tunbridge Wells Sand, the $\delta^{13}C_{org}$ values at the base are c. –25‰ but increase to c. –23‰, and then decrease and stabilise at c. –25‰ up-section through the borehole. The resolution of the HI and OI data is sparse as the S2 value for many samples were < 0.2 mg HC/g, particularly in the Wadhurst Clay. The available HI and OI values are mostly < 200. The TOC is between 0.2–1% for most of the core, with one sample containing fossil wood

fragments giving a value of 10%. This fossil wood sample is shown within Figure 3.3 and does not have a $\delta^{13}C_{wood}$ value significantly different to the $\delta^{13}C_{bulk}$ value samples at the similar stratigraphic levels.

3.1.4 Cuckfield borehole (Wadhurst Clay Formation, Tunbridge Wells Sand Formation, Weald Clay Group)

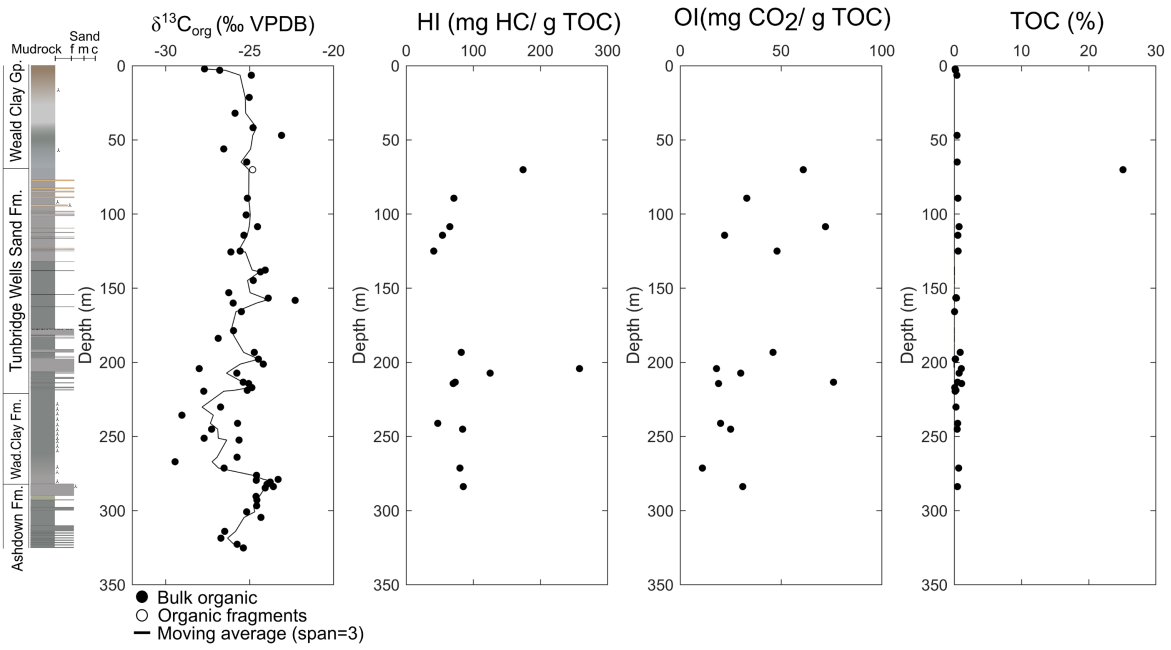


Figure 3.4: $\delta^{13}C_{bulk}$, $\delta^{13}C_{wood}$, Hydrogen Index (HI), Oxygen Index (OI) and Total Organic Content (TOC) with depth within the Cuckfield borehole. A moving average (span of 3) is fitted through all $\delta^{13}C_{org}$ data. 10 samples with low S2 peaks were discarded from the HI and OI plots.

The Cuckfield borehole contains 50 m of the top of the Ashdown Formation, 70 m of Wadhurst Clay, 140 m of Tunbridge Wells Sand, and 60 m of the base of the Weald Clay. Organic matter was generally present in small specks (< 1 mm) and clusters of fragments. In one horizon, a fossil wood fragment (>1 cm) was noted. The average $\delta^{13}C_{org}$ value of organic matter from the Weald Clay is –25.54‰ ±1.35 (1σ), from the Tunbridge Wells Sand is –25.17 ± 1.08 ‰ (1σ), and for the top of the Ashdown Formation is –24.94‰ ±0.99 (1σ). The average $\delta^{13}C_{org}$ value of organic matter from the Wadhurst Clay is –26.28‰ ±1.86 (1σ), approximately 0.7–1.3‰ lower on average than the other four lithostratigraphic units in this

borehole. Similar to the other boreholes studied, the $\delta^{13}C_{org}$ values from the Cuckfield borehole are within the range expected for Mesozoic plants (Bocherens et al., 1993).

The $\delta^{13}C_{org}$ values at the top of the Ashdown Formation gradually increase from c. –26‰ to c. –22‰. At the base of the Wadhurst Clay, there is an abrupt shift to lower $\delta^{13}C_{org}$ values which then fluctuate between –29‰ to –26‰, similar to carbon isotope compositions of the Wadhurst Clay noted in the Cooden and Westfield boreholes. In the Tunbridge Wells Sand, the $\delta^{13}C_{org}$ values increase compared to the Wadhurst Clay, to c.–27‰ to c.–24‰, and remain stable at c.-25‰, before decreasing to lower values in the Weald Clay. HI values are < 200 mg HC/g TOC and OI values are for the most part < 200 mg CO_2/g TOC, although there are significant gaps in resolution. The TOC content is < 2% for most of the samples, except for one $\delta^{13}C_{wood}$ labelled separately on the plot (Figure 3.4). The carbon isotope composition of the fossil wood fragments were not significantly different from that of the bulk organic matter at the same stratigraphic level.

3.1.5 Warlingham borehole (Tunbridge Wells Sand Formation, Weald Clay Formation)

The Warlingham borehole contains 100 m of Tunbridge Wells Sand and 190 m of Weald Clay. Organic matter was clustered in specks of < 1 mm and no large fragments of individual organic matter, like coalified wood, were found. The average $\delta^{13}C_{org}$ value in the Weald Clay is –26.64‰ ±1.79 (1σ), and for the Tunbridge Wells Sand is –25.63‰ ±0.38 (1σ). $\delta^{13}C_{org}$ values are c. –25‰ to –24‰ at the top of the Tunbridge Wells Sand before decreasing to c. –28‰ to –27‰ by the middle of the Weald Clay, with some samples showing values as low as –30‰. $\delta^{13}C_{org}$ values then gradually increase to higher values of c. –25‰ to the top of the Weald Clay. There are a few samples with HI values > 200 mg HC/g TOC but OI values are all < 200 mg CO_2/g TOC. TOC values of all samples are < 1.5%, but overall the organic content appears to increase slightly towards the top of the Weald clay.

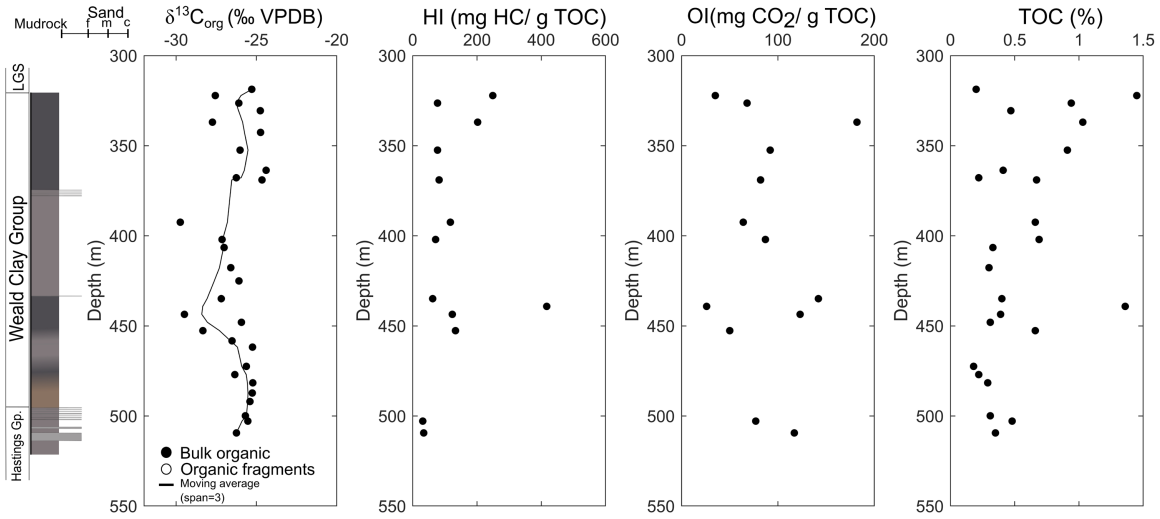


Figure 3.5: $\delta^{13}C_{bulk}$, Hydrogen Index (HI), Oxygen Index (OI), and Total Organic Content (TOC) with depth within the Warlingham borehole. A moving average (span of 3) is fitted through all $\delta^{13}C_{org}$ data. 11 samples with low S2 peaks were discarded from the HI and OI plots.

4 Discussion

4.1 Sampling and preservation of organic matter

In most samples, the organic matter was small (< 0.1 cm) and present in very small quantities. A few samples contained coalified organic matter, but in most cases, bulk rock was analysed to provide enough organic matter for multiple carbon isotope analyses.

Modern plants are known to show variation in carbon isotope values within constituent parts of a single plant, and photosynthetic pathways also influence the carbon isotope composition of plants (detailed in Chapter 1 Section 5) (Leavitt and Long, 1982; Leavitt and Long, 1986; Leavitt and Long, 1991; Loader et al., 1995; Schleser et al., 1999). However, the carbon isotopic composition of terrestrial organic matter has been shown to record, over geological timescales, similar temporal trends as found in marine carbonates and marine organic matter, and are thought to be dominantly controlled by the carbon isotope composition of atmospheric pCO_2 (e.g. Hasegawa, 1997; Gröcke et al., 1999; Hesselbo et al., 2002; Heimhofer et al., 2003; Hesselbo et al., 2003; Robinson and Hesselbo, 2004;

Gröcke et al., 2005; Hesselbo et al., 2007; Franks et al., 2014). The Early Cretaceous fossil plant record suggests that terrestrial palaeo-ecosystems predominantly consisted of plants utising the C3 (Calvin-Benson cycle) photosynthetic pathway based on the carbon isotope compositions (Hasegawa, 1997; Gröcke, 1998; Robinson and Hesselbo, 2004; Hesselbo et al., 2007). C4 (Hatch-Slack cycle) plants are thought to have evolved during the Miocene (Cerling 1993, Cerling and Quade, 1993), although some isotopic evidence suggests they may have sporadically appeared earlier in time (Spicer, 1989; Kuypers et al., 1999). Given the terrestrial depositional setting of the Wealden Supergroup in the Weald Basin, the terrestrial organic matter from the Weald Basin would be expected to comprise predominantly C3 plants. The carbon isotope composition from the Wealden Supergroup varies between c. –23‰ to c. –30‰, which is within the range expected from C3 plants (Bocherens et al., 1993). A few samples from the Weald Clay Group and Ashdown Formation contain values < –30‰. Wood fragments are limited to a few horizons, mainly within the Ashdown Formation and the Tunbridge Wells Sand Formation. The carbon isotope composition of these wood fragments was found to be similar to that of the bulk organic matter analysed from similar stratigraphic levels, further suggesting that the bulk organic matter is composed primarily of terrestrial plant matter. This is in keeping with findings from previous studies which have also shown the carbon isotope composition of bulk terrestrial organic matter, coalified or charcoalified wood fragments, and components like cuticles, are consistent with each other (e.g. Hasegawa, 1997; Heimhofer et al., 2003; Hesselbo et al., 2003).

The HI and OI values within the Wealden stratigraphy can be tentatively interpreted as mostly reflecting a terrestrial source of organic matter (Figure 3.6). Due to time constraints and instrument availability, only a selection of representative samples were measured, covering a range of $\delta^{13}C_{org}$ values and dispersed through the stratigraphy.

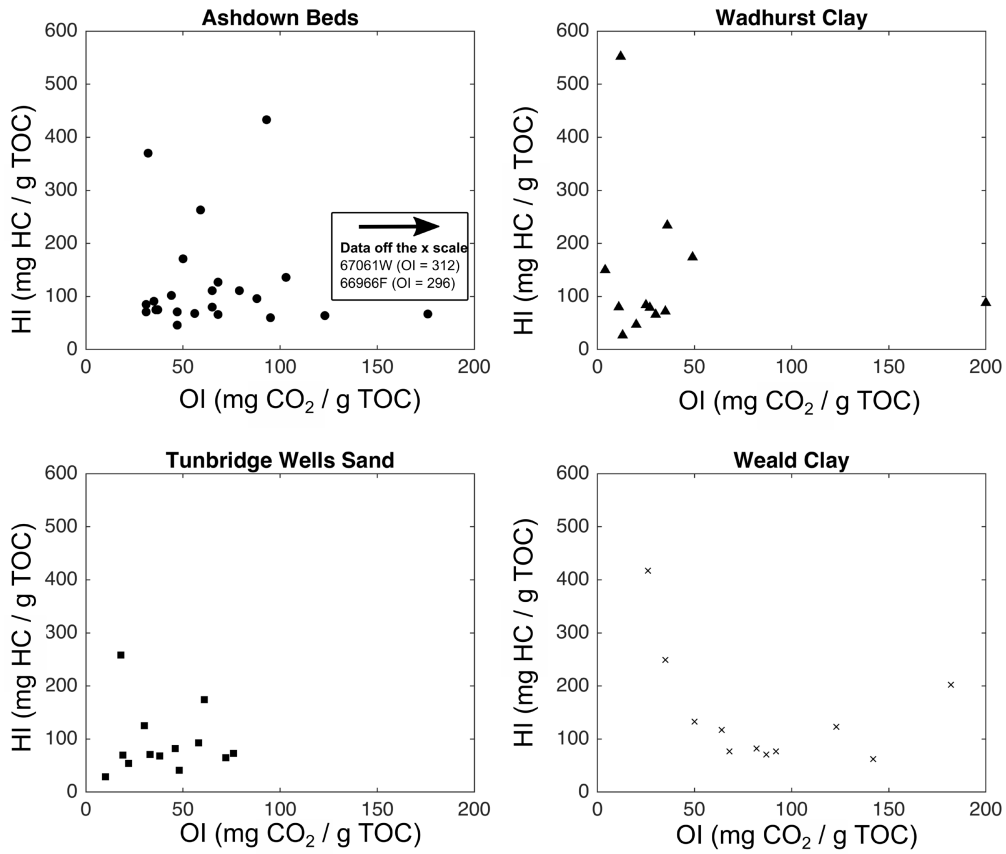


Figure 3.6: HI versus OI within formation of the Wealden Supergroup. HI values are mostly < 200 mg HC/g TOC and OI values are usually < 200 mg CO2/g TOC. There is some scatter in HI values, particularly in the Ashdown Formation and the Wadhurst Clay. The Wadhurst Clay values also cluster along the HI axis more than the other formations, although the trend cannot be conclusively determined due to the limited sampling resolution.

The samples from Ashdown, Tunbridge Wells Sand, and Weald Clay generally plot on a psuedo van Krevelan diagram along the OI axis with low HI values (< 200 mg HC/g TOC) (Figure 3.6). However, a few samples within the Ashdown Formation and Weald Clay have high HI values, as well as $\delta^{13}C_{org}$ values as low as –32‰. In contrast to the other three formations, the Wadhurst Clay samples have OI values < 100 mg CO_2/g TOC and appear to cluster along the HI axis. It could be tentatively suggested that the Ashdown Formation, Tunbridge Wells Sand, Weald Clay HI and OI values are generally indicative of Type 3 kerogen (< 150 mg HC/g TOC on HI scale), signifying a terrestrial source. In contrast, the

majority of the Wadhurst Clay, and a few samples from Ashdown Formation and Weald Clay, have HI and OI values that could be interpreted as degraded Type 1 (generally < 50 mg CO_2/g TOC on OI scale). These suggest a change in the source of organic matter, which is potentially significant for interpreting the stratigraphic record of $\delta^{13}C_{org}$.

As seen in Figures 3.2, 3.3, and 3.5, within the record there is a noticeable facies-specific offset in $\delta^{13}C_{org}$ at the base of the Wadhurst Clay to lower values. Using a t-test at 95% significance level, the significance of the difference between the $\delta^{13}C_{org}$ composition of the Wadhurst Clay and the combined values of the formations above and below it (Tunbridge Wells Sand and Ashdown, known all together as the Hastings Group) were tested. The p-value was found to be 0.009, indicating the carbon isotope composition of the Wadhurst Clay to be significantly different from the rest of the Hastings Group. No significant trends were found when comparing other parameters from Rock-Eval such as TOC vs HI, or HI vs T_{max} (Appendix B.1.2). The implications of the different carbon isotope composition of the Wadhurst Clay for the composite carbon isotope records produced from this data are further discussed in Section 4.2.2.

4.2 Correlation of Wealden basin strata

4.2.1 Inter basinal correlation

The carbon isotope records of the 5 boreholes studied are plotted alongside each other in Figure 3.7. Sampling resolution was limited by availability of material within the boreholes and thus gaps of > 10 m exists. There is a lack of well constrained stratigraphic tie in points for the deposits within the Weald Basin. This is important to consider, particularly as deposition rates are known have varied within the basin, and variability exists in the lithologies present within individual formations. To facilitate regional comparisons, lithostratigraphic correlations are made between boreholes based on the formations

recognised in those boreholes (Edmunds and Gallois., 1965; Worssam and Morter, 1978), and assuming that formation level changes are broadly synchronous across the basin.

Absolute $\delta^{13}C_{org}$ values along stratigraphic boundaries and trends are consistently similar between boreholes (Figure 3.7). For instance, in the top 10 m of the Ashdown Formation in Cuckfield and Fairlight boreholes, the $\delta^{13}C_{org}$ values are between –26‰ and –25‰, gradually increasing to –23‰ at the top of the Ashdown Formation. In the Wadhurst Clay, the $\delta^{13}C_{org}$ values become suddenly lighter. There is some evidence of erosional surfaces at this boundary described as 'widespread', but whether the erosional surfaces are laterally continuous enough to constitute an unconformity is debatable (Allen et al., 1998; Radley, 2006; Radley and Allen, 2012). The sudden change in carbon isotope compositions of bulk organic matter from the Ashdown Formation to Wadhurst Clay Formation could suggest a condensing of this section, indicative of low sedimentation rates and/or presence of erosional surfaces. The $\delta^{13}C_{org}$ values within the Wadhurst Clay range from c. –30‰ to c. –26‰ in both Cuckfield and Westfield boreholes. The Wadhurst Clay in the Cuckfield borehole does have a higher sampling resolution which may be contributing to the higher scatter in $\delta^{13}C_{org}$ values than in the Westfield borehole. At the base of the Tunbridge Wells Sand in the Cuckfield and Cooden boreholes, the $\delta^{13}C_{org}$ values range from c. –26‰ to c. –24‰. The top of the Tunbridge Wells Sand and boundary with Weald Clay also has similar values (between c.–26‰ and c. –24‰) in the Cuckfield and Warlingham boreholes. The similarity in $\delta^{13}C_{org}$ values at stratigraphic boundaries and long-term trends between boreholes suggests that despite scatter, the bulk organic matter is recording comparable carbon-isotope values at different localities, and its temporal evolution. Importantly, the similarities in regional $\delta^{13}C_{org}$ values within the four formations in the Wealden basin suggests the lithostratigraphic framework defined within these boreholes to be accurate. It also demonstrates that the individual stratigraphic units have identifiable and distinct carbon isotope records.

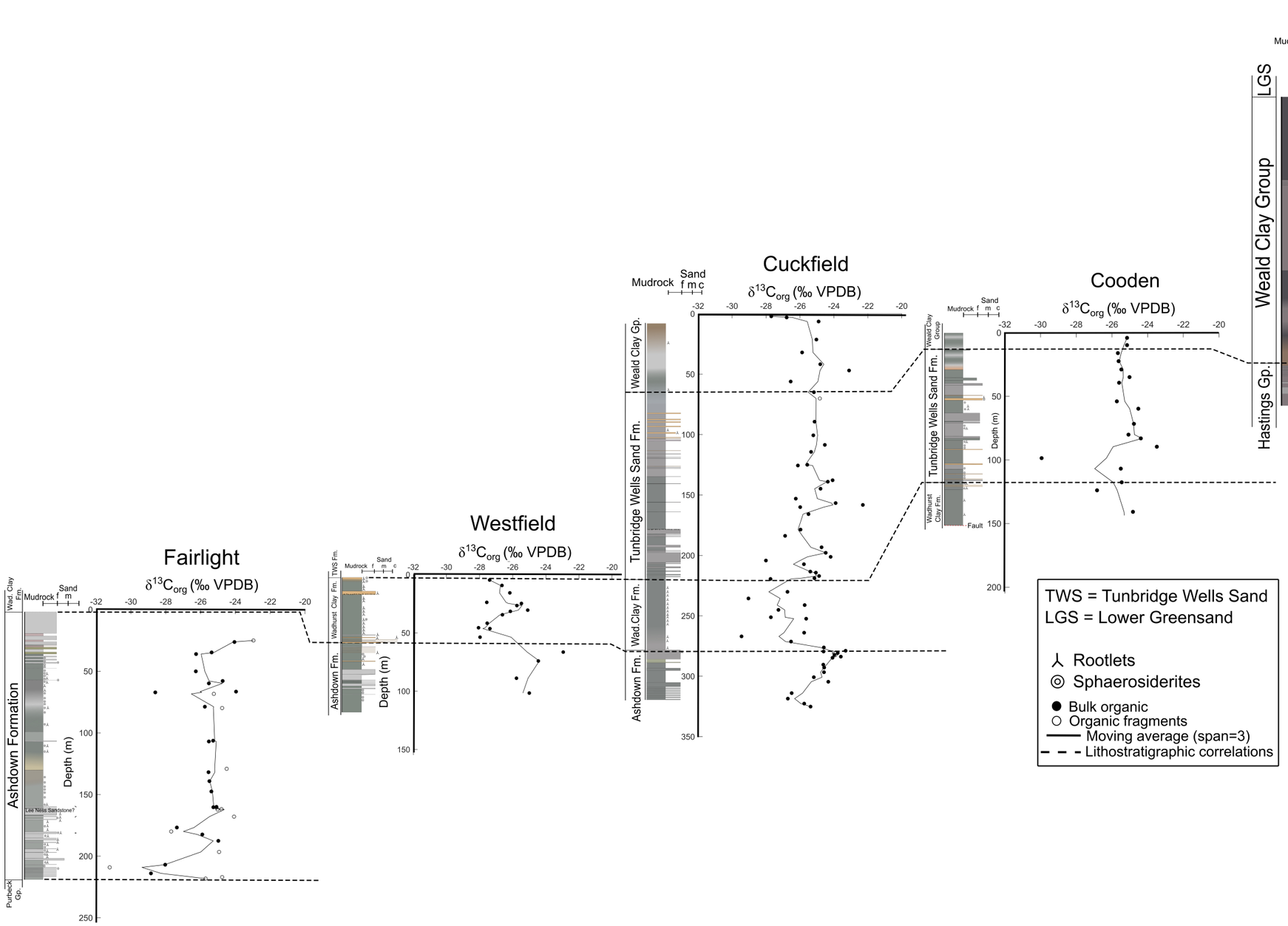


Figure 3.7: Regional correlation using carbon isotope composition in the Weald Basin using 5 boreholes with moving average best fit line through individual boreholes. Regional correlation suggests the long-term trends between the boreholes corroborate.

4.2.2 A Composite Early Cretaceous terrestrial $\delta^{13}C$ record

A composite carbon isotope record was produced through the Wealden stratigraphy to allow comparison with other Early Cretaceous records. The ages assigned to the Wealden lithostratigraphy in Figure 3.8 are based on ostracod biostratigraphy (Horne, 1995).

To account for the lateral variability in the thicknesses of formations, the composite depths were calculated by comparing against the Cuckfield borehole. The Ashdown Formation is only fully recovered in the Fairlight borehole. Cuckfield and Fairlight are approximately 40 miles apart but on the same limb of the Wealden anticline. In the absence of other information, the thickness of the Ashdown Formation is assumed to be similar between the Fairlight and Cuckfield boreholes. The Wadhurst Clay is 60 m thick in the Cuckfield borehole, while in the Westfield borehole it is 49 m thick. This implies the Wadhurst Clay in the Cuckfield borehole is 1.22 times thicker, and so the depth values of the Westfield borehole were scaled by a factor of 1.22. The Tunbridge Wells Sand in the Cuckfield borehole is 150 m in thickness, while in the Cooden borehole it is 100 m. This means the Tunbridge Wells Sand in the Cuckfield borehole is about 1.34 times thicker than in Cooden borehole, and so the depth values in the Cooden borehole were scaled by a factor of 1.34. The Weald Clay in the Warlingham borehole was 190 m thick. At Eastbourne, 15 miles east of Hastings, the Weald Clay is 180–190 m thick, similar to the thickness of the Weald Clay at Warlingham, and thus no scaling factor was applied to depth values of the Weald Clay in any borehole.

Apart from the Cuckfield borehole, the $\delta^{13}C_{org}$ values from partially recovered stratigraphic units were removed from the composite record to avoid using data for which a composite depth could not be assigned, as described above, without extrapolation. In the composite record (Figure 3.8), changes in facies do not seem to affect the carbon isotope compositions significantly, with the exception of the Wadhurst Clay. The $\delta^{13}C_{org}$ values

abruptly become lower in the lowermost Wadhurst Clay Formation, suggesting that the $\delta^{13}C_{org}$ values in the Wadhurst Clay are influenced by the facies change.

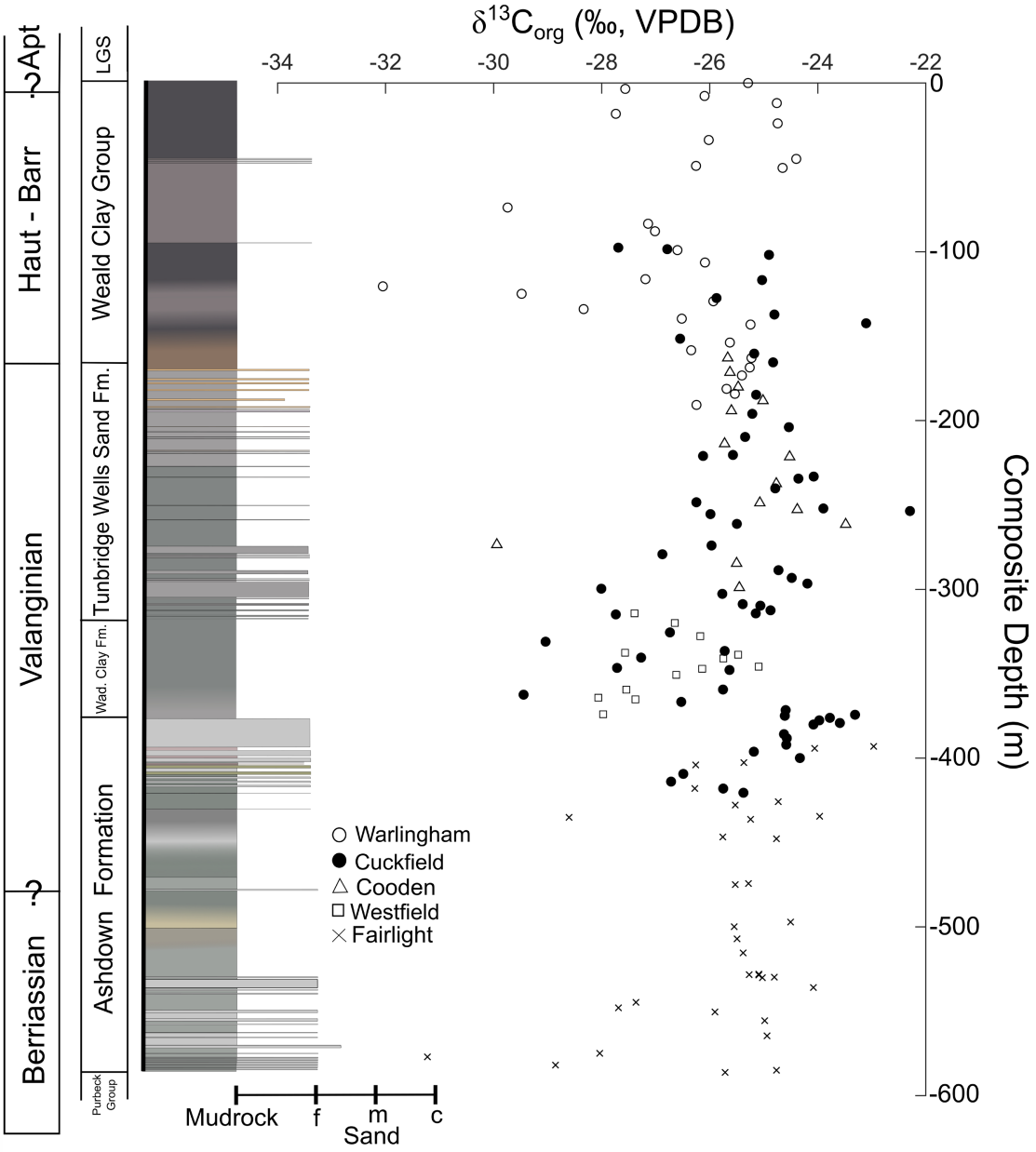


Figure 3.8: Composite carbon isotope record of the Wealden Supergroup from the Wealden Basin, based on 5 boreholes; Fairlight, Westfield, Cuckfield, Cooden, and Warlingham.

Figure 3.9 shows a moving average best fit line through the carbon isotope data against composite depth. $\delta^{13}C_{org}$ values fluctuate at the base of the Ashdown Formation, before becoming stable up-section. At the top of the Ashdown Formation, the $\delta^{13}C_{org}$ values increase, before abruptly decreasing to low $\delta^{13}C_{org}$ values consistently through the Wadhurst

Clay. At the base of the Tunbridge Wells Sand, $\delta^{13}C_{org}$ values are on average, higher than in the Wadhurst Clay, and similar to high $\delta^{13}C_{org}$ values at the top of the Ashdown Formation. Over the Tunbridge Wells Sand, the $\delta^{13}C_{org}$ values decrease and stabilise up to the base of the Weald Clay. The $\delta^{13}C_{org}$ values decrease to the middle of the Weald Clay before increasing again up to the top of the Weald Clay. The composite curve shows the $\delta^{13}C_{org}$ values within the Wadhurst Clay to be noticeably lower than the other formations (Figure 3.9). The carbon isotope composition in the Wadhurst Clay is still within the range expected from Mesozoic plants, however, the facies-specific nature of the abrupt change to low $\delta^{13}C_{org}$ values is unusual.

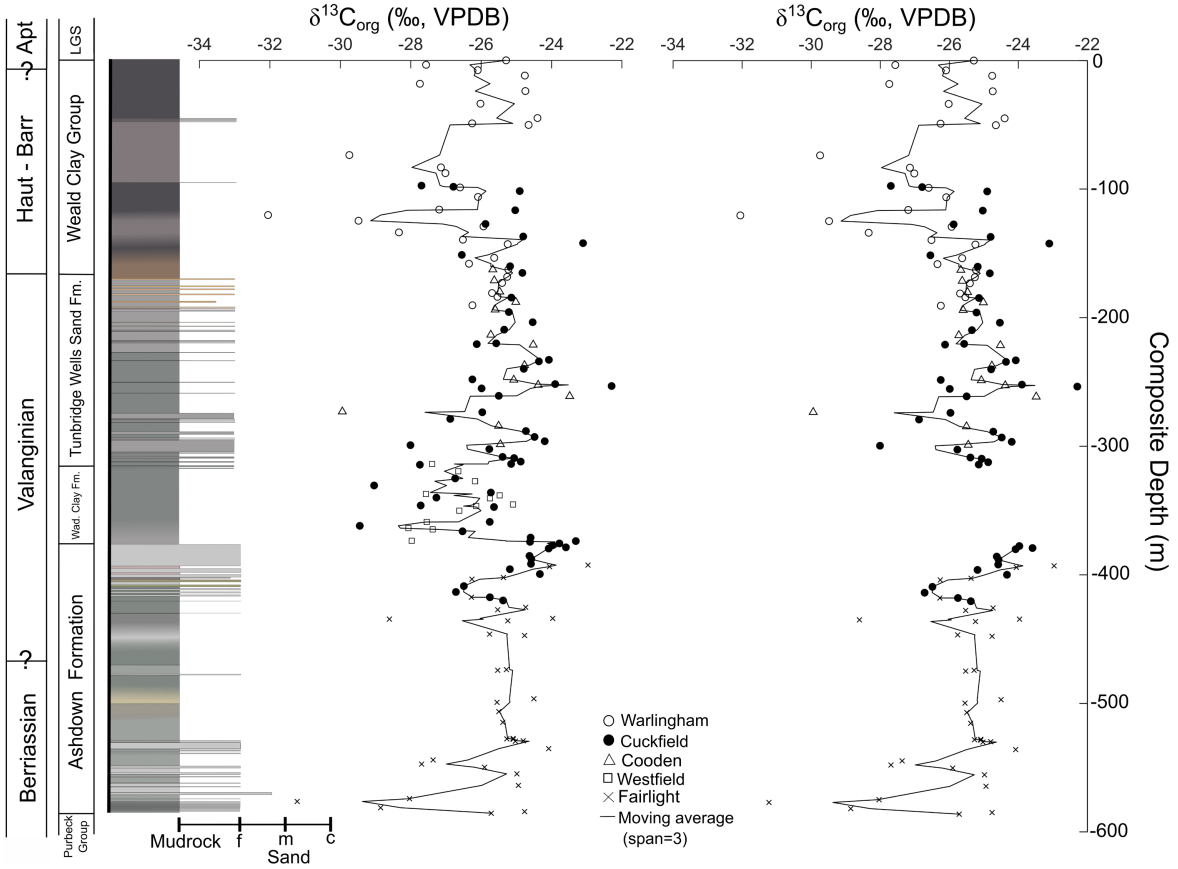


Figure 3.9: a) Composite carbon isotope record of the Weald Basin with a moving average with a span of 3. b) Composite $\delta^{13}C_{org}$ record of the Weald Basin with moving average fit once Wadhurst Clay data is removed.

Previous work has suggested the Wadhurst Clay may have experienced salinity changes, and that salinity fluctuations likely occurred during the deposition of the entire Wealden Supergroup (Hughes and Moody-Stuart, 1967; Hughes, 1975; Horne, 1995; Allen et al., 1998; Batten, 1998; Radley and Allen, 2012). Increased salinity could be inferred as a result of marine incursions, which could have provided an input of marine organic matter into the basin, thus influencing the overall carbon isotope composition from bulk organic matter. Palynomorph studies by Batten (1982) found the Wadhurst Clay Formation and Grinstead Clay (an argillaceous constituent of the Tunbridge Wells Sand Formation) contained a high concentration of degraded miospores (with reduced taxonomic diversity and mainly pollen of probable coniferalean origin), a scarcity of plant fossils and large megaspores, and occasional dinoflagellate cysts, all of which supported an interpretation of the Wadhurst Clay as an oxidised transgressive facies (Batten, 1982). In contrast, the Ashdown and Tunbridge Wells Sand Formations have better preserved miospore assemblages (dominated by pteridophyte spores as well as locally abundant cuticles), vitrinite and large plant fossils (Batten, 1982). However, the evidence of increased salinities and/or marine incursions in the Wadhurst Clay is not conclusive. Dinoflagellate cysts, thought to be indicative of brackish or marine conditions, have also been found in association with other freshwater or low salinity assemblages (Batten and Lister, 1988a; Batten and Lister, 1988b). It has since been suggested that interpreting the presence of dinoflagellates in the Weald Basin as increased salinity may be too simplistic (Batten and Lister, 1988a; Batten and Lister, 1988b).

There is a lack of definitive evidence for the nature of the palaeoenvironmental changes that may have affected the organic matter source and preservation in the Wadhurst Clay. However, the available palynological data, Rock-Eval data presented in this thesis, and abrupt changes in $\delta^{13}C_{org}$ values strongly suggest that the Wadhurst Clay may contain organic carbon from more (and/or different) sources than present in the other units analysed. Isolated negative $\delta^{13}C_{org}$ values also occur at the base of the Ashdown Formation and the

Weald Clay Group (up to values of –32‰) suggesting there may also be intermittent changes in organic matter sources within other formations. The data presented in this chapter cannot evaluate this further. Future work on the palynology, palaeontology, and organic geochemistry of the Wadhurst Clay could provide insight on organic matter sources. This could help to constrain the mechanism behind the facies-specific shift in carbon isotope composition in the Wadhurst Clay.

Given the uncertainties regarding the source of organic carbon in the Wadhurst Clay, a revised moving average trendline with depth is presented with the Wadhurst Clay $\delta^{13}C_{org}$ data removed. This revised trend suggests a broad positive excursion in $\delta^{13}C_{org}$ values exists from the top of the Ashdown Formation to the middle of the Tunbridge Wells Sand (Figure 3.9).

Salinity fluctuations between fresh and brackish conditions have been suggested for the Weald Clay Group too (Allen et al., 1998; Batten, 1998). The inferred changes in salinity are linked to marine inundations, attributed to decreased height of massifs and erosion of barriers during the deposition of the Weald Clay (Allen et al., 1998; Radley and Allen, 2012). The limited Rock-Eval data for Weald Clay Group in this chapter does not suggest a major source change that could indicate marine incursions. However, some of the HI values from the Weald Clay Group could be interpreted as Type 1 and may reflect a marine and/or mixture of sources. There is also no strong facies-specific shift such as seen in the Wadhurst Clay, and only one sample has carbon isotope compositions < –30‰, which could suggest marine sources of organic matter. Therefore, for the purposes of this study, the Weald Clay Group data was included in the composite record.

4.2.3 Correlation to the Wessex Basin

The $\delta^{13}C_{wood}$ values from the Wessex and Vectis Formations (Valanginian–Barremian) in the Wessex Basin range from c. –22‰ to c. –28‰ (Robinson and Hesselbo, 2004). This

range of $\delta^{13}C_{wood}$ values in the Wessex Basin correspond well to the $\delta^{13}C_{org}$ values in the Weald Basin (c. –23‰ to c. –30‰). A tentative correlation between the Wessex Basin and the Weald Basin is presented in Figure 3.10. It is difficult to correlate between the two basins as the biostratigraphy in the Wessex Basin has not been conclusive, and there are significant gaps in resolution in both the Weald and Wessex Basins.

From –450 m composite depth to –350 m composite depth of the Wessex Basin record (Robinson & Hesselbo, 2004), the record is sparse but suggests isotopically heavy $\delta^{13}C_{wood}$ values. These could tentatively be correlated to approximately –400 m to –250 m in the Weald Basin record which shows a broad positive excursion in $\delta^{13}C_{org}$ values. From the base of the Tunbridge Wells Sand Formation, the $\delta^{13}C_{org}$ values decrease up-section from –180 m composite depth to approximately –70 m composite depth in the Weald Basin. In the top 60 m of the Weald Basin composite record, the $\delta^{13}C_{org}$ values recover back to isotopically heavier values very steeply up-section, towards the unconformable boundary between the Weald Clay Group and Lower Greensand Group. By contrast, within the Wessex Basin, the carbon isotope record from –350 m composite depth to –150 m composite depth consists of gradually decreasing $\delta^{13}C_{wood}$ values, and then a gradual increase to higher $\delta^{13}C_{wood}$ values up to 0 m composite depth. The much more condensed recovery from isotopically lighter to isotopically heavier carbon isotope composition in the Weald Basin compared to the Wessex Basin suggests a comparatively slower sedimentation rate in the top 100 m in the Weald Clay group compared to the top of the Wessex formation.

The correlation between the Weald and Wessex Basins composite records tentatively suggests that the Weald Basin records a more expanded Valanginian section while the Wessex Basin records a more expanded Hauterivian–Barremian section. However, as each of the composite curves are scaled to a specific point within the basin (Cuckfield borehole for Weald Basin, Arreton borehole for the Wessex Basin), they may not be representative of

the basin in its entirety, but simply provide a useful comparison. It should also be noted that the Barremian-Aptian boundary is not well constrained in the Weald Basin, and there is a known unconformity between the Weald Clay and the Lower Greensand Group (Casey, 1961; Ruffell and Batten, 1994). In the Weald Basin, the negative carbon isotope excursion associated with the base of the Aptian is not identifiable, whereas it has been noted in the Wessex Basin (Gröcke et al., 1999; Robinson and Hesselbo, 2004). The Weald Clay may also be significantly condensed (~ 8 Myrs into 150 m) compared to the thickness of the strata from the Valanginian in the Weald Basin (~ 5 Myrs into 300 m). The condensation of the Hauterivian–Barremian also creates difficulty in interpreting the trend, when sample availability is low. Increased sampling resolution and/or regional comparisons to other boreholes with the Weald Clay would significantly improve the confidence in the $\delta^{13}C_{org}$ trend, and subsequently the correlations between the two basins.

The regional differences in thicknesses of strata could suggest sedimentation rates were locally variant, perhaps controlled by variations in rain shadows, catchment areas of major channels, basinal tectonics, and variations in regional climate (Allen et al., 1998). The lithofacies are not considered to be contemporaneous between the two basins, which has previously been invoked to suggest regional climatic differences between the basins (Allen et al., 1998; Radley and Allen, 2012). However, the biostratigraphic framework for the two basins contain several poorly constrained horizons, and coupled with the sampling gaps in both composite records, it is difficult to make a confident interpretation of regional climatic differences.

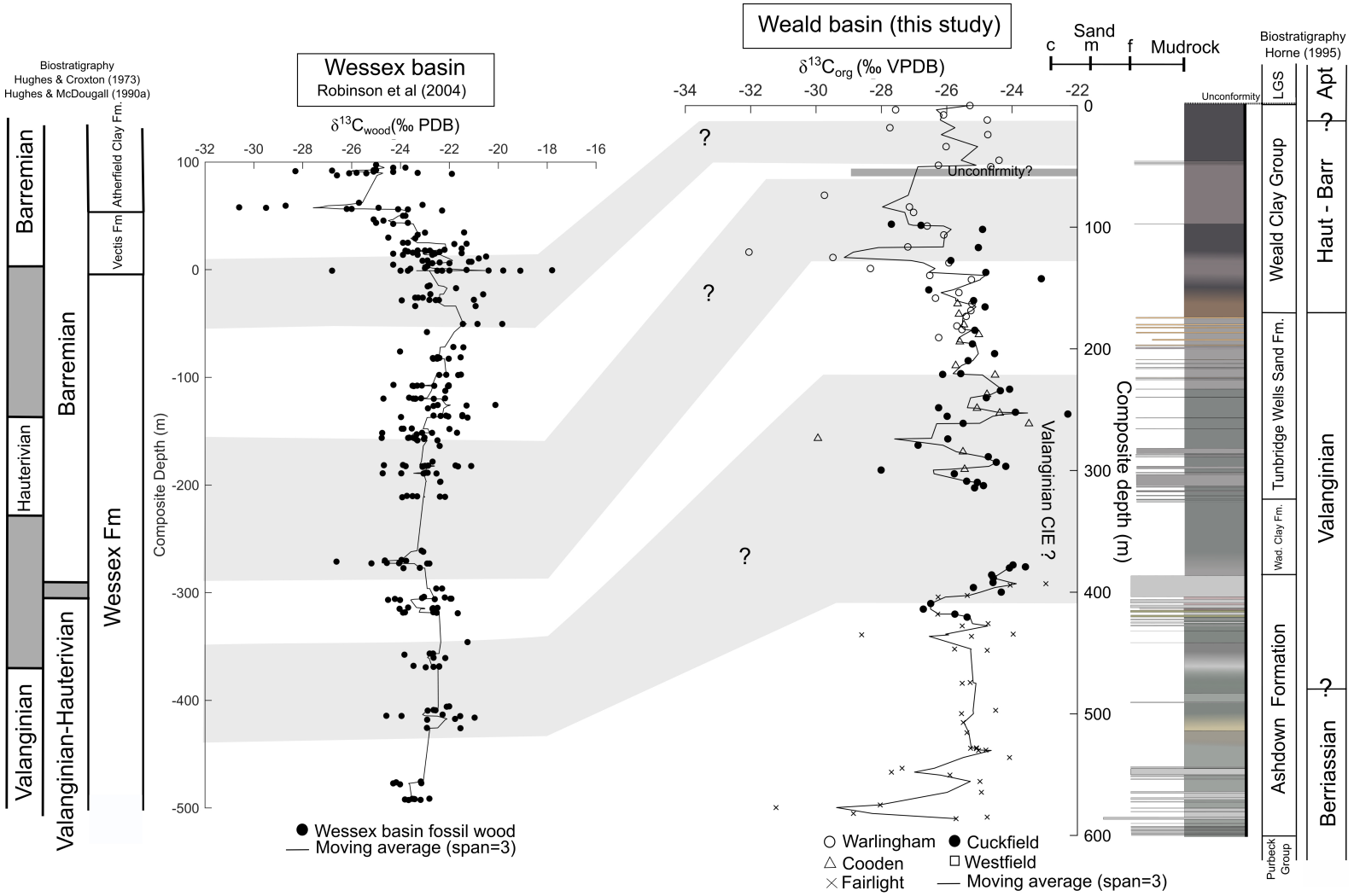


Figure 3.10: Comparison between the composite carbon isotope records from the Weald and Wessex Basins. The Wessex Basin composite record (Robinson and Hesselbo, 2004) and the Weald Basin composite are plotted with a moving average with span of 3. Tentative correlations between the two basins are drawn in grey.

4.2.4 Correlation to a composite marine carbon-isotope record

A comparison between a marine composite carbon isotope record (from Ogg et al., 2016 and references therein) and the composite carbon isotope record of the Weald Basin based on biostratigraphic correlations is presented in Figure 3.11.

In the Weald Basin, there is a broad positive excursion in $\delta^{13}C_{org}$ values notable in Valanginian-age strata. It begins with gradually increasing $\delta^{13}C_{org}$ values at the top of the Ashdown Formation, with consistently high $\delta^{13}C_{org}$ values at the base of the Tunbridge Wells Sand, which decrease up-section towards the Weald Clay. This positive excursion could be the local expression of the Valanginian Carbon Isotope Excursion (CIE), recorded in the marine realm in the Mid-Late Valanginian. In the marine record, carbonate $\delta^{13}C$ values increase towards higher values in the Mid Valanginian, similar to the trend in terrestrial $\delta^{13}C_{org}$ values in the Weald Basin. In both the marine and Weald Basin record, $\delta^{13}C$ values then gradually decrease up-section from Mid to Late Valanginian, indicating both marine and terrestrial carbon-isotope records were coupled. By comparison, in the late Barremian, the Weald Basin record shows a sudden change from low to high $\delta^{13}C_{org}$ values, which is at odds with a more gradual shift from low to high $\delta^{13}C$ values noted in the marine carbonate record, and also terrestrial records in the Wessex Formation (Section 4.2.3). This disparity in the carbon isotope trends between the Wealden and marine record during the Barremian, provides evidence of a possible unconformity or condensed section in the upper Weald Clay, deposited during the Late Barremian. There is no evidence in literature of sedimentological or biostratigraphic support for an unconformity in the Weald Clay within the Weald Basin, and therefore the presence of an unconformity cannot be as yet verified. The work presented in this chapter cannot evaluate this further, however, increased sampling resolution, sedimentological, palynological, and palaeontological work on the Weald Clay to search for evidence of condensed or missing sedimentation would be useful.

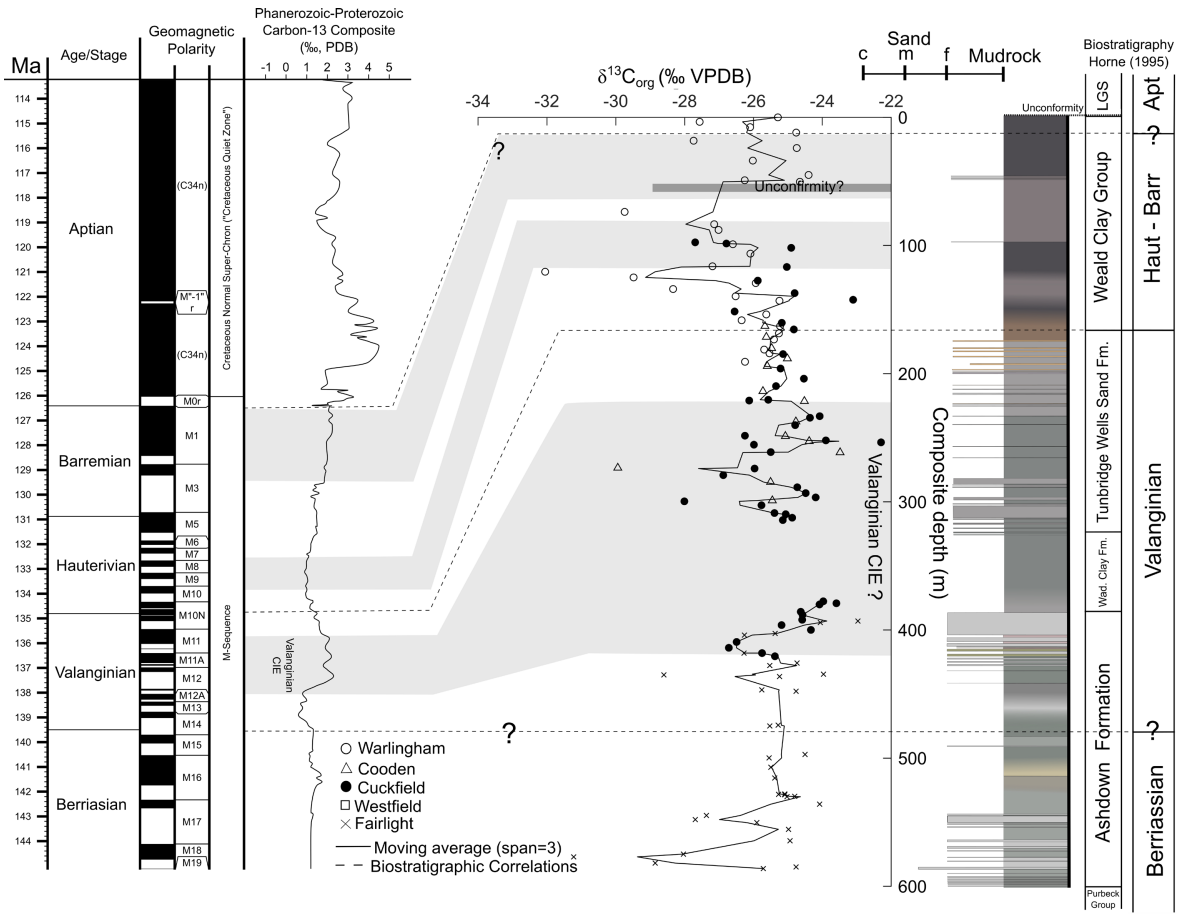


Figure 3.11: Comparison of the marine carbon isotope composite record (Ogg et al., 2016) with composite carbon isotope record of the Wealden Basin. Shaded areas are tentative correlations between the marine and terrestrial record.

The correlations between the terrestrial Wealden $\delta^{13}C_{org}$ record and the marine $\delta^{13}C$ record suggests that the ocean-atmosphere carbon cycle was coupled for the most part during the Early Cretaceous, in agreement with many previous studies (Hasegawa, 1997; Gröcke et al., 1999; Hesselbo et al., 2002; Heimhofer et al., 2003; Robinson and Hesselbo, 2004; Gröcke et al., 2005; Hesselbo et al., 2007; Yans et al., 2010).

4.3 Implications for Wealden stratigraphy and climate

The temporal trends in carbon isotope compositions in the Weald Basin correlate to long-term changes in the marine record, supporting the biostratigraphic ages from ostracods (Horne, 1995), and confirming the Wealden Supergroup to be of late Berriasian to Aptian

age. The peak of the Valanginian CIE within the Weald Basin likely occurs between the Ashdown Formation and Tunbridge Wells Sand Formation, although a significant gap in the resolution of the $\delta^{13}C_{org}$ record exists in the Wadhurst Clay Formation (detailed discussion in Section 4.2.2). By contrast, during the Hauterivian–Barremian in the Weald Basin, the $\delta^{13}C_{org}$ values shift quite suddenly from lower to higher values in the Weald Clay Group, suggesting a much more condensed record than in the Wessex Basin (Figure 3.10) than the marine composite record (Figure 3.11). This suggests that within the Weald Clay, other than the known unconformity between the Weald Clay and Lower Greensand groups (Casey, 1961), there may also be a cessation or slowing in sedimentation rates in the upper Weald Clay, condensing the carbon isotope record during the Hauterivian–Barremian, although this requires further verification. The biostratigraphic correlations are poorly constrained at the Berriasian-Valanginian and Barremian-Aptian boundaries in the Weald Basin. Therefore, it is difficult to determine the thickness of Valanginian age deposits and compare to the Weald-Wessex basins, which also have a conflicting biostratigraphic framework. In the Weald Basin, the Valanginian age deposits within the boreholes are approximately 300 m in thickness and coupled with the stratigraphically expanded peak of the Valanginian CIE identified in the Weald Basin, suggests sedimentation rates were high. In the Wessex Basin, the Valanginian CIE is poorly constrained and sampling resolution limits the confidence of the carbon isotope correlations between the two basins based on carbon isotope records.

There is evidence of increased terrigenous input during the Valanginian into the Tethys and North Atlantic suggesting an intensification of the hydrological cycle during the Valanginian, which could explain the expanded record of the Valanginian CIE in the Weald Basin (Weissert, 1989; Duchamp-Alphonse et al., 2007; Duchamp-Alphonse et al., 2011; Gréselle et al., 2011; Westermann et al., 2013; Morales et al., 2015; Charbonnier et al., 2016). Warmer and more humid conditions have been interpreted from clay assemblages in the Lombardian basin and Vocontian basin at the boundary between the Lower and Upper

Valanginian, preceded by more arid conditions as well as sea level variations, and proceeded by arid conditions followed by shifting arid-humid phases in the Upper Valanginian (Duchamp-Alphonse et al., 2011; Westermann et al., 2013; Morales et al., 2015). Spore-pollen assemblages from the Vocontian and Polish Basin indicate a similar shift to more humid conditions from Lower Valanginian to the boundary between Lower and Upper Valanginian (Kujau et al., 2013; Morales et al., 2015). Although regional differences almost certainly existed, which have not been confidently resolved, overall the climatic conditions in the low-mid latitudes during the Valanginian indicate multiple humid periods in which the hydrological cycle would have likely intensified, and contributed to higher weathering rates and increased terrigenous inputs into basins leading to higher sedimentation rates.

In the Weald Basin, these humid periods could have led to more weathering on the massifs and increase sediment input into the basin, allowing an expanded Valanginian record to be deposited. The evidence from the graphic logs (Figure 3.7) suggests the Valanginian age strata consist of coarser material than Weald Clay (Hauterivian-Barremian). Further complicating matters is the Wadhurst Clay (Valanginian) which consists mainly of mudrock, somewhat at odds with the higher weathering expected from the Valanginian period (supported by Ashdown and Tunbridge Wells Sand formations). However, these variations within the Valanginian age strata are likely controlled by local weathering and sedimentation rates, and the overall formation scale evidence suggests the Hauterivian-Barremian strata to be finer in grain size than the Valanginian, suggesting higher weathering/sedimentation during the Valanginian. However, the Ashdown Formation which spans Berriasian-Valanginian consistently contains fine to medium sand (Figure 3.7) suggesting coarser influxes during the Berriasian too. The boundary between Berriasian and Valanginian is not constrained in the Ashdown Formation, and therefore it is not possible to make further inferences as it is unclear how much of the Berriasian is contained within the Ashdown Formation.

During the Valanginian, there is also evidence of prolonged cold snaps in the Arctic (Vickers et al., 2019b and references therein). Vickers et al., (2019)b show glendonites pre-date the Valanginian CIE and prolonged cooling continued after, suggesting the cooling and the Valanginian CIE are not mechanistically linked. These differences between the Weald Basin and Tethyan sites, and the Arctic could suggest latitudinal differences in climate, with humid and warm conditions persisting within low latitudes (Erba et al., 2004; Duchamp-Alphonse et al., 2011; Föllmi, 2012; Kujau et al., 2013; Westermann et al., 2013). The latitudinal differences that may have existed during the Early Cretaceous could perhaps be an influence of palaeogeography and/or ocean circulation, allowing for cooler conditions to persist in high latitudes. It can be difficult to make comparisons however, particularly as many high latitude sites have a poor age control and therefore difficulties arise when comparing the effects of transient events. However, the latitudinal disparity in Early Cretaceous temperatures has been noted in several studies to date, but the mechanism behind this difference is yet unverified, but merits further work.

5 Conclusions

Reconstructed $\delta^{13}C_{org}$ from the Weald Basin using five boreholes (Cooden, Westfield, Fairlight, Cuckfield, and Warlingham) is comparable to carbon isotope compositions from C3 plants, and the trends in $\delta^{13}C_{org}$ values within formations are regionally consistent between boreholes. A composite carbon isotope record of the Weald Basin was produced which showed the $\delta^{13}C_{org}$ values were relatively stable through the Ashdown Formation, becoming increasingly isotopically heavy at the top of the Ashdown Formation. Above this, in the Wadhurst Clay there is a facies-specific shift to low $\delta^{13}C_{org}$ values. The $\delta^{13}C_{org}$ values are isotopically heavier than the Wadhurst Clay at the base of the Tunbridge Wells Sand, and show a long-term trend up-section through the Tunbridge Wells Sand and Weald Clay

Group to lower values. The trend then recovers up-section to higher $\delta^{13}C_{org}$ values at the top of the Weald Clay Group.

HI and OI values indicate that the Wadhurst Clay may have a mixture and/or different sources of organic matter which could be causing the facies-specific $\delta^{13}C_{org}$ shift. Palynology of the Wadhurst Clay has shown the organic matter in the formation to be degraded compared to the other formations, and some inconclusive indicators of increased salinity have been identified (Batten, 1982; Batten and Lister, 1988b; Batten and Lister, 1988a). Coupled with the data from literature, Rock-Eval, and the facies-specific shift of $\delta^{13}C_{org}$ values, the Wadhurst Clay samples are not considered to reflect a pure terrestrial organic matter source and therefore, are discarded from the composite carbon isotope record of the Weald Basin. The composite carbon isotope record of the Weald Basin was tentatively correlated to the Wessex Basin record (Robinson and Hesselbo, 2004) and a marine $\delta^{13}C$ composite record (Ogg et al., 2016). The correlations suggest the Weald Basin was recording an expanded Valanginian section and a more condensed Hauterivian–Barremian section. The expanded Valanginian section could be a result of increased humid phases which would have increased terrigenous inputs into basins. The increased humidity is supported by multiple proxies showing continued warm and humid conditions during the Valanginian in both marine and terrestrial records (Lini et al., 1992; Erba et al., 2004; Duchamp-Alphonse et al., 2011; Gréselle et al., 2011; Littler et al., 2011; Kujau et al., 2013; Westermann et al., 2013; Morales et al., 2015).

Chapter 4

Petrography and elemental characterisation of sphaerosiderites from the Wealden Supergroup

1 Introduction

The Lower Cretaceous non-marine Wealden Supergroup comprises mainly sandstones and mudstones predominantly deposited in freshwater fluvial, floodplain, and lagoonal environments, and provides an important Berriasian to Aptian record of terrestrial palaeoenvironments (Allen, 1975; Allen, 1981; Allen, 1989; Radley, 1994; Allen et al., 1998; Radley, 2006a; Radley, 2006b; Radley and Allen, 2012). This study focuses on the Wealden Supergroup in the Weald Basin which comprises four main lithostratigraphic units; the Ashdown Formation (contains the Fairlight Clays), Wadhurst Clay Formation, the Tunbridge Wells Sand Formation (contains the Grinstead Clay) and the Weald Clay Group. Detailed descriptions of the lithologies can be found in Chapter 1 Section 4.

Palaeosol horizons containing sphaerosiderites are common within the stratigraphy of the Wealden Supergroup. Sphaerosiderites are iron carbonate spheres thought to form in reducing, waterlogged soils in wetland environments (Ludvigson et al., 1998) and are an ideal archive for assessing long-term terrestrial palaeoclimatic changes in the Early Cretaceous. The elemental composition of sphaerosiderites is thought to reflect the paleoenvironmental conditions during growth (Mozley, 1989; Mortimer et al., 1997). Laboratory synthesis of siderite is currently unable to produce the range of elemental conditions noted in natural siderite (Mortimer et al., 1997; Romanek et al., 2009), although

it is clear that siderite composition reflects a complex suite of paleoenvironmental conditions such as siderite saturation, growth rate, cation concentrations, pH and temperature (Chapter 2).

Using the experimental understanding gained from Chapter 2, this chapter focuses on petrographically and geochemically characterising the sphaerosiderites from the Weald Basin to understand the palaeoenvironmental conditions within the wetland system at the time of deposition. This chapter also correlates the paleoenvironmental interpretations from the sphaerosiderites to our wider understanding of the palaeoenvironment of the Wealden Supergroup from sedimentology (Allen et al., 1998) and climate modelling (Haywood et al., 2004), and assesses the suitability of Wealden sphaerosiderites for palaeoclimatic reconstruction.

2 Materials and methods

2.1 Sampling from boreholes

Representative sphaerosiderite samples were collected from the Cooden, Westfield, Fairlight, and Cuckfield boreholes spanning the Ashdown, Wadhurst Clay, Tunbridge Wells Sand formations, and the Weald Clay Group. The stratigraphic position of each sample was recorded according to depth within the borehole it was collected from, and the stratigraphic unit within the Wealden Supergroup. Figure 4.1 provides the lithostratigraphy and locations of these boreholes but further details can be found in Chapter 1 Section 4. Based on preservation and a desire to maximise the stratigraphic resolution within each lithostratigraphic unit, 50 sphaerosiderites horizons were chosen (across all boreholes) for detailed investigation.

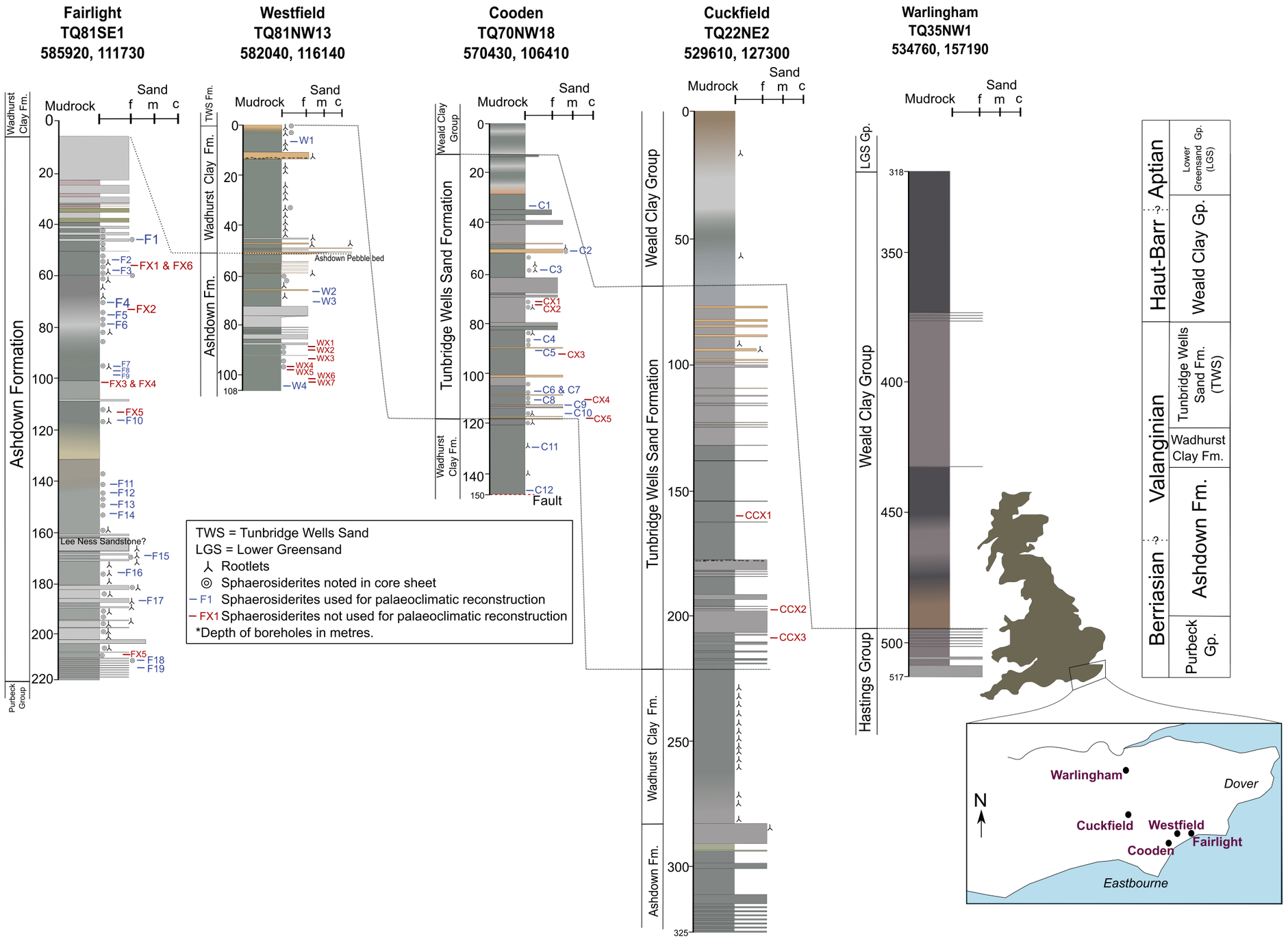


Figure 4.1: Lithostratigraphy and location of the sampled boreholes (Detailed in Chapter 1). Depth in metres within individual boreholes. Sphaerosiderite horizons samples are marked at depth within relevant boreholes, those in blue were found to be suitable for palaeoclimate reconstructions (based on geochemical and isotopic characterisation in Chapter 4 and 5), those in red were not used in palaeoclimate reconstructions.

2.2 Sample Preparation and Analytical Techniques

Individual sphaerosiderites were picked by placing the bulk sample in De-Ionised (DI) water for 10 minutes, allowing the matrix to soften. The spheres could then be picked individually and air dried at room temperature for five minutes on a petri dish. For analysis with Scanning Electron Microscope (SEM) and Electron Microprobe Analyzer (EPMA), sphaerosiderites were set in a 10 mm resin round and hand polished using diamond pads; the final polish was achieved using a 1μm grade diamond pad. These rounds were cleaned between pads by submerging them in isopropanol within a beaker placed in an ultrasonic bath for 5 mins.

The rounds were imaged using a FEI Quanta 650 SEM in the Department of Earth Sciences at the University of Oxford to produce Backscatter Electron (BSE) and Secondary Electron (SE) images. The SEM is also equipped with an Oxford Instruments Energy-dispersive X-ray Spectroscopy (EDS) system used for element mapping at 20kV. A CAMECA SX-5 FE EPMA was used for spot analyses along transects of spheres with spot sizes of 5μm, and an acquisition time of 30 seconds at 15kV. The elements of interest were Fe, Mn, Ca, Mg, Sr, Si, Na, Al, K, S, and Ti. Points with Al and Si oxide content > 5 mol% were filtered to remove points that incorporated inclusions within the sphaerosiderites, as were those below the detection limits of respective elements.

For X-Ray Diffraction (XRD), dried sphaerosiderites and bulk samples were crushed in an agate pestle and mortar to a fine powder. Powder was deposited as a slurry mixed with ethanol on a polished zero-background single crystal silicon substrate and air-dried; this ensured relatively random particle orientation. The powders were analysed at University of Oxford using a PANalytical Empyrean Series 2 powder diffractometer using a Co Kα source at 40 kV and 40 mA.

Thin sections were prepared for microscopy, however, the poorly consolidated matrix meant polishing was difficult and the thin sections were not of high quality. The limited number of thin sections were used to identify phases, examine textures where possible, and provide petrographic context for the XRD mineralogical identification.

3 Results

3.1 Hand Specimen petrography

Sphaerosiderites were found to be more common within the Ashdown Formation and Tunbridge Wells Sand Formation, allowing a significantly better sampling resolution than in the Wadhurst Clay Formation and Weald Clay Group, both of which only contained 2-3 horizons of relatively poorly preserved sphaerosiderites. The sphaerosiderites ranged in diameter from 60 μm to 1 mm, with the size distribution seemingly unrelated to stratigraphic position or host lithology. Sphaerosiderites appeared red to brown in colour in hand specimen, and in many cases, appeared quite oxidised (Figure 4.2). The matrix varied from fine sandstones to mudstones, was generally poorly consolidated, soft, friable and easily disintegrated when submerged in DI water. The matrix also contained < 1 mm organic clasts, including occasional larger (> 1 cm) fossil wood fragments.

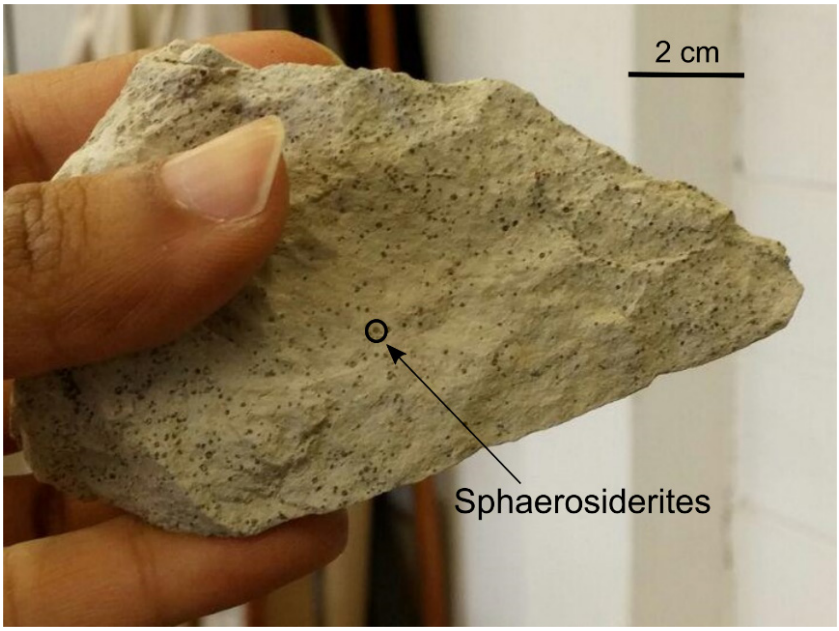


Figure 4.2: Representative hand specimen from the Ashdown Formation containing sphaerosiderites in a fine sandstone matrix.

3.2 Thin Section and SEM

3.2.1 Sphaerosiderite mineralogy and morphology

Sphaerosiderites in thin section are generally yellow to brown in colour and range from 100 µm to 1mm in diameter, and contain a variety of morphologies. Some sphaerosiderites contain siderite crystals radiating from a central nucleus point (often termed 'spherulitic'), exhibiting the characteristic Maltese cross extinction (Figure 4.3a). In other cases, the spheres comprise of fine grained siderite without an obvious orientation (Figure 4.3b). Due to the extensive oxidation and poor quality of the limited thin sections, BSE images of thin sections provided a better understanding of the morphology (Figure 4.3c, 4.3d) with evidence of both radial spherulitic textures and homogenous and microcrystalline sphere cores. The matrix consisted mainly of clays and quartz, of varying proportions (further discussed in Section 3.3). The quartz appeared yellow in cross polarised light as the thin

section thicknesses were usually > 30 µm due to polishing difficulties. There was no evidence of other carbonate cements in the matrix in thin sections (Figure 4.3).

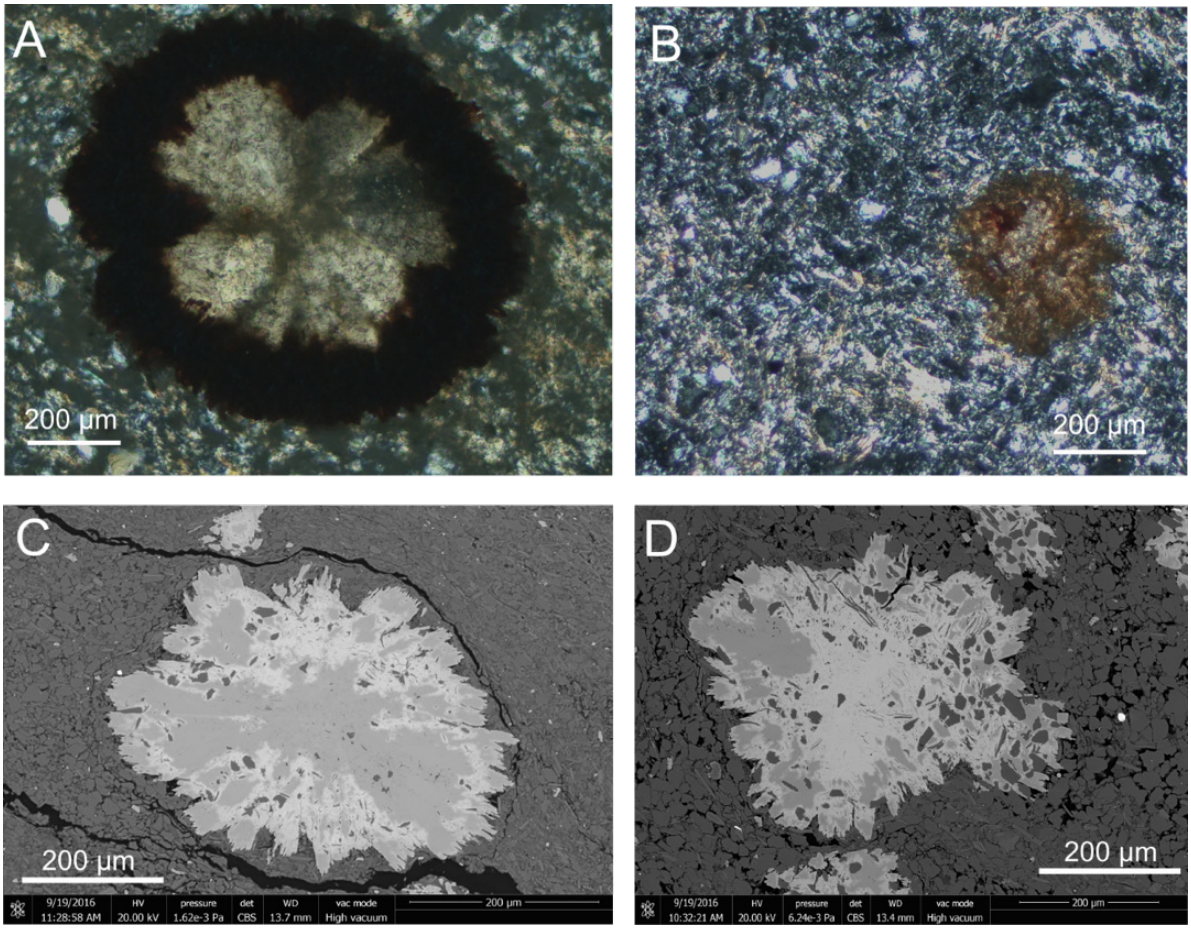


Figure 4.3: Thin Section photomicrographs in cross polarised light of sphaerosiderites from A) sample CX1 (Tunbridge Wells Sand) with characteristic maltese cross extinction in the central part of the sphere and an oxidised rim and B) sample F13 (Ashdown) which lacks internal zonations but overall colour is red/brown indicating oxidation. The matrix consists mainly of quartz and clays, although the yellowish hue of quartz crystals suggests the thin section was > 30 µm in thickness. C) Sample CX1 thin section from A in Backscatter Imaging (SEM) showing compositional differences through contrast changes and spherulitic texture. D) BSE image of a sphere from sample W2 showing compositional differences in the outer rim compared to core, and clay and quartz inclusions. The depths and locations of the sphaerosiderite horizons can be found in Figure 4.1.

The morphology of sphaerosiderites from the same horizons are usually similar. For instance, sample sphaerosiderites from sample CX1 all show a spherulitic texture (Example of one sphere from CX1 is in Figure 4.3c). Morphological heterogeneity between horizons is common and varies temporally and spatially (Figure 4.4), but locally spheres from the same hand sample consistently show similar morphology.

Morphological variations include a variety of internal zonation (core-rim differences, concentric zones) or a lack of zonation. Some spheres exhibit concentric zones such as a distinct core and a rim (Figure 4.4a, 4.4c, 4.4e) usually with a microcrystalline core and a spherulitic or bladed outer rim. By contrast, other sphaerosiderites appear homogenous, with no obvious internal zonation (Figure 4.4b), as evidenced by the lack of contrast changes across the sphere. Occasionally, some spheres, that appear homogenous, contain subtle compositional differences which produce a mottled change in contrast across the sphere (Figure 4.4 f). The mottled changes in contrast were not identifiable in EDS maps, but noticeable only within BSE images and indicate compositional heterogeneity at a fine scale (<1μm). A limited number of horizons contain recrystallised sphaerosiderites (Figure 4.4d). The edges of the spheres can be classified as either blocky or radial (Figure 4.4), dependent on the length of the edges of crystals forming the outer rim.

The proportion of inclusions varies within the sphaerosiderites (5–80 wt% inclusions, from XRD) and a few samples contain no inclusions (Figure 4.5). The dominant inclusion is quartz, but 5–15% of the inclusions are clays (kaolinite, illlite, and small amounts of muscovite), and/or minor (< 1%) pyrite. The number of inclusions incorporated within the spheres of any horizon are likely influenced by the matrix in which the sphere was growing. For instance, if a host lithology contained more quartz, the spheres would incorporate larger amounts of quartz. Figure 4.5 shows variations in inclusion quantity within spheres, with quartz being the main and usually largest inclusion noted in these samples. The inclusions

were also found to be randomly orientated, likely as the siderite sphere had grown around to incorporate them. For example, in Figure 4.5a, the radial crystals on the rim of the sphere are curved to accommodate quartz, and appear to be growing around it.

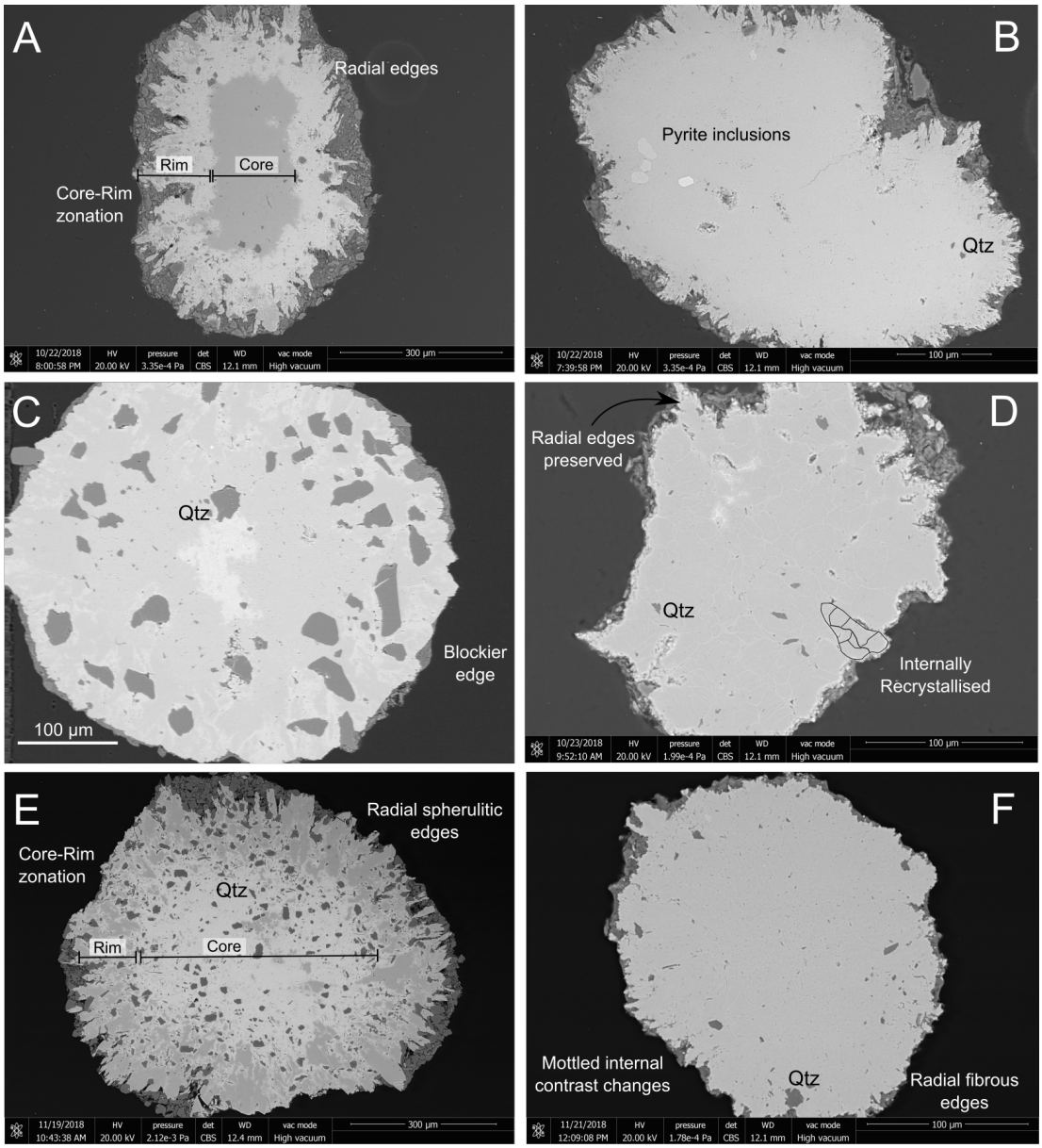


Figure 4.4: Representative sphaerosiderite morphologies. A) Spheres from F11 (Ashdown Formation, Fairlight borehole) with distinct central and outer zone with radial edges. B) Sphere from FX5 (Ashdown Formation, Fairlight borehole) which is homogenous and contains pyrite inclusions. C) Sample C9o (Tunbridge Wells Sand, Cooden borehole) containing a sphere with quartz inclusions and a blocky outer rim. D) Sphere from 67096 (Wadhurst Clay,

Cooden Borehole) which is recrystallised but preserves the primary radial edges. E) Sphere from W3 (Ashdown Formation, Westfield borehole) with a microcrystalline core and radial spherulitic crystals on outer rim which are compositionally different to the core. D) Sphere from 67209F (Ashdown Formation, Fairlight borehole) with mottled contrast changes indicating subtle compositional differences. The depths and locations of the sphaerosiderite horizons can be found in Figure 4.1.

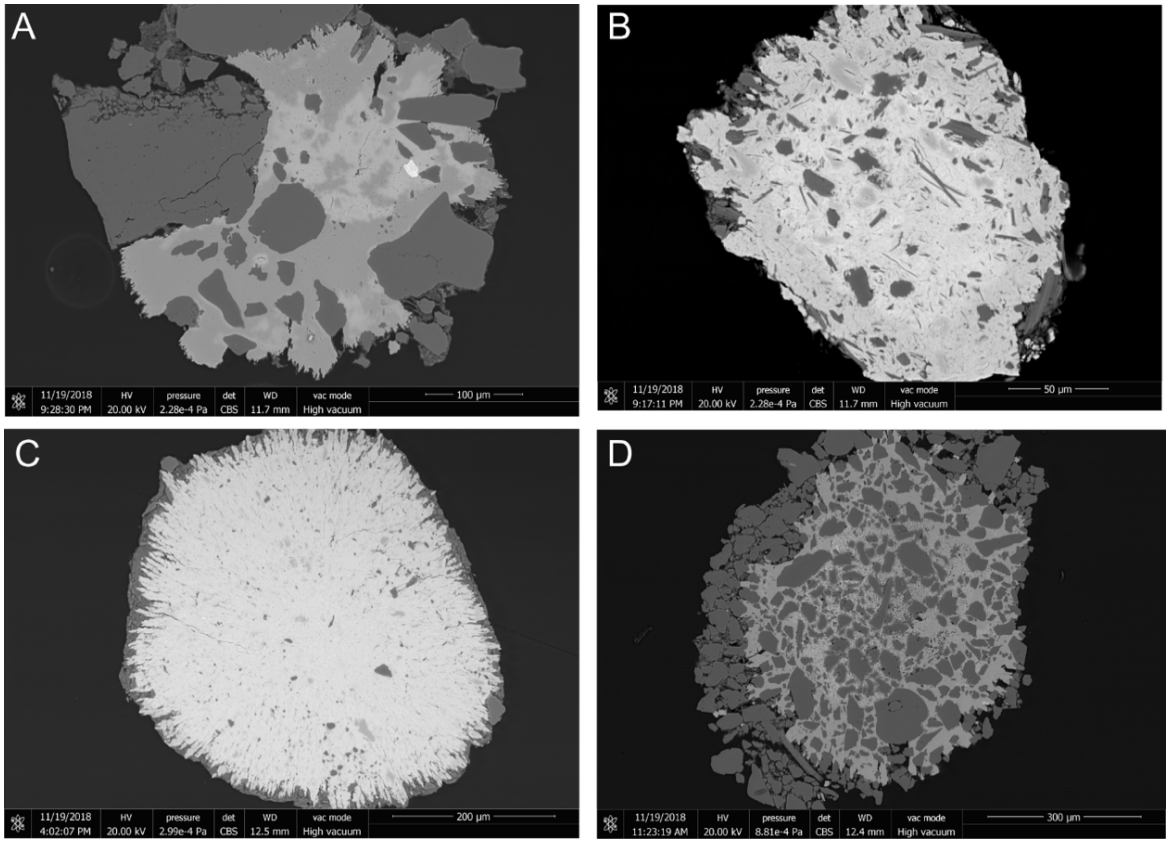


Figure 4.5: Examples of variation in quartz and clay inclusions in sphaerosiderites from a) Wadhurst Clay b) Tunbridge Wells Sand, c) Ashdown Formation, and d) Tunbridge Wells Sand. Quartz inclusions vary in size and quantity, and clays are usually smaller than quartz inclusions. The depths and locations of the sphaerosiderite horizons can be found in Figure 4.1.

Low quantities (< 1%) of pyrite were present in 50% of sphaerosiderite horizons, visible as high contrast specks (< 0.5 µm) within sphaerosiderites in BSE images and opaque in optical images (Figure 4.6). However, in two sphaerosiderite horizons, the sulphides are up

to 20 µm in diameter, spherical to sub spherical with blocky outer rims. The blocky edges comprise of cubic pyrite crystals growing from the edge of a microcrystalline pyrite centre, and are somewhat similar in appearance to the siderite spheres with cryptocrystalline centres and blocky rims discussed previously. The most interesting feature of these pyrite inclusions is they contain inclusions within them of angular elongated siderites in random orientations and minor quartz and clays (Figure 4.6). The pyrite spheres are missing from the outer regions of the sphaerosiderites (up to 100 µm from the edge of the outer rim), and are concentrated within or dispersed through a central zone of the sphere in random orientations. Pyrite is generally missing from the matrix in a representative number of thin sections, indicating that the pyrite formation is most commonly linked to the formation of the sphaerosiderites.

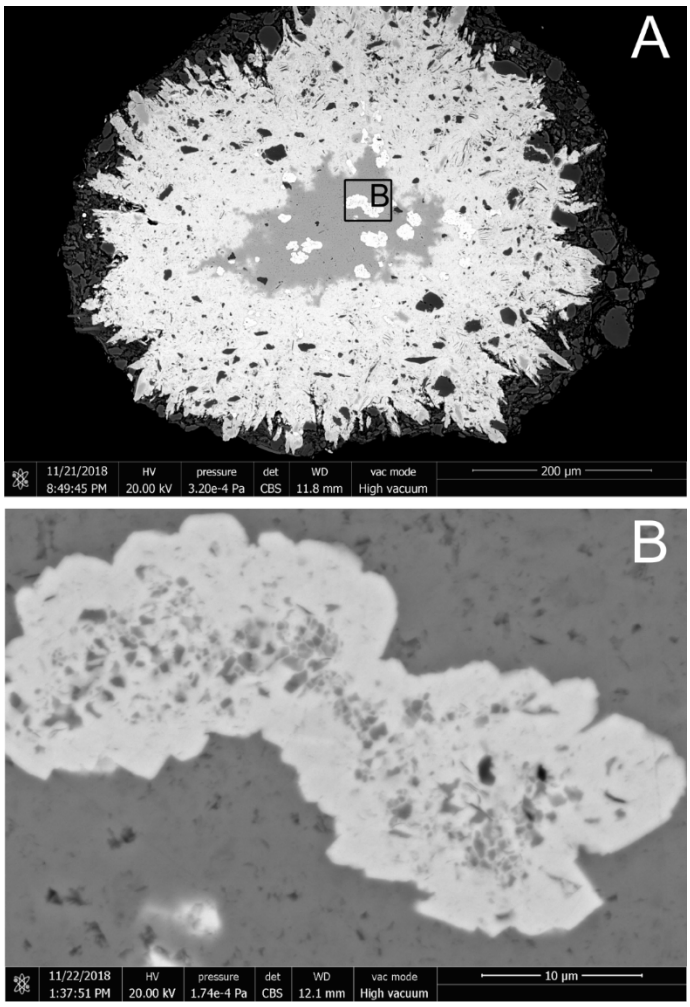


Figure 4.6: a) Example of sulphide inclusions (clusters of bright white contrast) in a sphaerosiderite from sample F10 (Ashdown Formation). b) Close up of a pyrite inclusion containing within it inclusions of siderite (light grey) and quartz and clays (dark grey). The depths and locations of the sphaerosiderite horizons can be found in Figure 4.1.

3.2.2 Dissolution textures

Examples of dissolution in sphaerosiderites, such as < 5 µm diameter dissolved areas within a sphere are notable in 4 horizons (Figure 4.7a), concentric zones of dissolution (Figure 4.7 b, c), and missing cores (Figure 4.7 b, d). Although the missing cores could be an indication of larger inclusions or cores preferentially falling out during sample preparation, the common inclusions such as quartz and clays are still visible within these same samples suggesting that they may be dissolution textures. It was not possible to map these sections of the sphere accurately with EDS as those dissolved areas caused a discrepancy in relief which affected the EDS semi-quantitative analysis. There were no other phases of carbonates noted in the bulk matrix of these samples, and they were similarly friable in DI water as the better preserved sphaerosiderite horizons.

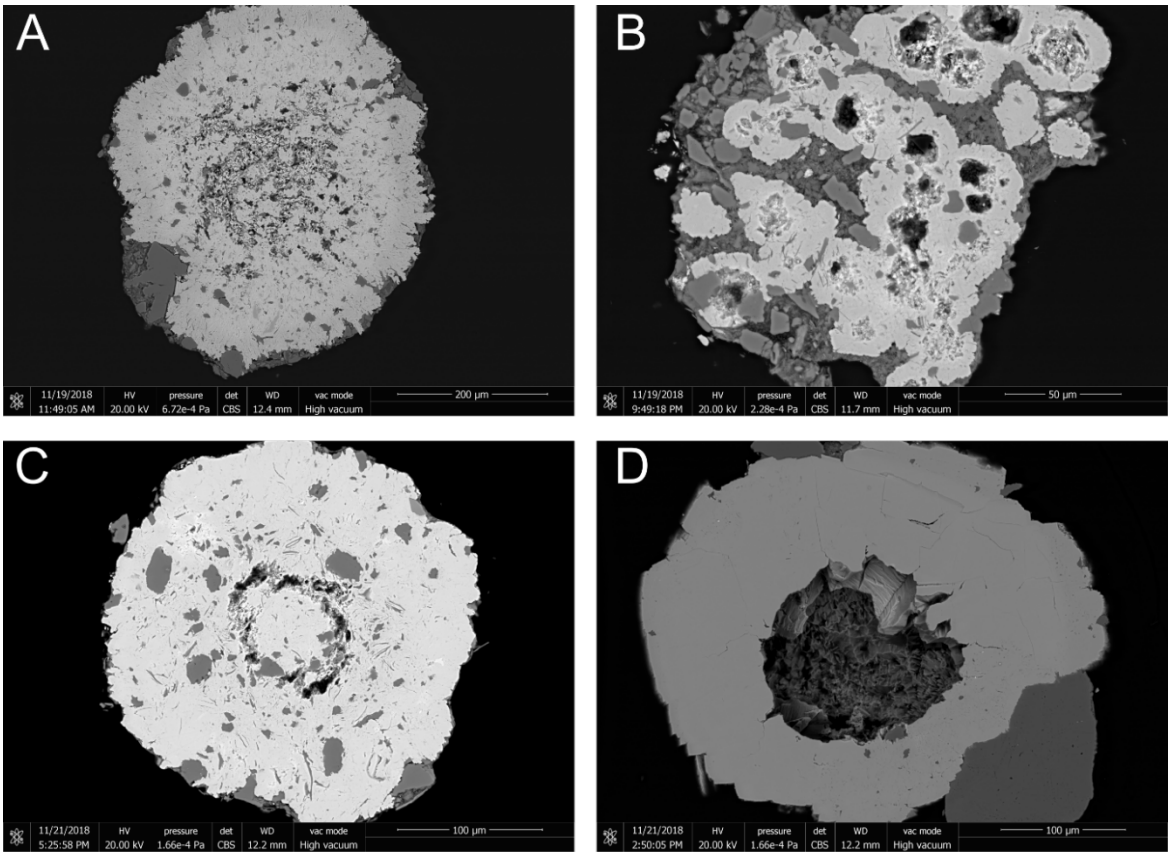


Figure 4.7: Dissolution textures (gaps or holes within spheres) from a range of stratigraphic horizons within the Wealden Supergroup A) FX6, Ashdown Formation B) F19, Ashdown

Formation, C) 67237Cuc, Weald Clay, D) 67241Cuc, Tunbridge Wells Sand, which may be due to the core falling out during sample preparation. The depths and locations of the sphaerosiderite horizons can be found in Figure 4.1.

3.2.3 Recrystallisation textures in the Wadhurst Clay Formation

Sphaerosiderites from the Wadhurst clay were generally poorly preserved, oxidised, and with rarer palaeosol horizons than in the other formations. There was no evidence of secondary carbonate phases within the matrix from bulk samples to suggest other forms of diagenetic alteration within palaeosol horizons. In the top 40 m of the Wadhurst Clay in both Cooden and Westfield boreholes, sphaerosiderites were recrystallised (Figure 4.8).

Figure 4.8a shows a representative sphaerosiderite from sample C11 exhibiting neomorphic recrystallisation, but with the radial edges of the primary spherulitic texture retained. The recrystallised core has crystals with edges ranging 5–20 μm and in many cases appear to have grown within existing spherulitic crystals (Figure 4.8a). Sample W1 also shows the presence of interlocking crystals of 50–100 μm edges indicating internal recrystallisation of the sphere with blocky outer edges (Figure 4.8c). By comparison, sample C12, stratigraphically 20 m below C11, shows only partial recrystallisation, mainly of the core with interlocking crystals of 5–10 μm edge length, while the outer rims preserve the original spherulites. The partial recrystallization could indicate heterogenous solubility within individual spheres, similar to the spheres displaying dissolution features (Figure 4.8b). However, it could also be a crystal size phenomenon, as finer crystals (micron size) are more soluble and less stable than larger crystals of the same mineral (Heberling et al., 2016; Gorski and Fantle, 2017). As morphological characterisation has shown, in many cases, the cores of spheres are cryptocrystalline compared to spherulitic or bladed rims, and therefore the cores are likely to be more soluble based on crystal size.

Differences in contrast within recrystallised sphaerosiderites seen in BSE images are prominent indicators of compositional heterogeneity in all three examples (Figure 4.8). These compositional differences could be preserving the heterogeneity that existed in the primary fabric of the sphaerosiderites. Further to this, some spheres contain a compositional difference between the core and rim (Figure 4.8b, 4.8c). In the case of C12 (Figure 4.8b), the difference in composition exists between the recrystallised core and the primary rim, but in W1 (Figure 4.8c) which appears wholly recrystallised, the compositional heterogeneity between core-rim is likely a relict of the primary fabric of the sphere.

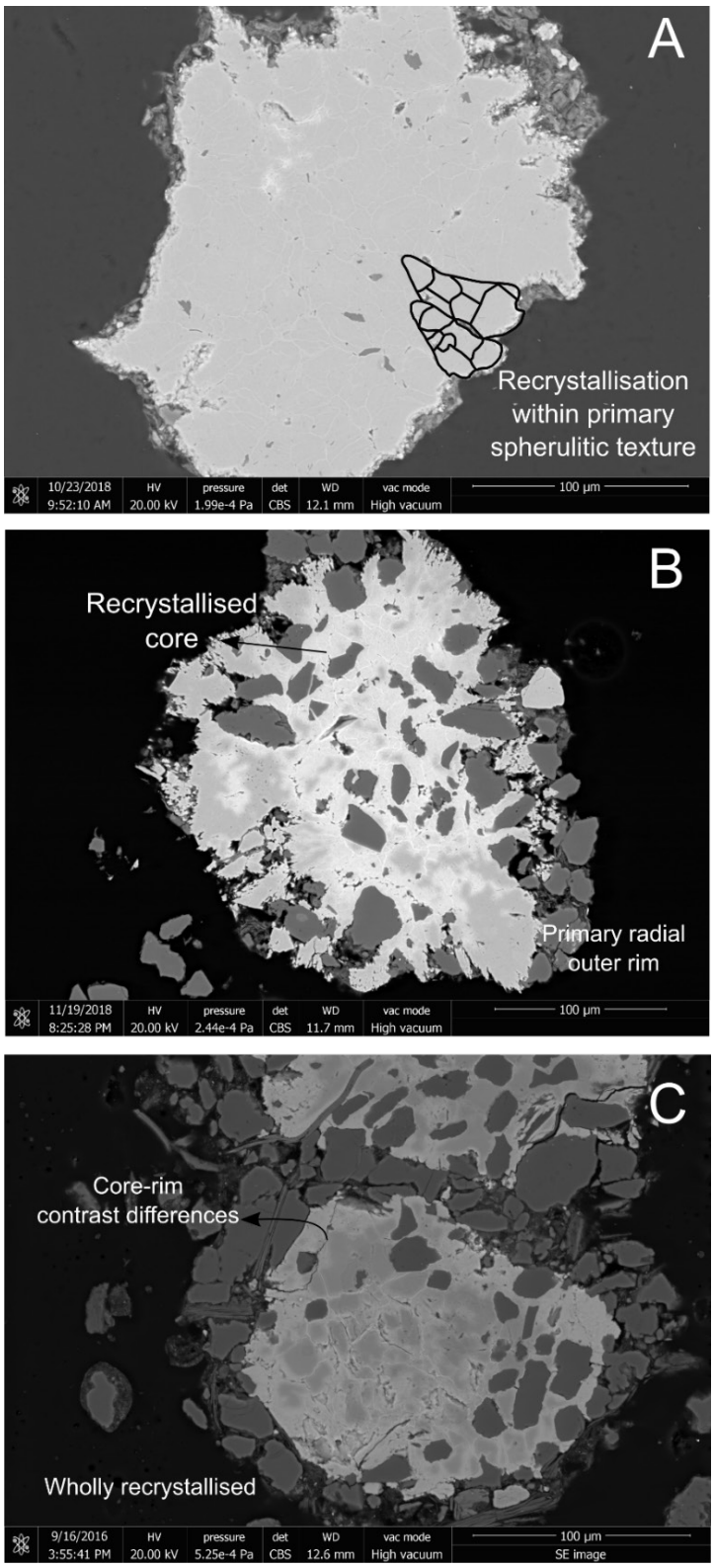


Figure 4.8: Recrystallisation in A) C11, Wadhurst Clay, B) C12 Wadhurst Clay, from Cooden borehole, and C) W1 Wadhurst Clay from Westfield borehole. The depths and locations of the sphaerosiderite horizons can be found in Figure 4.1.

3.3 XRD

A compilation of the mineralogical phases found in each siderite sample is provided in Appendix C.1.1. Picked sphaerosiderites were analysed using XRD via the method outlined in Section 2.2. Siderite content within spheres varied from 1–100 wt%, quartz from 13–89 wt%, and clays (kaolinite and illite) varied from 1–70 wt%. Detrital minerals in low concentrations such as anatase and pyrite were below the detection limits (< 1 wt%). The matrix consists mainly of quartz, kaolinite, and illite, with minor (< 3%) muscovite.

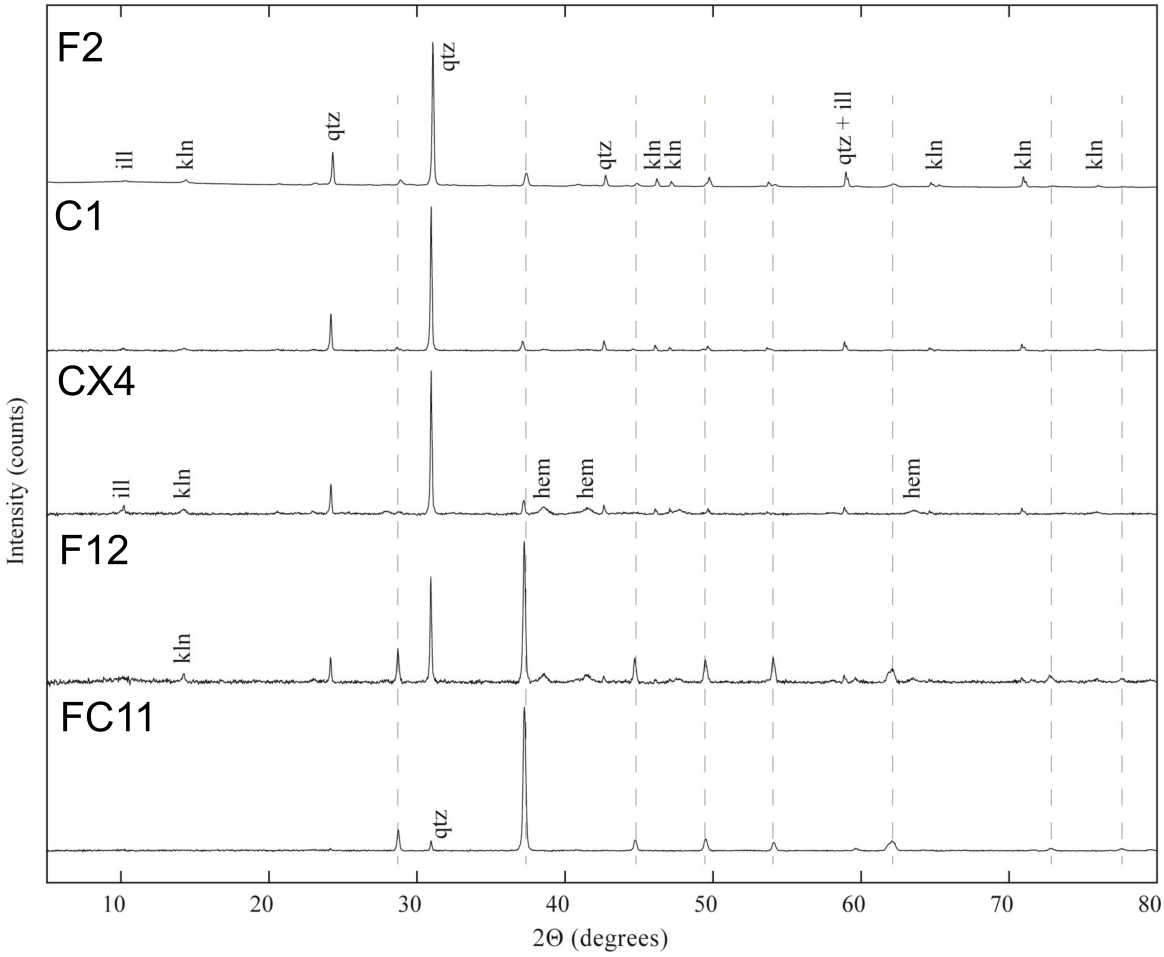


Figure 4.9: XRD spectra containing siderite from representative examples (F2, F12 and FC11 [Sample from Robinson et al., (2010)] from Ashdown, C1 and CX2 from Tunbridge Wells Sand,). Dotted line signifies siderite, abbreviations: qtz=quartz, kln=kaolinite, ill=illite. The depths and locations of the sphaerosiderite horizons can be found in Figure 4.1.

The dominant carbonate phase present in most of the sphaerosiderites was siderite (Figure 4.9), although the d-spacing of some diffraction peaks within XRD profiles often deviated from pure siderite due to substitutions of Mn, Ca, and Mg. In a few samples (e.g. CX4, C11), the spectral analysis suggested the presence of multiple carbonate phases, including siderite and rhodochrosite. These samples were not considered suitable for stable isotope analyses.

Figure 4.10 presents the wt% of siderite, hematite, quartz, kaolinite, illite, and other minor clays (biotite, muscovite) against composite depth. The composite depth is calculated based on the assumption that lithofacies between the three boreholes Fairlight, Cooden and Westfield have similar sedimentation rates due to their proximity to each other. Quartz appears to be the most common inclusion within Wealden sphaerosiderites. The sphaerosiderites from the Ashdown Formation also appear to contain more kaolinite than Tunbridge Wells Sand, but illite and quartz content varies similarly within the formations (Figure 4.10). Significant substitutions of Mg, Ca or Mn, and/or the presence of other carbonate phases are limited to the bottom of the Tunbridge Wells Sand Formation, the Wadhurst Clay Formation, and two samples within the top of the Ashdown formation. These samples were not considered suitable for palaeoclimatic reconstructions using stable isotopes.

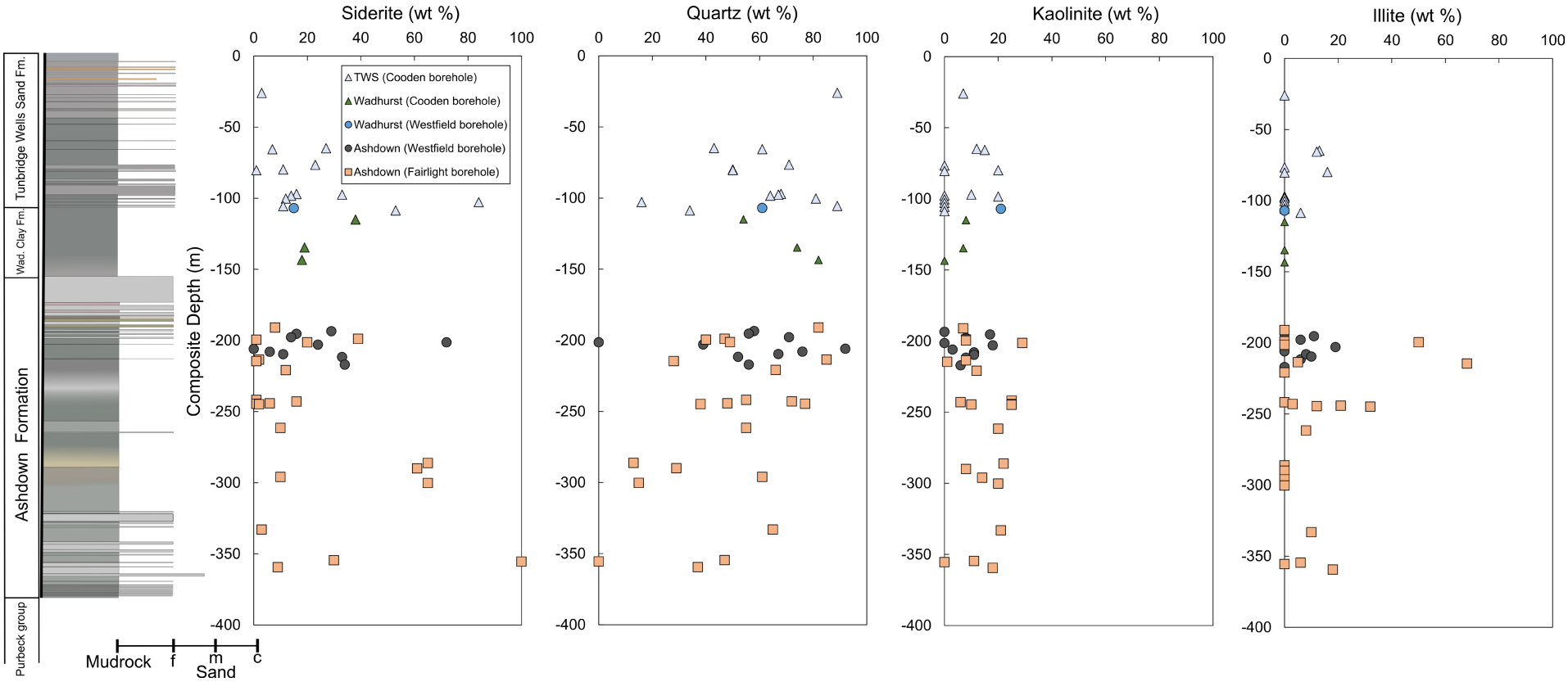


Figure 4.10: Siderite, Quartz, and Clay components within a composite depth produced with the assumption that sedimentation rates were similar in Fairlight, Westfield, and Cooden boreholes due to proximity.

3.4 Element mapping and transects

Element mapping using SEM-EDS and elemental transects using EPMA show the sphaerosiderites preserve compositional heterogeneity within individual spheres, which were initially noticeable due to the contrast differences in BSE imaging (Section 3.2). Samples of sphaerosiderites were analysed from each horizon and most horizons were found to contain sphaerosiderites with > 90 mol% siderite and were considered pure, with 1–10 mol% substitutions of Mn, Ca, Mg, and < 0.05 mol% Sr. Spheres from the same hand sample (i.e. belonging to the same sphaerosiderite horizon) show similar elemental uptake concentrations and similar patterns in uptake (e.g. zonations).

3.4.1 Mapping zones of minor element uptake

Concentric zones of increased Mn, Ca, or Mg substitution ranged from < 5 μm to 200 μm thickness. Mn enrichment is a common feature in many samples, and occurs as higher Mn concentration in cores of spheres and finer (< 20 μm thickness) concentric zones of substitution. Sample C9 (Figure 4.11) is an example of a sphaerosiderite with higher substitution of Mn (bright teal colour) in the core of the nodule and comparatively higher substitution of Ca (blue) and Mg (green) in the outer rim. EDS element maps are semi-quantitative and show relative enrichment with Fe still being the dominant cation. Average substitution of Mn within this single sphere was 3.3 (± 0.3) ox%, Ca was 1.2 (± 0.2) ox% and Mg was 0.2 (± 0.1) ox%.

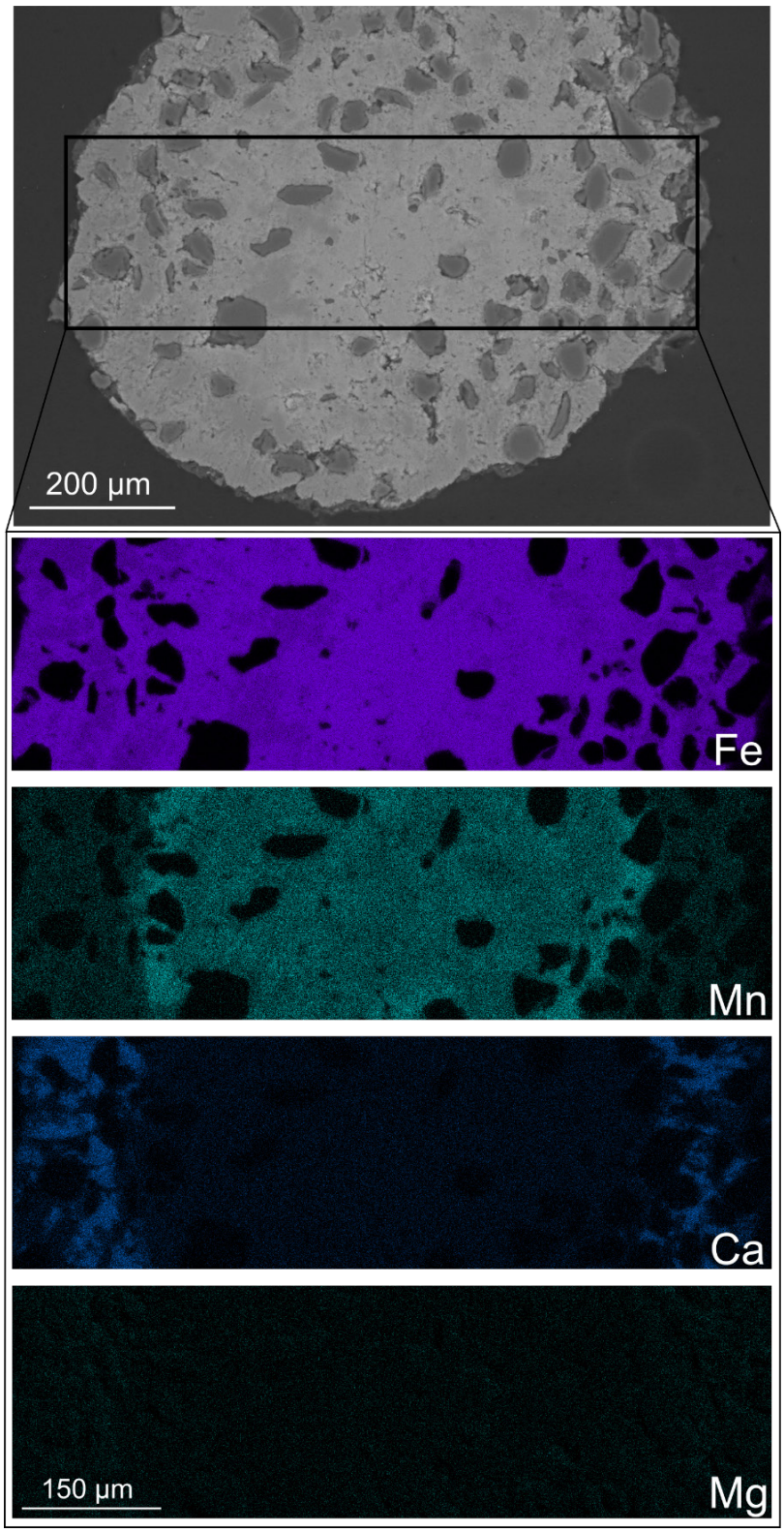


Figure 4.11: Compositional changes across a sphere from C9 with an Mn rich core and a rim enriched comparatively in Ca and Mg (Sample C9, Tunbridge Wells Sand). Average substitution of Mn within this single sphere was 3.3 (± 0.3) ox%, Ca was 1.2 (± 0.2) ox% and

Mg was 0.2 (± 0.1) ox%. The depths and locations of the sphaerosiderite horizons can be found in Figure 4.1.

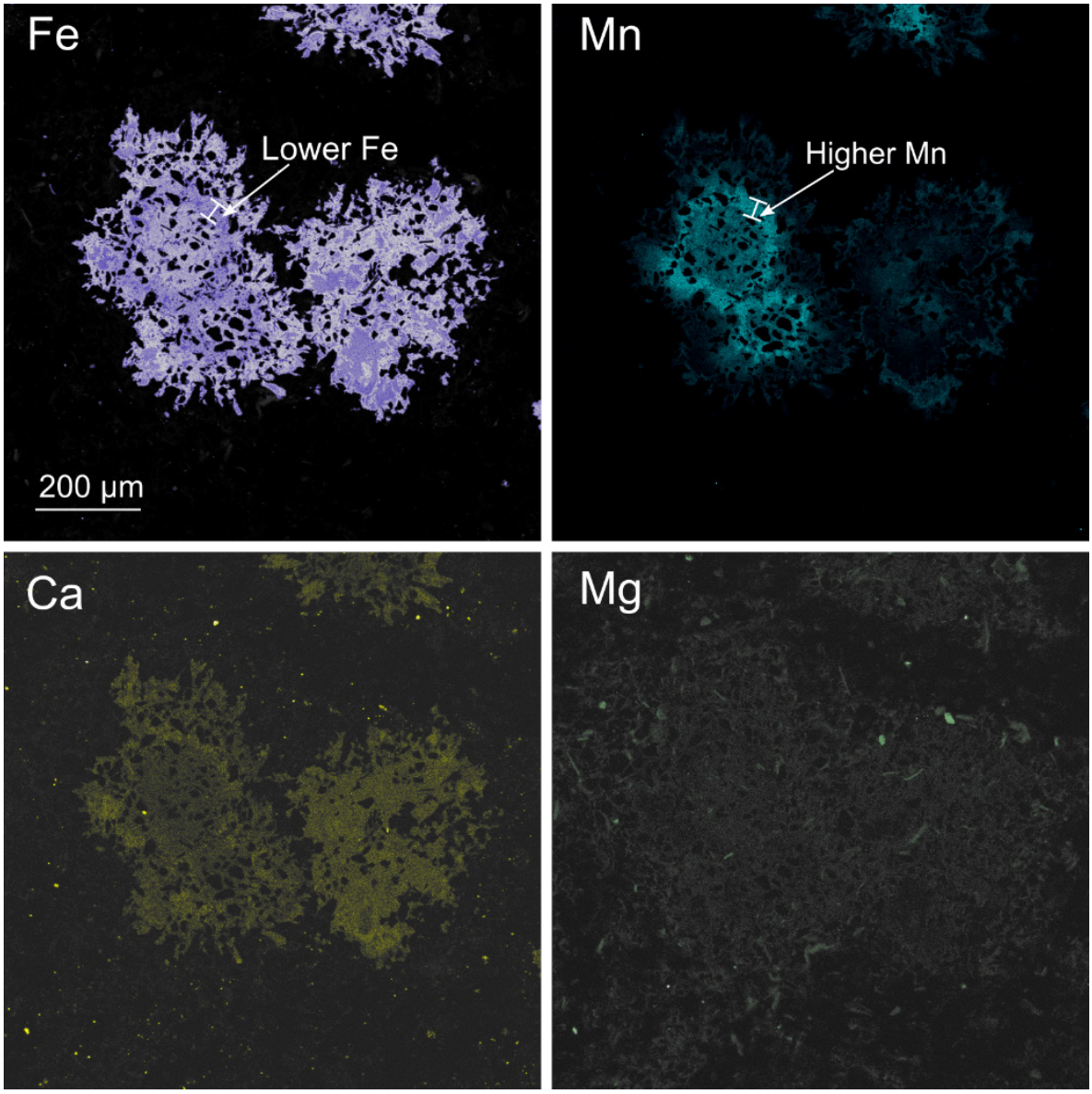


Figure 4.12: Element Map of C1 (Tunbridge Wells Sand) showing concentric zones of Fe and Mn enrichment, with concentrations anti-correlated to each other. This is a particularly oxidised sample (1:2 ratio of siderite to hematite) but preserves fine scale elemental variations in Fe and Mn concentrations. See text for compositional details. The depths and locations of the sphaerosiderite horizons can be found in Figure 4.1.

By contrast, Sample C1 is a representative example of higher Mn uptake in a concentric zone within the sphere (Figure 4.12). The core of the sphere has a higher concentration of Mn compared to the rim, and the edge of the core have fine (< 5 μm thickness) concentric zones of higher Mn substitution (bright teal colour). This element map was produced using EPMA and concentrations were quantifiable. The Mn varies between 2.5 mol% and 4 mol% in the core, and is 0.5 mol% in the rim, with highest values in the brightest zone on the Mn map. Ca and Mg are 1–2 mol% at the rim and approximately 0.5 mol% in the core. Although Fe is the dominant cation (average across the sphere of 97.1 mol%), the elemental maps show an anti-correlation between Fe and Mn with the brighter zones in the Mn map corresponding to duller zones in the Fe map. In contrast to the coupled relationship between Fe and Mn, Ca is only slightly enriched in the rim, and Mg enrichments are very low and indistinguishable from background within the element map.

In a few cases, differences in minor element composition was notable within angular zones in a sphere, thought to be representative of differentiated composition between crystal faces. For example, differences in composition between adjacent spherulitic crystals are shown in Figure 4.13. Mn varies up to 4 mol% in the angular zone, but is generally between 0.5–1 mol% elsewhere in the sphere. Ca shows a similar relationship with up to 4 mol % in the angular zone and varies between 0.3–1 mol% elsewhere in the sphere. Mg is consistently low (0.5 mol%) but within the angular zone falls to < 0.2 mol%. In this sphere, there is an anti-correlation between Fe and Mn, and Fe and Ca, due to substitutions of Mn and Ca in the angular zone, while no significant correlation exists between Fe and Mg. Along with the differences in elemental composition in the angular blocks, fine (< 10 μm) concentric zones of higher Mn and Ca uptake are also notable in the edges of the sphere, similar to the patterns of zonal elemental uptake discussed in the previous examples.

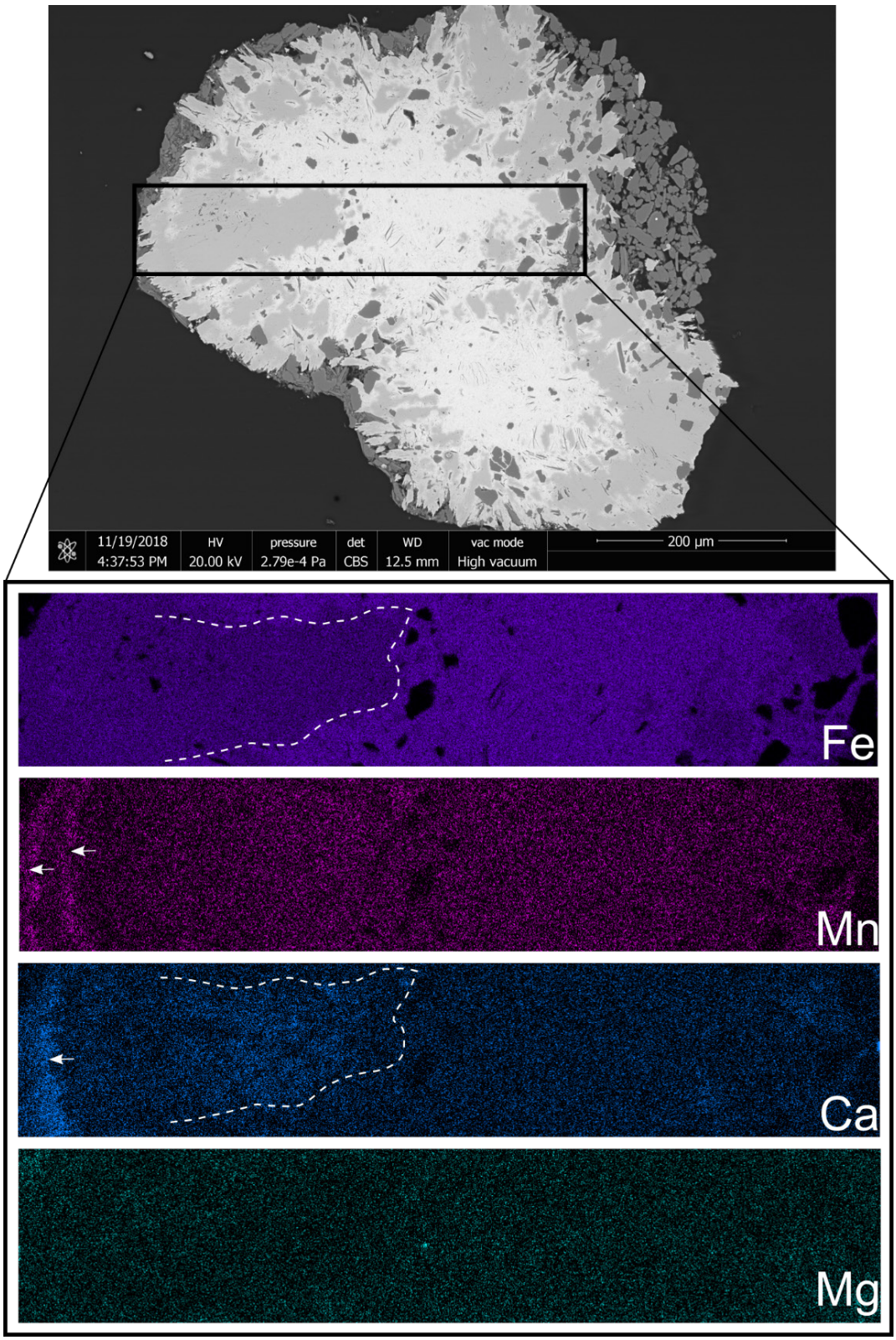


Figure 4.13: Sphere from sample W2(Ashdown Formation) showing evidence of some parts of the nodule enriched in Ca corresponding to lower Fe content (less bright areas in Fe map –

dotted white line), as well as evidence of Mn and Ca zoning in rim (arrows). The depths and locations of the sphaerosiderite horizons can be found in Figure 4.1.

3.4.2 Quantitative elemental transects

The EPMA transects were conducted on the same spheres used for EDS mapping and allowed quantification of the relationships between the cations noted in EDS maps. Transects support the range of compositional heterogeneity noted in element maps in Section 3.4.1 and confirms that the sphaerosiderites in the Weald Basin are largely pure $FeCO_3$, with generally > 90 mol% Fe. The strength of correlations between cations, and concentrations of minor cations are similar in spheres from the same horizon.

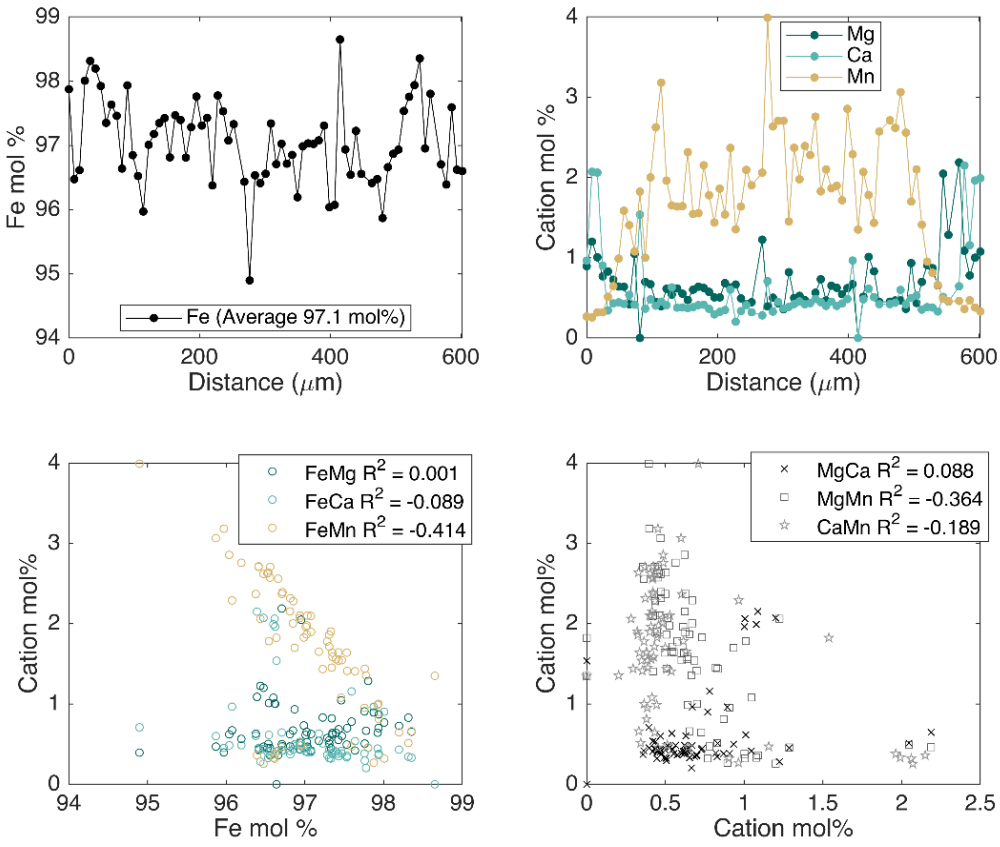


Figure 4.14: Elemental transect from C1 (Tunbridge Wells Sand), showing higher concentration of Mn in core, and higher concentration of Mg and Ca in rim. Fe and Mn show

a negative correlation. Correlations between other cations are weak. The depths and locations of the sphaerosiderite horizons can be found in Figure 4.1.

Mn concentration in the core of spheres is common and visible in transects, such as a representative transect from a sphere from C1 (Figure 4.14). The same sphere exhibits a negative correlation between Fe and Mn (R^2 = 0.414), and no correlations between Fe and Mg or Ca. Mg and Ca concentration comparatively increases at the rims up to 2 mol% as Mn concentration decreases. The correlations between the minor elements (Mg, Ca, and Mn) are weak.

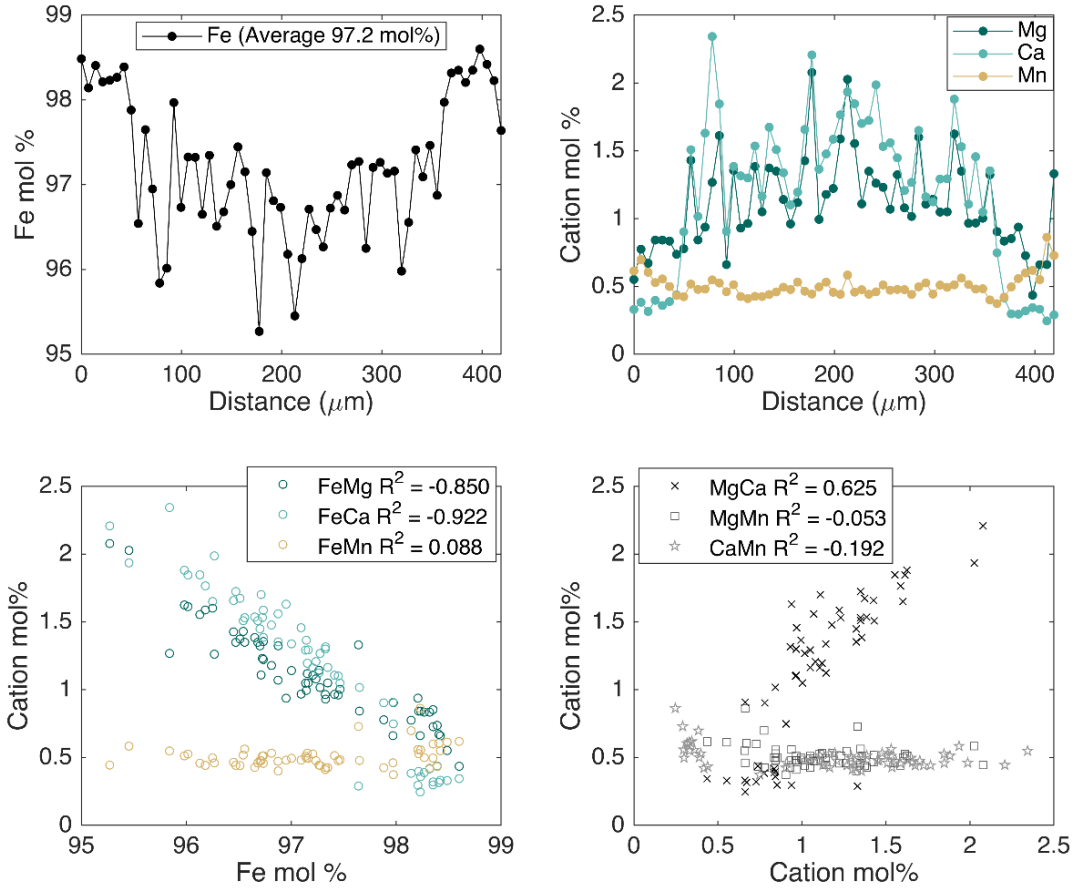


Figure 4.15: Elemental transect from F6 (Ashdown), showing higher concentration of Ca and Mg in core, negatively correlated to Fe. Mn concentrations remain low throughout the transect. The depths and locations of the sphaerosiderite horizons can be found in Figure 4.1.

Alternatively, some spheres show higher concentrations of Ca or Mg within the core, instead of Mn, like sample F6 (Figure 4.15). Sample F6 shows elemental concentrations highly dissimilar to C1, with strong negative correlations between Fe and Mg, and Fe and Ca, as the Fe concentration in the sphere decreases when Ca or Mg are higher. By comparison there is no correlation between Fe and Mn in sample F6, as the Mn values low (< 0.5 mol%) throughout the sphere. There is also a positive correlation between Mg and Ca in this sample, with both enriched in the core of the sphere ($R^2 = 0.625$).

The angular zones of enrichment introduced in the previous section are also quantifiable in transects (Figure 4.16). In sample W2, between 50–200 μm, the Ca concentration increases, along with some increase in Mn between 100–200 μm, corresponding to decreases of up to 4 mol% in Fe concentration. The negative correlation between Fe and Ca, and Fe and Mn is notable, while the other relationships between Fe and minor cation, and between the minor cations are poor. Individual R^2 values from the combination of cations for each transect can be found in Appendix C.1.2 (Table C.1).

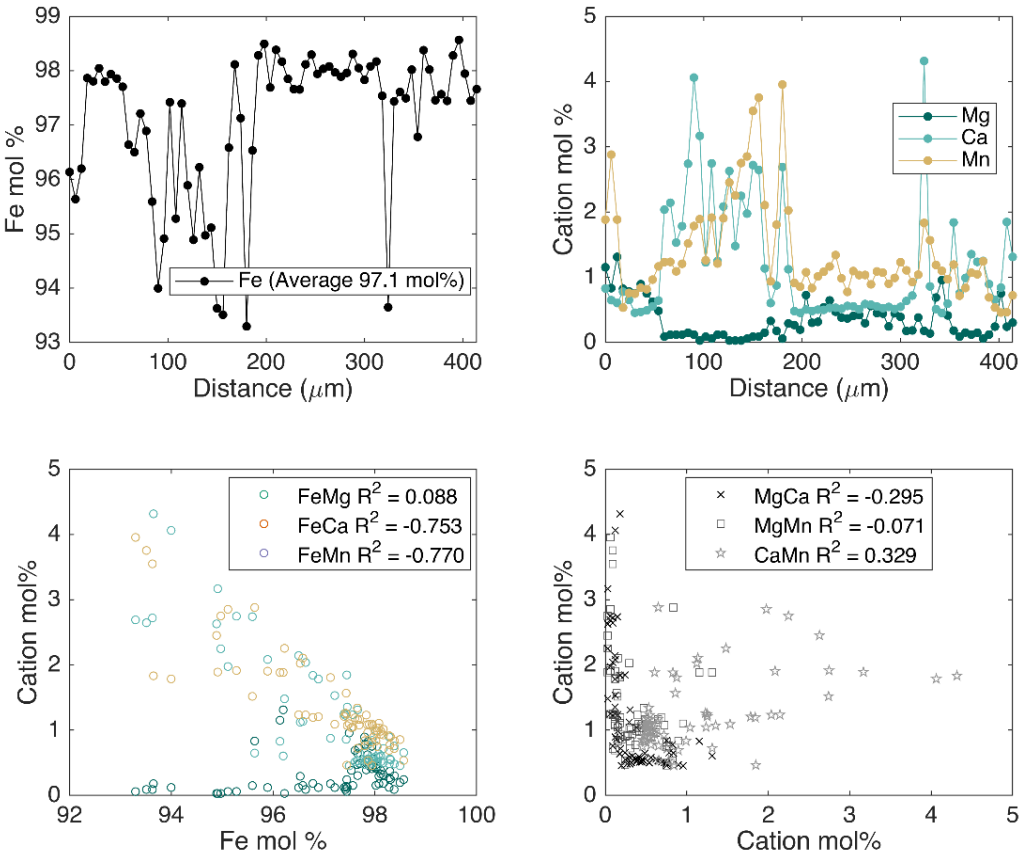


Figure 4.16: Elemental transect from W2 (Ashdown), showing higher concentrations of Mn and Ca, and decrease in Mg concentration along a 150 µm length of the transect while concentrations of minor elements elsewhere in the transetc vary. Strong negative correlation is notable between Fe and Ca, and Fe and Mn. The depths and locations of the sphaerosiderite horizons can be found in Figure 4.1.

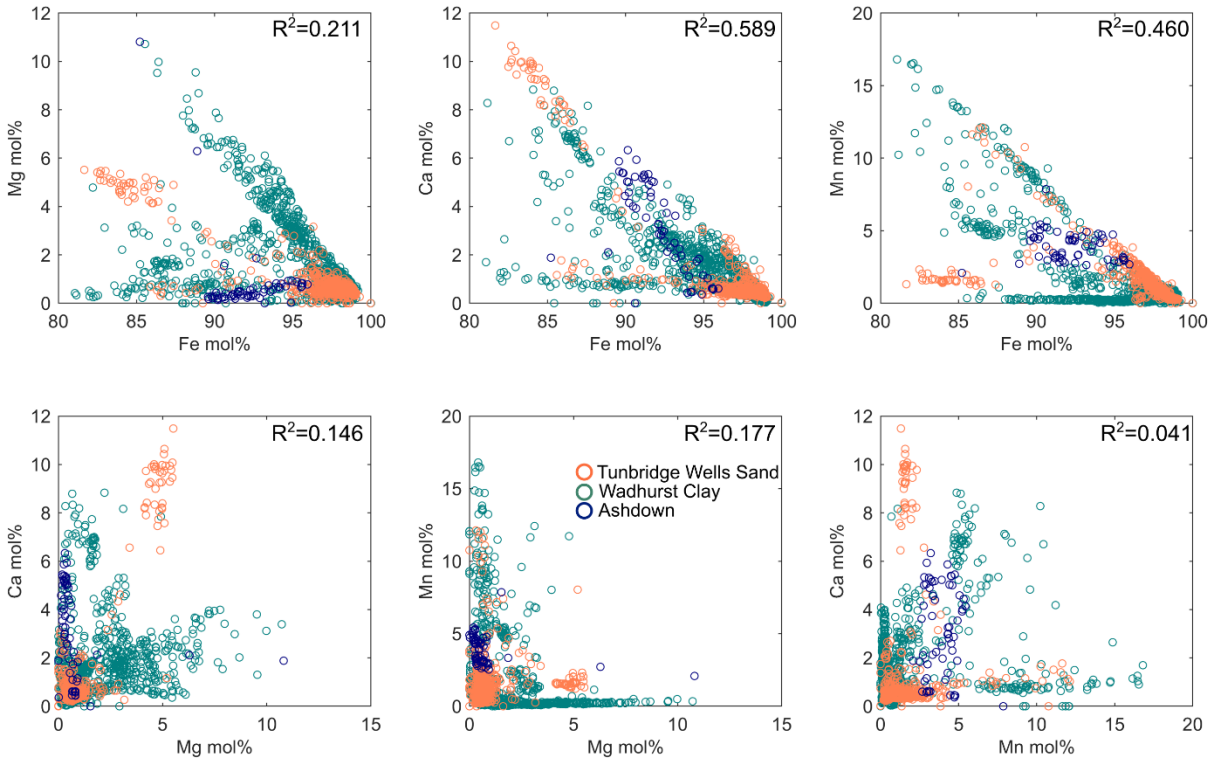


Figure 4.17: Correlations between all elemental transect data shows a large scatter. None of the correlations are statistically significant, apart from between Fe and Ca. These data comprise of 19 spheres from the Ashdown Formation, 2 from the Wadhurst Clay Formation, and 8 from the Tunbridge Wells Sand Formation.

To evaluate if the correlations between Fe and the minor cations were related to the stratigraphy, data from all formations was plotted together (Figure 4.17). Evaluating all the transect data together, weak negative correlations appears to exists between Fe and minor cations Mn, Ca, or Mg. However, the data are scattered, reflecting the variations in strength and relationships between cations of individual sphaerosiderite horizons. The only statistically significant correlation is between Ca and Fe (R^2 = 0.589). There is also some evidence of weak relationships between the minor cations themselves. The correlations and scatter does not improve when considering samples from single lithostratigraphic units either (Appendix C.1.2), particularly as there is also a disparity in number of data points in each

strata with particularly low sampling in the Wadhurst Clay. The patterns of elemental distribution (concentric zones, core-rim differences, angular spherulitic zones) are variable and do not correlate to stratigraphic position, host lithology, or formations.

3.4.3 Elemental mapping of recrystallized sphaerosiderites (Wadhurst Clay)

Element maps of recrystallized spheres were conducted to test if differences in elemental abundnance could provide an insight into the formation and subsequent diagenetic features of these spheres. The recrystallised spheres are all from the Wadhurst Clay and were discussed in Section 3.2.3.

The example discussed here in detail is from sample C12 (Wadhurst Clay, Cooden borehole), the same sphere discussed in Section 3.2.3, which contains a recrystallized core with interlocking crystals of various sizes and an outer rim of radial features which appear similar to primary spherulitic features (Figure 4.18). The elemental map shows a dispersed increase in Mn and Ca within the recrystallised core (Figure 4.18), although the average concentration of Mn and Ca remain low at 1.8 wt% for Mn, and 0.7 wt% for Ca. Within individual crystals, there are variable Mn and Ca concentrations, notable in both the contrast changes of BSE images and the brightness of element maps. Along with this, at the edges of the primary radial rim, there are concentric fine (< 5 μm) zones of increased Mn concentration, similar to the Mn levels identified in spheres with their primary fabric preserved.

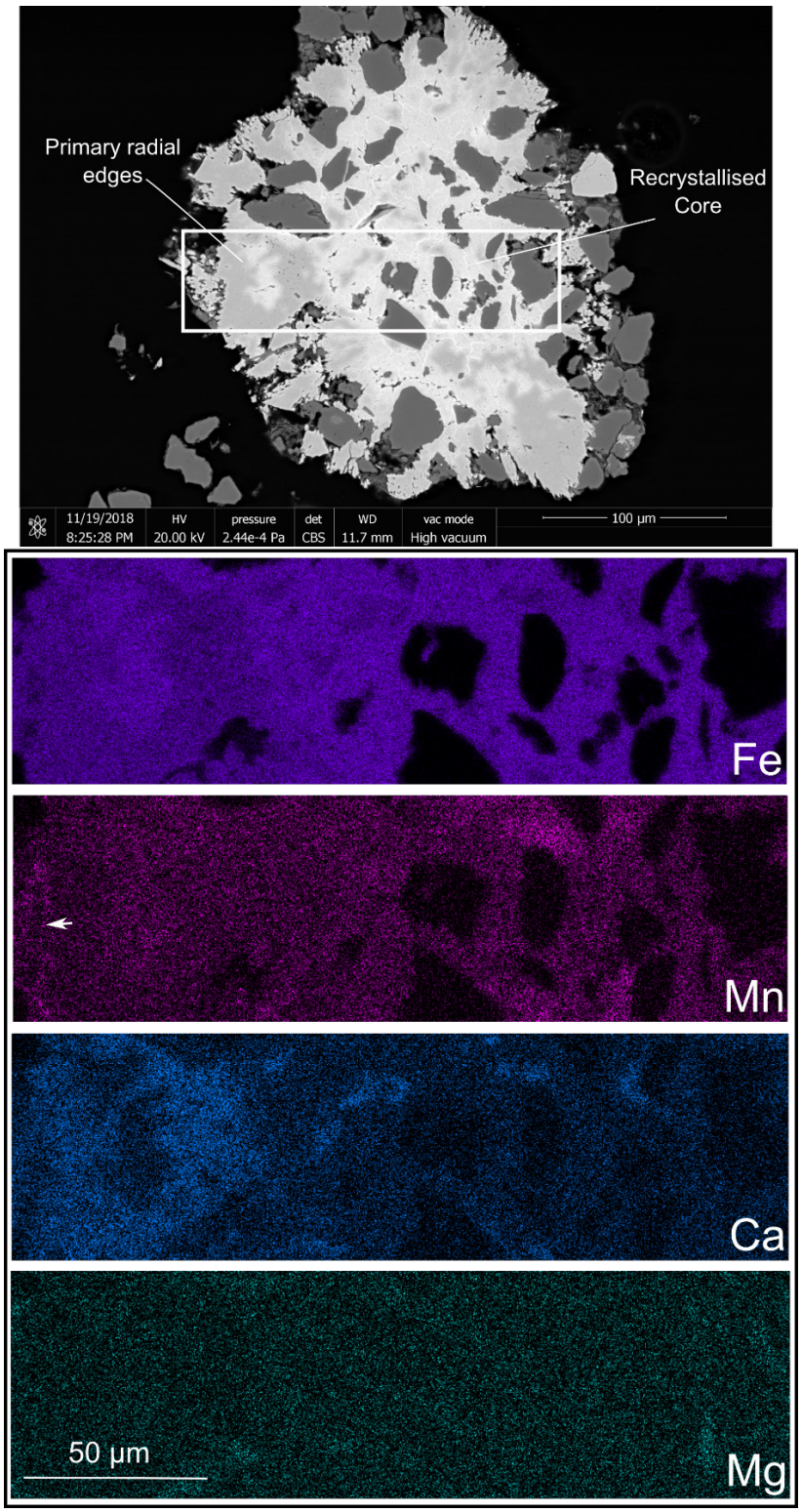


Figure 4.18: Sample C11 from the Wadhurst Clay shows internal recrystallisation in core and primary fabric preserved in outer rim. Elemental map shows dispersed uptake of Mn and Ca, and primary Mn concentric zoned uptake preserved at rims (white arrow). The depths and locations of the sphaerosiderite horizons can be found in Figure 4.1.

3.5 Comparison of petrography and elemental geochemistry

3.5.1 Siderite and Pyrite

Pyrite inclusions within sphaerosiderites are described in Section 3.2.1. In particular, a few sphaerosiderite horizons from the Ashdown Formation contained spheres with large inclusions of pyrite (>30 μm diameter), which included angular inclusions within themselves. Although sulphide inclusions are present in sphaerosiderites in other formations within the Wealden Supergroup, they do not contain siderite or other inclusions within them.

Elemental mapping of these large pyrites in the Ashdown Formation shows the inclusions are mainly siderite, with occasional quartz and clays (Figure 4.19), as indicated by the BSE images. The pyrites are concentrated within an area < 50 μm from the edge of the sphere corresponding to the darker contrast in the BSE image. Within the pyrite, the siderite inclusions were mainly concentrated in a central region about 5–10 μm in diameter, and were surrounded by an outer rim composed of blocky pyrite which is mostly devoid of inclusions. Three quartz inclusions and a few clay inclusions (thin and elongated) are notable in the Si map.

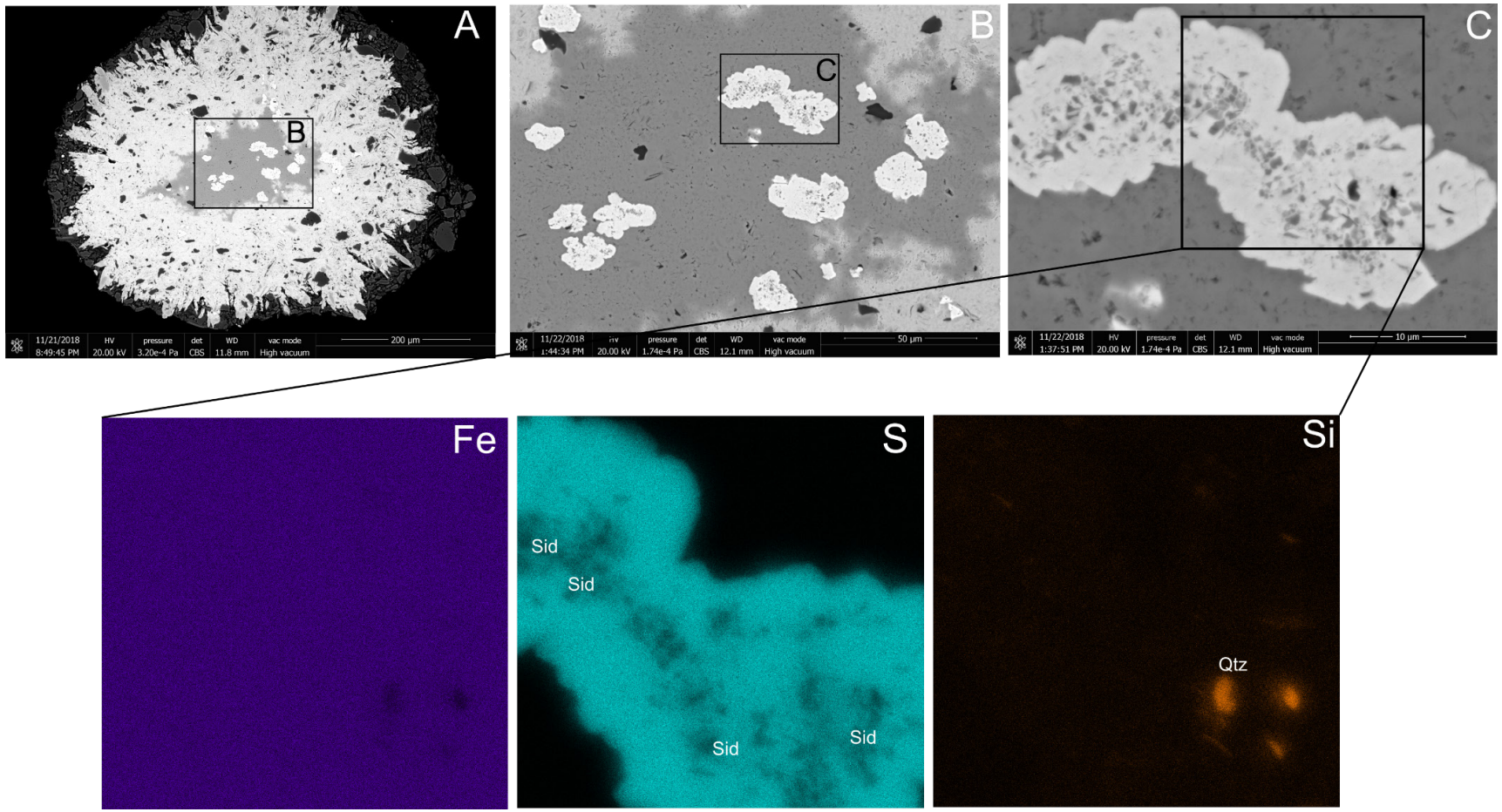


Figure 4.19: Sulphide inclusions within a sphaerosiderite. The sulphide inclusions are rounded with blocky edges, randomly orientated, and dispersed through the core of the sphere. Mapping the inclusion shows siderite inclusions within, and minor quartz and clays. The depths and locations of the sphaerosiderite horizons can be found in Figure 4.1.

3.5.2 Multiple carbonate phases

In two samples, F19 and 67241Cuc, from the Ashdown Formation and the Tunbridge Wells Sand Formation respectively, both calcite and siderite coexist within sphaerosiderites. In F19, the spheres in hand specimen looked like sphaerosiderites, but some were blocks of calcite, surrounded by a layer of siderite. At the edges of the calcite block there are fine (< 2 μm) layers of siderite intergrowing between calcite, forming a transition layer in between the calcite core and the siderite rim Figure 4.20). The spheres from this stratigraphic horizon were heterogenous in composition. Most were sphaerosiderites with extensive dissolution, while this sphere contained both calcite and siderite.

The second example of siderite and calcite coexistence features calcite rhombs in the clay/quartz matrix surrounding spheres in sample 67241Cuc (Figure 4.21). These calcite rhombs are equant with crystal edges of 1 μm, and present as inclusions within the sphaerosiderite as well as in the matrix. Within the sphere, the calcite rhombs were present in clusters of 6–12, dispersed mostly within 50–70 μm from the edge of the sphere, giving the sphere a mottled appearance in BSE images. On the edges of the sphere, the siderite can be seen growing around the calcite rhombs, implying the calcite rhombs were present in the matrix as the siderite sphere was growing and incorporating matrix phases. A large 60 μm diameter zone to the upper right of the sphere is also missing, indicating either a nucleus or a large inclusion which had likely fallen out during sample preparation.

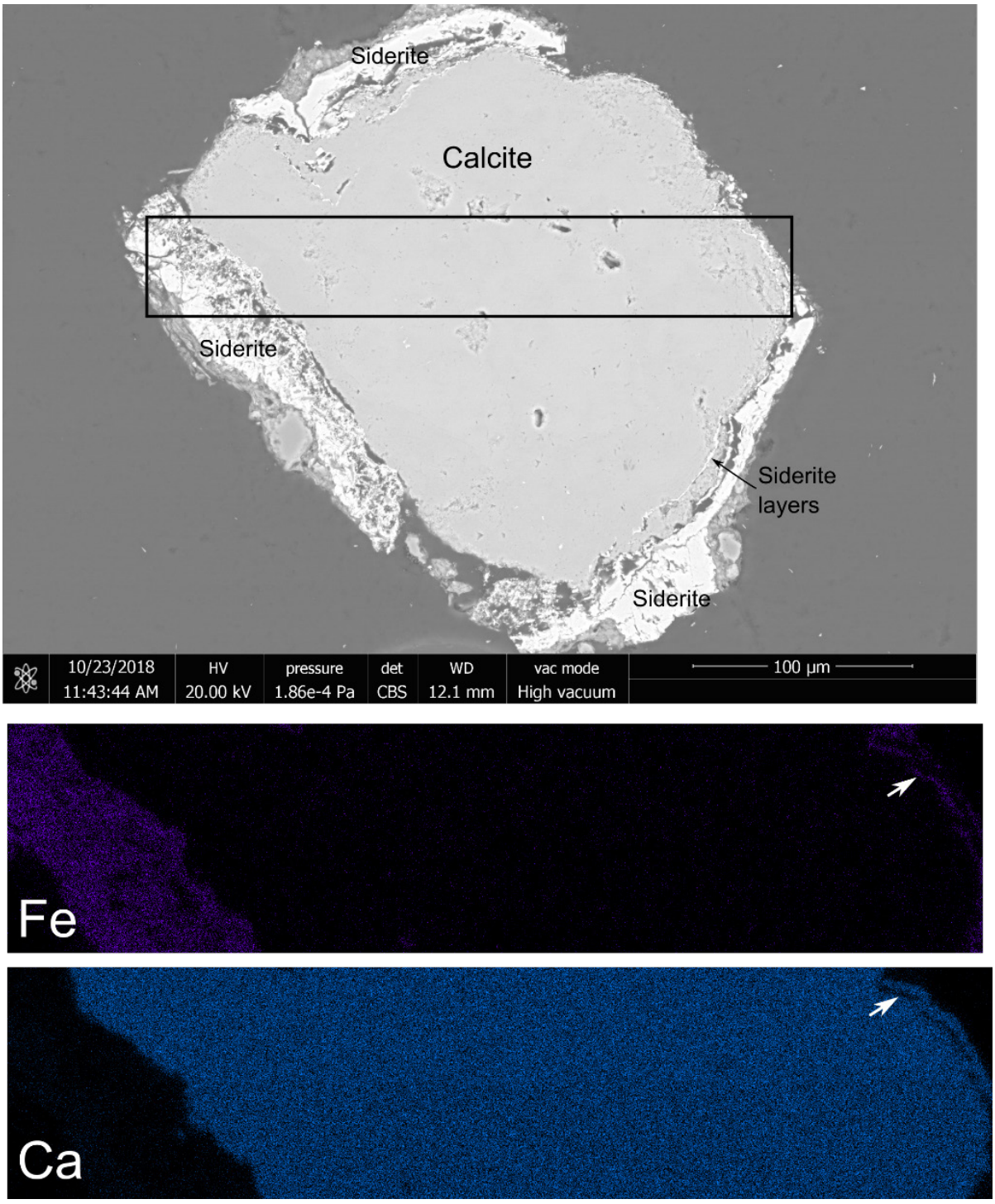


Figure 4.20: Sample F19 from the Fairlight Borehole and the Ashdown Formation showing a pseudo sphaerosiderite, consisting of a calcite block with siderite growing on the rim and layers of intergrowth in between. The depths and locations of the sphaerosiderite horizons can be found in Figure 4.1.

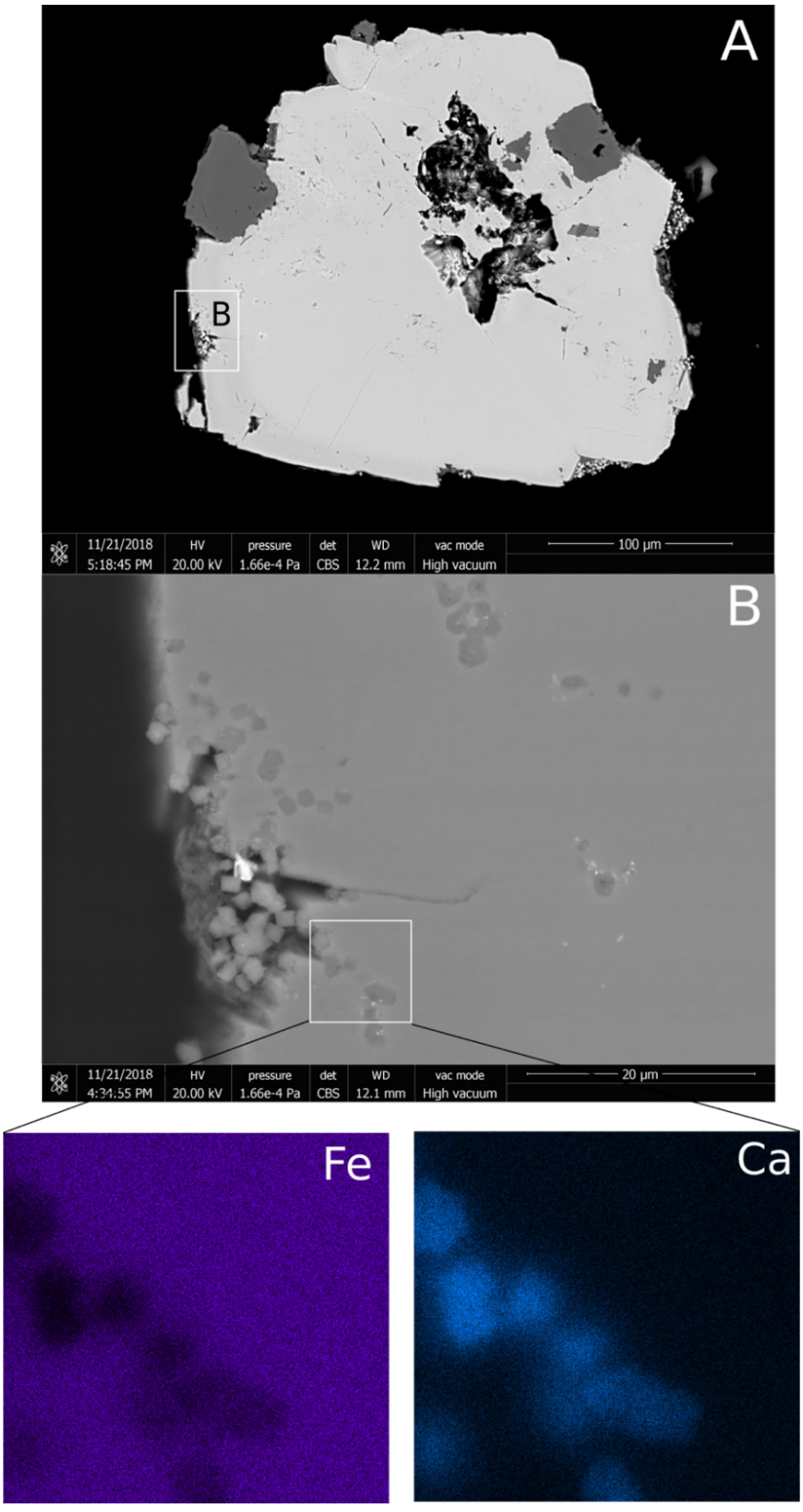


Figure 4.21: Sample 67241Cuc from the Tunbridge Wells Sand. A siderite sphere with uniform crystal sizes (cryptocrystalline centre) and evidence of calcite rhombs growing in the matrix surrounding the spheres, as well as incorporated into the sphere. The core of the sphere is

missing, either having come off during polishing. The depths and locations of the sphaerosiderite horizons can be found in Figure 4.1.

4 Discussion

4.1 Variable physiochemical conditions during the growth of Wealden sphaerosiderites

4.1.1 Morphological and compositional heterogeneity

The morphological and elemental heterogeneity in sphaerosiderites through the Wealden Supergroup suggests the physiochemical conditions in pore waters, such as pH, siderite saturation, pCO_2, and cation concentrations were varying temporally and spatially. The patterns of elemental uptake and morphological heterogeneity did not show any correlation to stratigraphic unit but were variable throughout the Wealden Supergroup.

Morphological changes, at a basic level, can be used to understand saturation states. For instance, the cryptocrystalline centre of spheres could have formed during a period of high siderite nucleation rate, which would be triggered by very high supersaturation (Passey, 2014). Progressively low nucleation rates, but sustained growth towards the outer rim would have produced the bladed/spherulitic crystals radiating from the centre, indicating supersaturation remained below the critical threshold for spontaneous nucleation but high enough to permit further growth (Passey, 2014). This mechanism can be applied to some examples (Figure 4.4), but the morphologies within the Wealden sphaerosiderites are far more diverse. The spheres include evidence of cryptocrystalline centres with spherulitic rims, but also of wholly cryptocrytsalline spheres, spheres with several growth zones indicating several periods of growth, and uneven morphological changes within individual spheres. The variety of morphologies indicates growth rate differences which can be linked to variability in siderite saturation in pore waters controlled by pH, temperature, Fe^{2+}

concentration, and pCO_2. The morphology of sphaerosiderites within the same horizons are similar, suggesting the morphological changes recorded are influenced by the evolution of pore waters within that horizon.

Like morphological changes, compositional changes within individual sphaerosiderites also show a great deal of variability. The Wealden sphaerosiderites are generally pure (> 90 mol% $FeCO_3$) and contain substitutions of Mg, Ca, and Mn (1–10 mol%). The patterns of minor element distributions includes, but is not limited to, spheres with higher concentrations of Mn, Ca, or Mg in cores, concentric zones of Mn or Ca up to 20 μm in thickness, Mg or Ca rich outer rim, and minor cation enrichment within angular, blocky or spherulitic regions within a sphere. Like morphological similarities in a sphaerosiderite horizon, the elemental compositions and distribution patterns are similar within sphaerosiderites from the same horizon, again suggesting a local control on element chemistry. The variability in elemental uptake is decoupled from lithological or facies changes, and the complexity of geochemical controls on elemental uptake in siderite (Mortimer et al., 1997; Romanek et al., 2009; Sengupta et al., 2020) can make it difficult to assess paleoenvironmental implications of elemental composition.

For instance, higher concentrations of Mn compared to Ca or Mg have been used to suggest sphaerosiderite growth in freshwater (Mozley, 1989), and Wealden sphaerosiderites commonly contain Mn as a minor element. However, in Chapter 2 (Sengupta et al, 2020), Mn incorporation into growing siderite is shown to be controlled by both the concentration of Mn in solution and the growth rate, and changes in uptake can occur over cation concentration changes as low as 0.05 mmol. It is not possible to distinguish between the growth rate and cation concentration parameters in the natural sphaerosiderites as Mn uptake is not usually accompanied by coincident morphological changes. Similarly, Mg or Ca enrichment, compared to Mn, has been suggested to indicate the presence of marine pore

waters (Mozley, 1989). No established pattern can be found in the correlations between Fe and Ca or Mg, and relationships between these cations can vary in the Wealden sphaerosiderites. Some transects show anti-correlation between Fe and Mg/Ca, although the strength of this correlation varies (R^2 values 0.1 to 0.9). This could simply be due to the enrichment of Mg and Ca within the rims of the spheres and not cores, and/or more homogeneously dispersed composition through the sphere. However, in some cases, Mg and Ca enrichment in cores is also noted, which is unusual considering experimental synthesis of siderite at ambient conditions indicates Mg and Ca uptake into siderite does not occur in abiotic siderite formation. The presence of Mg and Ca in Wealden sphaerosiderites is interesting as it could suggest diagenetic pathways (such as temperature increase), high pore-water alkalinity (perhaps as a function of microbial dissimilatory iron reduction), or unconstrained biological pathways (detailed discussion in Chapter 2). A lack of secondary cements such as ferroan carbonates, and a lack of alteration in most of the sphaerosiderite horizons (apart from Wadhurst Clay) suggests the spheres are primary, and that the elemental heterogeneities reflect complex but primary elemental uptake dependent on a complex suite of paleoenvironmental conditions.

The morphological and elemental heterogeneity can also be interpreted as growth close enough to the soil surface for the pore waters to be regularly affected by changes in groundwater chemistry, such as pH, temperature, cation concentrations and/or soil pCO_2, all affecting siderite growth. Sphaerosiderites in the Weald Basin have also been seen to be associated with root structures (Allen et al., 1998), providing further evidence that they grew at relatively shallow depths in the soil profile. Understanding the depth at which sphaerosiderites were growing is paramount to understanding the extents to which surface processes may have affected them. For instance, studies on modern siderites have shown that those growing deeper within a soil profile appear to record less seasonality, based on clumped isotope temperature measurements (Van Dijk et al., 2019). Assessing the depth of

the Wealden root systems is difficult, but coupled with the morphological and elemental heterogeneity, and the lack of extensive diagenetic alteration or cements, it can be argued the Wealden sphaerosiderites were recording meteoric groundwater but were growing at depths within the soil profile where pore waters experienced physiochemical variability during growth. The depth in the palaeosol profiles at which these sphaerosiderites occurred will be further discussed in Chapter 5 when considering stable isotope and clumped isotope data.

4.1.2 Origin of pyrite inclusions in sphaerosiderites

The formation of pyrite relies on presence of iron, the availability of dissolved SO_4^{2-}, and the amount of organic matter that can be used by sulphate reducing bacteria to produce H_2S (Berner, 1971). In the presence of sufficient sulphate, ferrous iron would typically react with H_2S first, precluding a siderite precipitation pathway (Berner, 1983; Pye et al., 1990). Based on the high concentrations of siderite in the Wealden Supergroup, it can be assumed that Fe^{2+} was in abundance relative to sulphide. Pyrite is present as inclusions within sphaerosiderites in low (< 1 wt%) concentrations, suggesting a limited availability of sulphate. Therefore, the pyrites likely formed from the consumption of low concentrations of initial sulphate and likely restricted to areas of locally dispersed organic matter.

In two samples, > 20 µm diameter pyrite inclusions contained siderite inclusions within, which suggest that pyrite and siderite precipitation occur in the same locations, and that local conditions within the wetland were fluctuating between sulphide and carbonate precipitation. The fluctuations between sulphide to carbonate dominant precipitation are localised, and likely related to micro-scale sulphate variations, controlled by diffusion between zone of sulphate reduction and siderite precipitation. The petrographic relationships suggest that initially, small siderites (< 5 µm length) precipitated in pore waters which were siderite-saturated in a freshwater environment, but then switched briefly to pyrite. The pyrite

growth incorporated existing siderites in an initial cryptocrytalline centre, and then slower growth rates produced a blocky cubic rim. The fact that the siderite inclusions are mostly incorporated in the central region of the pyrite spheres suggests that pyrite was growing in the same locations as siderite. Over time however, the pore waters became dominantly siderite saturated, presumably once sulphate was exhausted, and the pyrites were included within sphaerosiderites.

4.1.3 Minor calcite precipitation

Calcite was found in one horizon in the Ashdown Formation (F19), and one horizon in the Tunbridge Wells Sand (67241Cuc), both as a dominant component of a sphere (Figure 4.20) and as inclusions within a sphere (Figure 4.21), respectively. The relationship between calcite-siderite in petrography indicate periods of dominant siderite or calcite precipitation, as well as transition periods where the two phases are deposited in alternating fine layers (Sample F19, Figure 4.20). In the example from sample F19, the calcite block appears to have grown first, then alternating siderite and calcite fine bands precipitated around the calcite block, followed by dominantly siderite precipitation on the edges of the block. However, the other spheres of this horizon have siderite as a dominant phase (although calcite is still incorporated as a minor phase in spheres) suggesting that the dominance of calcite precipitation may have varied locally in a single palaeosol horizon. In the case of 67241Cuc (Figure 4.21) from a horizon in the Tunbridge Wells Sand, the presence of calcite rhombs in the matrix and as minor inclusions within the sphaerosiderite suggest the siderite sphere continued to grow when calcite had already precipitated. It is however, difficult to evaluate whether calcite and siderite started growing at the same time. Similar to the pyrite-siderite petrographic relationship, the siderite-calcite relationship suggests fluctuating conditions between calcite and siderite precipitation, as well as locally variant cation concentrations in pore waters. Fe^{2+} is known to hinder calcite growth (Di Lorenzo et al.,

2017), and siderite is less soluble than calcite by 2 orders of magnitude. Fe^{2+} concentration only needs to be $1/100^{th}$ of the concentration of Ca^{2+} to reach comparable saturation (Busenberg and Plummer, 1986, Jiang and Tosca, 2020, in review). This suggests that even if initial siderite precipitation had lowered the siderite saturation, it is unlikely that calcite saturation would have been comparable to siderite saturation. An influx of Ca^{2+}, possibly from brackish or marine waters controlled by local groundwater fluxes, would likely be required to increase calcite saturation.

The continued growth of sphaerosiderites in other parts of this sphaerosiderite horizon suggests that the soils were waterlogged and reducing, and that the dominant carbonate precipitation pathway was siderite in the long-term. The implications of the co-existence of multiple phases for the wider paleoenvironmental conditions within the Wealden wetlands is discussed in Section 4.2.

4.1.4 Diagenetic alteration

The sphaerosiderites are well preserved with primary fabrics in the Tunbridge Wells Sand and Ashdown formations. However, recrystallization of the top 20–40 m of the Wadhurst clay is noted in both the Cooden and the Westfield boreholes, indicating a regionally prevalent recrystallisation of palaeosol horizons within the Wadhurst Clay. In some cases, only the cores of spheres are recrystallised and the edges continue to preserve primary spherulitic morphology and minor element zoning. The recrystallised cores also preserve compositional differences, including higher Mn concentrations which are likely a relict of the primary elemental composition of Mn-rich cores, common in Wealden sphaerosiderites. The evidence suggests recrystallisation likely occurred *in situ*, preserving the primary compositional differences within spheres. Preferential recrystallisation of cores containing Mn is supported by the increased solubility of Mn^{2+} compared to Fe^{2+}, which means the Mn-rich cores would be more soluble (Jensen et al., 2002). As this cannot be

verified in SEM-EDS, another possible explanation is the variability of crystal sizes controlling the recrystallisation. For instance, cores usually have a smaller crystal size than the outer edges of the sphere, and smaller crystal sizes are more soluble and prone to recrystallisation (Gorski and Fantle, 2017). The alteration is specific to the siderites, and within the limited number of samples available there is no evidence of other carbonate phases or cementation in the matrix.

Apart from the facies-specific recrystallisation, occasional sphaerosiderite horizons also preserve dissolution textures in the Tunbridge Wells Sand and Ashdown formations. The dissolution is generally limited to the central part of the sphere, but re-precipitation of another phase does not appear to have occurred, as it has in the Wadhurst Clay. The dissolution is limited to the cores, again suggesting solubility differences based on composition or crystal sizes likely played a role. A lack of other carbonate phases or cementation in the matrix suggests that the dissolution is limited to the sphaerosiderites and the palaeosol horizons were not altered significantly otherwise.

These altered horizons were not considered suitable for palaeoclimate reconstructions but their palaeoenvironmental implications for the Wealden wetlands are discussed further in Section 4.2.2.

4.2 The Wealden palaeoenvironment

4.2.1 A dynamic palaeoenvironment

Modern wetlands are highly variable and dynamic environments. The hydrology of wetlands is considered an important factor in controlling respiration of organic matter, nutrient availability, and salinity (Mitsch and Gosselink, 2015). The major components of a wetland hydrological system include the amount and timing of precipitation and evaporation, surface inflows and outflows, and groundwater fluxes. Together these all

influence physiochemical conditions such as soil chemistry, water chemistry, and sediment composition (Mitsch and Gosselink, 2015). Variability in stable isotopes and elemental compositions of pore waters associated with modern nodule growth have been noted within modern wetland systems which reflect complex hydrological cycling (Pye, 1984; Pye et al., 1990; Moore et al., 1992; Driese et al., 2010; Ludvigson et al., 2013; Lin et al., 2019). The siderites growing in modern wetlands have been shown to record a seasonal bias (Van Dijk et al., 2019), variable groundwater $\delta^{18}O$ (Driese et al., 2010; Ludvigson et al., 2013), and variability in biological processes such as sulphate and ferrous iron reduction (Coleman, 1993; Lin et al., 2019).

It can be postulated that ancient wetlands would have experienced similarly dynamic environmental conditions. Indeed, sedimentological evidence from the Wealden Supergroup suggests the Weald Basin wetlands experienced wet conditions, for example storms and high channel discharge events based on sedimentological evidence of debris, storm coquinas, and coarse channel deposits (Allen et al., 1998; Wright et al., 2000). This lends support to the interpretations of variable physiochemical conditions in pore waters during sphaerosiderite growth based on sphaerosiderite elemental and morphological heterogeneity. Periodic groundwater recharging associated with the wet conditions would have affected cation concentrations, pH, pCO_2 in pore waters, affecting siderite growth and elemental composition. Seasonal changes in the Wealden Supergroup are also interpreted from sedimentological evidence and climate models, and further support the interpretation of the Wealden wetlands as a dynamic environment. Features indicative of seasonality include seasonal catenas and rapidly deposited storm coquinas (Allen et al., 1998; Wright et al., 2000), and evidence of periodic aridity such as mudcracks and evaporates (Allen et al., 1998). Climate modelling of the Wealden at 4 times pre-industrial levels of atmospheric CO_2 (~1120 ppm) suggests hot summers (average land temperature 30–36ºC) and cool winters (8–12ºC), as well as precipitation throughout the year with highest precipitation during

winter months (Haywood et al., 2004, Farnsworth, *pers comm*, 2019). The sedimentological evidence for wet and warm conditions match the climate modelling well, and suggest that the chemical variability notable in modern wetlands would likely have applied within the Weald Basin wetlands.

The wet and warm conditions in the Weald Basin during the Early Cretaceous would have been a major factor in controlling surface water flow and groundwater recharging, and therefore, the dynamics of the palaeoenvironment (Allen et al., 1998; Haywood et al., 2004). For instance, the timing of precipitation (winter, as suggested by climate models) would control the timing of groundwater recharging and therefore, the geochemical stability of pore waters, having a direct influence on siderite growth. The continued growth of sphaerosiderites suggests the soils remain largely waterlogged, but that they were likely growing high enough in the soil profile for the surrounding pore waters to be affected by seasonal surface changes and groundwater recharging. The stable isotope and clumped isotope analyses in Chapter 5 will further address the surface and/or seasonal biases in the sphaerosiderite record.

4.2.2 Brackish or marine influence in a freshwater wetland?

Establishing the salinity of the porewaters from which the siderites precipitated is an important aspect of their palaeoenvironmental interpretation and impacts on their ability to faithfully record the isotopic composition of meteoric groundwaters. Most sphaerosiderite studies assess the elemental compositions of siderites to provide evidence of marine influence (Mozley, 1989; Ludvigson et al., 1998). However, as discussed in Chapter 2 and Section 4.1.1 in this chapter, these methods of assessing palaeoclimate are likely too simplistic.

Modern nodules from intertidal coastal wetlands in Norfolk, UK (Pye, 1984; Pye et al., 1990; Lin et al., 2019) and the Mississippi river delta (Moore et al., 1992) contain multiple

phases such as siderite, calcite, dolomite, and pyrite, within the same nodule. The presence of Mg-calcite and pyrite in these modern systems was explained due to marine incursions in the wetlands and proximity to the coast (within 2–5 km). The proximity to the coast likely provides more sulphate and higher concentrations of Ca^{2+} and Mg^{2+} within pore waters leading to precipitation of pyrite and calcite (Pye et al., 1990; Moore et al., 1992). In the case of the Mississippi river nodules, the siderite is part of the core of the sphere, and calcite and pyrite precipitated around the rim, and the co-existence of calcite and pyrite was taken as evidence of marine pore waters (Moore et al., 1992).

Similar to these modern coastal wetlands, it is possible that marine influence in ancient wetlands may have allowed the growth of multiple phases such as siderite, calcite and pyrite. In the Wealden sphaerosiderites, pyrite is a common, but minor, inclusion (< 1 wt%) and within sphaerosiderites (Figure 4.19). By contrast, although calcite was only noted in two palaeosol horizons, the evidence suggests that calcite precipitation may have been locally dominant within these horizons. At these times of calcite formation, the pore-water chemistry in the Wealden could have been influenced by marine/brackish sources to allow co-precipitation of multiple carbonate phases (Pye et al., 1990; Moore et al., 1992). There is also a possibility that over time, the primary Mg-calcite, precipitating alongside siderite, could have recrystallised to Mg-rich siderite, based on observations of recrystallisation from the modern studies in Norfolk (Pye et al., 1990). Both thermodynamic studies (Berner, 1971) and recrystallisation of aragonite shells in Norfolk marshes (Pye et al., 1990; Lin et al., 2019) suggests siderite can result from the recrystallisation of a aragonite/calcite precursor over short periods of time (< 1500 years) when Fe/Ca > 0.2. However, there is no obvious textural evidence of areas with high Mg contents within the Wealden nodules that would suggest the presence of originally Mg-calcite. The Mg content within spheres from the Wealden is relatively low, and therefore the presence of other carbonate phases within the nodules, such as calcite, are stronger, less ambiguous evidence for brackish pore waters

than Mg concentration alone. Overall, siderite is the dominant phase within the majority of palaeosols horizons, and coupled with sedimentological and palaeontological evidence (Batten, 1982; Batten and Lister, 1988; Allen et al., 1998; Radley and Allen, 2012), suggests dominantly freshwater conditions.

The recrystallisation of sphaerosiderites in the Wadhurst Clay is evidence of regional stratigraphic alteration which could suggest widespread palaeoenvironmental changes. Similar recrystallization of sphaerosiderites has been reported from the Cretaceous-age Dakota and Swan River Formations in the western USA (Ufnar et al., 2004) and linked to local sea level changes due to the proximity palaeocoastlines to the sampled sites (< 10 km). However, both the Dakota and Swan River formations also exhibit replacement of siderite with pyrite, and the presence of calcite cements within the matrix, providing further evidence of marine diagenesis. The Wadhurst Clay Formation would have been deposited further from the coast (> 100 km from the Boreal Sea; Radley and Allen, 2012) than the North American deposits, and thus, the possibility of marine incursions as an explanation for recrystallisation seems less feasible. Along with this, evidence for pyrite or calcite is absent from the Wadhurst Clay, perhaps indicating minimal influence from marine diagenesis. Palynology from the Wadhurst Clay shows poor preservation of organic matter (also discussed in Chapter 3) and some evidence of fossil assemblages which may indicate salinity fluctuations (Batten, 1982; Batten and Lister, 1988; Horne, 1995). However, the evidence is not conclusive enough to suggest a marine inundation during the deposition of the Wadhurst Clay, and is generally interpreted as indicating the deposition of an oxidised and more transgressive facies than the formations above or below (Batten, 1982; Allen et al., 1998; Batten, 1998). Currently, the evidence for increased salinity during deposition of the Wadhurst Clay Formation is not conclusive based on palaeontology and palynology, but the regional recrystallisation in sphaerosiderites suggests a significant paleoenvironmental change; further work is required to understand the context and cause of this.

*Refer to Figure 4.1 for sphaerosiderite horizon depth and locations.

Based on the mineralogical and petrographic evidence, the Wealden Supergroup may have experienced some periods of more brackish conditions, but these do not seem to have been pervasive as there is no evidence of extensive pyrite or calcite deposition. The regional recrystallisation of sphaerosiderites in the Wadhurst Clay could suggest a more pervasive period of marine inundation, but the sedimentological, petrographic, and paleontological evidence for higher salinities is inconclusive. For the most part, the palaeosol horizons within the Ashdown Formation and Tunbridge Wells Formation were likely growing in freshwater conditions and are suitable for palaeoclimate reconstruction.

4.3 Implications for understanding sphaerosiderite formation in wetlands through the Phanerozoic

Throughout the Phanerozoic, sphaerosiderites preserve a variety of patterns in minor element uptake, including but not limited to, Mn-rich core, Mg- and/or Ca-rich rim, Ca- and/or Mn-concentrations in certain radial zones within a sphere, and relatively constant minor cation concentration throughout the spheres (Khim et al., 2000; Choi et al., 2003; Ufnar et al., 2004; Driese et al., 2010; Robinson et al., 2010; Passey, 2014; Weibel et al., 2016; Taylor, 2019). From the experimental work in Chapter 2, it is clear that the elemental heterogeneity noted in sphaerosiderites and the attributions to pore water elemental chemistry and/or growth in certain biogeochemical zones are too simplistic. Instead, the elemental heterogeneity within a single sphaerosiderite is likely to reflect a mixture of pH, saturation state, pCO_2, temperature, and cation concentrations experienced during the growth of the sphere.

The complexity of siderite growth in wetland systems is documented in modern nodules (Pye et al., 1990; Moore et al., 1992; Lin et al., 2019). The evidence suggests that precipitation of both calcite and siderite is common in these modern coastal settings, as is the presence of pyrite. All three of these phases are also notable in ancient wetland deposits

(Kantorowicz, 1985; Fisher et al., 1998; Ufnar et al., 2004; Weibel et al., 2016; Taylor, 2019), suggesting a strong link between the deposition of these phases, and their preservation in the geological record. Both Lin et al. (2019) and Pye et al. (1990) conclude that recrystallisation of calcite to siderite occurs within the modern nodules from Norfolk, providing another pathway to carbonate mineral formation other than direct precipitation. Lin et al. (2019) found that some localities in the Norfolk marshes contained pore waters with Fe/Ca > 0.2 (required for recrystallisation of calcite to siderite), but not others. This suggests that conditions may have been equally variable within ancient wetlands, allowing for recrystallisation processes to be operating locally based on cation concentrations in pore waters. The modern studies illustrate that, within the same wetland system, there are not only complexities regarding the palaeoenvironmental conditions (i.e. pH, cation concentration, saturation), but also regarding the pathway through which siderite can precipitate.

The association of phases found in Phanerozoic sphaerosiderites of siderite, calcite, and pyrite suggests that similar pathways were operating within ancient wetlands, too. The co-existence of siderite and pyrite within nodules has been previously noted in Triassic and Jurassic samples (Kantorowicz, 1985; Fisher et al., 1998; Taylor, 2019), but unexplored. Calcite and siderite has also been found together in ancient wetland deposits (Kantorowicz, 1985; Ufnar et al., 2004; Weibel et al., 2016), and may reflect fluctuations of sources of brackish and marine water, instead of those interpretations being solely attributed to siderite composition. The presence of pyrite and calcite in sphaerosiderites from modern and ancient wetlands suggests a commonality in biogeochemical processes within wetlands through the Phanerozoic which needs to be explored and considered more in deep-time palaeoenvironmental reconstructions. It is therefore important for sphaerosiderite studies to consider the complexities that may have been present within ancient wetlands by thoroughly assessing mineralogy and petrography of the sphaerosiderites, and contextualizing these data alongside sedimentological interpretations. Relying on only the elemental variations within

a concretion does not necessarily provide the broad understanding of how an ancient wetland system was operating at the time of deposition. An approach covering multiple aspects such as petrography, elemental composition, mineralogy and sedimentology is likely to provide new insights into natural variability within ancient wetlands, and into important dynamic paleoenvironmental conditions that likely existed in wetlands through the Phanerozoic.

5 Conclusions

Sphaerosiderites are a complex palaeoenvironmental recorder but provide a useful tool for understanding ancient palaeoenvironmental and paleoclimatic changes. The Wealden Supergroup (Berriasian–Hauterivian) contains multiple well preserved sphaerosiderite horizons which show a variety of morphologies and compositions. Importantly, the morphology, elemental composition, and pattern of element uptake within sphaerosiderites from the same horizons are similar, suggesting the textural and elemental changes recorded are influenced by the evolution of pore waters within that horizon. The sphaerosiderites from most horizons were found to be > 90 mol% siderite, but enrichments of Mn, Mg, and Ca can range from 0–15 mol% in individual points on transects, and on average up to 5 mol% across spheres. Generally, the substitutions cause a negative correlation between Fe and the minor cations, but this is not always straightforward to interpret as there is also some interplay between the minor cations in their elemental distribution. The elemental distribution is likely influenced by a complex range of factors such as pH, temperature, pCO_2, and saturation. The compositional heterogeneity within sphaerosiderites suggests they may have been growing close enough to the soil surface to record physiochemical changes of pore waters. Although in a few cases extensive substitution of minor cations are notable, in most cases, siderite was verifiable by XRD, and lack of diagenetic alteration textures with Mg substitution suggest the siderites were not produced from recrystallisation and/or post-burial overgrowths. The elemental and morphological compositions align with the

sedimentological evidence from the Weald Basin suggesting the wetland system was a variable and dynamic environment with humid conditions and frequent storms and groundwater recharging (Allen et al., 1998; Haywood et al., 2004). Minor amounts of pyrite (< 1 wt%) are also included within sphaerosiderites, as a result of limited sulphate reduction in freshwater settings, likely controlled by the spatial distribution of labile organic matter particles. The presence of calcite in two horizons, dissolution textures within a few horizons, and regional recrystallisation of the Wadhurst Clay sphaerosiderites have been tentatively interpreted as indicating periods of marine or brackish influence within the basin. However, compared to other reported sphaerosiderites which contain recrystallisation (Pye et al., 1990; Ufnar et al., 2004), the Wealden sphaerosiderites were further from the coastline. Most sphaerosiderite horizons in the Wealden Supergroup are well preserved, and carbonate cementation is absent, indicating a lack of post burial diagenesis. The preserved primary texture in Wealden sphaerosiderite horizons make them an ideal record for reconstructing palaeohydrology during the Early Cretaceous.

Chapter 5

Palaeohydrology of the Early Cretaceous Wealden Supergroup in the Weald Basin

1 Introduction

The Weald Basin provides an ideal target for generating an Early Cretaceous record of terrestrial palaeohydrology as it contains abundant sphaerosiderite horizons. As reviewed in Chapter 1, sphaerosiderites have been shown to preserve a locally invariant $\delta^{18}O_{siderite}$ and a variant $\delta^{13}C_{siderite}$ during their growth in waterlogged soils (Mozley and Wersin, 1992; Ludvigson et al., 1998; Ufnar et al., 2004b; Ludvigson et al., 2013). The locally invariant $\delta^{18}O_{siderite}$ is thought to reflect meteoric groundwater, in turn influenced by local hydrology.

Cretaceous palaeohydrological studies have focused mainly on North American sphaerosiderites of Albian–Cenomanian age (White et al., 2001; Ufnar et al., 2002; Ufnar et al., 2004a; Suarez et al., 2009; Suarez et al., 2011; Ross et al., 2017), with only one study on the earliest Cretaceous (Robinson et al., 2010). Robinson et al., (2010) presented results from a small number of samples taken from the Late Berriasian–Early Valanginian age 'Fairlight clays' of the Ashdown Formation in the UK (part of the Wealden Supergroup) (Robinson et al., 2010). The Albian North American sphaerosiderites suggest a steep latitudinal gradient in $\delta^{18}O_{siderite}$ existed in the Early Cretaceous, interpreted to be caused by an increased storm frequency at mid-latitudes, causing the $\delta^{18}O_{groundwater}$ to become isotopically light towards the poles (Ufnar et al., 2004a; Suarez et al., 2011). Although the $\delta^{18}O_{siderite}$ values from the Fairlight Clays compare favourably with the Albian $\delta^{18}O_{siderite}$ North American data at the

same palaeolatitude, it is unclear whether similar, relatively constant, low-latitude $\delta^{18}O_{siderite}$ persisted from the Berriasian to the Albian.

To bridge the gap between the existing datasets, this chapter presents $\delta^{18}O_{siderite}$ from sphaerosiderite horizons throughout the Wealden Supergroup, across three formations (Ashdown, Wadhurst Clay, and Tunbridge Wells Sand), to reconstruct hydrological changes across the Valanginian.

2 Methods

2.1 Sample selection and stable-isotope analyses

Sphaerosiderites were chosen for palaeoclimatic studies based on purity (> 90 mol% $FeCO_3$) and preservation of primary fabric (detailed in Chapter 4). Due to limited time and resources, samples were chosen from the suitable sphaerosiderite horizons to maximise stratigraphic resolution through the Tunbridge Wells Sand, Wadhurst Clay, and Ashdown formations. The samples analysed for stable isotopes are shown in Figure 5.1, with those in blue were found to be suitable for palaeoclimatic reconstruction based on the characterisation in Chapter 4 and the isotope analyses presented in this chapter. This figure provides a reference for the results and discussion sections of this chapter. The stratigraphic correlation between the samples from this study and those of Robinson et al., (2010) are also presented in Figure 5.1, and are based on the depth of the Lee Ness Sandstone identified within the Fairlight borehole.

A 1–2cm piece of hand specimen from each sphaerosiderite horizon was immersed in De-Ionised (DI) water within a petri dish, which softened the matrix and exposed the sphaerosiderites. Spheres were picked using tweezers and air dried for a few minutes on a petri dish.

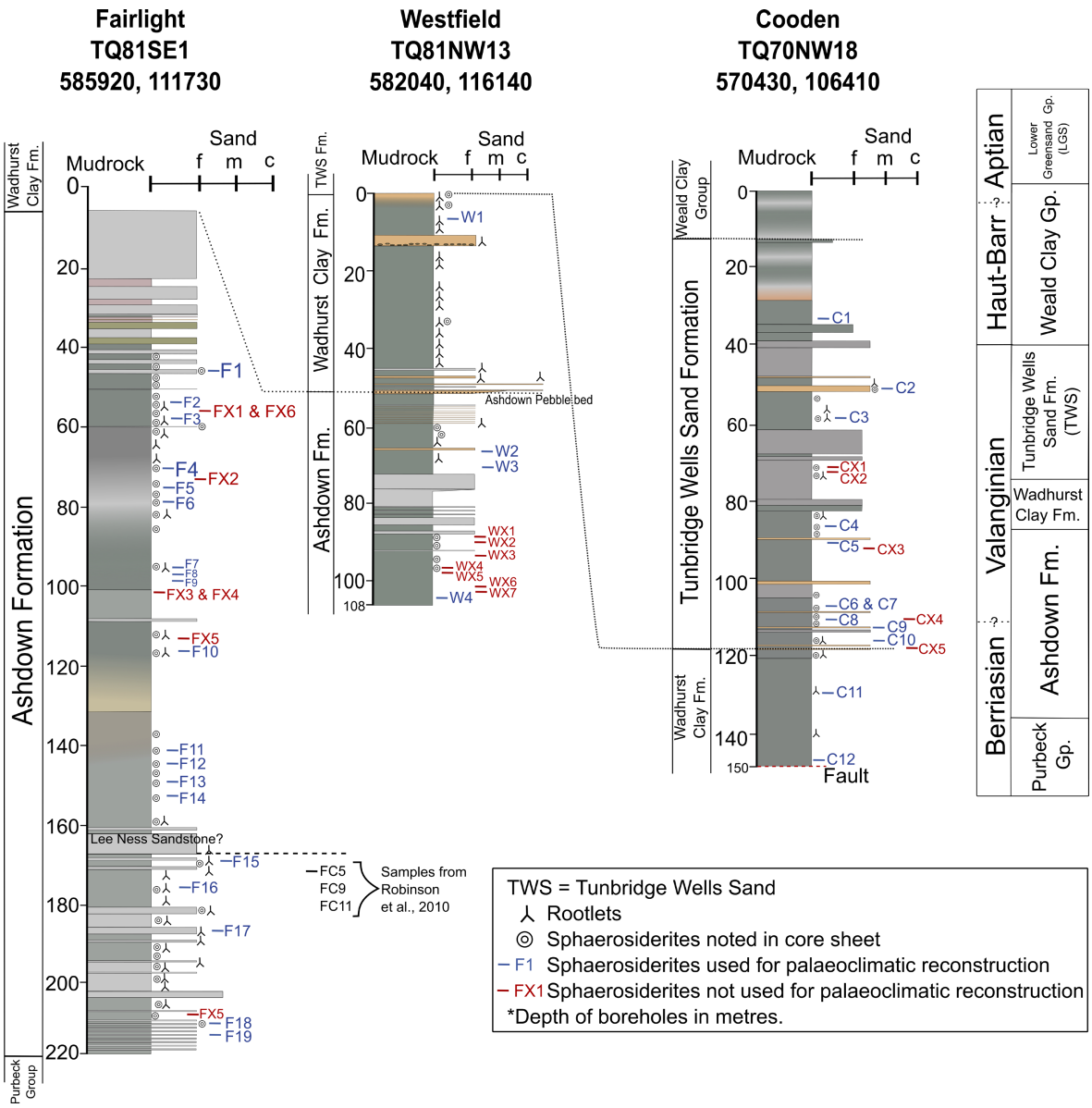


Figure 5.1: Sphaerosiderites sampled for stable isotope analyses. In blue are the sphaerosiderite samples deemed suitable for palaeoclimatic analyses. In red are the sphaerosiderites samples deemed unsuitable for palaeoclimatic reconstruction based on preservation (Figure presented first in Chapter 4, Figure 4.1).

Due to the lack of an internationally agreed siderite standard for stable C and O isotopes, and differences in analytical methods between studies, comparisons between $\delta^{18}O_{siderite}$ can be difficult. However, no significant variation in $\delta^{13}C_{siderite}$ is expected between techniques as it is unaffected by acid fractionation differences. Most of the data presented here were generated in Oxford using a closed digestion system (GasBench). To assess the external

reproducibility of these measurements, representative samples were also analysed in two other laboratories using different techniques (Eidgenössische Technische Hochschule, Zurich (ETH) and the University of Edinburgh). The conventional gas source Isotope Ratio Mass Spectrometry (IRMS) methods and corrections used in Oxford and ETH Zurich are described below; the use of Secondary Ion Mass Spectrometry (SIMS) at Edinburgh is described in Section 2.2.

At Oxford, sphaerosiderites from the same horizon were crushed together in an agate mortar and pestle to produce the 150–170 µg of siderite required for stable isotope analysis. The number of spheres in each analysis ranged from 5–30, depending on siderite content within spheres (verified through XRD mineral quantification, Chapter 4, Appendix C.1.1), and sphere size. 5–6 analyses were conducted for each sphaerosiderite horizon to assess the natural variability in $\delta^{18}O_{siderite}$ and $\delta^{13}C_{siderite}$. The siderite powder was placed in a glass exetainer and sealed using a plastic cap with a septum within a *Gasbench II* device connected to a ThermoFinnegan *Delta V* isotope ratio mass spectrometer, in the Department of Earth Sciences at Oxford. After injection of phosphoric acid, the sample was left to digest at 72ºC for 24 hours (Fernandez et al., 2016) to ensure complete digestion. The analysed $\delta^{18}O_{siderite}$ data was corrected for phosphoric acid fractionation using a method-specific fractionation factor, which at 72ºC, was calculated as 1.00964 (Fernandez et al., 2016). Calcite standards NBS-18, NBS-19, and NOCZ were used for every run and had a reproducibility of better than ±0.12‰ (1σ) for oxygen isotope, and ±0.07‰ (1σ) for carbon isotope analyses from 27 replicates in total.

The samples C9, C5, F5, F11 (Weald Basin – this study), and FC5, FC9, and FC11 (also Weald Basin, Robinson et al., 2010) were analysed at ETH, Zurich for stable isotope and clumped isotope (Section 2.3) measurements. The Weald Basin samples were chosen based upon their purity, size, and stratigraphic position within a long-term fluctuating

$\delta^{18}O_{siderite}$ trend noted from conventional IRMS analyses at Oxford. The FC samples from Robinson et al., (2010) were chosen to allow comparison between a previously published stable isotope dataset, particularly as the differences in siderite-acid fractionation factors between digestion methods are now better constrained (Fernandez et al., 2016). As a high number of replicates are required for clumped isotope measurements (detailed in Section 2.3), the siderite powders were prepared in a larger batch than at Oxford. 50–150 spheres were picked from each sample (depending on weight) to provide 50–60 mg of powder for 20–40 replicate analyses. 120–200 μg of siderite was reacted with phosphoric acid at 115ºC in a glass exetainer with a modified heating device within a *Kiel IV* device for 75 minutes in the Climate Geology Stable Isotope laboratory, Department of Earth Sciences, ETH Zurich, following the methods of Müller et al., (2017) and Bernasconi et al., (2018). The evolved CO_2 was purified through a Porapak® resin trap at –40ºC (Meckler et al., 2014; Müller et al., 2017) before analysis in a ThermoFinnegan *MAT253* isotope ratio mass spectrometer. Due to the long reaction and transfer times, each analysis was manually conducted and took 3–4 hours, thereby limiting the total number of samples that could be analysed in this project. ETH in-house calcite standards were analysed every evening at 70ºC for data correction and standardization. Accuracy and precision were maintained using a Carrarra Marble (MS2) standard at 70ºC. $\delta^{18}O_{siderite}$ and $\delta^{13}C_{siderite}$ were calculated to a VPDB scale using four previously calculated ETH standards via repeated measurements of international standards (NBS-19, NBS-18, and LVSEC) (Bernasconi et al., 2018).

A homogenised pure siderite powder sample from the Ivigtut cryolite deposit from Greenland was obtained from the British Geological Survey (BGS) was analysed after every 5–6 samples at Oxford. The $\delta^{18}O_{siderite}$ value for this siderite, referred to as BGS Ivigtut, ranged between –22.56‰ to –23.22‰ over three years, with an average value of –22.88‰ ±0.15 (1σ). At ETH, a single analysis of the BGS Ivigtut gave a $\delta^{18}O_{siderite}$ value of –23.00‰, within error of Oxford's long-term Ivigtut average of –22.88‰ ±0.15 (1σ). In both cases,

the $\delta^{18}O_{siderite}$ was corrected using method-specific fractionation factors from Fernandez et al., (2016). ETH also has four internal standards; ES, LT, Four, and IG (a siderite sample from an Ivigtut cryolite sample from ETH, Zurich Museum) previously reported in Fernandez et al., (2016). These siderite standards were also analysed at Oxford (Table 5.1). The $\delta^{18}O_{siderite}$ values measured at Oxford for ES, FOUR, and LT were slightly higher than measurements at ETH (0.15–0.26‰). All the offsets between Oxford and ETH measurements of these siderite standards were much less than the range of observed variability in natural siderite samples (tenths of a ‰ versus several ‰; Ludvigson et al., 1998; Ufnar et al., 2004b) and suggests good external reproducibility between laboratories.

Siderite Standards Fernandez et al.,(2016)	$\delta^{18}O_{siderite}$ (‰ VPDB) ETH	1σ	Replicates ETH	$\delta^{18}O_{siderite}$ (‰ VPDB) Oxford	1σ	Replicates Oxford	Difference (‰ VPDB)
ES	–13.71	0.22	12	–13.14	0.4	3	0.15
FOUR	–16.41	0.13	16	–15.81	0.7	3	0.26
IG	–23.07	0.29	22	–23.41	0.2	3	0.34
LT	–16.44	0.15	22	–15.77	0.0	3	0.19

Table 5.1: $\delta^{18}O_{siderite}$ from ETH and Oxford for four natural siderite samples used as internal standards at ETH and reported in Fernandez et al., (2016). Conversion from VPDB to VSMOW of values reported in Fernandez et al., (2016) are based on equations in Sharp (2017).

2.2 SIMS (Secondary Ion Mass Spectrometry) transects

Sphaerosiderites from Fairlight Clay samples FC5, FC9, and FC11 (described in Robinson et al., 2010) were analysed using a *Cameca IMS 1270* at the NERC (Natural Environment Research Council) facility at University of Edinburgh to produce $\delta^{18}O_{siderite}$ and $\delta^{13}C_{siderite}$ transects. Spheres were picked using the method outlined in Section 2.1, air dried, and set in resin before being polished using up to 500 nm grade diamond pads. 3 samples from a batch of Ivigtut siderite provided by NERC at University of Edinburgh were set in the resin round with the Wealden samples. Note this aliquot of Ivigtut siderite from Edinburgh is not the same as the one supplied by the BGS. The Ivigtut siderite was analysed

alongside the samples and used to correct the sphaerosiderite values, based on the NERC facility's own measurements of Ivigtut and the Oxford long-term average values. The precision for carbon was ±0.3‰ (1σ), and for oxygen ±0.6‰ (1σ), based on 15 point analyses on each 3 Ivigtut samples.

2.3 Clumped isotope thermometry (Δ_{47})

Clumped isotope analysis was used to measure the formation temperatures of the samples chosen for analysis at ETH (Section 2.1). Clumped isotope thermometry (Δ_{47}) has been widely used for analysing formation temperatures of pedogenic siderite and calcite (Ghosh et al., 2007; Quade et al., 2013; Snell et al., 2013; Came et al., 2014; Fernandez et al., 2014; Van Dijk et al., 2019). This method relates the growth temperature of a carbonate mineral to the abundance of $^{13}C–^{18}O$ bonds relative to a stochastic distribution (Ghosh et al., 2007). Unlike traditional oxygen-isotope palaeothermometry, this method does not rely on the oxygen isotope composition of the solution from which carbonate growth is occurring. Clumped isotope analyses can provide an accurate temperature estimate as long the carbonate has not undergone diagenetic recrystallization, or experienced solid state reordering of $^{13}C–^{18}O$ bonds at elevated burial temperatures (Passey and Henkes, 2012; Henkes et al., 2014). Although experimental studies indicate that the slope of clumped isotope calibrations for various carbonates are indistinguishable (Kelson et al., 2017; Peral et al., 2018; Staudigel et al., 2018), the intercept is likely to vary due to the differences in acid fractionation factors, and may have temperature sensitivities (Müller et al., 2017). The most recent siderite-specific calibration from Van Dijk et al., (2019) encompassing low temperatures (8–62˚C) is given below.

$$\Delta_{47} = 0.0428(\pm0.002) * 10^6/T^2 + 0.0683(\pm0.023) \text{ [± 95\% CL, T in ˚Kelvin] } R^2 = 0.92$$

Samples powders were prepared for Δ_{47} analyses using the method specified in Section 2.1, and measured using a *Kiel IV* device and a *MAT253* mass spectrometer at ETH Zurich

(Section 2.1). Up to 20 replicates can be required to produce a mean and usable standard deviation, thereby limiting the total number of samples that could be analysed for Δ_{47} in this thesis. For data standardization and correction, internal calcite standards were analysed at 70°C overnight using 15–17 automated measurements. The reproducibility of four internal standards was 0.030‰ based on 500 measurements. External reproducibility was determined using a Cararra Marble (MS2) sample analysed at 115˚C, with a long-term reproducibility of 0.030‰ (±1σ, n=50). The data correction protocol used is the same as in Van Dijk et al., (2019) and Bernasconi et al., (2018).

3 Results

3.1 Stable Isotopes

The average $\delta^{18}O_{siderite}$ value (Table 5.2) for each formation sampled is calculated from the means of sphaerosiderite horizons within that formation. This is to prevent the overall mean being biased towards horizons which contain a higher number of analyses. The average $\delta^{18}O_{siderite}$ values from the Tunbridge Wells Sand and Ashdown (–1.040‰ and –1.078‰ respectively) are similar, while the average $\delta^{18}O_{siderite}$ value from the Wadhurst Clay is isotopically heavier (–0.706‰), but within the variability in $\delta^{18}O_{siderite}$ values of the other two formations. The Ashdown Formation is the thickest formation, with highest number of suitable sphaerosiderite horizons for stable isotope analyses, and the highest standard deviation of $\delta^{18}O_{siderite}$ values (±1.26‰). By comparison, the Tunbridge Wells Sand and the Wadhurst Clay have lower standard deviations but also fewer suitable sphaerosiderite horizons.

The average $\delta^{13}C_{siderite}$ values are calculated in the same way as the $\delta^{18}O_{siderite}$ values, and show that horizons within the same formations have a large range of $\delta^{13}C_{siderite}$ values. For instance, although the mean of Ashdown and Tunbridge Wells Sand are similar (

Table 5.2), the standard deviation within each formation of the means of horizons is approximately ±8‰. The Wadhurst Clay average $\delta^{13}C_{siderite}$ value is higher than the other two formations with a comparatively low standard deviation, but is based on only four horizons.

Formation	Mean of the average of horizons (‰, VPDB), ±1σ		Sphaerosiderite Horizons
	$\delta^{18}O_{siderite}$	$\delta^{13}C_{siderite}$	
Tunbridge Wells Sand	–1.04 ± 0.93	–18.25 ± 8.53	10
Wadhurst Clay	–0.70 ± 0.93	–11.31 ± 0.68	4
Ashdown	–1.08 ± 1.26	–16.86 ± 8.20	20

Table 5.2: Mean δ18Osiderite and δ13Csiderite value of the average of each sphaerosiderite horizons assessed in each formation within the Wealden Supergroup. Standard deviation is of the means of horizons from each formation. Data generated by GasBench IRMS in Oxford.

The majority of sphaerosiderite horizons have relatively invariant $\delta^{18}O_{siderite}$ values and variant $\delta^{13}C_{siderite}$ values when plotted in carbon-oxygen space (Figure 5.2), producing the linear trends known as Meteoric Sphaerosiderite Lines (MSL's; Ludvigson et al., 1998). The average $\delta^{18}O_{siderite}$ values of individual MSLs vary from 0.6‰ to –3.5‰. 35 of the 40 sphaerosiderite horizons have a $\delta^{18}O_{siderite}$ standard deviation of < 0.6‰. Average $\delta^{13}C_{siderite}$ values ranged from c. +2‰ to c. –40‰ and standard deviation in individual horizons can be up to ±1‰, while the range within individual horizons can be up to 5‰ (Figure 5.2).

Samples that don't exhibit MSL's fall into two categories. Some samples, such as CX1 from the Tunbridge Wells Sand, show a positive relationship between $\delta^{18}O_{siderite}$ and $\delta^{13}C_{siderite}$ values (Figure 5.3). Alternately, 66970F and 66962F from the Ashdown Formation, and CX2 from the Tunbridge Wells Sand Formation, show a negative relationship between $\delta^{18}O_{siderite}$ and $\delta^{13}C_{siderite}$ values (Figure 5.3).These samples deviating from MSL trends were not considered suitable for reconstructions of palaeohydrology, but their paleoenvironmental implications are discussed further in Section 4.2.

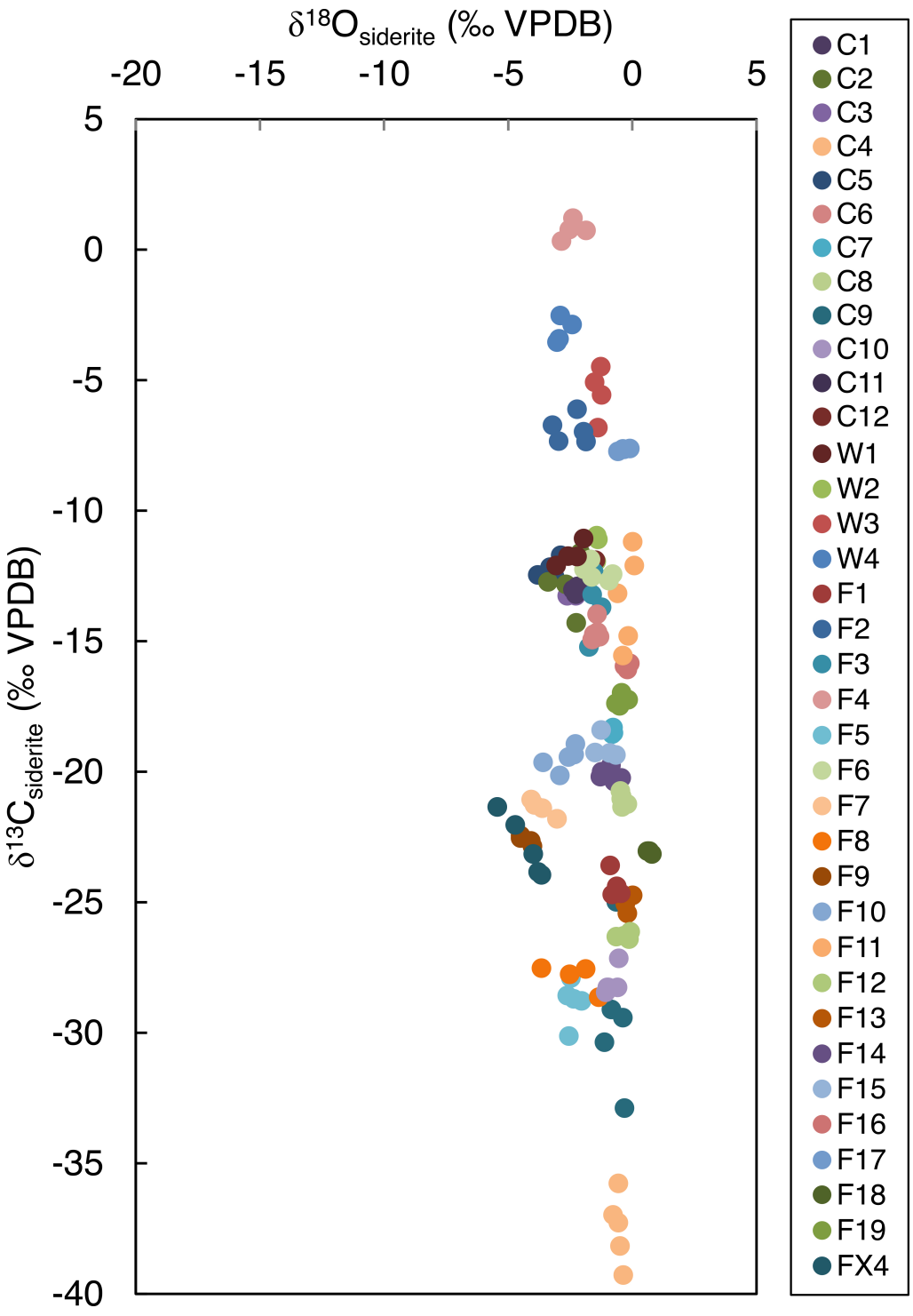


Figure 5.2: Invariant $\delta^{18}O_{siderite}$ and variant $\delta^{13}C_{siderite}$ of sphaerosiderites from the Wealden Supergroup. Spheres from the same horizon plot along these linear trends known as Meteoric Sphaerosiderite Lines (MSL's), suggesting they are recording a local $\delta^{18}O_{groundwater}$ signal, thought to be reflective of the meteoric groundwater in the waterlogged soils in which they are growing. Data generated by GasBench IRMS in Oxford.

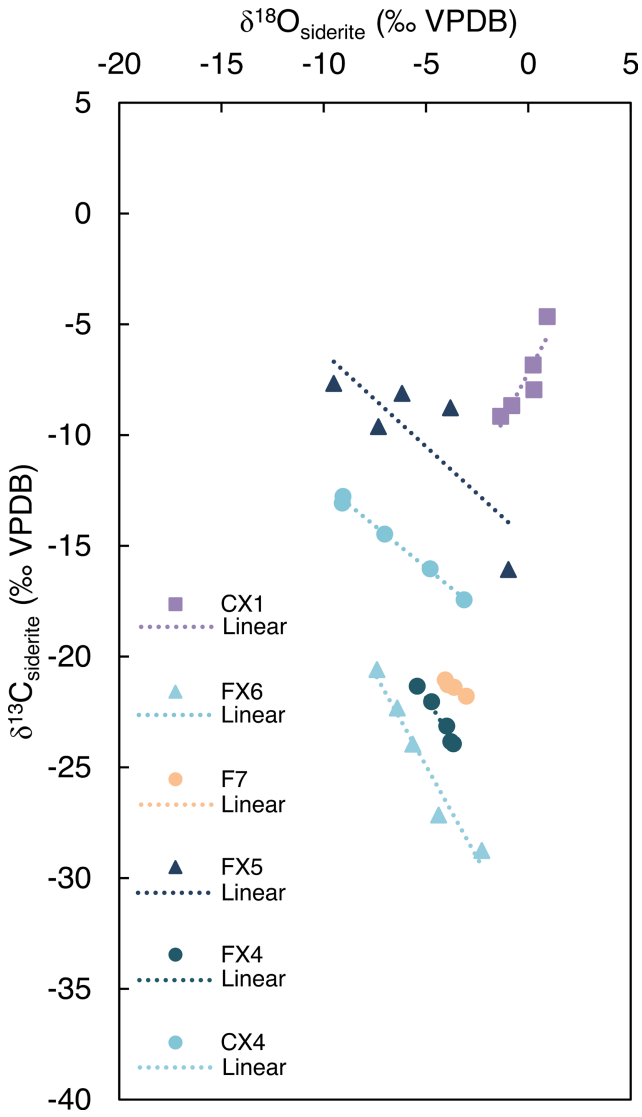


Figure 5.3: Stable isotope data from sphaerosiderite horizons that do not exhibit Meteoric Sphaerosiderite Lines. Data generated by GasBench IRMS in Oxford.

The average $\delta^{18}O_{siderite}$ value of the MSLs of individual horizons alternates between heavier and lighter values through the stratigraphy (Figure 5.4). $\delta^{18}O_{siderite}$ values are isotopically heavy in the lower Ashdown Formation (0–0.5‰). The $\delta^{18}O_{siderite}$ value decreases to c. –3‰ by the middle of the Ashdown Formation, and returns to c. –1‰ by the top of the Ashdown Formation. The $\delta^{18}O_{siderite}$ values at the top of the Ashdown Formation are similar between Fairlight and Westfield boreholes, suggesting the sphaerosiderites preserve a regional signal. Sphaerosiderites in the Wadhurst Clay were recrystallized in both Cooden and Westfield boreholes (detailed in Chapter 4), with $\delta^{18}O_{siderite}$ values ranging from

c. –2.5‰ to c. –0.4‰. In the Tunbridge Wells Sand, the $\delta^{18}O_{siderite}$ values are isotopically heavier (–0.84‰ to –0.39‰) at the base of the formation, and similar to $\delta^{18}O_{siderite}$ values of sphaerosiderites in the top 20m of the Ashdown Formation. $\delta^{18}O_{siderite}$ values in the Tunbridge Wells Sand gradually trend up-section to a value of –2.6‰ to the top of the formation.

The $\delta^{18}O_{siderite}$ analysed at ETH are also plotted in Figure 5.4 alongside the $\delta^{18}O_{siderite}$ measurements from Oxford. The $\delta^{18}O_{siderite}$ value is generally consistently lighter in measurements from ETH compared to Oxford by up to 1.37‰, although for most samples the difference is < 0.7‰ (Table 5.3), and within error of the Oxford $\delta^{18}O_{siderite}$ measurements. As the $\delta^{18}O_{siderite}$ values of standards analysed at ETH and Oxford were consistently similar (Section 2.1), the offset between $\delta^{18}O_{siderite}$ of natural Wealden samples between ETH and Oxford could be arising from differences in sample powder preparation. As discussed in Section 2.1, analysis of the powder prepared for ETH would produce average $\delta^{18}O_{siderite}$ encompassing a higher number of spheres than the smaller batches of powder produced for analysis at Oxford. By contrast, the $\delta^{13}C_{siderite}$ values between ETH and Oxford are consistently similar and within error, apart from in sample FC11 (Table 5.3). The $\delta^{13}C_{siderite}$ measurements in Oxford have a much higher standard deviation usually, up to 3‰, compared to 0.76‰ at ETH. This supports the suggestion that the size of the batch of the sample powders (large batch is more homogenous) produce more homogeneous measurements such as at ETH. However, the Oxford sample preparation method is the conventional method used in literature to produce MSL's (Robinson et al., 2010; Ludvigson et al., 2013) and is more likely to show the variability in $\delta^{18}O_{siderite}$ within sphaerosiderite horizons, and trends deviating from MSL's. As the differences between $\delta^{18}O_{siderite}$ at ETH and Oxford were for the most part, smaller than natural variability within horizons, the $\delta^{18}O_{siderite}$ measured at Oxford is used for palaeohydrological interpretations to maintain consistency. Further implications of sample powder preparation are discussed in Section 3.3.

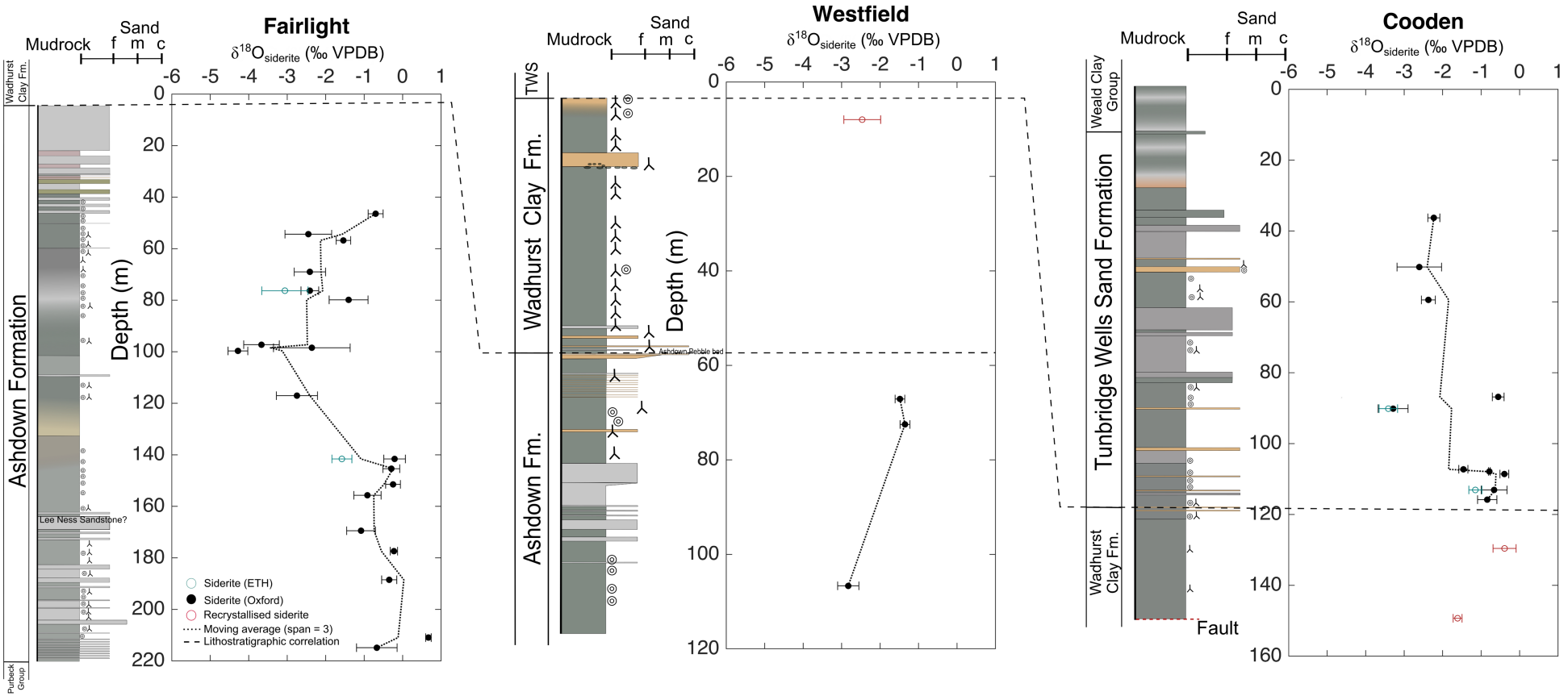


Figure 5.4: Average $\delta^{18}O_{siderite}$ values of MSL horizons in the Ashdown, Wadhurst Clay and Tunbridge Wells Sand Formations. $\delta^{18}O_{siderite}$ values alternate between isotopically heavy and light values and are decoupled from lithological changes.

Sample	Oxford				ETH			Difference
	Borehole, Depth (m)	$\delta^{18}O_{siderite}$ (‰ VPDB)	$\delta^{13}C_{siderite}$ (‰ VPDB)	Replicates	$\delta^{18}O_{siderite}$ (‰ VPDB)	$\delta^{13}C_{siderite}$ (‰ VPDB)	Replicates	$\delta^{18}O_{siderite}$ (‰ VPDB)
C9	Cooden. 113.1m	–0.66 ± 0.33	–29.40 ± 2.86	5	–1.15 ± 0.17	–28.27 ± 0.19	16	0.49
F5	Fairlight, 76.3m	–2.41 ± 0.23	–28.81 ± 0.81	5	–3.06 ± 0.60	–28.62 ± 0.34	12	0.65
F11	Fairlight, 141.6m	–0.21 ± 0.28	–13.36 ± 1.82	6	–1.58 ± 0.26	–16.58 ± 0.76	17	1.37
C5	Cooden, 91.1m	–3.29 ± 0.39	–12.21 ± 0.37	5	–3.41 ± 0.24	–11.87 ± 0.15	3	0.12
FC05	Fairlight Clays, Robinson et al., (2010)	–1.70 ± 0.30	–8.57 ± 1.82	2	–2.52 ± 0.12	–11.62 ± 0.25	9	0.71
FC09	Fairlight Clays, Robinson et al., (2010)	–2.41 ± 0.45	–10.22 ± 0.71	2	–3.46 ± 0.24	–11.95 ± 0.17	17	1.05
FC11	Fairlight Clays, Robinson et al., (2010)	–1.69 ± 0.35	–18.43 ± 0.50	1	–2.3 ± 0.25	–15.30 ± 0.32	17	0.61

Table 5.3: $\delta^{18}O_{siderite}$ of representative Wealden sphaerosiderites analysed at ETH and Oxford using respective sample powder preparation methods discussed in Section 2.1 (Depths in stratigraphy shown in Figure 5.1). Most of the samples have a $\delta^{18}O_{siderite}$ offset within natural variability of $\delta^{18}O_{siderite}$ observed in natural siderites. The samples which are not within error of $\delta^{18}O_{siderite}$ values (from different methods) of each other are highlighted in grey.

Figure 5.5 shows the ETH and Oxford measurements in a carbon-oxygen plot. For samples C9, C5, F5, and FC11, either the data from both ETH and Oxford cluster together, or the ETH data plots close together and within the spread of the Oxford data. In the cases of FC5, FC9, and F11, the Oxford data has lighter $\delta^{13}C_{siderite}$ and $\delta^{18}O_{siderite}$ values than the measurements at ETH.

Figure 5.6 shows individual carbon-oxygen plots of each of the samples presented in Figure 5.5. Along with this, the mean of the ETH measurements, mean of Oxford measurements, and the Oxford-ETH combined mean are presented with 1σ. They generally show the mean $\delta^{18}O_{siderite}$ value analysed at Oxford to be isotopically heavier, although in half the samples, also within error of the ETH $\delta^{18}O_{siderite}$ mean.

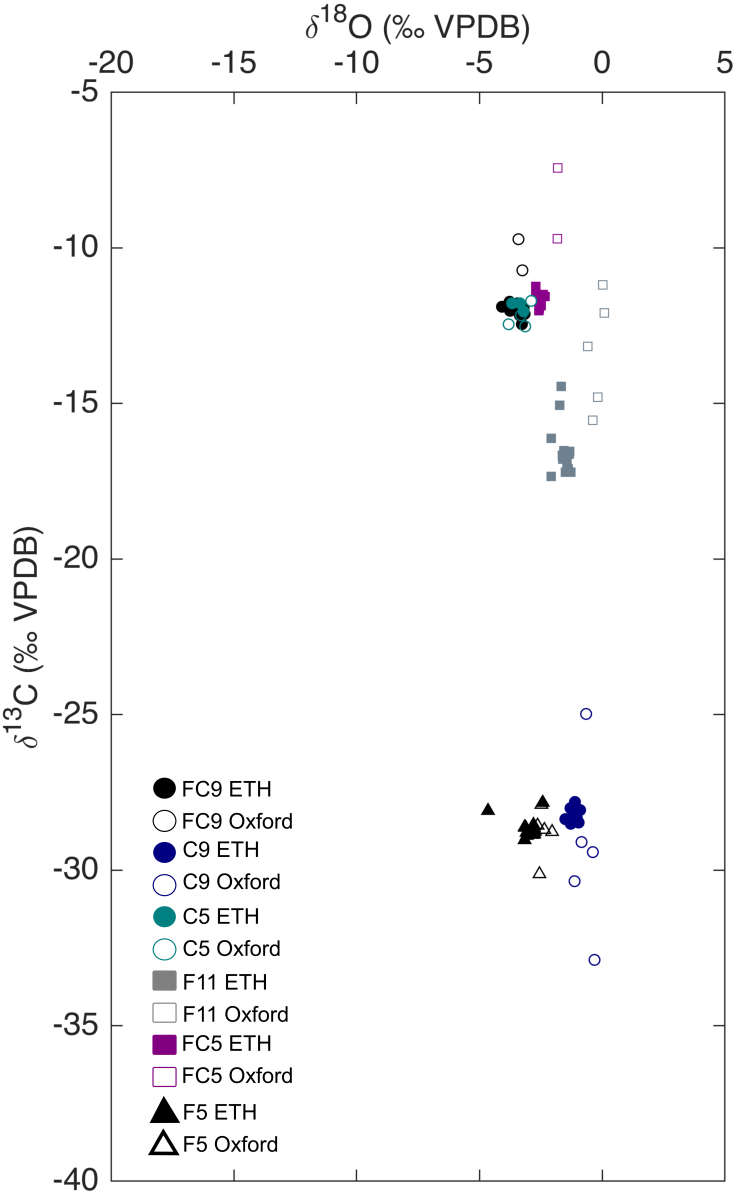


Figure 5.5: Carbon-Oxygen plot of siderite samples from this thesis (C5, C9, F5, F11) and from Robinson et al., (2010) (FC5,9 and 11) analysed at ETH and Oxford.

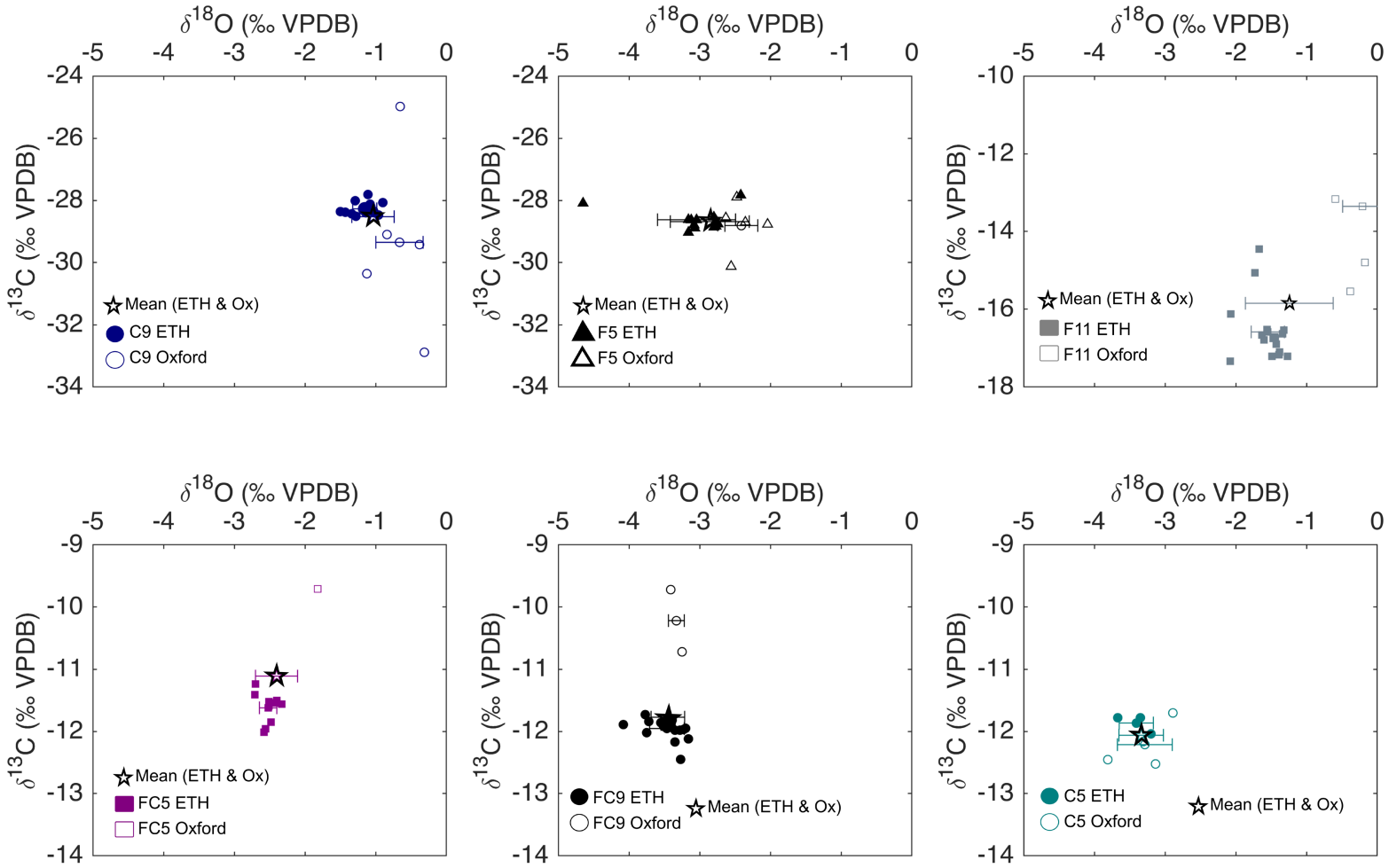


Figure 5.6: Average value from measurements at ETH, Oxford, and ETH-Oxford combined for samples from this thesis (C5, C9, F5, F11) and from Robinson et al., (2010) (FC5,9 and 11).

3.2 $\delta^{18}O_{siderite}$ transects (SIMS)

For SIMS analysis, samples FC5, FC9, and FC11 from the Fairlight Clays (Ashdown Formation) were analysed (Figures 5.6, 5.7, and Appendix D.1.2). Conventionally measured $\delta^{13}C_{siderite}$ and $\delta^{18}O_{siderite}$ values for these samples have been previously reported in Robinson et al., (2010). $\delta^{13}C_{siderite}$ transects generated by SIMS show a common pattern amongst all spheres analysed; a core with relatively isotopically light $\delta^{13}C_{siderite}$ (–20‰ to –35‰), and a gradual trend to isotopically heavier values towards to the rim (–1‰ to –10‰) (Figure 5.7, 5.7).

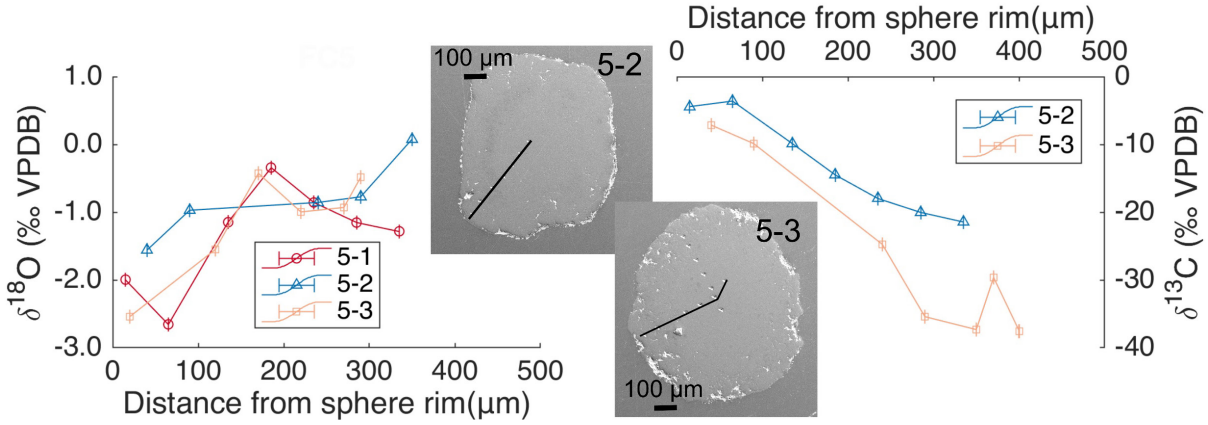


Figure 5.7: Stable isotope transects and representative backscatter images of two sphaerosiderite nodules (5-2 and 5-3) from FC5, one of three sphaerosiderite horizons sampled from the Fairlight Clays (Ashdown Formation) from Robinson et al., (2010). Data generated by SIMS, Edinburgh.

The spheres from FC5 all have similar $\delta^{18}O_{siderite}$; 0‰ to –1‰ in the core, decreasing to –1‰ to –3‰ in the rim (Figure 5.7). In FC9, $\delta^{18}O_{siderite}$ of the cores are similar, between 0.5‰ and –1‰, but vary between –1‰ to –7.5‰ at the rim (Appendix D.1.2). The trend of $\delta^{18}O_{siderite}$ from core to rim seen in FC9 and FC5 is less clear in FC11 (Figure 5.8), which has noisier $\delta^{18}O_{siderite}$ transects. The average values from the transects are given in

Table 5.4. Each sample has an average $\delta^{18}O_{siderite}$ and $\delta^{13}C_{siderite}$ that is within 1σ of the other samples. Average $\delta^{18}O_{siderite}$ values from SIMS are up to 0.92‰ heavier compared to $\delta^{18}O_{siderite}$ analysed using conventional IRMS at Oxford or ETH, which could be due to the poor understanding of matrix corrections required during SIMS analyses, as substitution of cations within the siderite matrix changes the correction factors required for measured $\delta^{18}O_{siderite}$ values (Rollion-Bard and Marin-Carbonne, 2011).

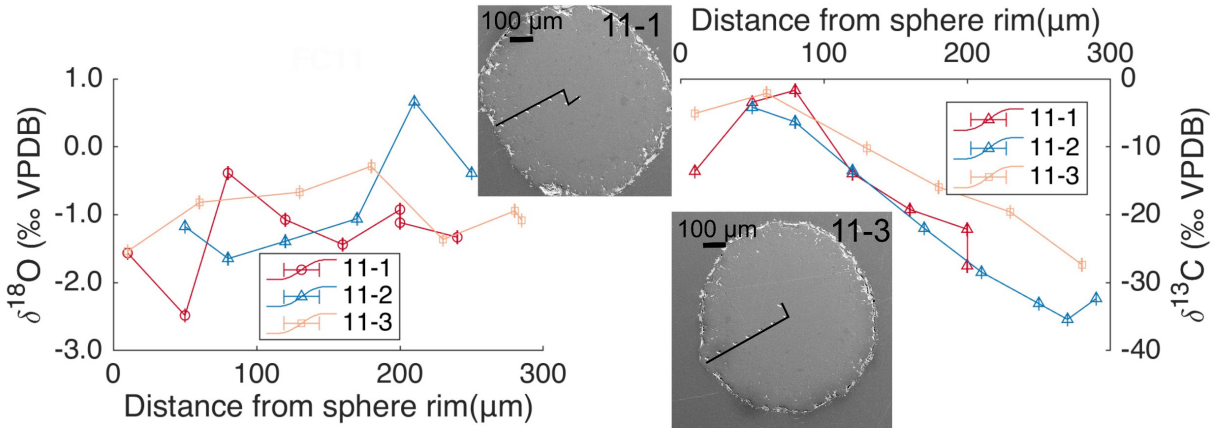


Figure 5.8: Stable isotope transects and representative backscatter images of two sphaerosiderite nodules (11-1 and 11-2) from FC11 (Robinson et al., 2010) showing a noisy $\delta^{18}O$ transect, but the $\delta^{13}C$ transect trends are similar to those noted in FC5 and FC9. Data generated by SIMS, Edinburgh.

Sample	$\delta^{18}O_{siderite}$ (‰ VPDB), ±1σ	$\delta^{13}C_{siderite}$ (‰ VPDB) , ±1σ	Replicates
FC5	–1.10 ±0.25	–19.53 ±9.07	3
FC9	–1.72 ±0.70	–17.18 ±3.76	4
FC11	–1.03 ±0.24	–16.16 ±4.63	3

Table 5.4: Average stable isotope compositions from SIMS transects of FC5, FC9, and FC11 (Fairlight Clays samples from Robinson et al., 2010). Data generated by SIMS, Edinburgh.

FC5, FC9, and FC11 are on average > 90 mol% siderite, but have some elemental heterogeneity, particularly in the sphere rims. Elemental transects of representative spheres from FC5 and FC9 show a 3–4 mol% Mg enrichment and 1–2 mol% Ca enrichment in the

core (Figure 5.9), increasing to 10 mol% Mg and 4 mol% Ca at the rim. The FC11 transect is noisier; Mg enrichment varies between 3–6 mol% in the core, increasing to 6–10 mol% at the rim. Ca enrichment in FC11 remains between 0.5–2 mol% throughout the transect.

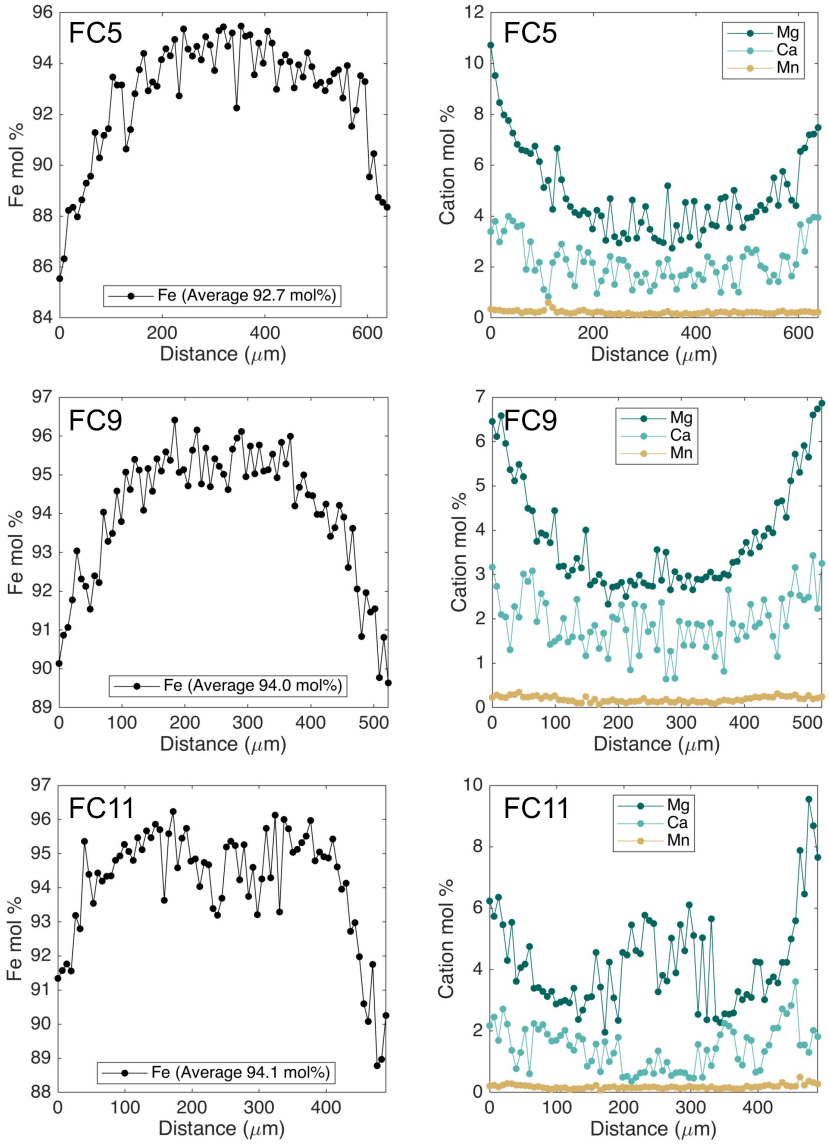


Figure 5.9: Representative elemental composition transects from sphaerosiderite horizons FC5, FC9, and FC11 showing changes in Fe, Mn, Mg, and Ca across spheres.

Although, these spheres used for elemental analyses are not the same ones used for SIMS, the elemental trends were noted in multiple spheres from the same horizon suggesting they are representative of the sphaerosiderite horizons. Therefore, the spheres which were used for SIMS analyses likely contain similar elemental heterogeneity (discussed in Section

4.1) which can lead to uncertainties when correcting $\delta^{18}O_{siderite}$ values (Rollion-Bard and Marin-Carbonne, 2011).

3.3 Measured clumped isotope temperatures (Δ_{47})

FC5, FC9, FC11 (samples from Robinson et al., 2010) from the Ashdown Formation, F11 and F5 from the Ashdown Formation, and C9 from Tunbridge Wells Sand Formation were chosen for Δ_{47} analysis. These samples were chosen based on their stratigraphic positions relative to the overall $\delta^{18}O_{siderite}$ trends through the Wealden Supergroup (Figure 5.3). The Δ_{47} values from FC5, FC9, FC11, F5, and C9 were all statistically indistinguishable from each other (using a t-test at 95% confidence interval) and together produced formation temperatures of 33–39°C (Table 5.5). Sample F11 gave an anomalously high formation temperature of 49°C, significantly different from the other 5 samples, based on a t-test (p-value =0.02).

Sample	Mean Δ_{47} (±1σ)	Temperature (± 95% CI)	Replicates
Ashdown (F5)	0.517 ± 0.027	36˚C ±5	15
Ashdown (FC11)	0.518 ± 0.031	35˚C ±5	17
Ashdown (FC9)	0.525 ± 0.033	33˚C ±5	15
Ashdown (FC5)	0.525 ± 0.015	33˚C ±2	11
Tunbridge Wells Sand (C9)	0.508 ± 0.029	39˚C ±5	16
Ashdown (F11)	0.480 ± 0.036	49˚C ±6	20

Table 5.5: Δ_{47} values and calculated temperatures from representative sphaerosiderite horizons through the Wealden Supergroup. Data generated at ETH.

4 Discussion

4.1 Standardization in siderite measurements

4.1.1 Stable isotope measurements

The lack of global standardisation in siderite stable isotope measurements is an important consideration to assess when comparing between siderite datasets from different sources. Sample digestion methods, reaction times and correction factors vary between laboratories and are not always reported in literature. This creates uncertainty with data comparison as differences in stable isotope analyses could potentially arise from method-specific differences. Four internal standards from ETH (ES, LT, Four, and IG) analysed at both Oxford and ETH by different methods showed good external reproducibility between these two laboratories. However, the natural samples from the Weald Basin show more variability in $\delta^{18}O_{siderite}$ values between ETH and Oxford.

The $\delta^{18}O_{siderite}$ offsets between measurements made of Wealden samples at ETH and Oxford were mostly small (< 0.7‰), and fell within the natural $\delta^{18}O_{siderite}$ variability observed in sphaerosiderite horizons (Section 3.1). The ETH measurements produced an average encompassing more spheres and can be considered more reflective of the average $\delta^{18}O_{siderite}$ in one horizon, but not necessarily reflective of the variability within the horizon. The variability in $\delta^{18}O_{siderite}$ and $\delta^{13}C_{siderite}$ within horizons reflect important palaeoenvironmental information which is lost in the large batch measurements at ETH. As the external reproducibility of standards was good between ETH and Oxford, these $\delta^{18}O_{siderite}$ differences in the natural samples are likely not due to differences in the analytical method. Instead, these offsets could arise from the natural variability in $\delta^{18}O_{siderite}$ within each horizon and the number of spheres analysed in each replicate. The $\delta^{18}O_{siderite}$ offsets between ETH and Oxford suggest that a combination of analysing both smaller and larger batches may be

required to gain a true sense of the natural variability within sphaerosiderite horizons to produce a confident mean of $\delta^{18}O_{siderite}$. However, in the case of the Wealden dataset, the mean $\delta^{18}O_{siderite}$ for horizons analysed at ETH and Oxford are relatively similar, suggesting the number of spheres and replicates measured at Oxford is sufficient in capturing both the Meteoric Sphaerosiderite Lines and the average $\delta^{18}O_{siderite}$ values. Therefore, the long-term $\delta^{18}O_{siderite}$ trend through the stratigraphy is considered valid.

4.1.2 SIMS measurements

The samples FC5, FC9, and FC11 reported in Robinson et al., (2010) are analysed further in this chapter. The FC samples are useful in illustrating the difficulty of interpreting siderite stable isotope data without a globally accepted standard.

SIMS transects consistently show isotopically heavier $\delta^{18}O_{siderite}$ than IRMS measurements at Oxford or ETH, likely due to uncorrected matrix effects from elemental heterogeneity within individual spheres. Mg substitution in calcite has been shown to cause $\delta^{18}O_{calcite}$ measured during SIMS analyses to be lighter than the true $\delta^{18}O_{calcite}$ (Rollion-Bard and Marin-Carbonne, 2011). $\delta^{18}O_{siderite}$ was also shown to be affected by Mg enrichment by Rollin Bard and Marin-Carbonne (2011) but matrix corrections were not quantified due to the lack of a globally accepted siderite standard. However, the lowering of $\delta^{18}O_{calcite}$ values with Mg enrichment seen in calcite, likely also applies to siderite. For instance, in the SIMS transects, the $\delta^{18}O_{siderite}$ values in FC5 and FC9 become lighter towards the rim as Mg enrichment increases, suggesting the lower $\delta^{18}O_{siderite}$ values could be due to the uncertainties in correcting for cation substitutions. The extent to which cation substitution would change the correction factors applicable to siderite oxygen isotope compositions is poorly constrained in literature and merits further work (Rollion-Bard and Marin-Carbonne, 2011). Therefore, the $\delta^{18}O_{siderite}$ values analysed by SIMS cannot be used for quantitative

palaeohydrological reconstructions as they cannot be corrected to produce a comparable value to measurements using IRMS at Oxford and ETH.

The mean $\delta^{18}O_{siderite}$ from SIMS transects are on average, 1–1.5‰ heavier and have higher standard deviations than the mean $\delta^{18}O_{siderite}$ from IRMS measurements of the same sample (Table 5.6). The mean $\delta^{13}C_{siderite}$ from SIMS transects is 2–10‰ lighter and with higher standard deviation than the IRMS measurements. The reasons for these differences could be due to a combination of natural variability in the horizon, and the low number of spheres analysed by SIMS (3 or 4 in each case) compared to by IRMS (> 10 per replicate, typically > 50 per average). It is possible the mean value from SIMS measurements would better reflect the mean from IRMS if additional transects from more spheres were produced to increase sample numbers. Both $\delta^{18}O_{siderite}$ and $\delta^{13}C_{siderite}$ values from SIMS transects are however, within the range of values measured using IRMS from all Wealden sphaerosiderites. Although the artefacts from unconstrained siderite matrix corrections mean $\delta^{18}O_{siderite}$ from SIMS transects cannot be used for palaeoclimatic reconstruction, the $\delta^{13}C_{siderite}$ should be unaffected by elemental substitution and can provide insight into paleoenvironmental conditions during growth.

The comparisons between the stable isotope measurements at Oxford, ETH, and Edinburgh highlights the importance of reporting the details of analytical techniques, reaction temperature, digestion method, reaction time, and the siderite-acid and siderite-water fractionations used, to ensure comparability between datasets. The community also needs to adopt a global standard to be used, such as Ivigtut siderite. This would ensure the discrepancies between methods are assessed, allowing for better collation of datasets.

Sample	$\delta^{18}O_{siderite}$ (‰ VPDB), ±1σ				$\delta^{13}C_{siderite}$ (‰ VPDB), ±1σ				Replicates			
	SIMS Transects	Oxford (Small)	Oxford (Large)	Zurich (Large)	SIMS Transects	Oxford (Small)	Oxford (Large)	Zurich (Large)	SIMS	Oxford (Small)	Oxford (Large)	Zurich (Large)
FC5	–1.10 ±0.25	–2.12 ±0.07	–2.30 ±0.08	–2.52 ±0.12	–19.53 ±9.07	–9.14 ±1.61	–11.68 ±0.20	–11.62 ±0.25	3	2	2	10
FC9	–1.72 ±0.70	–2.46 ±0.11	N/A	–3.46 ±0.24	–17.18 ±3.76	–14.70 ±0.71	N/A	–11.95 ±0.17	4	2	0	17
FC11	–1.03 ±0.24	–1.8	N/A	–2.30 ±0.25	–16.16 ±4.63	–18.43	N/A	–15.30 ±0.32	3	1	0	17

Table 5.6: Comparison of FC5, FC9, and FC11 (Fairlight Clays, Robinson et al., 2010) stable isotope values between analytical techniques (SIMS, IRMS), and sample powder preparation (spheres, small and large batches of powder). SIMS data are presented as mean of the averages of each transect (and standard deviation between the averages of the transects to avoid weighting transects higher due to more analysis points). This shows significant differences between methods, particularly between SIMS and IRMS, suggesting SIMS matrix effects need to be quantified. Differences between $\delta^{18}O_{siderite}$ with small and large batches of powder arise due to averaging over different number of spheres from horizons, suggesting some sphere horizons have a higher natural variability than is noted in smaller batches of powder.

4.2 Wealden palaeoenvironment

$\delta^{13}C_{siderite}$ is thought to reflect the Dissolved Inorganic Carbon (DIC) pool in pore waters during growth, which is, in turn, controlled by the reaction pathways converting organic matter to DIC. Experimental work has previously established the fractionation between organic matter and siderite to be between +13.3‰ and +14.5‰, when the sole source of carbon is from bacterially mediated degradation of organic matter (Romanek et al., 2003). In systems with heavier and lighter sources of CO_2, the fractionation is smaller and ranges from +0.5‰ to +7.4‰ (Romanek et al., 2003). Bulk organic carbon isotope composition ($\delta^{13}C_{org}$) in the Wealden Supergroup ranges from –24‰ to –30‰ (Chapter 3). Suboxic bacterial degradation of organic matter based on the average $\delta^{13}C_{org}$ in the Wealden Supergroup should therefore produce $\delta^{13}C_{siderite}$ between –10‰ and –16‰.

However, the $\delta^{13}C_{siderite}$ in the Wealden actually ranges from –40‰ to +5‰, outside the predicted range from bacterial degradation of organic matter, suggesting alternative respiration pathways were operating. Apart from suboxic bacterial degradation of organic matter, reactive pathways for converting organic matter to DIC include methanogenesis by acetate fermentation, methanogenesis by CO_2 reduction, and anaerobic methane oxidation. Methanogenesis produces isotopically heavy CO_2, typically occurring deeper in the soil profile than suboxic bacterial degradation, although gaseous products can migrate upwards (Whiticar et al., 1986; Ludvigson et al., 1998). Thus, methanogenesis could be responsible for some of the more positive $\delta^{13}C_{siderite}$ (> 0‰) measured in the Wealden sphaerosiderites (Ludvigson et al., 1998; Robinson et al., 2010). In contrast to methanogenesis, anaerobic methane oxidation produces very light CO_2, which could be responsible for very light $\delta^{13}C_{siderite}$ values recorded in some sphaerosiderites (< –20‰) (Ludvigson et al., 1998; Robinson et al., 2010).

$\delta^{13}C_{siderite}$ within individual sphaerosiderite horizons of the Wealden can vary by up to 5–10‰, while in SIMS transects across individual spheres, $\delta^{13}C_{siderite}$ varies by 20–30‰ from core to rim. The heterogeneity in $\delta^{13}C_{siderite}$ values within individual spheres and horizons suggests DIC to be spatially and temporally variant during the growth of these spheres, likely affected by multiple reactive pathways. The change from very negative to positive $\delta^{13}C_{siderite}$ values from core to rim likely reflects the burial of the sphere to deeper parts of the soil profile as growth progresses, with reactive pathways changing from predominantly bacterial degradation of organic matter to methanogenesis. However, this does not allow determination of burial depth as the depth in which these reactive pathways occur likely varied locally.

Figure 5.10 shows the average $\delta^{13}C_{siderite}$ values in each horizon on a composite depth scale from the Weald Clay and Tunbridge Wells Sand boundary. The average $\delta^{13}C_{siderite}$ values are approximately –20‰ to –15‰ at the base of the Ashdown Formation, and the range of values increases at the top of the Ashdown formation to between –30‰ to –10‰. In the Wadhurst Clay, the sphaerosiderites are recrystallised and all have similar $\delta^{13}C_{siderite}$ values (approximately –10‰). In the Tunbridge Wells Sand, $\delta^{13}C_{siderite}$ values are isotopically lighter at the base (up to –30‰) and become heavier towards the top of the formation (up to –12‰). These variations in $\delta^{13}C_{siderite}$ values with depth could suggest that palaeosols at the base of the Tunbridge Wells Sand and from –350m to –250m composite depth in the Ashdown beds were growing from DIC pools with higher inputs from mechanisms that produce lighter CO_2, for instance anaerobic methane oxidation. By contrast, in the top of the Ashdown formation the values could reflect inputs from heavier CO_2 sources, such as from methanogenesis. It is not possible to identify these mechanisms with confidence, as a mixture of pathways are likely to be operating. However, it is interesting that sphaerosiderites at the top of the Ashdown formation from both Westfield and Fairlight boreholes record $\delta^{13}C_{siderite}$ values collectively within range of each other,

suggesting a regional reflection in average $\delta^{13}C_{siderite}$ values. Analyses of sphaerosiderites in other overlapping parts of the boreholes would be useful in future to assess this further, but was beyond the scope of this study.

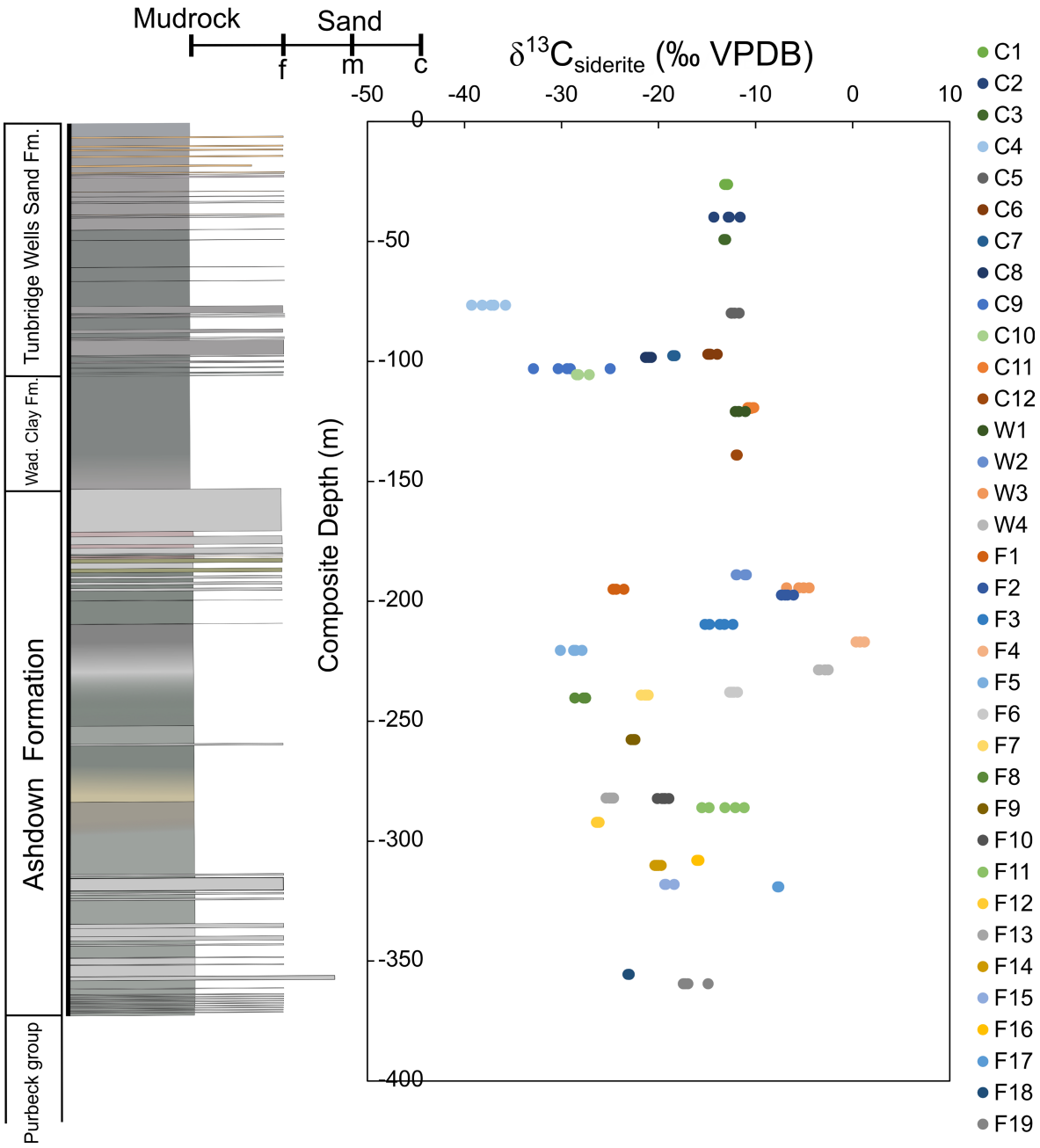


Figure 5.10: $\delta^{13}C_{siderite}$ values from each sphaerosiderite horizon with composite depth (composite depth based on assumption that due to the proximity of the Fairlight, Cooden, and Westfield boreholes, and that the sedimentation rates were similar between them).

$\delta^{13}C_{siderite}$ values of the Weald Basin have a large range, and are similar to $\delta^{13}C_{siderite}$ of sphaerosiderites from the wider geological record (Table 5.7). For example, Ludvigson et al., (2013) reported $\delta^{13}C_{siderite}$ values of –45‰ to +6‰ from North American Cretaceous deposits, spanning 20–75˚N palaeolatitude. The Wealden sphaerosiderites also have a large $\delta^{13}C_{siderite}$ range, akin to $\delta^{13}C_{siderite}$ ranges associated with low-latitude sphaerosiderites from the Cretaceous and Eocene (Ufnar et al., 2004b; Ufnar et al., 2004c; Ludvigson et al., 2013). This confirms the Wealden sphaerosiderites record $\delta^{13}C_{siderite}$ values indicative of growth in lower latitudes where a range of reactive pathways involving organic matter would have been operating.

Location	Age	Palaeolatitude	Depositional environment	δ^{13}C PDB (‰)		References
				Min	Max	
Chattanooga, Tennessee, USA	Historic (< 100 years)	35°N	Soil horizon	− 18	+ 7	Driese et al. (2010)
Namyang Bay, Korea	Holocene	37°N	Tidal flat			Lim et al. (2004)
Kyunggi Bay, Korea	Holocene	37°N	Fresh water	− 21.3	− 11.2	Choi et al. (2003)
Kansas, USA	Mid-Cretaceous	36°N		− 43	− 7.5	Ludvigson et al. (1998)
Kansas, USA	Late Albian	35°N	Overbank mudstones	− 23.1	− 19.0	Ufnar et al. (2004a)
Saskatchewan, Canada	Mid-Cretaceous			− 9.5		Ludvigson et al. (1998)
Saskatchewan, Canada	Late Albian	46°N	Fluvial	− 6.7	− 6.0	Ufnar et al. (2004a)
Upper Magdelena Valley, Columbia	Mid-Cretaceous	2°S	Paleosols	− 16.0	− 2.4	Suarez et al. (2010)
North Slope, Alaska	Mid-Cretaceous	75–85°N	Paleosols	− 4.6	+ 0.5	Ufnar et al. (2004b)
Saskatchewan, Canada	Hauterivian to Aptian	45°N	Fluvial/Overbank	− 0.8	+ 1.7	Ufnar et al. (2004a)
Wealden, UK	Early Cretaceous (Berr/Val)	30°N	Fluvial/Overbank	− 30	− 5	Robinson et al. (2010)
Australian	Early Triassic	65°S		− 18.4	2.9	Baker et al. (1996)
Sydney, Australian	Early Triassic	65–70°S	Palesols			Retallack (1997)
Maritime, Canada	Carboniferous (Pennsylvanian)	8°S	Palesols			Browne and Kingston (1993)
Illinois, USA	Carboniferous (Pennsylvanian)	0–5°N	Paleosol	− 12.8	− 3.2	Rosenau et al. (2013 a + b)
				− 17.9	+ 2.2	Rosenau et al. (2013 a + b)
Norra Albert, Sweden	end-Triassic	45°N	Fluvial	− 4.6	+ 1.8	Weibel et al (2016)
				− 3.6	+ 3.5	Weibel et al (2016)
				− 11.2	+ 6.0	Weibel et al (2016)
Columbia, North America	Eocene	15°S to 75°N	Palaeosols	-17	10	van Dijk, 2018
Yorkshire, UK	Jurassic	40°N	Fluvial	-15	-4.69	Taylor, 2019
Yorkshire, UK	Jurassic	40°N	Fluvial	-8	-3.9	Kantorowicz, 1985
Wealden, UK	Early Cretaceous (Berr/Val)	30°N	Fluvial/Overbank	-40	0	This Study
			Fluvial/Overbank	-35	+5	This Study

Table 5.7: Compilation of $\delta^{13}C_{siderite}$ from published sphaerosiderite studies (modified from table in Weibel et al., 2016).

4.3 Palaeohydrology in the Wealden

4.3.1 Local hydrology of the Wealden wetland

$\delta^{18}O_{siderite}$ and $\delta^{13}C_{siderite}$ from individual horizons from Meteoric Sphaerosiderite Line's (MSL's), suggest the sphaerosiderites grew in reducing waterlogged soils in pore waters reflective of meteoric groundwater. Palaeoclimatic reconstruction of terrestrial hydrology from $\delta^{18}O_{siderite}$ assumes growth in constant $\delta^{18}O_{groundwater}$, and that the $\delta^{18}O_{groundwater}$ is unaffected by evaporation or recharge, due to the waterlogged, and hence, buffered nature of the soils (Ludvigson et al., 1998). However, petrographic descriptions suggest that the Wealden sphaerosiderites grew in a somewhat dynamic environment. Based on internal oxidation zones, elemental and morphological heterogeneity (detailed in Chapter 4), the spheres were likely initially growing shallow enough in the soil profile to experience variable pH, siderite saturation, and cation concentrations that would influence changes in morphology and elemental composition. Over time, they were likely buried within the soil profile, as suggested by the transects recording isotopically heavier $\delta^{13}C_{siderite}$ towards the rims, associated with methanogenic pathways deeper in the soil profile (Section 4.2). It is difficult to determine the depths at which siderite was growing based on $\delta^{13}C_{siderite}$, as a mixture of pathways were likely to have operating, and the distribution of different pathways likely varied temporally and spatially based on water table variations (Ludvigson et al., 1998).

Evidence from the SIMS transects, and the existence of some samples with deviations away from linear MSL trends, suggests the Wealden sphaerosiderites are recording a complex palaeohydrological signal. Multiple sphaerosiderite horizons contain a correlation between light $\delta^{13}C_{siderite}$ and heavy $\delta^{18}O_{siderite}$, that is not consistent with trends expected from marine-freshwater mixing. A similar relationship has been noted in sample FC9 (Fairlight Clays, Ashdown Fm; Robinson et al., 2010), and was suggested to reflect changes in

groundwater chemistry as a result of the movement of redox or methanogenesis boundaries. At depth in the soil profile, the $\delta^{13}C_{siderite}$ values would reflect methanogenic sources and the $\delta^{18}O_{siderite}$ values would reflect a less evaporated water source. The FC samples from Robinson et al., (2010) analysed using SIMS (Section 3.2) record heavier $\delta^{18}O_{siderite}$ during the early part of growth in cores, but lighter $\delta^{18}O_{siderite}$ towards the latter part of their growth, implying that evaporation may have indeed affected the $\delta^{18}O_{siderite}$ values recorded during the early part of sphere growth, at relatively shallow levels in the soil profile. Note that the amplitude of change between $\delta^{18}O_{siderite}$ from core to rim in the SIMS transects ranges from 1–6‰, which is too large for increasing temperature to be a likely cause (equates to ~ 40˚C difference from core to rim, if $\delta^{18}O_{groundwater}$ remained constant, assuming initial growth at temperatures from Section 3.3, and the siderite-water fractionation of Carothers et al., 1988). The trend in $\delta^{13}C_{siderite}$ across sphere transects is opposite to that observed in $\delta^{18}O_{siderite}$, changing from an isotopically lighter core to an isotopically heavier rim. Heavier $\delta^{13}C_{siderite}$ values coupled with lighter $\delta^{18}O_{siderite}$ values at the rim suggests that during the latter stages of growth, the sphaerosiderites were buried deeper in the soil profile experiencing methanogenic conditions and recording groundwaters experiencing less evaporation. Despite the detailed evidence from microanalysis of the spheres, the presence of extensive sphaerosiderite horizons suggests the soils in the Weald Basin were largely waterlogged and reducing, and thus the effect of evaporation is likely to be slight overall, but an important factor to consider further in the following sections.

Figure 5.11 shows the $\delta^{18}O_{siderite}$ on a composite depth scale with moving average best fit lines for each formation from each borehole. The sphaerosiderites from the Wadhurst Clay are not included in the trend, as they contain evidence of recrystallisation, and are not included in palaeoclimatic interpretations but plotted for reference. The $\delta^{18}O_{siderite}$ values fluctuate from isotopically heavier to lighter, through the Wealden Supergroup, and are decoupled from the facies changes. The $\delta^{18}O_{siderite}$ fluctuations could be recording changes

in regional hydrology, which in turn could be affected by changes in temperature, amount of precipitation, and/or moisture sources. The following sections will discuss the possible reasons for the $\delta^{18}O_{siderite}$ fluctuations further.

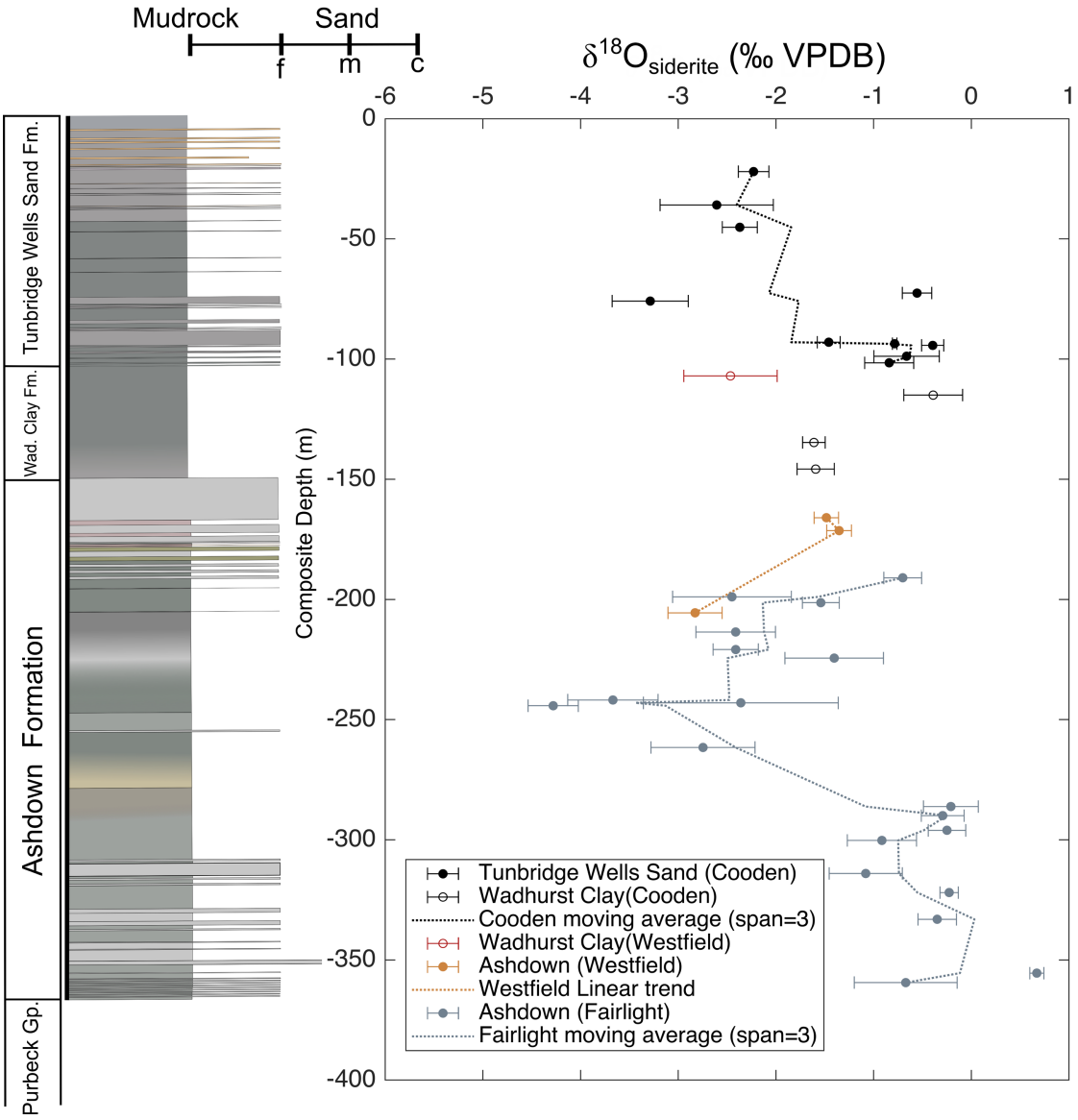


Figure 5.11: Mean $\delta^{18}O_{siderite}$ of sphaerosiderite horizons plotted with 1σ on a composite depth scale and a moving average (span of 3). Sphaerosiderites show a long-term $\delta^{18}O_{siderite}$ trend of alternating isotopically heavier and isotopically lighter values over the Berriasian–Valanginian, likely reflecting changes in local hydrology.

4.3.2 Local temperature of the Wealden wetland

The Δ_{47} temperatures from the Wealden sphaerosiderites are consistently high and range between 33–39°C throughout the Wealden stratigraphy. The only exception is sample F11 with a formation temperature of 49°C ±6. This formation temperature is considered far too high to reflect plausible Early Cretaceous terrestrial mean annual temperatures at this palaeolatitude considering the evidence from sedimentology, palaeontology, and climate modelling, suggesting MAT in the basin to be 20–28°C (Sladen and Batten, 1984; Allen et al., 1998; Haywood et al., 2004, Farnsworth, *pers. comm.*, 2019). Although no evidence of diagenetic alteration could be found in the petrography, this sample was considered an anomaly and therefore not considered in palaeoclimatic interpretations. The other 5 siderite horizons chosen for palaeoclimatic interpretations did not show signs of dissolution or recrystallisation, and no additional cement was detected in bulk samples by petrography or XRD (Appendix C.1.1). The Wealden Supergroup is estimated to have been buried up to 2 km (Sladen and Batten, 1984; Allen et al., 1998). Assuming a geothermal gradient of 30°C/km, the siderites would not have experienced temperatures greater than 60°C. Although the solid state reordering temperature of siderite has not been established, calcite undergoes solid state reordering at > 100°C (Henkes et al., 2014). Siderite is considered a more robust mineral, and therefore, the reordering temperature threshold would likely be the same as, or higher than calcite.

Previous work on palynology and mineralogy of the Wealden Supergroup has suggested Early Cretaceous temperatures in the Weald Basin were 10ºC during cooler periods and 20–25ºC during warm periods (Sladen and Batten, 1984). The Early Cretaceous is considered to have on average 4 times the pre-industrial CO_2 levels based on a range of proxies, and therefore, temperatures are thought to have been higher too (Berner and Kothavala, 2001; Foster et al., 2017) A climate model simulation of the Barremian using a version of the Hadley Centre Model with 4 times pre-industrial CO_2 levels (1120 ppmV)

suggests a Mean Annual Temperature (MAT) in the Weald Basin of 22°C, with seasonal averages of 10–12°C in cooler months, and 36–40°C in warmer months (Haywood et al., 2004). A more recent climate model (Lunt et al., 2016; Farnsworth et al., 2019a; Farnsworth et al., 2019b, Farnsworth, *pers. comm*., 2019) with CO_2 at 1120 ppmV and an updated version of the Hadley Centre Model (HadCM3) provides Berriasian–Hauterivian mean annual temperatures of 24–26°C, mean winter temperatures of 12–15°C, and mean summer temperatures 35–39°C in the Weald Basin. The mean annual temperatures from the climate models are within the range predicted by Sladen and Batten, (1984) during warmer periods in the basin and lends support to the climate model, but are 15°C higher than the cooler periods predicted from Sladen and Batten, (1984). However, the predictions by Sladen and Batten, (1984) of cooler periods may need updating, particularly considering the current warm low- and high-latitude sea surface temperature reconstructions of the Early Cretaceous (Littler et al., 2011; Jenkyns et al., 2012; Price and Passey, 2013; Vickers et al., 2019).

The Δ_{47}-derived temperatures of sphaerosiderites (33–39°C) from the Wealden (Figure 5.12) are higher than MAT predicted by Sladen and Batten (1984), but are within the range of summer temperatures predicted by General Circulation Models (GCM) at 4 times pre-industrial CO_2 levels (Farnworth *pers. comm.,* 2019, Haywood et al., 2004). Assuming the climate sensitivity and assumed pCO_2 in the climate models are reflective of a Cretaceous world, the formation temperature of the siderites suggests a seasonal bias. Modern siderites growing in Louisiana and Norfolk show seasonal bias towards summer in measured Δ_{47} temperatures, although the bias is thought to diminish with increased depth in the soil profile (Van Dijk et al., 2019). The petrographic and sedimentological evidence suggests that the Wealden sphaerosiderites were growing high enough in the soil profile to experience paleoenvironmental variations leading to morphological and elemental heterogeneity, and therefore lends support to the possibility of recording seasonal bias.

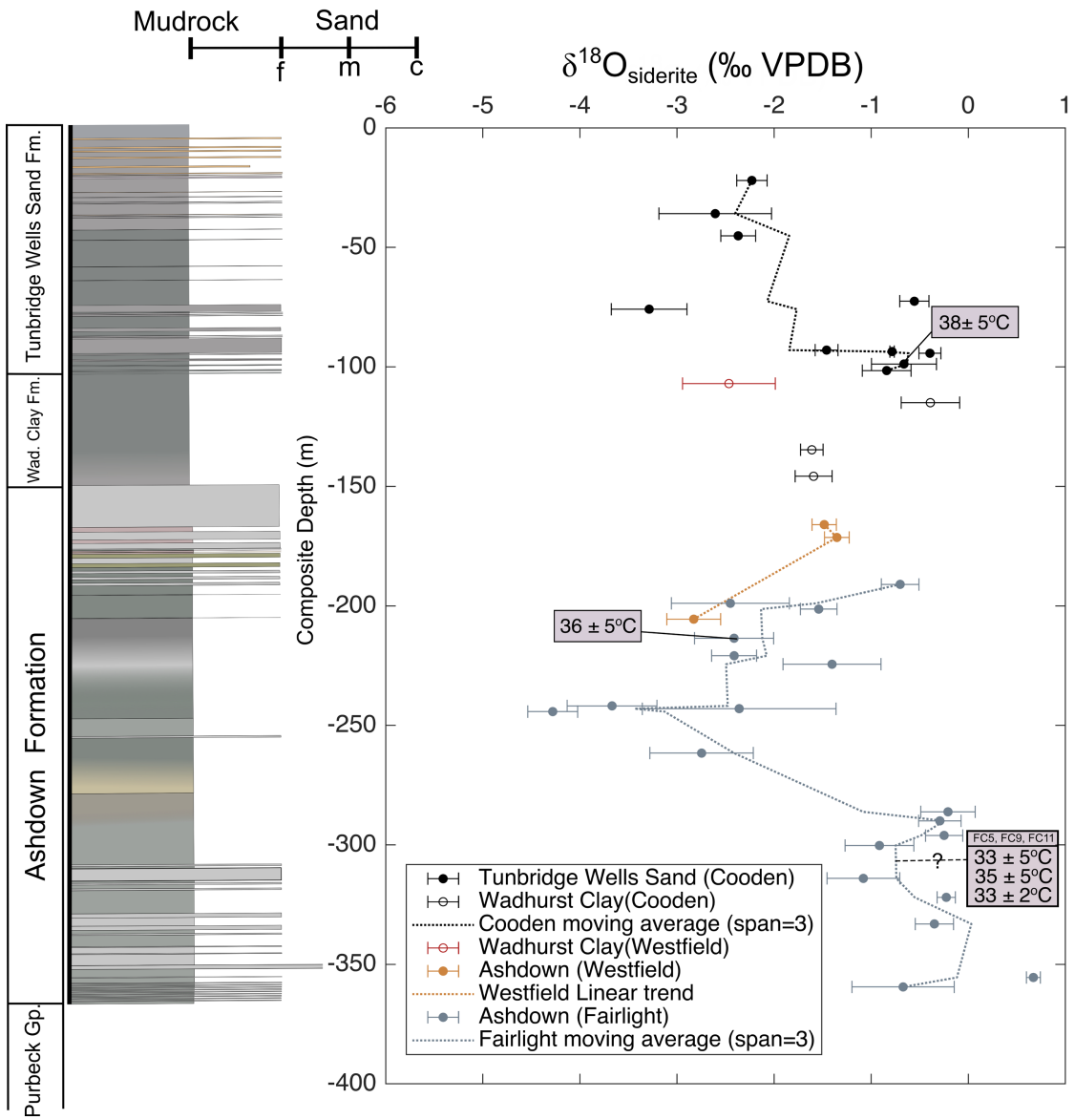


Figure 5.12: Average $\delta^{18}O_{siderite}$ of sphaerosiderite horizons plotted with 1σ on a composite depth scale, and a moving average best fit of each borehole with a span of 3. Δ_{47} temperatures from representative sphaerosiderite horizons through the stratigraphy are within error of each other and show the Weald Basin to have been consistently warm.

The formation temperatures of > 32°C for the Wealden sphaerosiderites suggests that warm conditions existed throughout Berriasian–Valanginian in the Weald Basin (Figure 5.12). The measured Δ_{47} temperatures are all statistically similar, and if it is assumed that these values are representative of summer temperatures throughout the Berriasian–

Hauterivian, it could be tentatively suggested that changes in regional temperatures were not a direct factor in regulating the changes in $\delta^{18}O_{siderite}$.

Sedimentological evidence and climate modelling of the Weald Basin suggests a wet climate, with wetter colder months with flash flooding and groundwater recharging (Allen et al., 1998; Wright et al., 2000; Haywood et al., 2004, Farnsworth, *pers. comm.,* 2019). Natural pore waters in wetlands have low (0.2–1) siderite saturation (Berner, 1971). Therefore, induced groundwater recharging during winter storms and high precipitation events may have caused changes to the pH, DIC, and siderite saturation in groundwaters, depending on depth in soil profile. In contrast, during less stormy periods the soils would have been waterlogged but not disturbed, and thus comparatively more stable geochemical conditions may have existed in pore waters allowing siderite saturation to build up, and for siderite growth to occur. Higher temperatures or increases in temperature would have also increased the siderite saturation within pore waters, as would have the microbial activity rate in soils, likely seasonal in nature (Mitsch and Gosselink, 2015), which has been shown to control siderite growth (Mortimer et al., 1997). Based on these considerations of modern siderite-bearing wetlands, the results from GCMs and other palaeoclimatic evidence, elemental and morphological heterogeneity indicating growth in a dynamic environment, and the Δ_{47} temperatures, the possibility of seasonality in the Wealden sphaerosiderite record needs to be evaluated.

4.3.3 Changes in hydrology: wetter and drier periods?

As temperature does not appear to control the $\delta^{18}O_{siderite}$ trend in stratigraphy, the periods of isotopically lighter $\delta^{18}O_{siderite}$ in the Wealden Supergroup are suggestive of intervals with wetter conditions. These wetter conditions could be indicative of more precipitation and/or less evaporation, creating a more isotopically light $\delta^{18}O_{groundwater}$ in which siderite growth occurred (Figure 5.12). By contrast, the isotopically heavier $\delta^{18}O_{siderite}$ values could reflect

drier periods, with less precipitation and/or more evaporation, reflecting growth in isotopically heavier meteoric $\delta^{18}O_{groundwater}$.

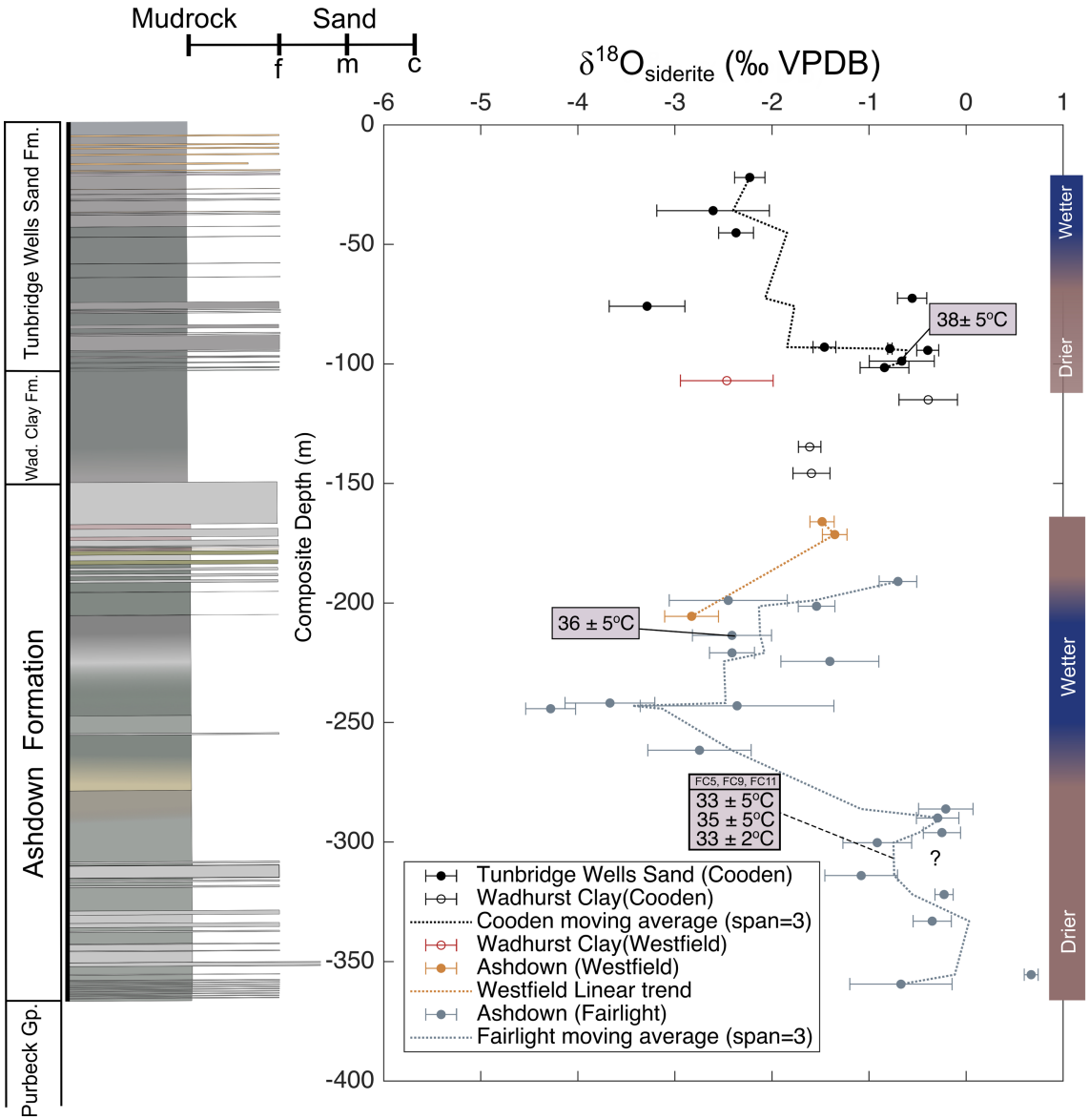


Figure 5.13: Fluctuating $\delta^{18}O_{siderite}$ could reflect wetter and drier periods in the Weald Basin due to regional changes in climate. Mean $\delta^{18}O_{siderite}$ of sphaerosiderite horizons plotted with 1σ and a moving average with a span of 3. The samples FC5, FC9, and FC11 (Robinson et al, 2010) are correlated to these boreholes by their depth in relation to the Lee Ness Sandstone, which is identified in the Fairlight borehole.

There has also been a longstanding discussion on the causes of the lithological changes from arenaceous to argillaceous in the Wealden Supergroup, interpreted to indicate humid

and arid periods, and whether they reflect a predominantly climatic or local tectonic control (Allen and Wimbledon, 1991; Allen et al., 1998). In the results presented here, the changes in $\delta^{18}O_{siderite}$ and inferred relative humidity changes are decoupled from the facies changes, suggesting the climate in the Weald Basin was not the predominant control on the major lithological changes, and that local tectonic uplift of the three massifs surrounding the basin may have been more significant.

4.3.4 $\delta^{18}O_{groundwater}$ values in the Wealden Wetland

In order to better understand the hydrology of the Wealden, $\delta^{18}O_{groundwater}$ values can be calculated to allow comparisons with existing data and isotope enabled climate models (Farnsworth, *pers. comm.,*, 2019), potentially allowing assessment of precipitation amounts.

In previous studies, groundwater oxygen-isotope values from pedogenic siderites have been calculated assuming that growth was year-round and that the isotopic composition reflected Mean Annual Temperature (MAT) (Ludvigson et al., 1998; Ufnar et al., 2004b; Suarez et al., 2009; Robinson et al., 2010; Ross et al., 2017). For instance, for the Fairlight Clays (Ashdown Formation), Robinson et al., (2010) assumed sphaerosiderite growth at 20–25°C (Sladen and Batten, 1984), and calculated $\delta^{18}O_{groundwater}$ between –3.8‰ to –7.3‰ (Robinson et al., 2010), similar to values from the same palaeolatitude in the Albian of North America (Ufnar et al., 2004a). To allow a similar comparison, $\delta^{18}O_{groundwater}$ of Wealden sphaerosiderites were calculated based on the minimum, mean, and maximum $\delta^{18}O_{siderite}$ for a range of temperatures using the Carothers et al., (1988) siderite-water fractionation equation. At 20–25ºC, the Wealden $\delta^{18}O_{groundwater}$ ranges from –0.60‰ to –6.8‰, encompassing the $\delta^{18}O_{groundwater}$ calculated from sphaerosiderites reported in Robinson et al., (2010), with some values isotopically lighter (Figure 5.14). The average Wealden $\delta^{18}O_{groundwater}$ calculated with this approach from the mean $\delta^{18}O_{siderite}$ is –4‰.

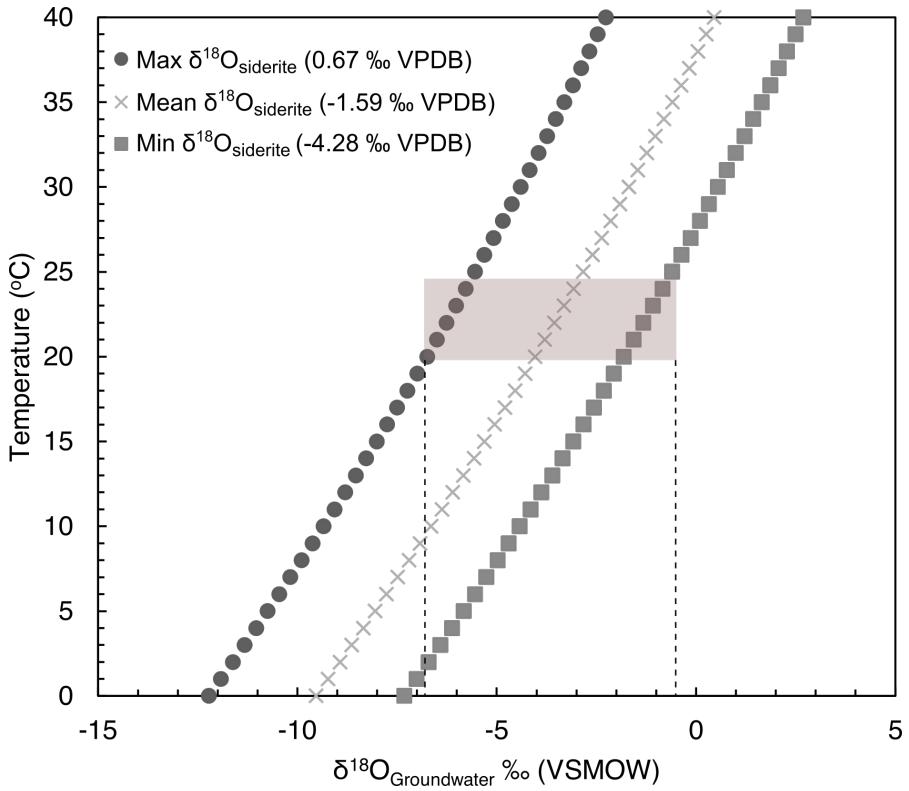


Figure 5.14: $\delta^{18}O_{groundwater}$ calculated using the maximum, mean, and minimum $\delta^{18}O_{siderite}$ on assumed MAT of 20-25°C (Slade and Batten, 1984) using the siderite-water fractionation equation of Carrothers et al., (1988).

However, if the $\delta^{18}O_{groundwater}$ is calculated using the Δ_{47} formation temperatures (Section 4.3.2), then the calculated meteoric groundwater is on average 3‰ heavier (range of –3.7‰ to 1.2‰). Figure 5.15 shows the calculated $\delta^{18}O_{groundwater}$ based on the minimum and maximum Δ_{47} siderite formation temperatures (33°C and 39°C), and mean $\delta^{18}O_{siderite}$ from each horizon using two siderite-water fractionation equations (Carothers et al., 1988; Van Dijk et al., 2018). The experimental siderite-water fractionation results of Carothers et al., (1998) are restricted to > 33°C, while Van Dijk et al., (2018) covers siderite-water fractionations from 8–68°C. The updated mean $\delta^{18}O_{groundwater}$ of Fairlight Clay samples FC5, FC9, and FC11 based on Δ_{47} formation temperatures are 2–6‰ heavier compared to the previously reported values in Robinson et al., (2010), and are comparable to the other Wealden values of $\delta^{18}O_{groundwater}$ calculated here using clumped temperatures. In the case of

the sphaerosiderite horizons in the Weald Basin, the estimates of MAT from literature are approximately 10°C lower than the formation temperatures analysed from Δ_{47}. This stresses the importance of evaluating the assumptions of temperature and paleoenvironmental conditions applied to sphaerosiderites as they may change according to the depositional environment.

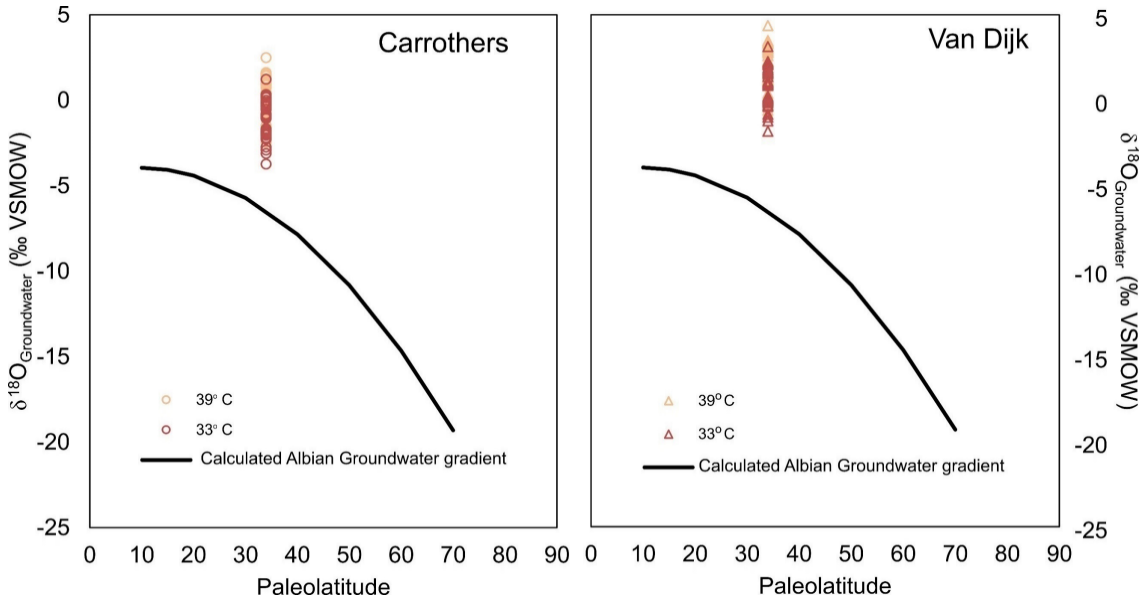


Figure 5.15: $\delta^{18}O_{groundwater}$ calculated from the Wealden sphaerosiderites (using the minimum and maximum Δ_{47} siderite formation temperatures) are more isotopically heavy than the Albian gradient (Ufnar et al , 2004a) predicts for the palaeolatitude of the Weald Basin during the Early Cretaceous.

The calculated groundwaters are isotopically heavy, and suggests that the siderites may have been recording a modified groundwater, rather than one reflective of average annual stable isotope compositions. Isotopically heavier values could reflect the moisture source, or the modification of groundwaters over time, such as, through evaporation. If indeed the sphaerosiderites were growing preferentially in summer, as correlation between high clumped isotope values (Section 4.3.2) and climate models suggest, then the groundwaters may have experienced evaporation beforehand, depending on the timing of precipitation, groundwater recharge, and moisture sources. As the clumped isotope temperatures correlate

well to GCM summer temperatures (Haywood et al., 2004, Farnsworth, *pers comm*., 2019), and lead to calculated isotopically heavy groundwater, the potential for the sphaerosiderite record to be summer-biased needs to be addressed.

4.3.5 Enriched $\delta^{18}O_{groundwater}$ values: A reflection of moisture source or evaporation?

To assess whether the $\delta^{18}O_{groundwater}$ values calculated in Section 4.3.4 are feasible, isotope enabled GCM simulations of Early Cretaceous climate are presented here for comparison (Farnsworth, *pers. comm.,* 2019). The model is based on the experimental design detailed in Farnsworth et al (2019a,b) and Lunt et al (2016). The simulations were carried out using a UK Met Office coupled ocean-atmosphere GCM HadCM3L version 4.5, with a resolution of 3.75° longitude and 2.5° latitude in both the atmosphere and ocean, coupled to a dynamic global vegetation model (TRIFFID) via the land surface scheme MOSES 2.1 (Lunt et al., 2016; Farnsworth et al., 2019). The simulations were carried out at x4 CO_2 and run for 10,422 years for each geologic stage simulation so that they have reached climate equilibrium in the atmosphere and deep ocean.

During the Early Cretaceous, the Proto-Atlantic would have been a relatively restricted basin, and GCM results suggest that the annual average $\delta^{18}O_{seawater}$ of the Proto Atlantic and the Tethys was 0.5–1‰ (Figure 5.16), higher than the average –1‰ assumed for an ice-free Cretaceous world. These models (and those of Haywood et al., 2004) suggest that the predominant moisture source for precipitation in the Weald Basin was the Proto-Atlantic and/or Tethys ocean. This would also mean the moisture source from these ocean basins would be relatively isotopically heavy, and therefore could potentially explain the isotopically heavy $\delta^{18}O_{groundwater}$ values calculated from siderites.

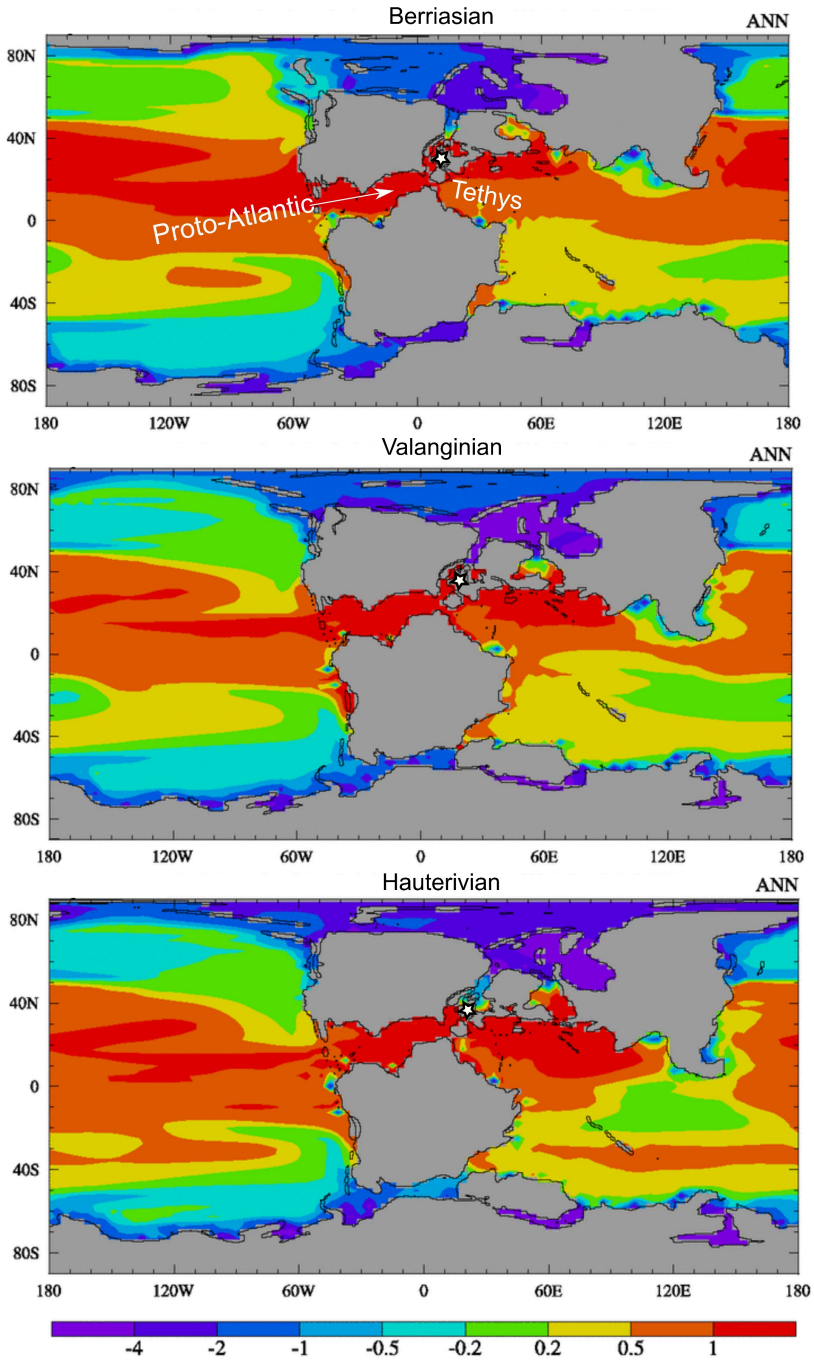


Figure 5.16: Early Cretaceous global annual average $\delta^{18}O_{seawater}$ from the Berriasian, Valanginian, and Hauterivian (Farnsworth, *pers. comm.*, 2019). The white star is approximate location of Weald Basin.

The mean clumped isotope temperatures of siderites agree well with the June–August temperatures from Farnsworth, *pers. comm.,* (2019) (Figure 5.17; grey shaded region) and are within error of the temperatures in May and September. The clumped temperatures

suggest siderite growth was restricted to May–September. The $\delta^{18}O_{precipitation\ values}$ during these suggested formation months of the sphaerosiderites (Figure 5.17) are 2–6‰ lighter than the mean $\delta^{18}O_{groundwater}$ calculated from the Wealden siderites. However, some of the $\delta^{18}O_{precipitation}$ values during the warmer months, particularly for the Valanginian, are within range of $\delta^{18}O_{groundwater}$ calculated. This suggests that the groundwater from which the sphaerosiderites were growing may have been modified by evaporation, and that the Proto-Atlantic or Tethyan moisture source alone may not account for the isotopically heavy $\delta^{18}O_{groundwater}$ values. As discussed in Section 4.2, deviations from MSL's in sphaerosiderite horizons and stable isotope transects also suggest that the Wealden soils may have experienced evaporation, particularly during the early stages of sphaerosiderite growth, occurring higher up in the soil profile.

The precipitation regimes within the model (and that of Haywood et al., 2004) suggests the Weald Basin experienced humid conditions throughout the year. However, in the case of Farnsworth, *pers. comm.,* (2019), comparison between each stage shows a distinct change in monthly precipitation patterns from the Berriassian to the Valanginian, and a relatively similar climate between Valanginian and Hauterivian (Figure 5.19). In the Berriasian, the highest precipitation occurs during April–September (the warmer months), while during the Valanginian, the lowest precipitation occurs during January–March and September–December (colder months). The differences in average monthly precipitation also changes from predominantly seasonal precipitation (biased to summer) in the Berriasian, with 4mm/day difference between summer and winter, to more evenly spread precipitation flux throughout the year during the Valanginian and Hauterivian. The Valanginian–Hauterivian precipitation also fits well with the predicted wet Barremian climate in the Weald Basin from Haywood et al., (2004). The change in climate from the Berriasian to Valanginian is thought to be linked to palaeogeographic changes within the climate model.

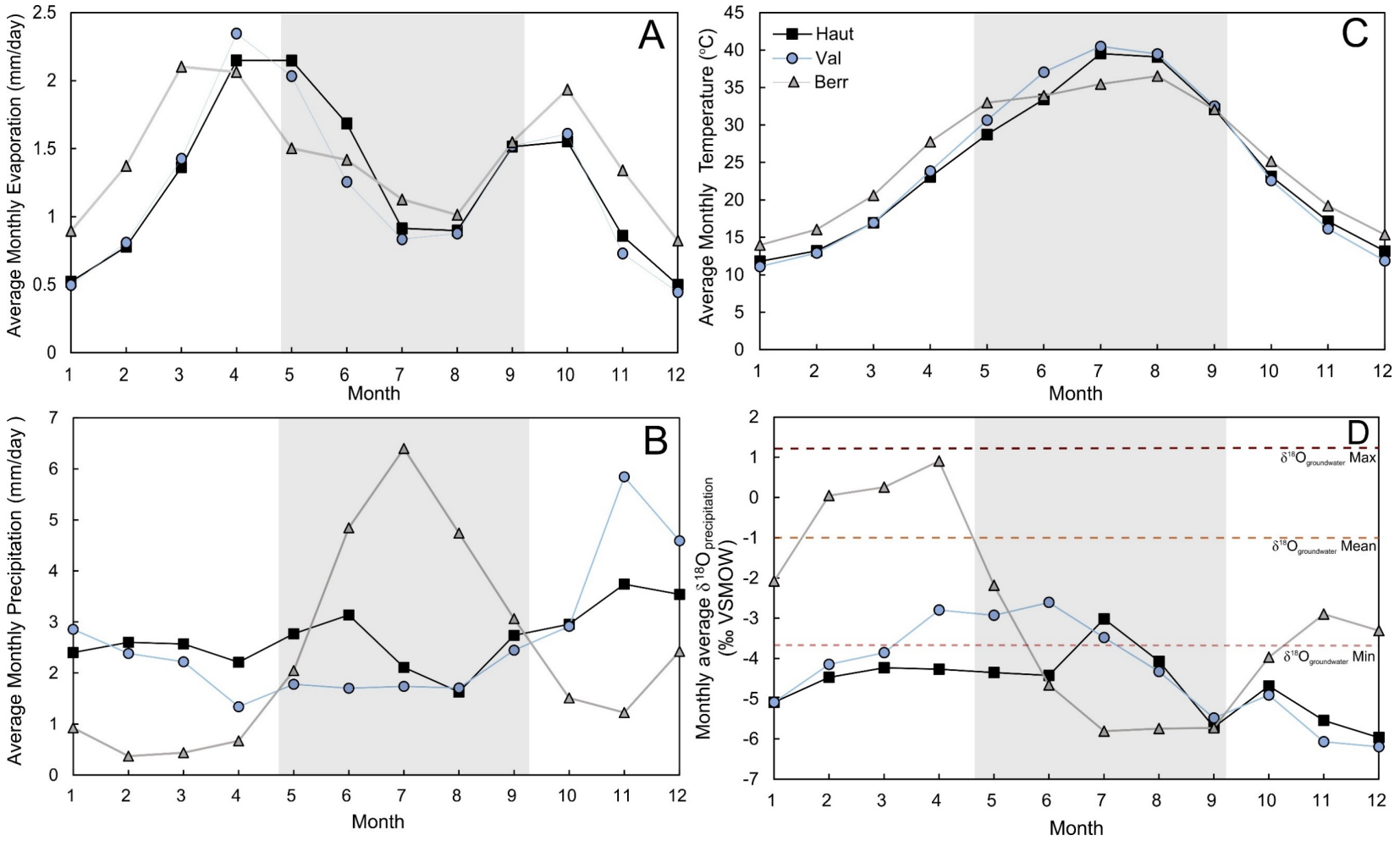


Figure 5.17: Average monthly changes from Berriasian-Hauterivian using data from Farnsworth, *pers. comm.*, 2019. The range of $\delta^{18}O_{groundwater}$ values are plotted for reference.

By comparison, the evaporation flux (mm/day) peaks in April–May in all three stages in the model, just before the annual period considered to be favoured for siderite growth. For the Valanginian, it is likely the groundwater recharging would have been restricted to the colder months, and that the groundwater may have undergone evaporation before the warmer months, based on the increase of evaporative flux from January–May. While in the Berriasian, the model suggests peak precipitation during the warmer months, but the evaporation regime stays similar, which suggests the sphaerosiderites growing in the Berriasian may have also experienced evaporation, but also more dynamic conditions than in the Valanginian. However, in the siderite record, the $\delta^{18}O_{siderite}$ values at the base 80m of the Ashdown Formation, considered to be in the Upper Berriasian, are isotopically heavy (–1‰ to 0.6‰), and similar to those at the top of the Ashdown Formation. The isotopically heavy values are somewhat contradictory to the high precipitation rate, low evaporation rate, and isotopically light precipitation shown in the model during summer months in the Berriasian. $\delta^{13}C_{siderite}$ from the samples at the base of the Ashdown Formation are within the range of values of Wealden sphaerosiderites and do not appear to show significant palaeoenvironmental changes. As the ages at the Berriasian-Valanginian boundary are not well constrained, it is also difficult to be certain of the ages of the sphaerosiderites in the base of the Ashdown Formation. The record does not show shifts in oxygen isotope composition (outside of the fluctuations from heavy to light values) through the Ashdown Formation that may indicate changes in climate between Berriasian and Valanginian.

However, overall, the ostracod biostratigraphy suggests the sphaerosiderites were predominantly forming in the Valanginian. The model results for the Valanginian alone are presented in Figure 5.17 to allow more detailed understanding of the groundwater conditions just prior to siderite precipitation.

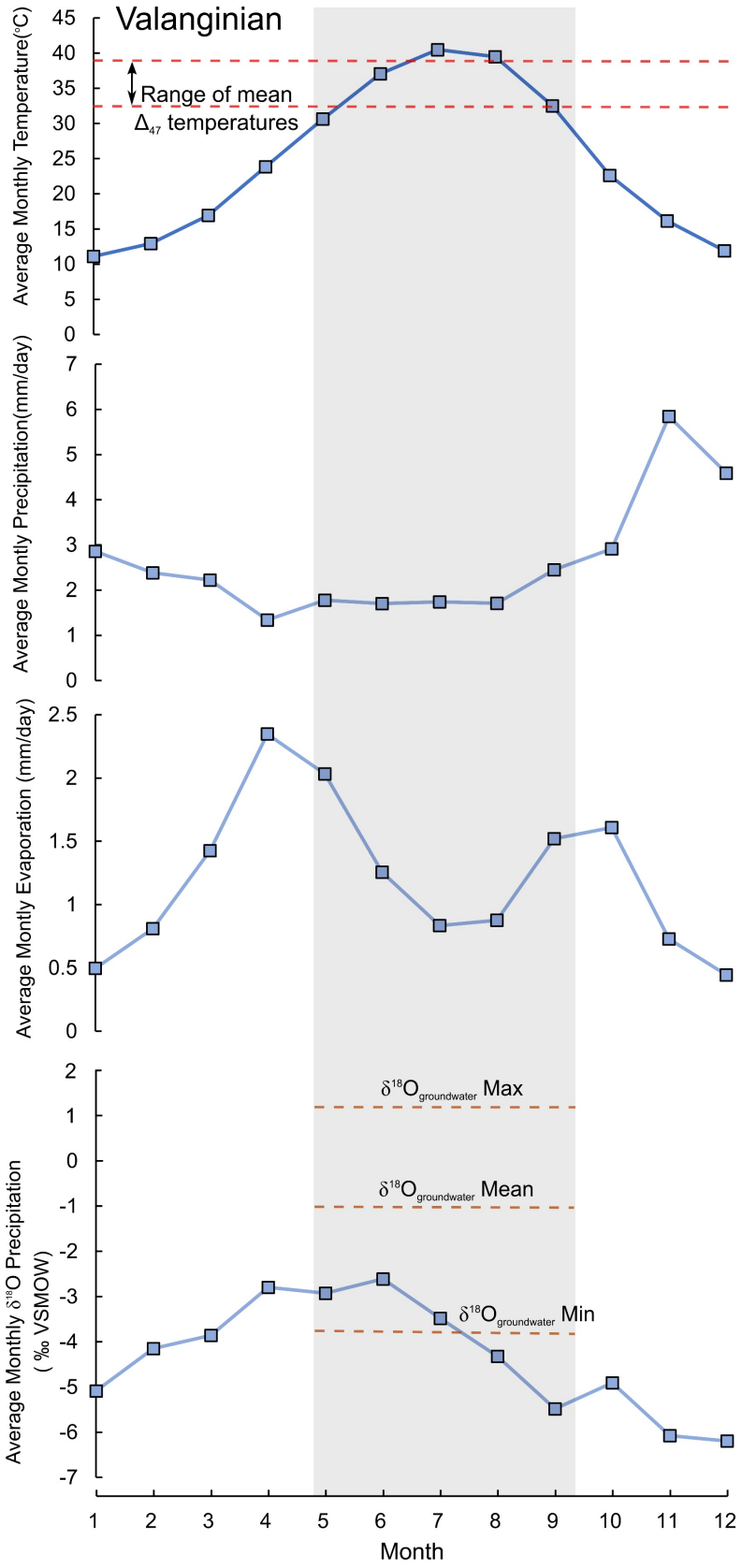


Figure 5.18: Valanginian model parameters: Monthly temperature (°C), precipitation (mm/day), evaporation (mm/day), and $\delta^{18}O_{precipitation}$.

During the Valanginian, the climate model suggests wet conditions throughout the year (Figure 5.18), with peak groundwater recharging during colder months. This means, the recharged groundwater from winter would have experienced evaporation and modification to heavier $\delta^{18}O_{groundwater}$ values from January to April, as temperatures rose from 10°C to 30°C. This is supported by the increase in evaporation over the same period in the model, from approximately 0.5 mm/day to 2.5 mm/day. This temperature increase of 20°C over 4 months would have not only driven evaporation, but also helped increase siderite saturation within pore waters. The warmer months and increases in temperature may also be linked to increased microbial activity (Mortimer et al., 1997; Mitsch and Gosselink, 2015) allowing increased bacterial iron reduction, which would increase siderite saturation and drive siderite precipitation. The mean $\delta^{18}O_{groundwater}$ is 2–6‰ higher than precipitation during warmer months, further supporting the presence of evaporation-modified groundwater. The inferred summer-biased sphaerosiderite growth, based on the climate model and clumped isotope temperatures, suggest the spheres would be recording groundwaters which have experienced peak annual evaporation during the Valanginian, supporting the high reconstructed $\delta^{18}O_{groundwater}$ values.

It is possible that between stages, there may be temporal differences in precipitation and evaporation which cannot be evaluated further in this dataset. However, the continued growth of siderites suggests the soils remained waterlogged and reducing, despite experiencing evaporation. Based on the evidence evaluated here, the interpretation of wetter conditions (more precipitation/less evaporation) and drier conditions (less precipitation/more evaporation) is considered valid.

4.3.6 Comparison with temperature data from other Early Cretaceous studies

Site	P-Lat	Age	T (°C)	Terrestrial /Marine	Depth in water column	Proxy	Annual average Model T (°C)	Source
DSDP 534	20°N	Val-Barr	33–34	Marine	Surface	TEX_{86}	29–31	Littler et al (2011)
DSDP 603	18°N	Val-Barr	32–33	Marine	Surface	TEX_{86}	27–29	Littler et al (2011)
Weald Basin	30°N	Berr–Haut	33–39 (±5°C)	Terrestrial	-	Δ_{47} temperature (siderite)	25°C	This Study

Table 5.8: Comparison of low-latitude proxy-based temperatures (Littler et al., 2011) and model temperatures (Farnsworth, *pers. comm.,* 2019).

The climate model (Farnsworth, *pers. comm.*, 2019) appears to agree relatively well with proxy-based reconstructions at low-latitude sites (Littler et al., 2011), at least for annual averages (Table 5.8). The low-latitude site temperatures vary between 3°C and 8°C seasonally in the climate model, depending on the time period sampled (Appendix D.1.3) (Littler et al., 2011). However, proxy temperatures from clumped isotopes on belemnites and TEX_{86} at high latitudes are up to 10ºC warmer on average than the model MAT (Appendix D.1.3) (Price and Passey, 2013; Jenkyns et al., 2012; Vickers et al., 2019). For the high-latitude sites, the model and proxies agree best on the temperatures of the warmer months, however, seasonal biases and artefacts associated with proxies likely contribute to this disparity (Price and Passey, 2013; O'Brien et al., 2017). Further to this, the climate sensitivity and pCO_2 ascribed in the model are an assumption, and may be too low, and thus not suitable to capture the high-latitude temperatures suggested by the proxies. Both model and proxy temperatures, however, support continued warmth in the Early Cretaceous in the marine and terrestrial realm, and agree relatively well for low latitudes.

4.4 Implications for Early Cretaceous climate

The Wealden sphaerosiderites add a valuable new dataset for interpreting the Early Cretaceous climate in low–mid palaeolatitudes. Comparison between the bulk organic carbon isotope record ($\delta^{13}C_{org}$) (detailed in Chapter 3) and the long-term $\delta^{18}O_{siderite}$ trend through the stratigraphy are presented in Figure 5.19. The changes in the $\delta^{13}C_{org}$ in the Weald Basin can be tentatively corroborated to the long-term changes in the marine composite record of the Early Cretaceous (Ogg et al., 2016), recording global carbon cycle changes (detailed in Chapter 3).

In the Weald Basin, the $\delta^{13}C_{org}$ record is relatively stable in the Ashdown Formation, until the top of the formation where $\delta^{13}C_{org}$ values become isotopically heavier, interpreted as the onset of the Valanginian CIE. The $\delta^{18}O_{siderite}$ trend records changes throughout the stratigraphy, thought to be indicating relative shifts in humidity. The $\delta^{18}O_{siderite}$ records a drier climate at the base of the Ashdown Formation, shifting to a more humid climate in the middle of the formation, apparently decoupled from the $\delta^{13}C_{org}$ changes. However, at the onset of the Valanginian CIE, as $\delta^{13}C_{org}$ values start to increase (top of Ashdown Formation), the $\delta^{18}O_{siderite}$ values also increase, indicating a shift towards aridity starting at the onset of the CIE. The high $\delta^{18}O_{siderite}$ values persist in the Tunbridge Wells Sand, but become lighter up-section, indicating a shift from drier to wetter conditions as the $\delta^{13}C_{org}$ values start to decrease. Therefore, it appears the $\delta^{13}C_{org}$ record and the $\delta^{18}O_{siderite}$ may be decoupled at times, but at other times (e.g. onset of the Valanginian CIE), the climatic changes are coupled to global carbon cycle changes in the Weald Basin.

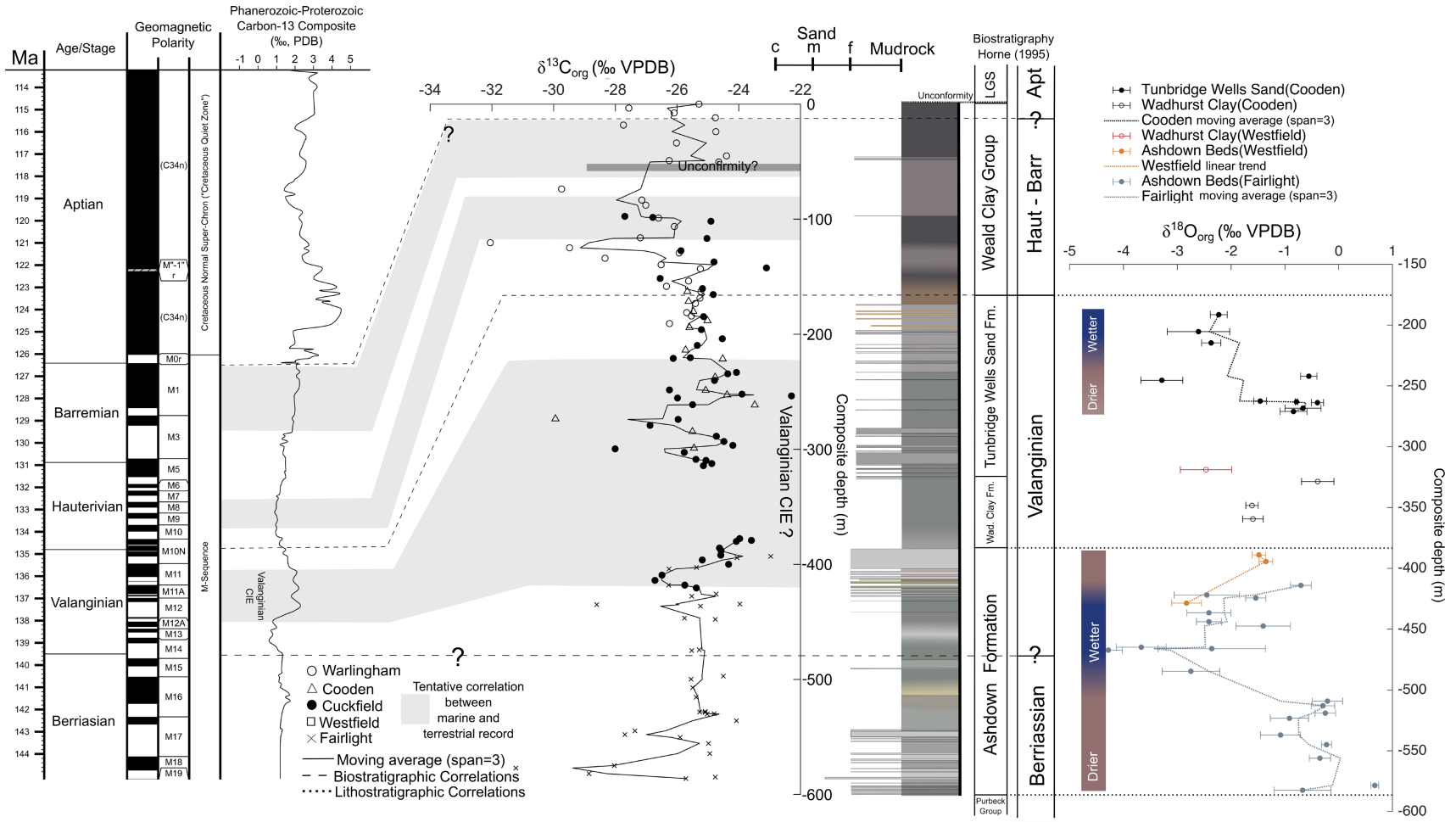


Figure 5.19: Comparison between the Wealden carbon isotope composite record and the siderite composite record. Periods of humidity and aridity are at times decoupled from the carbon cycle changes. However, at other times like the onset of the Valanginian CIE, the siderites record synchronous climatic changes. Timescale of the Tethyan record is GTS16 (Ogg et al., 2016).

Using the $\delta^{13}C_{org}$ record, the Weald Basin sphaerosiderites are compared to the Vocontian Basin and Mid Polish Basin spore-pollen assemblages from Kujau et al., (2013). Some of the inferred relative arid and/or humid periods between the basins correlate well. For instance, the arid period at the top of the Ashdown Formation at the onset of the Valanginian CIE correlates temporally to the arid period notable in the Vocontian Basin (Figure 5.20). Kujau et al., (2013) found this arid period did not occur in the Mid Polish Basin however, but a coeval humid period occurred in both the Vocontian and Mid Polish basins during the peak of the Valanginian CIE. Unfortunately, in the Weald Basin, following the arid period noted in the sphaerosiderites at the onset of the CIE, the sphaerosiderites up-section in the Wadhurst Clay are recrystallised. Therefore, the humid period associated with the CIE cannot be inferred directly in the Wealden record. The palynological (Batten, 1982; Batten, 1998), sedimentological (Allen, 1998), and petrographic evidence (Chapter 4) suggests the Wadhurst Clay may have experienced more oxidising and perhaps more transgressive conditions than the formations above or below . It is possible the Wadhurst Clay is in fact, evidence of increased humidity, particularly as evidence of increased salinity was found to be inconclusive (Batten, 1998). However, the possibility of increased humidity in the Wadhurst Clay cannot be assessed further in this thesis, and merits future work. Above the Wadhurst Clay, the sphaerosiderites in the Tunbridge Wells Sand record a dry period, and then a shift to wetter conditions towards the Valanginian-Hauterivian boundary. This trend is also in keeping with the Vocontian Basin where conditions become more arid as $\delta^{13}C_{org}$ values start to gradually decrease, and then more humid before the Valanginian-Hauterivian boundary.

The arid periods during the Valanginian in the Vocontian Basin were interpreted to be reflective of poleward shifts in the Northern Hemisphere arid belt (Hasegawa et al., 2012; Kujau et al., 2013). By contrast, the humid periods are interpreted to be due to the movement

of the Inter Tropical Convergence Zone (ITCZ), or changes in monsoonal circulation, and/or extension of annual humid periods controlled by Milankovitch cycles, with secondary factors such as vegetation feedbacks controlling the extent of the intensification of the hydrological cycle (Kujau et al., 2013 and references therein). The similarities in the humid-arid periods between the Vocontian spore-pollen and the Weald Basin sphaerosiderite records suggest similar controls may have been operating on the regional hydrological cycle of these locations. By comparison, the Mid Polish Basin was at a higher palaeolatitude than the Vocontian and Weald basins, and hence the shifts in the arid climate belt may have been limited to lower palaeolatitudes (Kujau et al., 2013).

The Weald Basin and Vocontian Basin records also agree to some extent with Tethyan clay assemblage records from the Helvetic Alps and Lombardian Basin (Westermann et al., 2010; Duchamp-Alphonse et al., 2011; Westermann et al., 2013), in that arid periods are recognised at the onset of the CIE, and humid periods followed by arid periods occur during the peak and gradual recovery from the Valanginian CIE. However, further up-section into the Late Valanginian, higher variability is notable in the Tethyan clay assemblage records, interpreted as an unstable climate shifting between arid and humid phases. By contrast, the Weald Basin record shows onset of humidity towards the Valanginian-Hauterivian boundary. These differences between the clay assemblage and siderite record after the Valanginian CIE may be related to the differences in resolutions between records. The Wealden record of sphaerosiderites in the Tunbridge Wells Sand is too poor in resolution to evaluate the fluctuations from humidity to aridity inferred in some of the Tethyan records. It should also be noted that these shifts noted in humidity and aridity in the Weald Basin and Vocontian Basin are relative to the average humidity at the time. Therefore, the fact that arid phases are notable during the Valanginian does not discredit the evidence that the Valanginian may have been, in general, wetter relative to the Berriasian or Hauterivian.

The new terrestrial temperature data presented in this chapter suggests that despite the inferred regional hydrological changes, the Weald Basin continued to experience warm temperatures during the Early Cretaceous, which persisted through the Valanginian CIE. This corroborates well with marine proxies suggesting continued warm temperatures during the Early Cretaceous (Littler et al., 2011; Jenkyns et al., 2012; Vickers et al., 2019). As previously mentioned, prolonged 'cold snaps' have also been noted in the Arctic during the Early Cretaceous (Vickers et al., 2019b), while conditions in the low latitudes continued to be warm (Duchamp-Alphonse et al., 2011; Kujau et al., 2013; Westermann et al., 2013; Charbonnier et al., 2020). The Wealden sphaerosiderite data provides further evidence of warm low-latitude temperatures during the Valanginian CIE, supporting previous datasets. It is important to consider that high latitude sites from the Valanginian often have poorly constrained ages, and the evidence from glendonites suggests the 'cold snaps' were prolonged, and appear to pre-date and continue after the Valanginian CIE. However, it is important to note that these disparities in low and high latitude temperatures have been noted in several studies, and suggest this to be a real trend showing a steeper latitudinal gradient than expected in the Early Cretaceous, which merits further work, in particular to constrain the palaeogeography and ocean circulation in high latitude Arctic which may further our understanding of the differences in temperature between latitudes. Further work on understanding the duration of 'cold snap' events and how they fit in the context of the transient climate perturbations of the Early Cretaceous is also required to fully gage the differences in climate between latitudes, and their underlying causes.

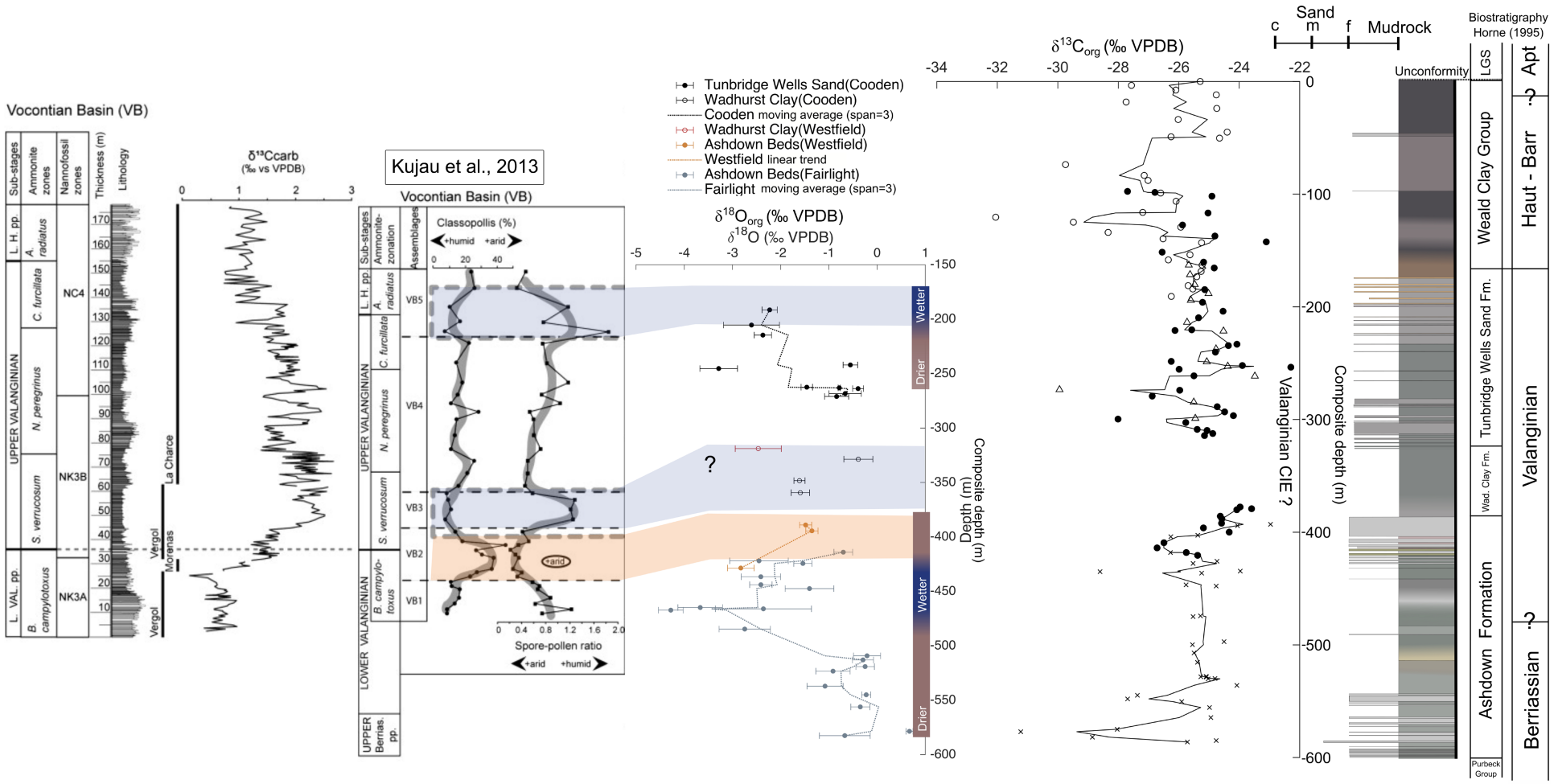


Figure 5.20: Comparison of the Wealden sphaerosiderite record to spore-pollen assemblages from Kujau et al., 2013. At the onset of the Valanginian CIE, the siderite record matches the aridity in the Vocontian Basin. The siderite record correlated well to the humid/arid periods noted in the Upper Valanginian in the Vocation Basin.

5 Conclusions

A record of sphaerosiderites through the Wealden Supergroup from the Weald basin show variant $\delta^{13}C_{siderite}$ and invariant $\delta^{18}O_{siderite}$ producing the characteristic Meteoric Sphaerosiderite Lines (MSL's) in most cases. The average $\delta^{18}O_{siderite}$ within the stratigraphy shows a long-term fluctuating trend from isotopically lighter (–4‰) to isotopically heavier values (0.66‰). The $\delta^{13}C_{siderite}$ values ranged from –40‰ to +2‰, suggesting multiple pathways of converting organic matter to Dissolved Inorganic Carbon (DIC) were operating, as expected of low-latitude wetland environments. Representative sphaerosiderites dispersed through the stratigraphy show formation temperatures of 33–39ºC, suggesting continued warmth, supporting sea surface temperature proxies from low latitudes during the Early Cretaceous (Littler et al., 2011). The reconstructed groundwaters using these temperatures are isotopically heavy (–3.7‰ to 1.2‰), suggesting pore waters may have undergone modification through evaporation, as also suggested by the limited SIMS transects and mixing lines. As the formation temperatures remain relatively similar throughout the record, the $\delta^{18}O_{siderite}$ changes are thought to be unrelated to temperature. Instead, climate models and sedimentological evidence suggests the moisture source for the Weald Basin was the Proto-Atlantic and/or Tethys, with $\delta^{18}O_{seawater}$ of 0.5–1‰. This only partially explains the high $\delta^{18}O_{groundwaters}$ values, as modelled $\delta^{18}O_{precipitation}$ values during the formation months are lower. The good correlation between siderite clumped temperatures and modelled summer temperatures (Haywood et al., 2004; Farnsworth, *pers. comm.,* 2019), and isotopically heavy reconstructed groundwaters are interpreted as evidence of a seasonally summer-biased record. To account for the high reconstructed $\delta^{18}O_{groundwaters}$ values, the sphaerosiderites are interpreted as growing in groundwaters mainly recharged over winter (as suggested by GCM's), and modified over spring due to increased evaporation as temperatures increased.

This modification by evaporation is supported by SIMS transects and evidence from mixing lines which deviate from MSL's.

In the long-term trend, the heavier average $\delta^{18}O_{siderite}$ values from sphaerosiderite horizons in the stratigraphy are interpreted as arid periods of lower precipitation and/or higher evaporation, while the lighter $\delta^{18}O_{siderite}$ values are interpreted to be more humid conditions with higher precipitation and/or less evaporation. The humid-arid periods also align well with the spore-pollen record of Kujau et al., (2013) from the Vocontian Basin at the onset of the Valanginian CIE, and during the gradual decrease of $\delta^{13}C$ values, with both records suggesting aridity. The Vocontian record suggests increased humidity at the peak of the CIE, which cannot be assessed in the recrystallised sphaerosiderites present in the Wadhurst Clay during the presumed peak of the CIE. However, the Wadhurst Clay also contains degraded and poorly preserved organic matter, recrystallisation of sphaerosiderites, and has been hypothesised to indicate a more oxidative transgressive palaeoenvironment (Batten, 1982; Allen et al., 1998; Batten, 1998). The Wadhurst Clay could perhaps be interpreted as evidence of humid conditions in line with the humid conditions at the peak of the Valanginian CIE in the Vocontian Basin, Mid Polish Basin, Lombardian Basin, and Helvetic Alps (Kujau et al., 2013; Westermann et al., 2013). Up-section from the Wadhurst Clay, the Wealden record agrees relatively well with Tethyan records, recording a period of aridity and then humidity towards the Valanginian-Hauterivian boundary (Kujau et al., 2013). The changes in humidity and aridity are interpreted to be controlled by the movement of the Northern Hemisphere arid belt and ITCZ, modulated by Milankovitch cycles (Kujau et al., 2013). Although astrochronology cannot be assessed in the Weald Basin, the similarities between the sphaerosiderite record of inferred humid-arid periods and that of the Tethyan deposits suggests that similar controls on hydrology were operating in the Weald Basin.

Chapter 6
Conclusions and Future Work

1 Conclusions

1.1 Sphaerosiderites as a proxy for palaeoenvironment

Siderite synthesis experiments suggest the following general order of elemental preference during siderite growth: Mn > Ca >> Mg. Cation uptake was found to be controlled by a mixture of growth rate, pH, pCO_2, and cation concentrations. In nucleation experiments at high siderite saturation, Mn and Ca uptake was detectable, while in growth experiments, at lower siderite saturations and with growth rates more analogous to natural settings, only Mn uptake was identified. Mg uptake was not discernible at ambient temperatures in nucleation or growth experiments. These results suggest that abiotic siderite precipitation does not involve appreciable uptake of Ca and/or Mg at slow growth rates, more analogous to natural wetlands, and therefore, other parameters are likely influencing the Ca or Mg uptake in natural siderites. Importantly, this evidence demonstrates the elemental composition of siderite cannot be solely controlled by pore water cation concentrations (i.e. freshwater or marine) as previously thought (Mozley, 1989). An extensive literature review of ancient and modern siderites, and the composition of natural Wealden sphaerosiderites, suggests that presence of other carbonate phases such as calcite, pyrite, and the sedimentological context of sphaerosiderite bearing units can instead provide insights into the palaeoenvironmental conditions.

Although the elemental composition of siderites cannot provide information on marine incursions, the heterogeneity or homogeneity in patterns of elemental uptake, morphological variability within sphaerosiderites, and the sedimentological context of their depositional units can still provide important insight into the dynamics of ancient wetland systems. The heterogeneity in sphaerosiderites suggest they record multiple periods of siderite growth with changing palaeoenvironmental conditions. As sphaerosiderites are pedogenic carbonates, associated with palaeosols and often rootlets, it can be confidently assumed that the sphaerosiderites within one palaeosol horizon grew over a time period in which that soil horizon was active. Hence, the sphaerosiderites that preserve primary textures should be preserving conditions during the deposition of this palaeosol horizon in which it is growing. This exact period of growth is unconstrained, and modern siderites have been known to grow between 6 months and 100's of years. However, in understanding the presence of sphaerosiderites in the geological record, it can be assumed that each sphaerosiderite horizon is likely active during the period where the soil horizon was active (on a scale of 10^1 -10^3 years, (Retallack, 2008)). Based on the low sampling resolution possible in the Wealden Basin, this does not hinder their use as palaeoclimatic tools within stratigraphy spanning millions of years.

Siderites used in palaeoclimatic studies should undergo extensive mineralogical, morphological, elemental, and isotopic characterisation to better assess suitability for palaeoclimatic reconstructions. This allows a screening process for secondary textures, such as recrystallisation, allowing identification of samples which may have undergone post-burial diagenesis and may no longer record a primary signal. Isotopic analyses are another method to screen sphaerosiderites, as shown in Chapter 5, through producing several data points from single sphaerosiderite horizons, and assessing whether they show mixing lines which may suggest marine incursions or other burial diagenesis which may alter the isotopic signature. Coupled with this, the matrix surrounding the sphaerosiderites also needs to be

studied to assess whether secondary cements have precipitated, which may suggest that secondary growth may also have occurred around sphaerosiderites. As shown in this thesis, multiple analytical methods together produce a better understanding of the sphaerosiderite preservation.

1.2 An Early Cretaceous terrestrial carbon isotope record from the Weald Basin

Based on the bulk organic carbon isotope ($\delta^{13}C_{org}$) record, the Wealden Supergroup can be tentatively correlated to the Wessex Basin (Robinson and Hesselbo, 2004) and a marine composite (Ogg et al., 2016). The correlations suggest the Wealden Supergroup is of Berriasian–Aptian in age, as previously suggested by biostratigraphy (Horne, 1995).

The Valanginian Carbon Isotope Excursion (CIE) onset is notable at the top of the Ashdown Formation, and the continued relatively high $\delta^{13}C_{org}$ values are notable at the base of the Tunbridge Wells Sand, together interpreted as the broad peak of the CIE. The $\delta^{13}C_{org}$ values show a gradual shift to lower values up-section through the Tunbridge Wells Sand and into the Weald Clay Group. The Wadhurst Clay samples (stratigraphically between Ashdown and Tunbridge Wells Sand) were not included within this record, as the organic matter preservation is considered poor, and $\delta^{13}C_{org}$ shows a facies-specific shift likely due to the presence of a mixture of organic matter sources. Above the Tunbridge Wells Sand, the resolution within the Weald Clay Group was also limited by sampling availability, and the correlations to the marine composite record in the Hauterivian–Aptian are inconclusive and tentative at best.

The Valanginian section is also more expanded compared to the Hauterivian–Barremian section in the Weald Basin. An increased sedimentation flux during the Valanginian is in keeping with predicted increase in weathering and sediment input into basins, and

intensification of the hydrological cycle during the Valanginian (Lini et al., 1992; Weissert and Erba, 2004; Westermann et al., 2010; Kujau et al., 2013; Westermann et al., 2013).

1.3 Early Cretaceous palaeohydrology of the Weald Basin

The sphaerosiderites from the Wealden Supergroup of the Weald Basin record morphological and compositional heterogeneity within individual spheres, and throughout the stratigraphy, indicating growth in a dynamic wetland system.

The average $\delta^{18}O_{siderite}$ from the Weald Basin varies from –3.5‰ to 0.6‰ (VPDB), while $\delta^{13}C_{siderite}$ varies from –40‰ to 5‰ (VPDB). The $\delta^{18}O_{siderite}$ and $\delta^{13}C_{siderite}$ of Wealden sphaerosiderite horizons dominantly plot along Meteoric Sphaerosiderite Lines (MSL's) with invariant $\delta^{18}O_{siderite}$ and variant $\delta^{13}C_{siderite}$, suggesting growth in meteoric groundwaters. A limited number of horizons contain examples of mixing lines that suggest marine mixing, or an evaporative trend associated with increased depth in soil profile. SIMS transects reveal isotopic heterogeneity within individual spheres, recording isotopically heavier $\delta^{18}O_{siderite}$ and isotopically lighter $\delta^{13}C_{siderite}$ in the core compared to the rim. The trends in SIMS transects are interpreted to reflect decreased evaporation during latter stages of growth, due to gradual burial of the spheres deeper in the soil profile. The Δ_{47} formation temperatures from representative sphaerosiderites are 33–39ºC and correlate well with high reconstructed sea surface temperatures and climate model temperatures (Haywood et al., 2004; Littler et al., 2011; Farnsworth, *pers comm.* 2019), suggesting continued warmth in the Early Cretaceous.

The $\delta^{18}O_{groundwater}$ reconstructed using Δ_{47} temperatures and average $\delta^{18}O_{siderite}$ from sphaerosiderite horizons suggest the groundwaters were isotopically heavy throughout the Wealden supergroup (–3.7‰ to 2.6‰ VSMOW). Comparisons with oxygen isotope composition of seawater and precipitation in climate models (Farnsworth, *pers. comm.*, 2019) suggests groundwaters were likely modified through evaporation during spring, also

supported by SIMS transects and mixing lines. The high Δ_{47} temperatures and high reconstructed groundwater, alongside comparison to modern siderites (Driese et al., 2010; Ludvigson et al., 2013; Van Dijk et al., 2019), suggest the Wealden sphaerosiderites are likely recording a summer-biased signal. The elemental and morphological heterogeneity, and SIMS transects also suggest the spheres were growing high enough in the soil profile to be experiencing a dynamic environment, supporting the inferred summer bias.

The $\delta^{18}O_{siderite}$ trend of alternating isotopically heavier and lighter values through the stratigraphy is interpreted as periods of aridity with lower precipitation and/or higher evaporation, and periods of humidity with higher precipitation and/or less evaporation respectively. The humid-arid periods inferred from the siderite record correlate to spore-pollen inferred humidity changes in the Vocontian Basin during the Early Cretaceous (Kujau et al., 2013), and to clay assemblages in Tethyan records (Westermann et al., 2013). The humid-arid phases occur both prior to and after the CIE in all basins, suggesting some of these climate changes were controlled by factors other than global carbon cycle perturbations. The suggested control on humidity and aridity is the movement of the climate belts (mainly the Northern Hemisphere Arid Belt) as well as the Inter Tropical Convergence Zone (ITCZ), modulated by Milankovitch cycles (Hasegawa et al., 2012; Kujau et al., 2013). Kujau et al., (2013) suggest secondary parameters coupled with astronomical forcing, such as vegetation feedbacks, may have intensified the climatic changes (e.g., enhanced the hydrological cycle) during some periods but not others. It is likely that similar controls on climate were influencing sedimentary processes in the Weald Basin, which was located at a similar palaeolatitude to the Vocontian Basin.

However, Kujau et al., (2013) also suggest the humid periods may have reflected intensified monsoonal precipitation, as eccentricity is known to control long-term monsoonal intensity. Charbonnier et al., (2016) also suggested an eccentricity controlled

monsoonal circulation to be responsible for these Tethyan humid-arid periods. However, the definition of a monsoon—'*>55% of annual precipitation falling during local summer and local summer-minus-winter precipitation rate being >2 mm/day*' (Farnsworth et al., 2019b) contradicts the climate models discussed in this thesis (Haywood et al., 2004; Farnsworth, pers. comm., 2019). In the climate models, seasonal wind reversals are notable, but the Weald Basin remains wet year-round from Valanginian–Hauterivian, although precipitation is higher in winter. The Berriasian results indicate a summer-based precipitation regime which could potentially match the monsoon definition; however, evidence of monsoons cannot be verified from the siderite data. Hence, using the term 'monsoonal precipitation', as has been used for some of the Tethyan sites, is deemed unsuitable for the Weald Basin. The simple explanations for the humidity-aridity changes in the Weald Basin remain Milankovitch cycle-controlled shifting of the climatic belts and/or ITCZ, in addition to global carbon cycle perturbations.

Carbon burial at particular latitudes during the Valanginian could have been enhanced via intensified humidity that can be attributed to the shifting climate belts and ITCZ. Indeed, intensification of the hydrological cycle has been suggested as a driver for the Valanginian CIE, as it would have contributed to increased weathering, runoff, and the fertilization of basins, thus, an increase in productivity and subsequent carbon burial (Weissert and Erba, 2004; Charbonnier et al., 2016). Though evidence for enhanced terrestrial organic carbon burial is lacking from the Weald Basin, the expanded Valanginian succession compared to that of the Hauterivian–Barremain is indicative of an increased sedimentation rate.

Apart from Milankovitch cycles, global carbon cycle perturbations may have affected the movement of the climate belts/ITCZ. Recent work suggests the emplacement of the Parana-Etendeka Large Igneous Province (P-E LIP) and the Valanginian CIE are coincident,

implying a volcanic trigger for the event (Thiede and Vasconcelos, 2010; Martinez et al., 2015; Charbonnier et al., 2017). The emplacement of the P-E LIP would have contributed to increased atmospheric pCO_2, and thus to changes in radiative forcing, decoupled from the orbital forcing, reinforcing greenhouse conditions. Warming associated with the P-E LIP during the Valanginian has been suggested as a mechanism for the intensification of the hydrological cycle and changes in ocean chemistry (pH, carbonate ion availability) (Lini et al., 1992; Weissert and Erba, 2004), linked to the crisis in pelagic carbonate producers (Erba et al., 2004; Weissert and Erba, 2004; Duchamp-Alphonse et al., 2007). Furthermore, changes in atmospheric pCO_2 and temperatures are also thought to influence changes in Hadley circulation, thereby affecting the location of climate belts (Hasegawa et al., 2012). Therefore, increased atmospheric pCO_2 from the P-E LIP and subsequent reinforced greenhouse conditions may have operated during the Valanginian, and contributed to the movements of the climate belts and/or the ITCZ (Hasegawa et al., 2012). However, marine (Littler et al., 2011) and terrestrial (this study) records suggest no significant temperature change at low-latitude sites during the Valanginian CIE. Perhaps, the increases in pCO_2 affected high latitudes more, and therefore, the latitudinal temperature gradients, without significantly changing temperatures at low-latitude sites. Whether the high latitudes experienced warmth throughout the Valanginian CIE is still debatable, as existing records often have poor age constraints on the onset of the CIE, and palaeogeographic or palaeoceanographic differences remain poorly understood. Further work on high-latitude sites could help evaluate the link between climatic changes and the Valanginian CIE further.

2 Future Work

2.1 Sphaerosiderites as a proxy for palaeoenvironment

This thesis has provided new constraints on abiotic elemental uptake in siderite, which suggests Ca and Mg uptake is negligible at saturation states relevant to natural wetland systems. However, natural siderites show a background level of Mg and/or Ca uptake in many cases (up to 2 mol%) which cannot be explained by abiotic constraints and/or diagenetic processes. Existing constraints on biologically mediated precipitation is limited and precipitation mechanisms within experiments are poorly constrained. Hence, further work on the role of biological components on siderite precipitation and elemental uptake is necessary. For instance, the role of peptides has been explored in elemental uptake in calcite through experimental synthesis (Stephenson et al., 2008). Experimental synthesis of siderite in the presence of organic macromolecules could be explored similarly. Constraining further temperature controls (e.g. > 55°C) on Mg and Ca uptake in siderite may also help to distinguish between the primary and post-burial elemental compositions in siderite.

2.2 Age constraints and sampling resolution in the carbon isotope record from the Weald Basin

Age constraints based on ostracod biostratigraphy are poor in certain horizons of the Wealden Supergroup (eg. Berriasian-Valanginian boundary, Barremian-Aptian boundary), which results in difficulties when correlating to the Wessex basin and/or the marine records. Although the onset and gradual recovery of the Valanginian CIE is demonstrated, the Wadhurst Clay section leaves a significant gap. The Wadhurst Clay Formation has proved to contain several interesting indicators of a palaeoenvironmental change; facies-specific $\delta^{13}C_{org}$ shift in bulk organic matter and regional recrystallisation of sphaerosiderites. Although prior sedimentological and palynological work has indicated that the Wadhurst

Clay palaeoenvironment may be distinct from the other formations of the Wealden Supergroup, the evidence is inconclusive (Batten, 1982; Allen et al., 1998; Batten, 1998). Further detailed organic petrography, palynology, palaeontology, sedimentology, and compound specific carbon isotope records of the Wadhurst Clay could better constrain the sources of organic matter, and help constrain the Valanginian CIE. Further characterisation of the Wadhurst Clay could also help to determine whether the transgressive conditions inferred reflect humid conditions or salinity changes, and to further elucidate on the facies-specific $\delta^{13}C_{org}$ changes notable in the bulk organic record.

Furthermore, the Barremian-Aptian boundary could not be reliably identified due to the poor resolution of bulk organic $\delta^{13}C_{org}$ in the Weald Clay Group. Alongside this, the Weald Clay Group has been suggested to have fluctuated in salinity (Batten, 1998), and stratigraphic comparisons in this thesis indicate the sedimentation rate may have been lower than in the Valanginian sections, leading to a more condensed Hauterivian–Barremian section. Further work on the stratigraphy of the Weald Clay would help better assess the trend in $\delta^{13}C_{org}$ during the Hauterivian–Barremian in the Weald Basin, and in particular, the variability in sedimentation rates between different localities. A quantitative understanding of the sedimentation rates and/or the identification of regional erosional surfaces could better evaluate the carbon isotope record and provide new localities that may increase the sampling resolution of the carbon isotope record within the Weald Clay Group. Magnetostratigraphy of the Weald Clay Group may also help identify the Hauterivian–Barremian boundary, as arguably, it should show a relatively stable Hauterivian compared to a Barremian with several reversals.

2.3 Sphaerosiderites and palaeohydrology

Average $\delta^{18}O$ from sphaerosiderite horizons through the Wealden Supergroup constitute a unique record of stratigraphic change in $\delta^{18}O$ from sphaerosiderites. It is now

important to review the regional extent of such stable isotope compositional trends from sphaerosiderite records from various time periods. It is also important to evaluate isotopic heterogeneity within individual spheres to constrain whether the evaporation and burial trends inferred from the $\delta^{13}C$ and $\delta^{18}O$ trends within individual transects are universal.

The data from the Wealden sphaerosiderites also emphasises the need to re-evaluate our understanding of existing sphaerosiderite data. As demonstrated in this thesis, select samples from Robinson et al., (2010) were shown to record clumped isotope temperatures 10ºC higher than the MAT assumed for growth during initial groundwater calculations. This has important implications for calculated groundwater, which for the samples from Robinson et al., (2010), were 2–3‰ higher than previously published. The comparisons between the different analytical methods and sample preparation using the Robinson et al., (2010) 'FC' samples (e.g digestion in Kiel, Gasbench, analyses using IRMS, SIMS, and sample preparation of small/large batches of powder) also illustrates the complexity of siderite records. Previous studies may have been too simplistic in their palaeoclimatic inferences due to the assumptions of year-round growth in MAT and constant groundwater, without considering the compositional and isotopic heterogeneity to fully constrain palaeoclimatic implications. The Wealden record also shows that sphaerosiderites are important recorders of the variability in ancient wetlands, providing unique insight into terrestrial hydrology, and may be an unexplored record of seasonality in deep time.

Furthermore, much emphasis has been placed on the Aptian–Albian latitudinal $\delta^{18}O_{siderite}$ gradient produced from North American sphaerosiderites in our understanding of Cretaceous hydrology (White et al., 2001; Ufnar et al., 2004a; Ufnar et al., 2004b; Suarez et al., 2011). In light of the data presented in this thesis, it would be prudent to re-analyse representative siderite samples where possible, for stable isotope compositions, isotope transects, and clumped isotopes, with current method-specific correction factors (Fernandez et al., 2016).

This would allow an improved understanding of the absolute values of the North American sphaerosiderites, which could ultimately impact the broader understanding of the Cretaceous hydrological cycle. In particular, an assessment of the palaeoenvironmental implications of sphaerosiderites from the North American deposits in light of our current understanding of siderite growth in dynamic modern wetlands is required (Pye et al., 1990; Moore et al., 1992; Driese et al., 2010; Ludvigson et al., 2013; Van Dijk et al., 2019; Lin et al., 2019). For instance, did the North American sphaerosiderites indeed grow in constant temperature and constant groundwaters as assumed? Do they show similarly heterogenous isotope transects as the Wealden sphaerosiderites? If the North American sphaerosiderites also contain a seasonal bias (e.g. summer bias), then perhaps the groundwaters during growth were isotopically heavier (due to modification through evaporation) than published data suggests, and subsequently the latitudinal precipitation gradient would need to be reassessed. Palaeogeography has already been suggested as a possible influence that needs consideration when interpreting the steep latitudinal gradient in the North American siderites (Poulsen et al., 2007). However, newer isotope enabled climate models with better regional resolution could help further understand the implications of the North American siderite data. For instance, comparing the precipitation and evaporation rates, moisture sources, and temperature evolution in the North American localities in climate models to siderite clumped isotope temperatures and re-analysed stable isotope compositions could provide insights into some of the questions discussed above.

References Cited

Addadi L., Raz S. and Weiner S. (2003) Taking advantage of disorder: Amorphous calcium carbonate and its roles in biomineralization. Adv. Mater. 15, 959–970.

Aguado R., Company M., Castro J. M., de Gea G. A., Molina J. M., Nieto L. M. and Ruiz-Ortiz P. A. (2018) A new record of the Weissert episode from the Valanginian succession of Cehegín (Subbetic, SE Spain): Bio- and carbon isotope stratigraphy. *Cretac. Res.* **92**, 122–137.

Allen J. (1981) Lower Cretaceous tides revealed by cross-bedding with mud drapes. *Nature* **289**, 579–581.

Allen P. (1946) Notes on Wealden fossil soil-beds. *Proc. Geol. Assoc.* **57**, 303–314.

Allen P. (1967) Origin of the Hastings facies in North-western Europe. *Proc. Geol. Assoc.* **78**, 27–105.

Allen P. (1981) Pursuit of Wealden models. *J. Geol. Soc. London.* **138**, 375–405.

Allen P. (1975) Wealden of the Weald: a new model. *Proc. Geol. Assoc.* **86**, 389–437.

Allen P. (1989) Wealden research—ways ahead. *Proc. Geol. Assoc.* **100**, 529–564.

Allen P., Alvin K. L., Andrews J. E. and Batten D. J. (1998) Purbeck-Wealden (early Cretaceous) climates. *Proc. Geol. Assoc.* **109**, 197–236.

Allen P. and May F. R. S. R. (1959) The Wealden environment: Anglo-Paris Basin. *Philos. Trans. R. Soc. Lond. B. Biol. Sci.* **242**, 283–346.

Allen P. and Wimbledon W. A. (1991) Correlation of NW European Purbeck-Wealden (nonmarine Lower Cretaceous) as seen from the English type-areas. *Cretac. Res.* **12**, 511-526

Amiot R., Lécuyer C., Buffetaut E., Fluteau F., Legendre S. and Martineau F. (2004) Latitudinal temperature gradient during the Cretaceous Upper Campanian-Middle Maastrichtian: $\delta^{18}O$ record of continental vertebrates. *Earth Planet. Sci. Lett.* **226**, 255–272.

Amiot R., Wang Xu, Zhou Z., Wang Xiaolin, Buffetaut E., Lécuyer C., Ding Z., Fluteau F., Hibino T., Kusuhashi N., Mo J., Suteethorn V., Wang Y., Xu X. and Zhang F. (2011) Oxygen isotopes of East Asian dinosaurs reveal exceptionally cold Early Cretaceous climates. *Proc. Natl. Acad. Sci. U.S.A.* **108**, 5179–5183.

Arthur M. A., Dean W. E. and Schlanger S.O. (1985) Variations in the global carbon cycle during the Cretaceous related to climate, volcanism, and changes in atmospheric CO_2. *The carbon cycle Atmos. CO2 Nat. Var. Archean to Present* **32**, 504–529.

Austen P. A. and Batten D. J. (2018) English Wealden fossils: an update. *Proc. Geol. Assoc.* **129**, 171–201.

Azoulay I., Rémazeilles C. and Refait P. (2012) Determination of standard Gibbs free energy of formation of chukanovite and Pourbaix diagrams of iron in carbonated media. *Corros. Sci.* **58**, 229–236.

Bahrig B. (1989) Stable isotope composition of siderite as an indicator of the paleoenvironmental history of oil shale lakes. *Palaeogeogr. Palaeoclimatol. Palaeoecol.* **70**, 139–151.

Baker J. C., Kassan J. and Hamilton P. J. (1996) Early diagenetic siderite as an indicator of depositional environment in the Triassic Rewan Group, southern Bowen Basin, eastern Australia. *Sedimentology* **43**, 77–88.

Barbarin N., Bonin A., Mattioli E., Pucéat E., Cappetta H., Gréselle B., Pittet B., Vennin E. and Joachimski M. (2012) Evidence for a complex Valanginian nannoconid decline in the Vocontian basin (South East France). *Mar. Micropaleontol.* **84**–**85**, 37–53.

Barrera, E., & Savin S. M. (1999) Evolution of late Campanian-Maastrichtian marine climates and oceans. *Spec. Pap. Soc. Am.*, 245–282.

Barron E. J. (1983) A warm, equable Cretaceous: The nature of the problem. *Earth Sci. Rev.* **19**, 305–338.

Barron E. J. and Peterson W. H. (1989) Model simulation of the cretaceous ocean circulation. *Science (80).* **244**, 684–686.

Batten D. J. (1998) Palaeonenvironmental implications of plant, insect and other organic-walled microfossils in the Weald Clay Formation (Lower Cretaceous) of southeast England. *Cretac. Res.* **19**, 279–315.

Batten D. J. (1982) Palynofacies and salinity in the Purbeck and Wealden of southern England. *Asp. Micropalaeontology*, 278–308.

Batten D. J. and Lister J. K. (1988a) Early Cretaceous dinoflagellate cysts and chlorococcalean algae from freshwater and low salinity palynofacies in the English Wealden. *Cretac. Res.* **9**, 337–367.

Batten D. J. and Lister J. K. (1988b) Evidence of freshwater dinoflagellates and other algae in the English Wealden (Early Cretaceous). *Cretac. Res.* **9**, 171–179.

Beerling D., Berner R. A., Mackenzie F. T., Harfoot M. B. and Pyle J. A. (2009) Methane and the CH_4-related greenhouse effect over the past 400 million years. *Am. J. Sci.* **309**, 97–113.

Beerling D. J. and Royer D. L. (2011) Convergent Cenozoic CO_2 history. *Nat. Geosci.* **4**, 418–420.

Bender M. M. (1971) Variations in the $^{13}C/^{12}C$ ratios of plants in relation to the pathway of photosynthetic carbon dioxide fixation. *Phytochemistry* **10**, 1239–1244.

Benner R., Fogel M. L., Sprague E. K. and Hodson R. E. (1987) Depletion of C in lignin and its implications for stable carbon isotope studies. *Nature* **329**, 708–710.

Bennett M. R., Doyle P. and Mather A. E. (1996) Dropstones: Their origin and significance. *Palaeogeogr. Palaeoclimatol. Palaeoecol.* **121**, 331–339.

Bernasconi S. M., Müller I. A., Bergmann K. D., Breitenbach S. F. M., Fernandez A., Hodell D. A., Jaggi M., Meckler A. N., Millan I. and Ziegler M. (2018) Reducing Uncertainties in Carbonate Clumped Isotope Analysis Through Consistent Carbonate-Based Standardization. *Geochemistry, Geophys. Geosystems* **19**, 2895–2914.

Bernasconi S. M., Schmid T. W., Grauel A. L. and Mutterlose J. (2011) Clumped-isotope geochemistry of carbonates: A new tool for the reconstruction of temperature and oxygen isotope composition of seawater. *Appl. Geochemistry* **26**, S279–S280.

Berner R. A. (1999) A new look at the long-term carbon cycle. *GSA Today* **9**, 1–6.

Berner R. A. (1971) Principles of Chemical Sedimentology., McGraw Hill.

Berner R. A. (1983) Sedimentary pyrite formation. *Geochemica Cosmochem. Acta* **48**, 605–615.

Berner R. A. and Kothavala Z. (2001) Geocarb III: A revised model of atmospheric CO2over phanerozoic time. *Am. J. Sci.* **301**, 182–204.

Berner R. A (2003) Fuels and Atmospheric Composition. *Nature* **426**, 323–326.

Bice K. L., Birgel D., Meyers P. A., Dahl K. A., Hinrichs K. U. and Norris R. D. (2006) A multiple proxy and model study of Cretaceous upper ocean temperatures and atmospheric CO_2 concentrations. *Paleoceanography* **21**, 1–17.

Blue C. R. and Dove P. M. (2015) Chemical controls on the magnesium content of amorphous calcium carbonate. *Geochim. Cosmochim. Acta* **148**, 23–33.

Blue C. R., Giuffre A., Mergelsberg S., Han N., De Yoreo J. J. and Dove P. M. (2017) Chemical and physical controls on the transformation of amorphous calcium carbonate into crystalline $CaCO_3$ polymorphs. *Geochim. Cosmochim. Acta* **196**, 179–196.

Bocherens H., Friis E. M., Mariotti A. and Pedersen, K R. (1993) Carbon isotopic abundances in Mesozoic and Cenozoic fossil plants: Palaeoecological implications. *Lethaia* **26**, 347–358.

Brečević L. and Nielsen A. E. (1989) Solubility of amorphous calcium carbonate. *J. Cryst. Growth* **98**, 504–510.

Browne G. H. and Kingston D. M. (1993) Early diagenetic spherulitic siderites from Pennsylvanian palaeosols in the Boss Point Formation, Maritime Canada. *Sedimentology* **40**, 467–474.

Burgess J. (1978) *Metal ions in solution.*, Ellis Horwood Limited, Chichester.

Burla S., Heimhofer U., Hochuli P. A., Weissert H. and Skelton P. (2008) Changes in sedimentary patterns of coastal and deep-sea successions from the North Atlantic (Portugal) linked to Early Cretaceous environmental change. *Palaeogeogr. Palaeoclimatol. Palaeoecol.* **257**, 38–57.

Butler I. B., Schoonen M. A. A. and Rickard D. T. (1994) Removal of dissolved oxygen from water: A comparison of four common techniques. *Talanta* **41**, 211–215.

Came R. E., Brand U. and Affek H. P. (2014) Clumped isotope signatures in modern brachiopod carbonate. *Chem. Geol.* **377**, 20–30.

Cao M., Gregson K. and Marshall S. (1998) Global methane emission from wetlands and its sensitivity to climate change. *Atmos. Environ.* **32**, 1–7.

Carothers W. W., Adami L. H. and Rosenbauer R. J. (1988) Experimental oxygen isotope fractionation between side&-water and phosphoric acid liberated CO_2 in siderite. *Geochem n Cosmochim. Acta* **52**, 2445–2450.

Casey R. (1961) The stratigraphical palaeontology of the Lower Greensand. *Palaeontology* **3**, 486–621.

Celestino R., Wohlwend S., Rehakova D. and Weissert H. (2017) Carbon isotope stratigraphy, biostratigraphy and sedimentology of the Upper Jurassic–Lower Cretaceous Rayda Formation, Central Oman Mountains. *Newsletters Stratigr.* **50**, 91–109.

Cerling T. E, Wang Y. and Quade J. (1993) Expansion of C4 ecosystems as an indicator of global ecological change in the late Miocene. *Nature* **361**, 344–345.

Cerling T E, Wang Y. and Quade J. (1993) Global ecological change in the late Miocene: expansion of C4 ecosystems. *Nature* **361**, 344–345.

Channell J. E. T., Erba E. and Lini A. (1993) Magnetostratigraphic calibration of the Late Valanginian carbon isotope event in pelagic limestones from Northern Italy and Switzerland. *Earth Planet. Sci. Lett.* **118**, 145–166.

Charbonnier G., Duchamp-Alphonse S., Adatte T., Föllmi K. B., Spangenberg J. E., Gardin S., Galbrun B. and Colin C. (2016) Eccentricity paced monsoon-like system along the northwestern Tethyan margin during the Valanginian (Early Cretaceous): New insights from detrital and nutrient fluxes into the Vocontian Basin (SE France). *Palaeogeogr. Palaeoclimatol. Palaeoecol.* **443**, 145–155.

Chen T., Neville A. and Yuan M. (2005) Assessing the effect of Mg^{2+} on $CaCO_3$ scale formation–bulk precipitation and surface deposition. *J. Cryst. Growth* **275**, e1341–e1347.

Choi K. and Kim S. P. (2006) Late Quaternary evolution of macrotidal Kimpo tidal flat, Kyonggi Bay, west coast of Korea. *Mar. Geol.* **232**, 17–34.

Choi K. S., Khim B. K. and Woo K. S. (2003) Spherulitic siderites in the Holocene coastal deposits of Korea (eastern Yellow Sea): Elemental and isotopic composition and depositional environment. *Mar. Geol.* **202**, 17–31.

Chumakov N. M., Zharkov M. A., Herman A. B., Doludenko M. P., Kalandadze N. N., Lebedev E. L., Ponomarenko A. G. and Rautian A. S. (1995) Climatic belts of the mid-Cretaceous time. *Stratigr. Geol. Correl.* **3**, 42–63.

Coleman M. L. (1993) Microbial processes: Controls on the shape and composition of carbonate concretions. *Mar. Geol.* **113**, 127–140.

Curtis C. D., Coleman M. L. and Love L. G. (1986) Pore water evolution during sediment burial from isotopic and mineral chemistry of calcite, dolomite and siderite concretions. *Geochim. Cosmochim. Acta* **50**, 2321–2334.

Davis K. J., Dove P. M., Wasylenki L. E. and De Yoreo J. J. (2004) Morphological consequences of differential Mg^{2+} incorporation at structurally distinct steps on calcite. *Am. Mineral.* **89**, 714–720.

DeConto R. M., Hay W. W., Thompson S. L. and Bergengren J. (1999) Late Cretaceous climate and vegetation interactions: Cold continental interior paradox. *Spec. Pap. Geol. Soc. Am.* **332**, 391–406.

Dideriksen K., Frandsen C., Bovet N., Wallace A. F., Sel O., Arbour T., Navrotsky A., De Yoreo J. J. and Banfield J. F. (2015) Formation and transformation of a short range ordered iron carbonate precursor. *Geochim. Cosmochim. Acta* **164**, 53–70.

Driese S. G., Ashley G. M., Li Z.-H. H., Hover V. C. and Owen R. B. (2004) Possible Late Holocene equatorial palaeoclimate record based upon soils spanning the Medieval Warm Period and Little Ice Age, Loboi Plain, Kenya. *Palaeogeogr. Palaeoclimatol. Palaeoecol.* **213**, 231–250.

Driese S. G., Ludvigson G. A., Roberts J. A., Fowle D. A., González L. A., Smith J. J., Vulava V. M. and McKay L. D. (2010) Micromorphology and stable-isotope geochemistry of historical pedogenic siderite formed in PAH-contaminated alluvial clay soils, Tennessee, USA. *J. Sediment. Res.* **80**, 943–954.

Dromgoole E. L. and Walter L. M. (1990) Iron and manganese incorporation into calcite: Effects of growth kinetics, temperature and solution chemistry. *Chem. Geol.* **81**, 311–336.

Duchamp-Alphonse S., Fiet N., Adatte T. and Pagel M. (2011) Climate and sea-level variations along the northwestern Tethyan margin during the Valanginian C-isotope excursion: Mineralogical evidence from the Vocontian Basin (SE France). *Palaeogeogr. Palaeoclimatol. Palaeoecol.* **302**, 243–254.

Duchamp-Alphonse S., Gardin S., Fiet N., Bartolini A., Blamart D. and Pagel M. (2007) Fertilization of the northwestern Tethys (Vocontian basin, SE France) during the Valanginian carbon isotope perturbation: Evidence from calcareous nannofossils and trace element data. *Palaeogeogr. Palaeoclimatol. Palaeoecol.* **243**, 132–151.

Edmunds F. H. and Gallois. R. W. (1965) *British regional geology: the Wealden district*., HM Stationery Office.

Ekart D. D. (1999) A 400 million year carbon isotope record of pedogenic carbonate: Implications for palaeoatmospheric carbon dioxide. *Am. J. Sci.* **299**, 805–827.

Emeis K. C. and Weissert H. (2009) Tethyan-Mediterranean organic carbon-rich sediments from Mesozoic black shales to sapropels. *Sedimentology* **56**, 247–266.

Erba E., Bartolini A. and Larson R. L. (2004) Valanginian Weissert oceanic anoxic event. *Geology* **32**, 149–152.

Erba E. and Tremolada F. (2004) Nannofossil carbonate fluxes during the Early Cretaceous: Phytoplankton response to nutrification episodes, atmospheric CO_2, and anoxia. *Paleoceanography* **19**, PA1008, 1-18

Erwin K. L. (2009) Wetlands and global climate change: The role of wetland restoration in a changing world. *Wetl. Ecol. Manag.* **17**, 71–84.

Farnsworth A., Lunt D. J., O'Brien C. L., Foster G. L., Inglis G. N., Markwick P., Pancost R. D. and Robinson S. A. (2019) Climate Sensitivity on Geological Timescales Controlled by Nonlinear Feedbacks and Ocean Circulation. *Geophys. Res. Lett.* **46**, 9880–9889.

Farnsworth A., Lunt D. J., Robinson S. A., Valdes P. J., Roberts W. H. G., Clift P. D., Markwick P., Su T., Wrobel N., Bragg F., Kelland S. J. and Pancost R. D. (2019) Past East Asian monsoon evolution controlled by paleogeography, not CO_2. *Sci. Adv.* **5**, 1–14.

Fernandez A., van Dijk J., Müller I. A. and Bernasconi S. M. (2016) Siderite acid fractionation factors for sealed and open vessel digestions at 70°C and 100°C. *Chem. Geol.* **444**, 180–186.

Fernandez A., Tang J. and Rosenheim B. E. (2014) Siderite "clumped" isotope thermometry: A new paleoclimate proxy for humid continental environments. *Geochim. Cosmochim. Acta* **126**, 411–421.

Fisher Q. J., Raiswell R. and Marshall J. D. (1998) Siderite concretions from nonmarine shales (Westphalian A) of the Pennines, England; controls on their growth and composition. *J. Sediment. Res.* **68**, 1034–1045.

Föllmi K. B. (2012) Early Cretaceous life, climate and anoxia. *Cretac. Res.* **35**, 230–257.

Follmi K. B., Weissert H., Bisping M. and Funk H. (1994) Phosphogenesis, carbon-isotope stratigraphy, and carbonate-platform evolution along the Lower Cretaceous northern Tethyan margin. *Geol. Soc. Am. Bull.* **106**, 729–746.

Fosbøl P. L., Thomsen K. and Stenby E. H. (2010) Review and recommended thermodynamic properties of $FeCO_3$. *Corros. Eng. Sci. Technol.* **45**, 115–135.

Foster G. L., Royer D. L. and Lunt D. J. (2017) Future climate forcing potentially without precedent in the last 420 million years. *Nat. Commun.* **8**, 1–8.

Frakes L. A., Alley N. . and Deynoux M. (1995) Early Cretaceous Ice Rafting and Climate Zonation in Australia. *Int. Geol. Rev.* **37**, 567–583.

Frakes L. A. and Francis J. E. (1988) A guide to Phanerozoic cold polar climates from high latitude ice-rafting in the Cretaceous. *Nature* **333**, 547–549.

Franks P. J., Royer D. L., Beerling D. J., Van De Water P. K., Cantrill D. J., Barbour M. M. and Berry J. A. (2014) New constraints on atmospheric CO_2 concentration for the Phanerozoic. *Geophys. Res. Lett.* **41,** 1–10

Friedrich O., Erbacher J., Moriya K., Wilson P. A. and Kuhnert H. (2008) Warm saline intermediate waters in the Cretaceous tropical Atlantic Ocean. **1260**, 453–457.

Friedrich O., Norris R. D. and Erbacher J. (2012) Evolution of middle to late Cretaceous oceans: A 55 m.y. Record of Earth's temperature and carbon cycle. *Geology* **40**, 107–110.

Ghosh P., Eiler J., Campana S. E. and Feeney R. F. (2007) Calibration of the carbonate "clumped isotope" paleothermometer for otoliths. *Geochim. Cosmochim. Acta* **71**, 2736–2744.

Glynn P. (2000) Solid-Solution Solubilities and Thermodynamics: Sulfates, Carbonates and Halides. *Rev. Mineral. Geochemistry* **40**, 481–511.

Goldschmidt J. R. (1983) Phase relations of rhombohedral carbonates. *Rev. Mineral. Geochemistry* **11**, 49-76.

Gradstein F. M. and Ogg J. G. (2004) Geologic time scale 2004 - Why, how, and where next! *Lethaia* **37**, 175–181.

Grasby S. E., McCune G. E., Beauchamp B. and Galloway J. M. (2017) Lower Cretaceous cold snaps led to widespread glendonite occurrences in the Sverdrup Basin, Canadian High Arctic. *Bull. Geol. Soc. Am.* **129**, 771–787.

Gratz A. J., Hillner P. E. and Hansma P. K. (1993) Step dynamics and spiral growth on calcite. *Geochim. Cosmochim. Acta* **57**, 491–495.

Greinert J. and Derkachev A. (2004) Glendonites and methane-derived Mg-calcites in the Sea of Okhotsk, Eastern Siberia: Implications of a venting-related ikaite/glendonite formation. *Mar. Geol.* **204**, 129–144.

Gréselle B. and Pittet B. (2010) Sea-level reconstructions from the Peri-Vocontian Zone (South-east France) point to Valanginian glacio-eustasy. *Sedimentology* **57**, 1640–1684.

Gréselle B., Pittet B., Mattioli E., Joachimski M., Barbarin N., Riquier L., Reboulet S. and Pucéat E. (2011) The Valanginian isotope event: A complex suite of palaeoenvironmental perturbations. *Palaeogeogr. Palaeoclimatol. Palaeoecol.* **306**, 41–57.

Grocke D. R. (2002) The carbon isotope composition of ancient CO_2 based on higher-plant organic matter. *Philos. Trans. R. Soc. London. Ser. A Math. Phys. Eng. Sci.* **360**, 633–658.

Gröcke D. R. (1998) Carbon-isotope analyses of fossil plants as a chemostratigraphic and palaeoenvironmental tool. *Lethaia* **31**, 1–13.

Gröcke D. R., Hesselbo S. P. and Jenkyns H. C. (1999) Carbon-isotope composition of Lower Cretaceous fossil wood: Ocean-atmosphere chemistry and relation to sea-level change. *Geology* **27**, 155–158.

Gröcke D. R., Price G. D., Robinson S. A., Baraboshkin E. Y., Mutterlose J. and Ruffell A. H. (2005) The Upper Valanginian (Early Cretaceous) positive carbon-isotope event recorded in terrestrial plants. *Earth Planet. Sci. Lett.* **240**, 495–509.

Gorski C. A. and Fantle M. S. (2017) Stable mineral recrystallization in low temperature aqueous systems: A critical review. Geochim. Cosmochim. Acta 198, 439–465. Available at: http://dx.doi.org/10.1016/j.gca.2016.11.013.

Haq B. U. (2014) Cretaceous eustasy revisited. *Glob. Planet. Change* **113**, 44–58.

Hasegawa H., Tada R., Jiang X., Suganuma Y., Imsamut S., Charusiri P., Ichinnorov N. and Khand Y. (2012) Drastic shrinking of the Hadley circulation during the mid-Cretaceous Supergreenhouse. *Clim. Past* **8**, 1323–1337.

Hasegawa T. (1997) Cenomanian-Turonian carbon isotope events recorded in terrestrial organic matter from northern Japan. *Palaeogeogr. Palaeoclimatol. Palaeoecol.* **130**, 251–273.

Haworth M., Hesselbo S. P., McElwain J. C., Robinson S. A. and Brunt J. W. (2005) Mid-Cretaceous pCO_2 based on stomata of the extinct conifer Pseudofrenelopsis (Cheirolepidiaceae). *Geology* **33**, 749–752.

Hay W. W. (2008) Evolving ideas about the Cretaceous climate and ocean circulation. *Cretac. Res.* **29**, 725–753.

Hay W. W. and DeConto R. M. (1999) Comparison of modern and Late Cretaceous meridional energy transport and oceanology. *Spec. Pap. Soc. Am.*, 283–300.

Hay W. W., DeConto R. M., de Boer P., Flögel S., Song Y. and Stepashko A. (2019) *Possible solutions to several enigmas of Cretaceous climate*., Springer Berlin Heidelberg.

Hay W. W. and Floegel S. (2012) New thoughts about the Cretaceous climate and oceans. *Earth-Science Rev.* **115**, 262–272.

Haywood A. M., Valdes P. J. and Markwick P. J. (2004) Cretaceous (Wealden) climates: a modelling perspective. *Cretac. Res.* **25**, 303–311.

Heberling F., Paulig L., Nie Z., Schild D. and Finck N. (2016) Morphology Controls on Calcite Recrystallization. *Environ. Sci. Technol.* **50**, 11735–11741.

Heimhofer U., Hochuli P. A., Burla S., Andersen N. and Weissert H. (2003) Terrestrial carbon-isotope records from coastal deposits (Algarve, Portugal): A tool for chemostratigraphic correlation on an intrabasinal and global scale. *Terra Nov.* **15**, 8–13.

Henkes G. A., Passey B. H., Grossman E. L., Shenton B. J., Pérez-Huerta A. and Yancey T. E. (2014) Temperature limits for preservation of primary calcite clumped isotope paleotemperatures. *Geochim. Cosmochim. Acta* **139**, 362–382.

Hennig S., Weissert H. and Bulot L. (1999) C-isotope stratigraphy, a calibration tool between ammonite- and magnetostratigraphy; the Valanginian-Hauterivian transition. *Geol. Carpathica* **50**, 91–96.

Hesselbo S., Morgans-Bell H., McElwain J. C., Rees P. M., Robinson S. A. and Ross C. E. (2003) Carbon-cycle perturbation in the Middle Jurassic and accompanying changes in the terrestrial paleoenvironment. *J. Geol.* **111**, 259–276.

Hesselbo S. P., Jenkyns H. C., Duarte L. V. and Oliveira L. C. V. (2007) Carbon-isotope record of the Early Jurassic (Toarcian) Oceanic Anoxic Event from fossil wood and marine carbonate (Lusitanian Basin, Portugal). *Earth Planet. Sci. Lett.* **253**, 455–470.

Hesselbo S. P., Morgans-Bell H. S., McElwain J. C., Rees P. M., Robinson S. A. and Ross C. E. (2003) Carbon-Cycle Perturbation in the Middle Jurassic and Accompanying Changes in the Terrestrial Paleoenvironment. *J. Geol.* **111**, 259–276.

Hesselbo S. P., Robinson S. A., Surlyk F. and Piasecki S. (2002) Terrestrial and marine extinction at the Triassic-Jurassic boundary synchronized with major carbon-cycle perturbation: A link to initiation of massive volcanism? *Geology* **30**, 251–254.

Hofmann P., Stüsser I., Wagner T., Schouten S. and Sinninghe Damsté J. S. (2008) Climate-ocean coupling off North-West Africa during the Lower Albian: The Oceanic Anoxic Event 1b. *Palaeogeogr. Palaeoclimatol. Palaeoecol.* **262**, 157–165.

Horne D. J. (1995) A revised ostracod biostratigraphy for the Purbeck-Wealden of England. *Cretac. Res.* **16**, 639–663.

Huber B. T., Hodell D. A. and Hamilton C. P. (1995) Middle-late Cretaceous climate of the southern high latitudes: stable isotopic evidence for minimal equator-to-pole thermal gradients. *Geol. Soc. Am. Bull.* **107**, 1164–1191.

Huber B. T., Norris R. D. and MacLeod K. G. (2002) Deep-sea paleotemperature record of extreme warmth during the Cretaceous. *Geology* **30**, 123–126.

Hughes N. F. (1975) Plant succession in the English Wealden strata. *Proc. Geol. Assoc.* **86**, 439–455.

Hughes N. F. and Moody-Stuart J. C. (1967) Palynological facies and correlation in the English Wealden. *Rev. Palaeobot. Palynol.* **1**, 259–268.

Jacobs B. F., Kingston J. D. and Jacobs L. (1999) The Origin of Grass-Dominated Ecosystems Author (s): Bonnie F . Jacobs , John D . Kingston and Louis L . Jacobs. *Ann. Missouri Bot. Gard.* **86**, 590–643.

Jahren A. H., Arens N. C., Sarmiento G., Guerrero J. and Amundson R. (2001) Terrestrial record of methane hydrate dissociation in the Early Cretaceous. *Geology* **29**, 159–162.

Jarzembowski E. . (1995) Early Cretaceous insect faunas and palaeoenvironment. *Cretac. Res.* **16**, 681–693.

Jenkyns H. C. (2003) Evidence for rapid climate change in the Mesozoic - Palaeogene greenhouse world. *Philos. Trans. R. Soc. London. Ser. A Math. Phys. Eng. Sci.* **361**, 1885–1916.

Jenkyns H. C. (2010) Geochemistry of oceanic anoxic events. *Geochemistry, Geophys. Geosystems* **11**, n/a-n/a.

Jenkyns H. C. (1997) Mesozoic anoxic events and palaeoclimate. *Zbl. Geol. Paläont.* **Teil 1**, 943–949.

Jenkyns H. C., Schouten-Huibers L., Schouten S. and Sinninghe Damsté J. S. (2012) Warm Middle Jurassic-Early Cretaceous high-latitude sea-surface temperatures from the Southern Ocean. *Clim. Past* **8**, 215–225.

Jenkyns H. C., Schouten-Huibers L., Schouten S. and Sinninghe Damsté J. S. (2012) Warm Middle Jurassic-Early Cretaceous high-latitude sea-surface temperatures from the Southern Ocean. *Clim. Past* **8**, 215–225.

Jensen D. L., Boddum J. K., Tjell J. C. and Christensen T. H. (2002) The solubility of rhodochrosite ($MnCO_3$) and siderite ($FeCO_3$) in anaerobic aquatic environments. **17**, 503–511.

Jiang C. Z. and Tosca N. J. (2019) Fe(II)-carbonate precipitation kinetics and the chemistry of anoxic ferruginous seawater. *Earth Planet. Sci. Lett.* **506**, 231–242.

Jimenez-Lopez C. and Romanek C. S. (2004) Precipitation kinetics and carbon isotope partitioning of inorganic siderite at 25°C and 1 atm. *Geochim. Cosmochim. Acta* **68**, 557–571.

Johnson C. M., Beard B. L., Klein C., Beukes N. J. and Roden E. E. (2008) Iron isotopes constrain biologic and abiologic processes in banded iron formation genesis. *Geochim. Cosmochim. Acta* **72**, 151–169.

Johnson C. M., Roden E. E., Welch S. A. and Beard B. L. (2005) Experimental constraints on Fe isotope fractionation during magnetite and Fe carbonate formation coupled to dissimilatory hydrous ferric oxide reduction. *Geochim. Cosmochim. Acta* **69**, 963–993.

Jones T. P. and Chaloner W. G. (1991) Fossil charcoal, its recognition and palaeoatmospheric significance. *Palaeogeogr. Palaeoclimatol. Palaeoecol.* **97**, 39–50.

Kandegedara A. and Rorabacher D. B. (1999) Noncomplexing tertiary amines as “better” buffers covering the range of pH 3-11. Temperature dependence of their acid dissociation constants. *Anal. Chem.* **71**, 3140–3144.

Kantorowicz J. D. (1985) The petrology and diagenesis of Middle Jurassic clastic sediments, Ravenscar Group, Yorkshire. *Sedimentology* **32**, 833–853.

Katz A. (1973) The interaction of magnesium with calcite during crystal growth at 25–90°C and one atmosphere. *Geochim. Cosmochim. Acta* **37**, 1563–1586.

Kelson J. R., Huntington K. W., Schauer A. J., Saenger C. and Lechler A. R. (2017) Toward a universal carbonate clumped isotope calibration: Diverse synthesis and preparatory methods suggest a single temperature relationship. *Geochim. Cosmochim. Acta* **197**, 104–131..

Khim B.-K., Choi K.-S., Park Y.-A. and Oh J.-K. (1999) Occurrence of authigenic siderites in the Early Holocene coastal deposit in the west coast of Korea: an indicator of depositional environment. *Geosci. J.* **3**, 163–170.

Khim B.-K., Choi K.-S. and Park Y. A. (2000) Elemental composition of siderite grains in early-Holocene deposits of Youngjong Island (west coast of Korea), and its palaeoenvironmental implications. *Proc. Mar. Sci.* **2**, 205–217.

Kirk-Davidoff D. B., Schrag D. P. and Anderson J. G. (2002) On the feedback of stratospheric clouds on polar climate. *Geophys. Res. Lett.* **29**, 1–4.

Kohn M. J. (2010) Carbon isotope compositions of terrestrial C3 plants as indicators of (paleo)ecology and (paleo)climate. *Proc. Natl. Acad. Sci. U. S. A.* **107**, 19691–19695.

Kujau A., Heimhofer U., Hochuli P. A., Pauly S., Morales C., Adatte T., Föllmi K., Ploch I. and Mutterlose J. (2013) Reconstructing Valanginian (Early Cretaceous) mid-latitude vegetation and climate dynamics based on spore–pollen assemblages. *Rev. Palaeobot. Palynol.* **197**, 50–69.

Kujau A., Heimhofer U., Ostertag-Henning C., Gréselle B. and Mutterlose J. (2012) No evidence for anoxia during the Valanginian carbon isotope event—An organic-geochemical study from the Vocontian Basin, SE France. *Glob. Planet. Change* **92**, 92–104.

Kump L. R. and Pollard D. (2008) Amplification of cretaceous warmth by biological cloud feedbacks. *Science (80-.).* **320**, 195.

Kuypers M. M. M., Pancost R. D. and Damste J. S. S. (1999) A large and abrupt fall in atmospheric CO 2 concentration during Cretaceous times. *Nature* **399**, 342.

Lal R. (2009) Sequestering atmospheric carbon dioxide. *CRC. Crit. Rev. Plant Sci.* **28**, 90–96.

Larson R. L. (1991) Latest pulse of Earth: Evidence for a mid-Cretaceous superplume. *Geology* **19**, 547–550.

Leavitt S. W. and Lone A. (1991) Seasonal stable-carbon isotope variability in tree rings: possible paleoenvironmental signals. *Chem. Geol. Isot. Geosci. Sect.* **87**, 59–70.

Leavitt S. W. and Long A. (1982) Evidence for 13C/12C fractionation between tree leaves and wood. *Nature* **298**, 742–744.

Leavitt S. W. and Long A. (1986) Stable Carbon Isotope Variability in Tree Foliage and Wood. *Ecology* **67**, 1002–1010.

Li Q., McArthur J. M., Doyle P., Janssen N., Leng M. J., Müller W. and Reboulet S. (2013) Evaluating Mg/Ca in belemnite calcite as a palaeo-proxy. *Palaeogeogr. Palaeoclimatol. Palaeoecol.* **388**, 98–108.

Lim D. I., Jung H. S., Yang S. Y. and Yoo H. S. (2004) Sequential growth of early diagenetic freshwater siderites in the Holocene coastal deposits, Korea. *Sediment. Geol.* **169**, 107–120.

Lin C. Y., Turchyn A. V., Steiner Z., Bots P., Lampronti G. I. and Tosca N. J. (2018) The role of microbial sulfate reduction in calcium carbonate polymorph selection. *Geochim. Cosmochim. Acta* **237**, 184–204.

Lin C. Y., Turchyn A. V, Krylov A. and Antler G. (2019) The microbially driven formation of siderite in salt marsh sediments. *Geobiology*, 1–18.

Lini A., Weissert H. and Erba E. (1992) The Valanginian carbon isotope event: a first episode of greenhouse climate conditions during the Cretaceous. *Terra Nova*, **4**, 374-364

Littler K., Robinson S. A., Bown P. R., Nederbragt A. J. and Pancost R. D. (2011) High sea-surface temperatures during the Early Cretaceous Epoch. *Nat. Geosci.* **4**, 169–172.

Littlewood J. L., Shaw S., Peacock C. L., Bots P., Trivedi D. and Burke I. T. (2017) Mechanism of Enhanced Strontium Uptake into Calcite via an Amorphous Calcium Carbonate Crystallization Pathway. *Cryst. Growth Des.* **17**, 1214–1223.

Loader N. J., Switsur V. R. and Field C. M. (1995) High-resolution stable isotope analysis of tree rings: Implications of microdendroclimatology' for palaeoenvironmental research. *Holocene* **5**, 457–460.

Di Lorenzo F., Burgos-Cara A., Ruiz-Agudo E., Putnis C. V. and Prieto M. (2017) Effect of ferrous iron on the nucleation and growth of CaCO3 in slightly basic aqueous solutions. *CrystEngComm* **19**, 447–460.

Ludvigson G. A., González L. A., Fowle D. A., Roberts J. A., Driese S. G., Villarreal M. A., Smith J. J. and Suarez M. B. (2013) Paleoclimatic Applications and Modern Process Studies of Pedogenic Siderite. *New Front. Paleopedol. Terr. Paleoclimatology*, 79–87.

Ludvigson G. A., González L. A., Metzger R. A., Witzke B. J., Brenner R. L., Murillo A. P. and White T. S. (1998) Meteoric sphaerosiderite lines and their use for paleohydrology and paleoclimatology. *Geology* **26**, 1039–1042.

Lunt D. J., Farnsworth A., Loptson C., L Foster G., Markwick P., O'Brien C. L., Pancost R. D., Robinson S. A. and Wrobel N. (2016) Palaeogeographic controls on climate and proxy interpretation. *Clim. Past* **12**, 1181–1198.

De Lurio J. L. and Frakes L. A. (1999) Glendonites as a paleoenvironmental tool: Implications for early Cretaceous high latitude climates in Australia. *Geochim. Cosmochim. Acta* **63**, 1039–1048.

Martinez M., Deconinck J., Pellenard P., Reboulet S. and Riquier L. (2013) Astrochronology of the Valanginian Stage from reference sections (Vocontian Basin, France) and palaeoenvironmental implications for the Weissert Event. *Palaeogeogr. Palaeoclimatol. Palaeoecol.* **376**, 91–102.

Martinez M., Deconinck J., Pellenard P., Riquier L. and Company M. (2015) Astrochronology of the Valanginian – Hauterivian stages (Early Cretaceous): Chronological relationships between the Paraná – Etendeka large igneous province and the Weissert and the Faraoni events. *Glob. Planet. Change* **131**, 158–173.

Mattioli E., Pittet B., Riquier L. and Grossi V. (2014) The mid-Valanginian Weissert Event as recorded by calcareous nannoplankton in the Vocontian Basin. *Palaeogeogr. Palaeoclimatol. Palaeoecol.* **414**, 472–485.

McArthur J., Mutterlose J., Price G., Rawson P., Ruffell A. and Thirlwall M. (2004) Belemnites of Valanginian, Hauterivian and Barremian age: Sr-isotope stratigraphy, composition ($^{87}Sr/^{86}Sr$, $\delta^{13}C$, $\delta^{18}O$, Na, Sr, Mg), and palaeo-oceanography. *Palaeogeogr. Palaeoclimatol. Palaeoecol.* **202**, 253–272.

McArthur J. M., Janssen N. M. M., Reboulet S., Leng M. J., Thirlwall M. F. and van de Schootbrugge B. (2007) Palaeotemperatures, polar ice-volume, and isotope stratigraphy (Mg/Ca, $\delta^{18}O$, $\delta^{13}C$, $^{87}Sr/^{86}Sr$): The Early Cretaceous (Berriasian, Valanginian, Hauterivian). *Palaeogeogr. Palaeoclimatol. Palaeoecol.* **248**, 391–430.

McCabe P. J. and Parrish J. T. (1992) *Controls on the distribution and quality of Cretaceous coals.*, Geological Society of America.

Meckler A. N., Ziegler M., Millán M. I., Breitenbach S. F. M. and Bernasconi S. M. (2014) Long-term performance of the Kiel carbonate device with a new correction scheme for clumped isotope measurements. *Rapid Commun. Mass Spectrom.* **28**, 1705–1715.

Meissner P., Mutterlose J. and Bodin S. (2015) Latitudinal temperature trends in the northern hemisphere during the Early Cretaceous (Valanginian–Hauterivian). *Palaeogeogr. Palaeoclimatol. Palaeoecol.* **424**, 17–39.

Miller K. G., Kominz M. A., Browning J. V., Wright J. D., Mountain G., Katz M. E., Sugarman P. J., Cramer B. S., Christie-Blick N. and Pekar S. F. (2011) The Phanerozoic Record of Global Sea-Level Change. *Science.* **1293**, 1293–1298.

Mitsch W. and Gosselink J. (2015) *Wetlands*. 5th ed., John wiley and Sons.

Mitsch W. J., Bernal B., Nahlik A. M., Mander Ü., Zhang L., Anderson C. J., Jørgensen S. E. and Brix H. (2013) Wetlands, carbon, and climate change. *Landsc. Ecol.* **28**, 583–597.

Mitsch W. J., Nahlik A., Wolski P., Bernal B., Zhang L. and Ramberg L. (2010) Tropical wetlands: Seasonal hydrologic pulsing, carbon sequestration, and methane emissions. *Wetl. Ecol. Manag.* **18**, 573–586.

Moore S. E., Ferrell R. E. and Aharon P. (1992) Diagenetic Siderite and Other Ferroan Carbonates in a Modern Subsiding Marsh Sequence. *SEPM J. Sediment. Res.* **Vol. 62**, 357–366.

Morales C., Gardin S., Schnyder J., Spangenberg J., Arnaud-Vanneau A., Arnaud H., Adatte T. and Föllmi K. B. (2013) Berriasian and early Valanginian environmental change along a transect from the Jura Platform to the Vocontian Basin. *Sedimentology* **60**, 36–63.

Morales C., Kujau A., Heimhofer U., Mutterlose J., Spangenberg J. E., Adatte T., Ploch I. and Föllmi K. B. (2015) Palaeoclimate and palaeoenvironmental changes through the onset of the Valanginian carbon-isotope excursion: Evidence from the Polish Basin. *Palaeogeogr. Palaeoclimatol. Palaeoecol.* **426**, 183–198.

Morter A. A. (1984) Purbeck-Wealden Beds Mollusca and their relationship to ostracod biostratigraphy, stratigraphical correlation and palaeoecology in the Weald and adjacent areas. *Proc. Geol. Assoc.* **95**, 217–234.

Mortimer R. J. G., Coleman M. L. and Rae J. E. (1997) Effect of bacteria on the elemental composition of early diagenetic siderite: Implications for palaeoenvironmental interpretations. *Sedimentology* **44**, 759–765.

Mozley P. S. (1989) Relation between depositional environment and the elemental composition of early diagenetic siderite. *Geology* **17**, 704–706.

Mozley P. S. and Carothers W. W. (1992) Elemental and Isotopic Composition of Siderite in the Kuparuk Formation, Alaska: Effect of Microbial Activity and Water/Sediment Interaction on Early Pore-Water Chemistry. *SEPM J. Sediment. Res.* **62**, 681–692.

Mozley P. S. and Wersin P. (1992) Isotopic composition of siderite as an indicator of depositional environment. *Geology* **20**, 817–820.

Mucci A. (1987) Influence of temperature on the composition of magnesian calcite overgrowths precipitated from seawater. *Geochim. Cosmochim. Acta* **51**, 1977–1984.

Müller I. A., Fernandez A., Radke J., van Dijk J., Bowen D., Schwieters J. and Bernasconi S. M. (2017) Carbonate clumped isotope analyses with the long-integration dual-inlet (LIDI) workflow: scratching at the lower sample weight boundaries. *Rapid Commun. Mass Spectrom.* **31**, 1057–1066.

Müller R. D., Sdrolias M., Gaina C., Steinberger B. and Heine C. (2008) Long-Term Sea-Level Fluctuations. *Science* **319**, 1357–1363.

Mutterlose J. and Kessels K. (2000) Early Cretaceous calcareous nannofossils from high latitudes: Implications for palaeobiogeography and palaeoclimate. *Palaeogeogr. Palaeoclimatol. Palaeoecol.* **160**, 347–372.

Mutterlose J., Malkoc M., Schouten S., Sinninghe Damsté J. S. and Forster A. (2010) TEX_{86} and stable $\delta^{18}O$ paleothermometry of early Cretaceous sediments: Implications for belemnite ecology and paleotemperature proxy application. *Earth Planet. Sci. Lett.* **298**, 286–298.

Nielsen M. H., Aloni S. and De Yoreo J. J. (2014) In situ TEM imaging of $CaCO_3$ nucleation reveals coexistence of direct and indirect pathways. *Science.* **345**, 1158 LP – 1162.

Nunn E. V., Price G. D., Gröcke D. R., Baraboshkin E. Y., Leng M. J. and Hart M. B. (2010) The Valanginian positive carbon isotope event in Arctic Russia: Evidence from terrestrial and marine isotope records and implications for global carbon cycling. *Cretac. Res.* **31**, 577–592.

O'Brien C. L., Robinson S. A., Pancost R. D., Damsté J. S. S., Schouten S., Lunt D. J., Bornemann A., Bottini C., Brassell S. C., Farnsworth A., Forster A., Huber B. T., Inglis N., Jenkyns H. C., Linnert C., Littler K., Mcanena A., Mutterlose J., Naafs B. D. A., Püttmann W., Sluijs A., Helmond N. A. G. M. Van, Vellekoop J., Wagner T., Wrobel N. E., Bottini C., Brassell S. C., Farnsworth A., Forster A., Huber B. T., Inglis G. N., Jenkyns H. C., Linnert C., Littler K., Mcanena A., Mutterlose J., Naafs B. D. A. and Püttmann W. (2017) Cretaceous sea-surface temperature evolution: Constraints from TEX_{86} and planktonic foraminiferal oxygen isotopes. *Earth-Science Rev.* **172**, 224–247.

Ogg J. G., Ogg G. and Gradstein F. (2016) *A Concise Geologic Time Scale*. 1st ed.,

Oomori T., Kaneshima H., Maezato Y. and Kitano Y. (1987) Distribution coefficient of Mg^{2+} ions between calcite and solution at 10–50°C. *Mar. Chem.* **20**, 327–336.

Opsahl S. and Benner R. (1999) Characterization of carbohydrates during early diagenesis of five vascular plant tissues. *Org. Geochem.* **30**, 83–94.

Paquette J. and Reeder R. J. (1990) New type of compositional zoning in calcite: Insights into crystal-growth mechanisms. *Geology* **18**, 1244–1247.

Paquette J. and Reeder R. J. (1995) Relationship between surface structure, growth mechanism, and trace element incorporation in calcite. *Geochim. Cosmochim. Acta* **59**, 735–749.

Passey B. H. and Henkes G. A. (2012) Carbonate clumped isotope bond reordering and geospeedometry. *Earth Planet. Sci. Lett.* **351**–**352**, 223–236.

Passey S. R. (2014) The habit and origin of siderite spherules in the Eocene coal-bearing Prestfjall Formation, Faroe Islands. *Int. J. Coal Geol.* **122**, 76–90.

Peral M., Daëron M., Blamart D., Bassinot F., Dewilde F., Smialkowski N., Isguder G., Bonnin J., Jorissen F., Kissel C., Michel E., Vázquez Riveiros N. and Waelbroeck C. (2018) Updated calibration of the clumped isotope thermometer in planktonic and benthic foraminifera. *Geochim. Cosmochim. Acta* **239**, 1–16.

Peters K. E. (1986) Guidelines for evaluating petroleum source rock using programmed pyrolysis. *Am. Assoc. Pet. Geol. Bull.* **70**, 318–329.

Pitman W. and Talwani M. (1972) Sea-floor spreading in the North Atlantic. *Geol. Soc. Am. Bull.* **83**, 619–646.

Politi Y., Arad T., Klein E., Weiner S. and Addadi L. (2009) Sea Urchin Spine Calcite Forms via a Transient Amorphous Calcium Carbonate Phase. *Science* **306**, 1161–1164.

Poole I., Braadbaart F., Boon J. J. and Van Bergen P. P. (2002) Stable carbon isotope changes during artificial charring of propagules. *Org. Geochem.* **33**, 1675–1681.

Postma D. (1980) Formation of siderite and vivianite and the pore-water composition of a Recent bog sediment in Denmark. *Chem. Geol.* **31**, 225–244.

Poulsen C. J., Gendaszek A. S. and Jacob R. L. (2003) Did the rifting of the Atlantic Ocean cause the Cretaceous thermal maximum? *Geology* **31**, 115–118.

Poulsen C. J., Pollard D. and White T. S. (2007) General circulation model simulation of the $\delta^{18}O$ content of continental precipitation in the middle Cretaceous: A model-proxy comparison. *Geology* **35**, 199–202.

Price G. D. (1999) The evidence and implications of polar ice during the Mesozoic. *Earth Sci. Rev.* **48**, 183–210.

Price G. D., Főzy I., Janssen N. M. M. and Pálfy J. (2011) Late Valanginian–Barremian (Early Cretaceous) palaeotemperatures inferred from belemnite stable isotope and Mg/Ca ratios from Bersek Quarry (Gerecse Mountains, Transdanubian Range, Hungary). *Palaeogeogr. Palaeoclimatol. Palaeoecol.* **305**, 1–9.

Price G. D. and Mutterlose J. (2015) Isotopic signals from late Jurassic–Early Cretaceous (Volgian–Valanginian) sub-Arctic belemnites , Yatria River , Western Siberia. **161**, 959–968.

Price G. D. and Nunn E. V. (2010) Valanginian isotope variation in glendonites and belemnites from Arctic Svalbard: Transient glacial temperatures during the Cretaceous greenhouse. *Geology* **38**, 251–254.

Price G. D. and Passey B. H. (2013) Dynamic polar climates in a greenhouse world: Evidence from clumped isotope thermometry of early cretaceous belemnites. *Geology* **41**, 923–926.

Pucéat E., Joachimski M. M., Bouilloux A., Monna F., Bonin A., Motreuil S., Morinière P., Hénard S., Mourin J., Dera G. and Quesne D. (2010) Revised phosphate-water fractionation equation reassessing paleotemperatures derived from biogenic apatite. *Earth Planet. Sci. Lett.* **298**, 135–142.

Pucéat E., Lécuyer C., Sheppard S. M. F., Dromart G., Reboulet S. and Grandjean P. (2003) Thermal evolution of Cretaceous Tethyan marine waters inferred from oxygen isotope composition of fish tooth enamels. *Paleoceanography* **18**

Pye K. (1984) SEM analysis of siderite cements in intertidal marsh sediments, Norfolk, England. *Mar. Geol.* **56**, 1–12.

Pye K., Dickson J. A. D., Schiavon N., Coleman M. L. and Cox M. (1990) Formation of siderite-Mg-calcite-iron sulphide concretions in intertidal marsh and sandflat sediments, north Norfolk, England. *Sedimentology* **37**, 325–343.

Quade J., Eiler J., Daëron M. and Achyuthan H. (2013) The clumped isotope geothermometer in soil and paleosol carbonate. *Geochim. Cosmochim. Acta* **105**, 92–107.

Radley J. D. (2006a) A Wealden guide I: the Weald Sub-basin. *Geol. Today* **22**, 109–118.

Radley J. D. (2006b) A Wealden guide II: the Wessex Sub-basin. *Geol. Today* **22**, 187–193.

Radley J. D. (1994) Stratigraphy, palaeontology and palaeoenvironment of the Wessex Formation (Wealden Group, Lower Cretaceous) at Yaverland, Isle of Wight, southern England. *Proc. Geol. Assoc.* **105**, 199–208.

Radley J. D. and Allen P. (2012) The non-marine Lower Cretaceous Wealden strata of southern England. *Proc. Geol. Assoc.* **123**, 235–244.

Radley J. D. and Barker M. J. (1998) Stratigraphy, palaeontology and correlation of the Vectis Formation (Wealden Group, Lower Cretaceous) at Compton Bay, Isle of Wight, southern England. *Proc. Geol. Assoc.* **109**, 187–195.

Rakovan J. and Reeder R. J. (1996) Intracrystalline rare earth element distributions in apatite: Surface structural influences on incorporation during growth. *Geochim. Cosmochim. Acta* **60**, 4435–4445.

Reboulet S., Mattioli E., Pittet B., Baudin F., Olivero D. and Proux O. (2003) Ammonoid and nannoplankton abundance in Valanginian (early Cretaceous) limestone-marl successions

from the southeast France Basin: Carbonate dilution or productivity? *Palaeogeogr. Palaeoclimatol. Palaeoecol.* **201**, 113–139.

Reeder R. J. (1983) Crystal chemistry of the rhombohedral carbonates. *Rev. Mineral. Geochemistry* **11**, 1–47.

Reeder R. J. (1996) Interaction of divalent cobalt, zinc, cadmium, and barium with the calcite surface during layer growth. *Geochim. Cosmochim. Acta* **60**, 1543–1552. Available at: https://www.sciencedirect.com/science/article/pii/0016703796000348 [Accessed July 28, 2018].

Reeder R. J., Fagioli R. O. and Meyers W. J. (1990) Oscillatory zoning of Mn in solution-grown calcite crystals. *Earth-Science Rev.* **29**, 39–46.

Reeder R. J. and Rakovan J. (1999) Surface Structural Controls on Trace Element Incorporation during Crystal Growth. In *Growth, Dissolution and Pattern Formation in Geosystems* (eds. B. Jamtveit and P. Meakin). Springer Netherlands, Dordrecht. pp. 143–162.

Retallack G. J. (2001) A 300-million-year record of atmospheric carbon dioxide from fossil plant cuticles. *Nature* **415**, 287–290.

Retallack G. J. (2002) Carbon Dioxide and Climate over the past 300 Myr. *Philos. Trans. Math. Phys. Eng. Sci.* **360**, 659–673.

Retallack, G. J. (2008). Soils of the past: an introduction to paleopedology. John Wiley & Sons.

Rimstidt J. D., Balog A. and Webb J. (1998) Distribution of trace elements between carbonate minerals and aqueous solutions. *Geochim. Cosmochim. Acta* **62**, 1851–1863.

Robinson S. A., Andrews J. E., Hesselbo S. P., Radley J. D., Dennis P. F., Harding I. C. and Allen P. (2002) Atmospheric pCO_2 and depositional environment from stable-isotope geochemistry of calcrete nodules (Barremian, Lower Cretaceous, Wealden Beds, England). *J. Geol. Soc. London.* **159**, 215–224.

Robinson S. A., Scotchman J. I., White T. S. and Atkinson T. C. (2010) Constraints on palaeoenvironments in the Lower Cretaceous Wealden of southern England, from the geochemistry of sphaerosiderites. *J. Geol. Soc. London.* **167**, 303–311.

Robinson S. and Hesselbo S. (2004) Fossil-wood carbon-isotope stratigraphy of the non-marine Wealden Group (Lower Cretaceous, southern England). *J. Geol. Soc. London.* **161**, 133–145.

Rodriguez-Navarro C., Burgos Cara A., Elert K., Putnis C. V. and Ruiz-Agudo E. (2016) Direct Nanoscale Imaging Reveals the Growth of Calcite Crystals via Amorphous Nanoparticles. *Cryst. Growth Des.* **16**, 1850–1860.

Rollion-Bard C. and Marin-Carbonne J. (2011) Determination of SIMS matrix effects on oxygen isotopic compositions in carbonates. *J. Anal. At. Spectrom.* **26**, 1285–1289.

Romanek C. S., Jiménez-López C., Navarro A. R., Sánchez-Román M., Sahai N. and Coleman M. (2009) Inorganic synthesis of Fe-Ca-Mg carbonates at low temperature. *Geochim. Cosmochim. Acta* **73**, 5361–5376.

Romanek C. S., Zhang C. L., Li Y., Horita J., Vali H., Cole D. R. and Phelps T. J. (2003) Carbon and hydrogen isotope fractionations associated with dissimilatory iron-reducing bacteria. *Chem. Geol.* **195**, 5–16.

Rosenau N. A., Tabor N. J., Elrick S. D. and Nelson W. J. (2013) Polygenetic History of Paleosols In Middle-Upper Pennsylvanian Cyclothems of the Illinois Basin, U.S.A.: Part II. Integrating Geomorphology, Climate, and Glacioeustasy.,

Ross J. B., Ludvigson G. A., Möller A., Gonzalez L. A. and Walker J. D. (2017) Stable isotope paleohydrology and chemostratigraphy of the Albian Wayan Formation from the wedge-top depozone, North American Western Interior Basin. *Sci. China Earth Sci.* **60**, 44–57.

Royer D., Berner R., Montanez I. ., Tabor N. and Beerling D. (2004) CO_2 as a primary driver of Phanerozoic climate. *Geol. Soc. Am. Today* **14**, 4–10.

Royer D. L. (2010) Fossil soils constrain ancient climate sensitivity. *Proc. Natl. Acad. Sci. U. S. A.* **107**, 517–518.

Royer D. L. (2008) Linkages between CO_2, climate, and evolution in deep time. **105**, 407–408.

Royer D. L., Pagani M. and Beerling D. J. (2012) Geobiological constraints on Earth system sensitivity to CO_2 during the Cretaceous and Cenozoic. *Geobiology* **10**, 298–310.

Ruffell A. H. and Batten D. J. (1994) Uppermost Wealden facies and Lower Greensand Group (Lower Cretaceous) in Dorset, southern England: correlation and palaeoenvironment. *Proc. Geol. Assoc.* **105**, 53–69.

Ruffell A., Ross A. and Taylor K. (1996) *Early Cretaceous environments of the Weald*., Geologists' Association.

Ruffell A. and Worden R. (2000) Palaeoclimate analysis using spectral gamma-ray data from the Aptian (Cretaceous) of southern England and southern France. *Palaeogeogr. Palaeoclimatol. Palaeoecol.* **155**, 265–283.

Sames B., Wagreich M., Wendler J. E., Haq B. U., Conrad C. P., Melinte-Dobrinescu M. C., Hu X., Wendler I., Wolfgring E., Yilmaz I. and Zorina S. O. (2015) Review: Short-term sea-level changes in a greenhouse world - A view from the Cretaceous. *Palaeogeogr. Palaeoclimatol. Palaeoecol.* **441**, 393–411.

Schlanger S. O. and Jenkyns H. C. (1976) Cretaceous anoxic events - causes and consequences. *Geol. en Minjnbouw* **55**, 179–184.

Schleser G. H., Frielingsdorf J. and Blair A. (1999) Carbon isotope behaviour in wood and cellulose during artificial aging. *Chem. Geol.* **158**, 121–130.

Scholle P. A. and Arthur M. A. (1980) Carbon isotope fluctuations in Cretaceous pelagic limestones: potential stratigraphic and petroleum exploration tool. *Am. Assoc. Pet. Geol. Bull.* **64**, 67–87.

Schouten S., Hopmans E. C., Forster A., van Breugel Y., Kuypers M. M. M. and Sinninghe Damsté J. S. (2003) Extremely high sea-surface temperatures at low latitudes during the middle Cretaceous as revealed by archaeal membrane lipids. *Geology* **31**, 1069–1072.

Sel O., Radha A. V., Dideriksen K. and Navrotsky A. (2012) Amorphous iron (II) carbonate: Crystallization energetics and comparison to other carbonate minerals related to CO_2 sequestration. *Geochim. Cosmochim. Acta* **87**, 61–68.

Sellwood B. W. and Valdes P. J. (2006) Mesozoic climates: General circulation models and the rock record. *Sediment. Geol.* **190**, 269–287.

Sengupta R., Tosca N. J. and Robinson S. A. (2020) Geochemical controls on the elemental composition of siderite: Implications for palaeo-environmental reconstructions. *Geochim. Cosmochim. Acta*. **271**, 1-15

Sharp Z. (2017) Principles of Stable Isotope Geochemistry. 2nd Edition.

Skelton P., Spicer R. A., Kelley S. and Gilmour I. (2003) *The Cretaceous World*., Cambridge University Press.

Sladen C. P. and Batten D. J. (1984) Source-area environments of late Jurassic and early Cretaceous sediments in Southeast England. *Proc. Geol. Assoc.* **95**, 149–163. Available at: http://dx.doi.org/10.1016/S0016-7878(84)80002-4.

Smith B. N. and Epstein S. (1971) Two Categories of $^{13}C/^{12}C$ Ratios for Higher Plants . *Plant Physiol.* **47**, 380–384.

Snell K. E., Thrasher B. L., Eiler J. M., Koch P. L., Sloan L. C. and Tabor N. J. (2013) Hot summers in the Bighorn Basin during the early Paleogene. *Geology* **41**, 55–58.

Spicer R. A. (1989) The formation and interpretation of plant fossil assemblages. In *Advances in botanical research* Elsevier. pp. 95–191.

Spicer R. A. and Corfield R. M. (1992) A review of terrestrial and marine climates in the Cretaceous with implications for modelling the 'Greenhouse Earth.' *Geol. Mag.* **129**, 169–180.

Spicer R. A., Ahlberg A., Herman A. B., Hofmann C. C., Raikevich M., Valdes P. J. and Markwick P. J. (2008) The Late Cretaceous continental interior of Siberia: A challenge for climate models. *Earth Planet. Sci. Lett.* **267**, 228–235.

Spiker E. C. and Hatcher P. G. (1987) The effects of early diagenesis on the chemical and stable carbon isotopic composition of wood. *Geochim. Cosmochim. Acta* **51**, 1385–1391.

Sprovieri M., Coccioni R., Lirer F., Pelosi N. and Lozar F. (2006) Orbital tuning of a lower Cretaceous composite record (Maiolica Formation, central Italy). *Paleoceanography* **21**, 1–19.

Staudigel P. T., Murray S., Dunham D. P., Frank T. D., Fielding C. R. and Swart P. K. (2018) Cryogenic brines as diagenetic fluids: Reconstructing the diagenetic history of the Victoria Land Basin using clumped isotopes. *Geochim. Cosmochim. Acta* **224**, 154–170.

Steefel C. I. and Van Cappellen P. (1990) A new kinetic approach to modeling water-rock interaction: The role of nucleation, precursors, and Ostwald ripening. *Geochim. Cosmochim. Acta* **54**, 2657–2677.

Steinmann P. and Shotyk W. (1997) Chemical composition, pH, and redox state of sulfur and iron in complete vertical porewater profiles from two Sphagnum peat bogs, Jura Mountains, Switzerland. *Geochim. Cosmochim. Acta* **61**, 1143–1163.

Stephenson A., DeYoreo J., Wu L., Wu K., Hoyer J. and Dove P. (2008) Peptides Enhance Magnesium Origins of Vital Effects. *Science (80-.).* **322**, 724–727.

Stoll H. M. and Schrag D. P. (1996) Evidence for Glacial Control of Rapid Sea Level Changes in the Early Cretaceous. *Science* **272**, 1771–1774.

Suarez M. B., Gonzalez L. A. and Ludvigson G. A. (2011) Quantification of a greenhouse hydrologic cycle from equatorial to polar latitudes: The mid-Cretaceous water bearer revisited. *Palaeogeogr. Palaeoclimatol. Palaeoecol.* **307**, *4, 301-312*

Suarez M. B., González L. A., Ludvigson G. A., Vega F. J. and Alvarado-Ortega J. (2009) Isotopic composition of low-latitude paleoprecipitation during the Early Cretaceous. *Geol. Soc. Am. Bull.* **121**, 1584–1595.

Sunagawa I. (2007) *Crystals : Growth, morphology, and perfection*., Cambridge University Press.

Tarduno J. A., Brinkman D. B., Renne P. R., Cottrell R. D., Scher H. and Castillo P. (1998) Evidence for Extreme Climatic Warmth from Late Cretaceous Arctic Vertebrates. *Science.* **282**, 2241 LP – 2243.

Taylor H. (2019) Assessing the Terrestrial Climate and Palaeoenvironment of the Mid-Jurassic (Bajocian-Bathonian) using Sphaerosiderites from the Long Nab Member, Yorkshire (MSci Thesis). University of Oxford.

Taylor K. G. (1996) Pedogenic clay-mineral transformation in the Weald Basin: Implications for Early Cretaceous hinterland climate reconstructions. *Cretac. Res.* **17**, 103–108.

Teng H. H., Dove P. M. and De Yoreo J. J. (2000) Review on MAC Protocols for Underwater Acoustic Networks. *Geochemica Cosmochem. Acta* **64**, 2255–2266.

Thiede D. S. and Vasconcelos P. M. (2010) Parana flood basalts: Rapid extrusion hypothesis confirmed by new $^{40}Ar/^{39}Ar$ results. *Geology* **38**, 747–750.

Thornber M. R. and Nickel E. H. (1976) Supergene alteration of sulphides. III. The composition of associated carbonates. *Chem. Geol.* **17**, 45–72.

Ufnar D. F., A. González L., Ludvigson G. A., Brenner R. L. and Witzke B. J. (2002) The mid-Cretaceous water bearer: isotope mass balance quantification of the Albian hydrologic cycle. *Palaeogeogr. Palaeoclimatol. Palaeoecol.* **188**, 51–71.

Ufnar D. F., González L. A., Ludvigson G. A., Brenner R. L. and Witzke B. J. (2004a) Evidence for increased latent heat transport during the Cretaceous (Albian) greenhouse warming. *Geology*. **32**, 1049-1052

Ufnar D. F., Gonzalez L. A., Ludvigson G. A., Brenner R. L. and Witzkes B. J. (2004b) Diagenetic overprinting of the sphaerosiderite palaeoclimate proxy: Are records of pedogenic groundwater $\delta^{18}O$ values preserved? *Sedimentology* **51**, 127–144.

Ufnar D. F., Ludvigson G. A., González L. A., Brenner R. L. and Witzke B. J. (2004c) High latitude meteoric $\delta^{18}O$ compositions: Paleosol siderite in the Middle Cretaceous Nanushuk Formation, North Slope, Alaska. *Geol. Soc. Am. Bull.* **116**, 463.

Upchurch G. R., Kiehl J., Shields C., Scherer J. and Scotese C. (2015) Latitudinal temperature gradients and high-latitude temperatures during the latest Cretaceous: Congruence of geologic data and climate models. *Geology* **43**, 683–686.

Van Cappellan P. (1992) The formation of marine apatite: A kinetic study. Yale University.

Van Dijk J., Fernandez A., Müller I. A., Lever M. and Bernasconi S. M. (2018) Oxygen isotope fractionation in the siderite-water system between 8.5 and 62 °C. *Geochim. Cosmochim. Acta* **220**, 535–551.

Van Dijk J., Fernandez A., Storck J. C., White T. S., Lever M. and Müller I. A. (2019) Experimental calibration of clumped isotopes in siderite between 8.5 and 62°C and its application as paleo-thermometer in paleosols. *Geochem. Cosmochim. Acta **254***,1-20.

Vickers M. L., Bajnai D., Price G. D., Linckens J. and Fiebig J. (2019) Southern high-latitude warmth during the Jurassic-Cretaceous: New evidence from clumped isotope thermometry. *Geology* **47**, 724–728.

Vickers M. L., Price G. D., Jerrett R. M., Sutton P., Watkinson M. P. and FitzPatrick M. (2019) The duration and magnitude of Cretaceous cool events: Evidence from the northern high latitudes. *Bull. Geol. Soc. Am.* **131**, 1979–1994.

Wagner T., Herrle J. O., Damsté J. S. S., Schouten S., Stüsser I. and Hofmann P. (2008) Rapid warming and salinity changes of Cretaceous surface waters in the subtropical north Atlantic. *Geology* **36**, 203–206.

Wallmann K. (2001) Controls on the Cretaceous and Cenozoic evolution of seawater composition , atmospheric CO_2 and climate. *Geochim. Cosmochim. Acta* **65**, 3005–3025.

Wang D., Wallace A. F., De Yoreo J. J. and Dove P. M. (2009) Carboxylated molecules regulate magnesium content of amorphous calcium carbonates during calcification. *Proc. Natl. Acad. Sci.* **106**, 21511–21516.

Wang Y., Huang C., Sun B., Quan C., Wu J. and Lin Z. (2014) Paleo-CO_2 variation trends and the Cretaceous greenhouse climate. *Earth-Science Rev.* **129**, 136–147.

Wang Y. and Merino E. (1992) Dynamic model of oscillatory zoning of trace elements in calcite: Double layer, inhibition, and self-organization. *Geochim. Cosmochim. Acta* **56**, 587–596.

Weibel R., Lindstrom S., Pedersen G. K., Johansson L., Dybkj??r K., Whitehouse M. J., Boyce A. J. and Leng M. J. (2016) Groundwater table fluctuations recorded in zonation of microbial siderites from end-Triassic strata. *Sediment. Geol.* **342**, 45–65.

Weiner S. and Dove P. M. (2003) An Overview of Biomineralization Processes and the Problem of the Vital Effect. *Rev. Mineral. Geochemistry* **54**, 1–29.

Weiss I. M., Tuross N., Addadi L. and Weiner S. (2002) Mollusc larval shell formation: Amorphous calcium carbonate is a precursor phase for aragonite. *J. Exp. Zool.* **293**, 478–491.

Weissert H. (1989) C-isotope stratigraphy, a monitor of paleoenvironmental change: a case study from the Early Cretaceous. *Surv. Geophys.* **10**, 1–61.

Weissert H. and Erba E. (2004a) Volcanism, CO_2 and palaeoclimate: a Late Jurassic-Early Cretaceous carbon and oxygen isotope record. *J. Geol. Soc. London.* **161**, 695–702.

Weissert H. and Erba E. (2004b) Volcanism , CO^2 and palaeoclimate : a Late Jurassic – Early Cretaceous carbon and oxygen isotope record. *J. Geol. Soc. London* **161**, 1–8.

Weissert H., Lini A., Föllmi K. B. and Kuhn O. (1998) Correlation of Early Cretaceous carbon isotope stratigraphy and platform drowning events: A possible link? *Palaeogeogr. Palaeoclimatol. Palaeoecol.* **137**, 189–203.

Weissert H., McKenzie J. A. and Channell J. E. T. (1985) Natural variations in the carbon cycle during the Early Cretaceous. carbon cycle Atmos.CO_2 *Nat. Var. Archean to Present* **32**, 531–545.

Westermann S., Duchamp-Alphonse S., Fiet N., Fleitmann D., Matera V., Adatte T. and Föllmi K. B. (2013) Paleoenvironmental changes during the Valanginian: New insights from variations in phosphorus contents and bulk- and clay mineralogies in the western Tethys. *Palaeogeogr. Palaeoclimatol. Palaeoecol.* **392**, 196–208.

Westermann S., Föllmi K. B., Adatte T., Matera V., Schnyder J., Fleitmann D., Fiet N., Ploch I. and Duchamp-Alphonse S. (2010) The Valanginian δ13C excursion may not be an expression of a global oceanic anoxic event. *Earth Planet. Sci. Lett.* **290**, 118–131.

Westhead R. K. and Mathert A. E. (1996) An updated lithostratigraphy for the Purbeck Limestone Group in the Dorset type-area. *Proc. Geol. Assoc.* **107**, 117–128.

White T., Gonzalez L., Ludvigson G. and Poulsen C. (2001) Middle K greenhouse hydrologic cycle of North America. *Geology* **29**, 363–366.

Whiticar M. J. and Faber E. (1986) Methane oxidation in sediment and water column environments - Isotopic Evidence. *Org. Geochem.* **10**, 759–768.

Whiticar M. J., Faber E. and Schoell M. (1986) Biogenic methane formation in marine and freshwater environments: CO_2 reduction vs. acetate fermentation-Isotope evidence. *Geochim. Cosmochim. Acta* **50**, 693–709.

Wolfe J. A. and Upchurch G. R. (1987) North American nonmarine climates and vegetation during the Late Cretaceous. *Palaeogeogr. Palaeoclimatol. Palaeoecol.* **61**, 33–77.

Worssam B. C. and Morter A. A. (1978) *The stratigraphy of the Weald Clay*., HMSO., London.

Wortmann U. G. and Weissert H. (2000) Tying platform drowning to perturbations of the global carbon cycle with a delta d13COrg-curve from the Valanginian of DSDP Site 416. *Terra Nov.* **12**, 289–294.

Wright V. P., Taylor K. G. and Beck V. H. (2000) The Paleohydrology of Lower Cretaceous Seasonal Wetlands, Isle of Wight, Southern England. *J. Sediment. Res.* **70**, 619–632.

Yans J., Gerards T., Gerrienne P., Spagna P., Dejax J., Schnyder J., Storme J.-Y. and Keppens E. (2010) Carbon-isotope analysis of fossil wood and dispersed organic matter from the terrestrial Wealden facies of Hautrage (Mons Basin, Belgium). *Palaeogeogr. Palaeoclimatol. Palaeoecol.* **291**, 85–105.

Zhang C. L., Horita J., Cole D. R., Zhou J., Lovley D. R. and Phelps T. J. (2001) Temperature-dependent oxygen and carbon isotope fractionations of biogenic siderite. *Geochim. Cosmochim. Acta* **65**, 2257–2271.

Zhang Y. and Dawe R. A. (2000) Influence of Mg^{2+} on the kinetics of calcite precipitation and calcite crystal morphology. *Chem. Geol.* **163**, 129–138.

Zhou J., Poulsen C. J., Pollard D. and White T. S. (2008) Simulation of modern and middle Cretaceous marine $\delta^{18}O$ with an ocean-atmosphere general circulation model. *Paleoceanography* **23**, n/a-n/a.

Zhou J., Poulsen C. J., Rosenbloom N., Shields C. and Briegleb B. (2012) Vegetation-climate interactions in the warm mid-Cretaceous. *Clim. Past* **8**, 565–576.

Zhou X., Lu Z., Rickaby R. E. M., Domack E. W., Wellner J. S. and Kennedy H. A. (2015) Ikaite abundance controlled by porewater phosphorus level: Potential links to dust and productivity. *J. Geol.* **123**, 269–281.

Ziegler A. M., Raymond A. L., Gierlowski T. C., Horrell M. A., Rowley D. B. and Lottes A. L. (1987) Coal, climate and terrestrial productivity: The present and early Cretaceous compared. *Geol. Soc. Spec. Publ.* **32**, 25–49.

Table of Contents

Appendices: List of Tables **237**
Appendices: List of Figures **238**
Appendix A **241**
1.1 X-ray diffraction profile of Siderite Seed (used for growth experiments) ..241
1.2 Representative X-ray diffraction profile of precipitates 241
1.2.1 Precipitates from Nucleation Experiments 241
1.2.2 Siderite (pH 7.5 to 8.5) 242
1.2.3 Siderite and Chukanovite mixture (pH 8 to pH 8.5) 243
1.2.4 Chukanovite (pH > 8.5) 244
1.3 Precipitates from Growth Experiments 244
1.3.1 Experiments 1,6 and 8 (Data presented Figure 2 in manuscript) 244
1.3.2 Ca control experiments (CA1, CA2) 246
1.3.3 Mg high temperature experiments (MG1, MG2) 247
1.4 Representative EDS Spectra of experiments with varying salinity 248
1.4.1 Experiment 1aF/1a/1aFRp 248
1.4.2 Experiment 3aF/3a 251
1.5 Data files 252
Appendix B **253**
1.1 Data files 253
1.2 Rock-Eval 253
Appendix C **256**
1.1 Data files 256
1.2 Formation scale cation relationships 256
Appendix D **259**
1.1 Data files 259
1.2 FC9 SIMS transect 259
1.3 Temperatures from Farnsworth, *pers comm,* (2019) 260

Appendices: List of Tables

Table C.1: R^2 values between cations from elemental transects. Fe-Ca, and Fe-Mn are usually anti correlated, although the strength of correlation varies. Fe-Mg correlations are variable in strength and direction. Mg-Ca, Mg-Mn correlations are variable in strength and direction. Ca-Mn correlations are variable in strength and direction. 258

Appendices: List of Figures

Figure A.1: Powder X-ray diffraction profile (with corresponding d-spacing values for major peaks noted in Angstroms) of pure siderite seed prepared for at pH 7.45 for seeded growth experiments. Siderite seed material consisted of 2-3 μm aggregates of small rhombs 241

Figure A.2: Typical Powder X-ray diffraction profile (with corresponding d-spacing values for major peaks noted in Angstroms) of siderite precipitate (example from Experiment 1aFLF) produced at pH 7.5.....242

Figure A.3: Typical Powder X-ray diffraction profile (with corresponding d-spacing values for major peaks noted in Angstroms) of siderite precipitate (example from Experiment 3aFLF) produced at pH 7.5.....242

Figure A.4: Typical Powder X-ray diffraction profile (with corresponding d-spacing values for major peaks noted in Angstroms) of a siderite and chukanovite mixture precipitate (example from experiment 3bFLF). Chukanovite was also confirmed in SEM (representative.....243

Figure A.5: Typical Powder X-ray diffraction profile (with corresponding d-spacing values for major peaks noted in Angstroms) of a siderite and chukanovite mixture precipitate (example from experiment 1bFLF). Chukanovite was also confirmed in SEM (representative.....243

Figure A.6: Typical Powder X-ray diffraction profile (with corresponding d-spacing values for major peaks noted in Angstroms) of chukanovite precipitate (example from experiment 1dFLF). 244

Figure A.7: Powder X-ray diffraction profile (with corresponding d-spacing values for major peaks noted in Angstroms) of precipitate in Experiment 1. Siderite is the only mineral phase. 244

Figure A.8: Powder X-ray diffraction profile (with corresponding d-spacing values for major peaks noted in Angstroms) of precipitate in Experiment 6. Siderite is the only mineral phase. 245

Figure A.9: Powder X-ray diffraction profile (with corresponding d-spacing values for major peaks noted in Angstroms) of precipitate in Experiment 8. Siderite is the only mineral phase. 245

Figure A.10: Powder X-ray diffraction profile (with corresponding d-spacing values for major peaks noted in Angstroms) of precipitate in experiment CA1 (Supplementary Data sheet 'Ca control exp'). Siderite is the only mineral phase. 246

Figure A.11: Powder X-ray diffraction profile (with corresponding d-spacing values for major peaks noted in Angstroms) of precipitate in experiment CA2. Siderite is the only mineral phase. 246

Figure A.12: Powder X-ray diffraction profile (with corresponding d-spacing values for major peaks noted in Angstroms) of precipitate from Experiment MG1 at 40˚C (Supplementary Data sheet 'High temp Mg exp') . Siderite is the only mineral phase. ...247

Figure A.13: Powder X-ray diffraction profile (with corresponding d-spacing values for major peaks noted in Angstroms) of precipitate from Experiment MG1 at 55˚C (Supplementary Data sheet 'High temp Mg exp') . Siderite is the only mineral phase. ...247

Figure A.14: BSE image and average EDS spectra from multiple point analyses (white dots) on siderite precipitate from experiment 1aF , with initial concentrations of Fe 10 mmol, Mn 5 mmol, Ca 5 mmol and Mg 5mmol, in freshwater conditions with no NaCl. No discernible uptake of Mg. 248

Figure A.15: BSE image and average EDS spectra from multiple point analyses (white dots) on siderite precipitate from experiment 1a , with initial concentrations of Fe 10 mmol, Mn 5 mmol, Ca 5 mmol and Mg 5mmol, in brackish conditions with 475 mmol NaCl. No discernible uptake of Mg. 249

Figure A.16: BSE image and average EDS spectra from multiple point analyses (white dots) on siderite precipitate from experiment 1aFLFRp , with initial concentrations of Fe 1 mmol, Mn 0.5 mmol, Ca 0.5 mmol and Mg 0.5 mmol, in marine conditions with 700 mmol NaCl. No discernible uptake of Mg. 250

Figure A.17: BSE image and average EDS spectra from multiple point analyses (white dots) on siderite precipitate from experiment 3aF , with initial concentrations of Fe 10 mmol, Mn 10 mmol, Ca 5 mmol and Mg 5mmol, in freshwater conditions with no NaCl. No discernible uptake of Mg. 251

Figure A.18: BSE image and average EDS spectra from multiple point analyses (white dots) on siderite precipitate from experiment 3a, with initial concentrations of Fe 10 mmol, Mn 10 mmol, Ca 5 mmol and Mg 5mmol, and 475 mmol NaCl to simulate brackish conditions. 252

Figure B.19:Carbon Isotope compositions vs TOC within formation of the Wealden Supergroup. The values are generally scattered. 253

Figure B.20: Tmax vs TOC within formation of the Wealden Supergroup. The values are generally scattered. 254

Figure B.21: Tmax vs HI within formation of the Wealden Supergroup. The values are generally scattered. 254

Figure B.22: HI vs TOC within formation of the Wealden Supergroup. The values are generally scattered. 255

Figure C.1: Cation concentrations and their relationships in Ashdown Formation (Spheres = 17). R^2 values are Fe-Mg 0.13, Fe-Ca 0.54, Fe-Mn 0.41, Mg-Ca 0.01, Mg-Mn 0.04, Mn-Ca 0.14. 256

Figure C.2: Cation concentrations and their relationships in the Wadhurst Clay Formation (Spheres =3). R^2 values are Fe-Mg 0.14, Fe-Ca 0.45, Fe-Mn 0.04, Mg-Ca 0.06, Mg-Mn 0.09, Mn-Ca 0.004. 257

Figure C.3: Cation concentrations and their relationships in the Tunbridge Wells Sand Formation (Spheres = 7). R^2 values are Fe-Mg 0.76, Fe-Ca 0.79, Fe-Mn 0.23, Mg-Ca 0.82, Mg-Mn 0.004, Mn-Ca 0.002. 257

Figure D.1: Stable isotope transects and representative Backscatter Images from FC9 , from Fairlight Clays (Ashdown Formation) from Robinson et al (2010). Bulk $\delta^{18}O_{siderite}$ of these horizons were previously published in Robinson et al, (2010).....259

Figure D.2: Model parameters for 6 sites on which published data exists, annually for Berriasian, Valanginian and Hauterivian. DSDP 534 (palaeolatitude during the Valanginian: 18ºN) and DSDP 603(palaeolatitude during the Valanginian: 24ºN) are low latitudes, ODP 692(palaeolatitude during the Valanginian: 54ºS), DSDP 249(palaeolatitude during the Valanginian: 54ºS), ODP 511(palaeolatitude during the Valanginian: 51ºS) and Yatria river (palaeolatitude during the Valanginian: 51ºN) are high latitudes.....260

Appendix A

Data presented here is applicable to Chapter 2, which has been published in Sengupta et al., (2020)

1.1 X-ray diffraction profile of Siderite Seed (used for growth experiments)

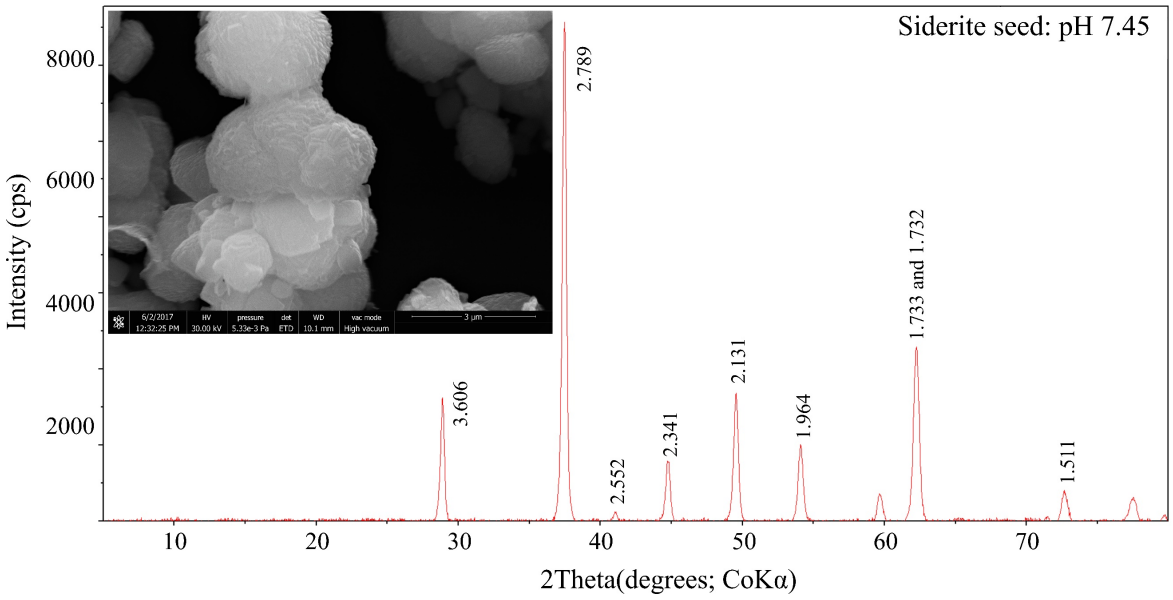


Figure A.1: Powder X-ray diffraction profile (with corresponding d-spacing values for major peaks noted in Angstroms) of pure siderite seed prepared for at pH 7.45 for seeded growth experiments. Siderite seed material consisted of 2-3 µm aggregates of small rhombs

1.2 Representative X-ray diffraction profile of precipitates

1.2.1 Precipitates from Nucleation Experiments

As discussed in section 4.1 in the manuscript, the nucleation experiments produced a mixture of Fe(II) carbonate phases (siderite, chukanovite). Here we present representative XRD profiles of siderite, chukanovite and siderite/chukanovite mixtures from nucleation experiments. Details of starting conditions of experiments are in Supplementary Data 1.

1.2.2 Siderite (pH 7.5 to 8.5)

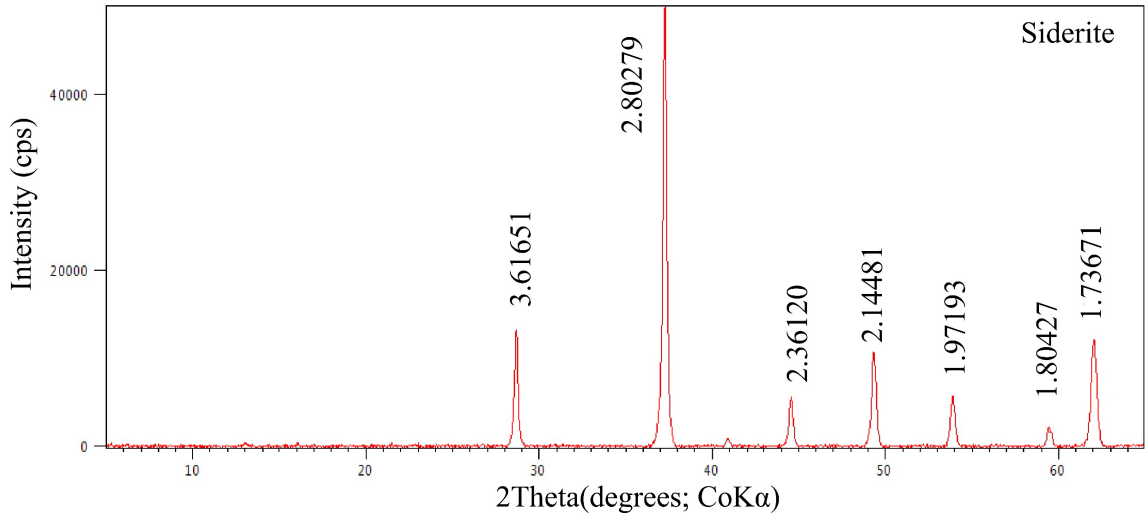


Figure A.2: Typical Powder X-ray diffraction profile (with corresponding d-spacing values for major peaks noted in Angstroms) of siderite precipitate (example from Experiment 1aFLF) produced at pH 7.5.

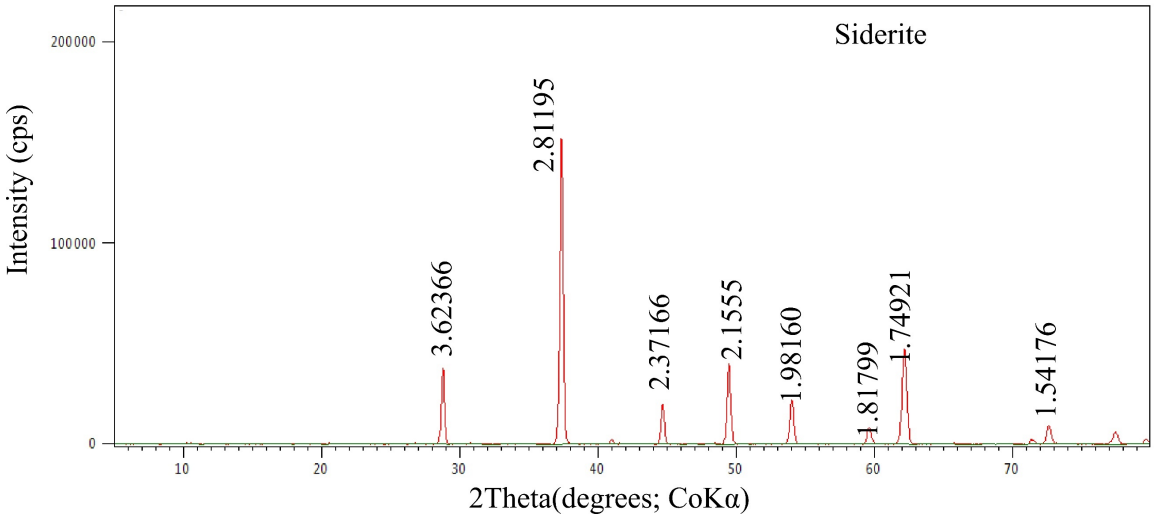


Figure A.3: Typical Powder X-ray diffraction profile (with corresponding d-spacing values for major peaks noted in Angstroms) of siderite precipitate (example from Experiment 3aFLF) produced at pH 7.5.

1.2.3 Siderite and Chukanovite mixture (pH 8 to pH 8.5)

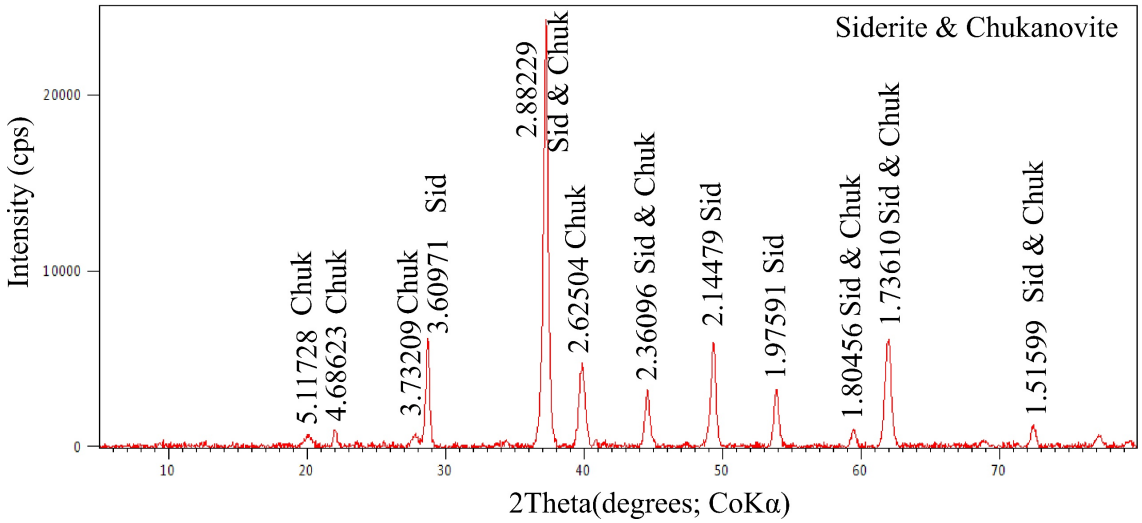


Figure A.4: Typical Powder X-ray diffraction profile (with corresponding d-spacing values for major peaks noted in Angstroms) of a siderite and chukanovite mixture precipitate (example from experiment 3bFLF). Chukanovite was also confirmed in SEM (representative

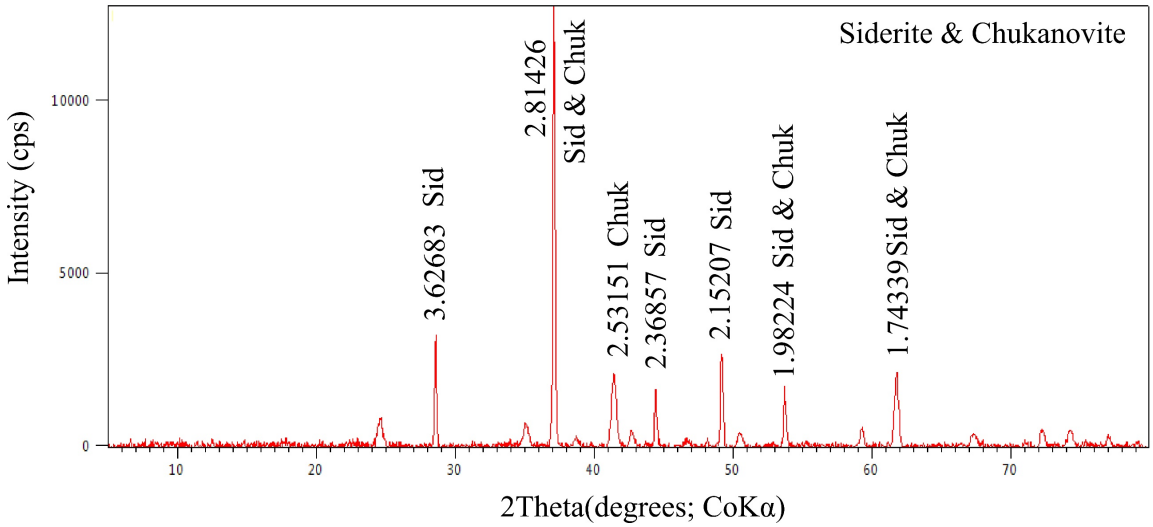


Figure A.5: Typical Powder X-ray diffraction profile (with corresponding d-spacing values for major peaks noted in Angstroms) of a siderite and chukanovite mixture precipitate (example from experiment 1bFLF). Chukanovite was also confirmed in SEM (representative

1.2.4 Chukanovite (pH > 8.5)

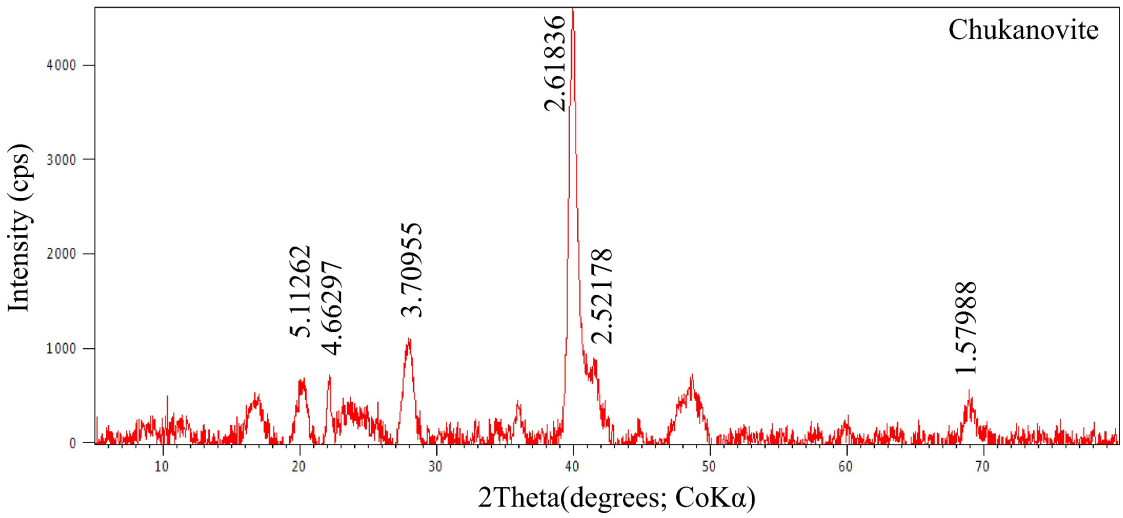


Figure A.6: Typical Powder X-ray diffraction profile (with corresponding d-spacing values for major peaks noted in Angstroms) of chukanovite precipitate (example from experiment 1dFLF).

1.3 Precipitates from Growth Experiments

Growth Experiments were conducted in presence of a pure siderite seed, details of which are provided in section 1. Here we present representative spectra of precipitates from the growth experiments.

1.3.1 Experiments 1,6 and 8 (Data presented Figure 2 in manuscript)

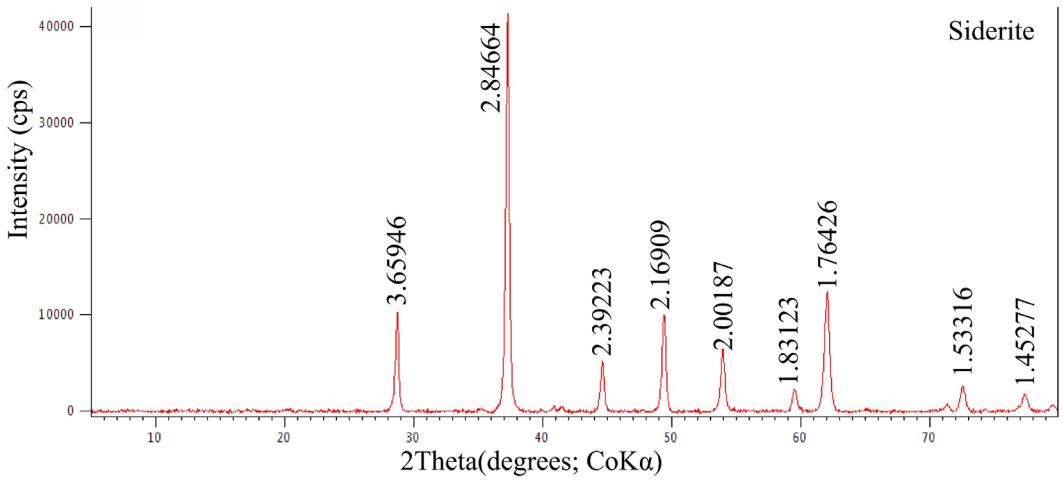


Figure A.7: Powder X-ray diffraction profile (with corresponding d-spacing values for major peaks noted in Angstroms) of precipitate in Experiment 1. Siderite is the only mineral phase.

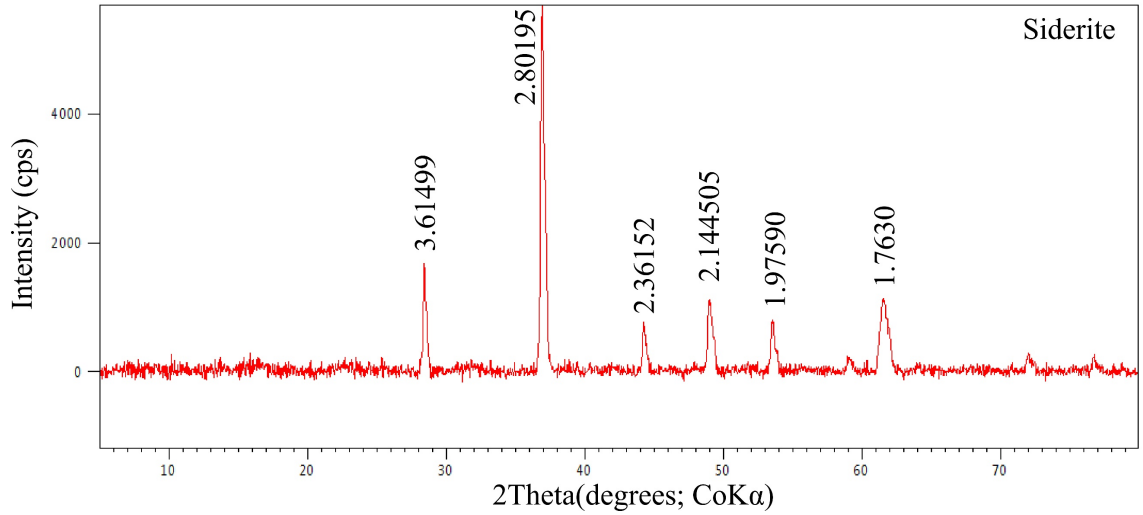


Figure A.8: Powder X-ray diffraction profile (with corresponding d-spacing values for major peaks noted in Angstroms) of precipitate in Experiment 6. Siderite is the only mineral phase.

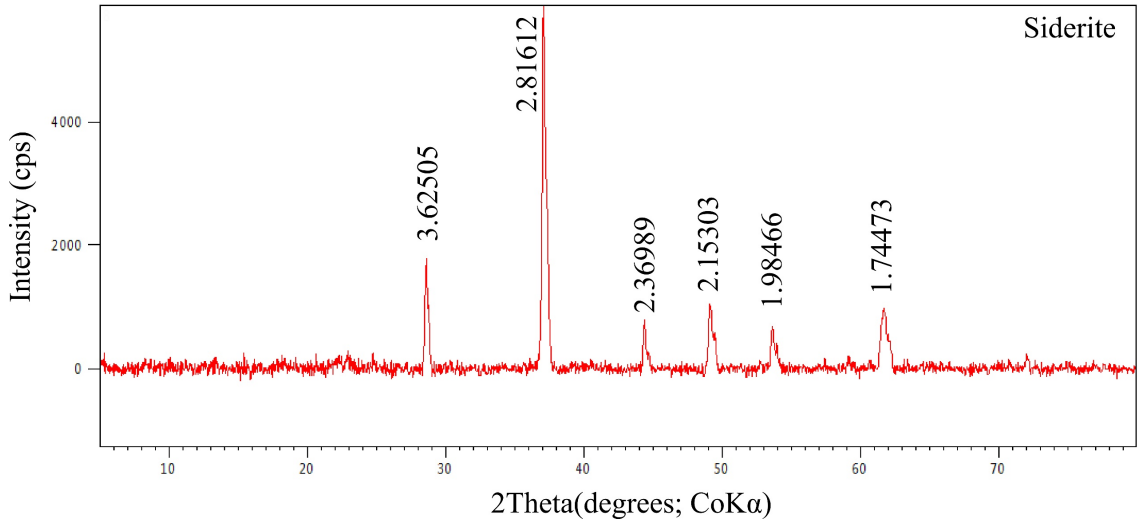


Figure A.9: Powder X-ray diffraction profile (with corresponding d-spacing values for major peaks noted in Angstroms) of precipitate in Experiment 8. Siderite is the only mineral phase.

1.3.2 Ca control experiments (CA1, CA2)

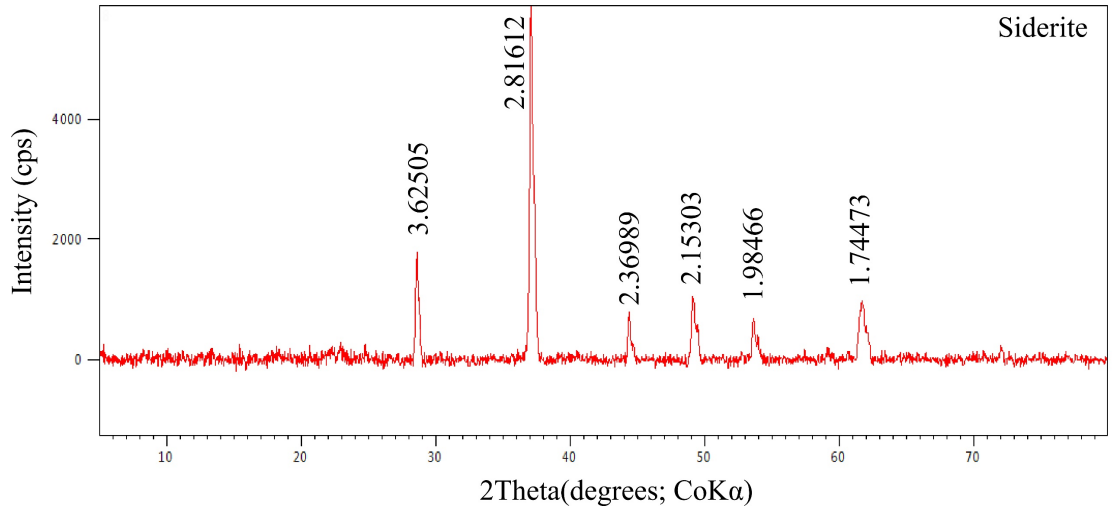


Figure A.10: Powder X-ray diffraction profile (with corresponding d-spacing values for major peaks noted in Angstroms) of precipitate in experiment CA1 (Supplementary Data sheet 'Ca control exp'). Siderite is the only mineral phase.

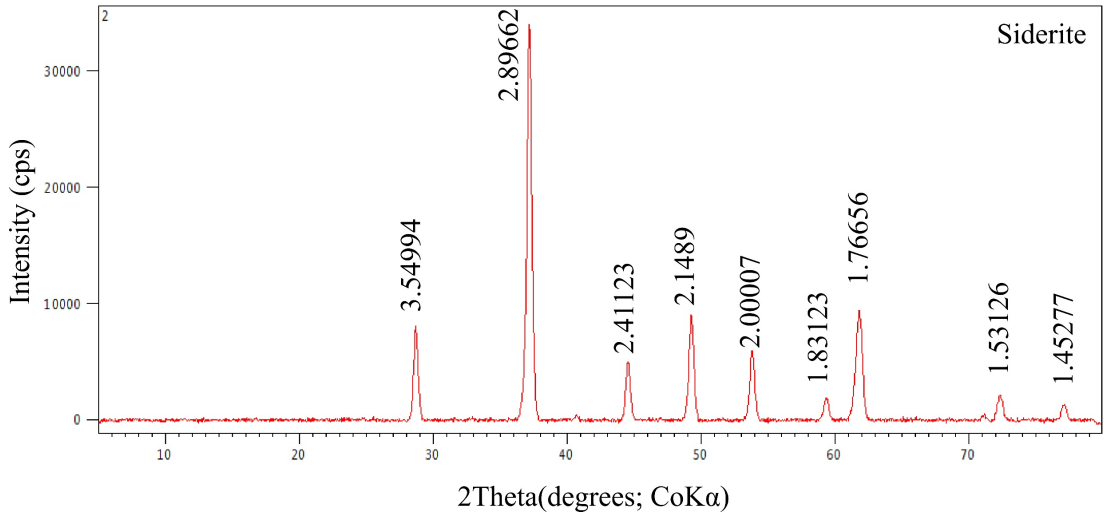


Figure A.11: Powder X-ray diffraction profile (with corresponding d-spacing values for major peaks noted in Angstroms) of precipitate in experiment CA2. Siderite is the only mineral phase.

1.3.3 Mg high temperature experiments (MG1, MG2)

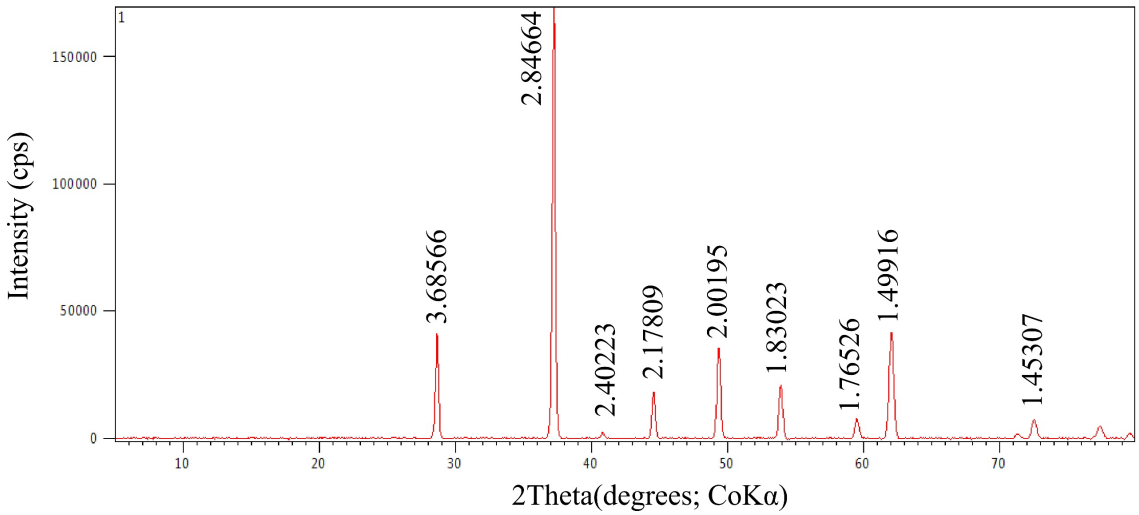


Figure A.12: Powder X-ray diffraction profile (with corresponding d-spacing values for major peaks noted in Angstroms) of precipitate from Experiment MG1 at 40˚C (Supplementary Data sheet 'High temp Mg exp') . Siderite is the only mineral phase.

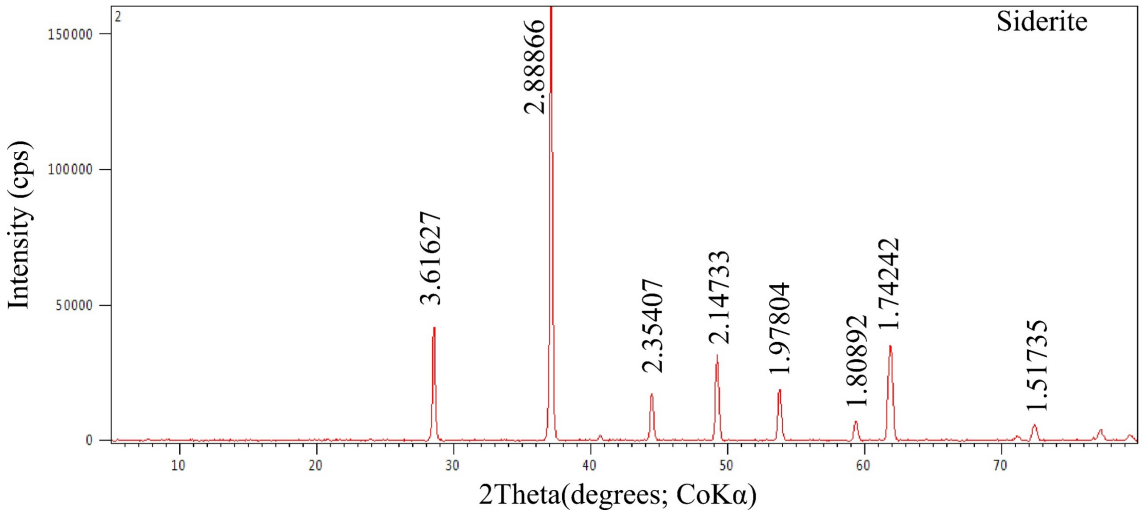


Figure A.13: Powder X-ray diffraction profile (with corresponding d-spacing values for major peaks noted in Angstroms) of precipitate from Experiment MG1 at 55˚C (Supplementary Data sheet 'High temp Mg exp') . Siderite is the only mineral phase.

1.4 Representative EDS Spectra of experiments with varying salinity

Experiments were conducted with varying Fe, Ca, Mn and Mg concentrations (details in Supplementary Data 1) at NaCl concentrations of 0 mmol (fresh), 475 mmol (brackish) and 700 mmol (marine). Here we present representative spectra from fresh, brackish and marine nucleation experiments with similar initial conditions. The spectra are averages from multiple points (white dots) on crystal faces within each precipitate.

1.4.1 Experiment 1aF/1a/1aFRp

1.4.1.1 Fresh (1aF)

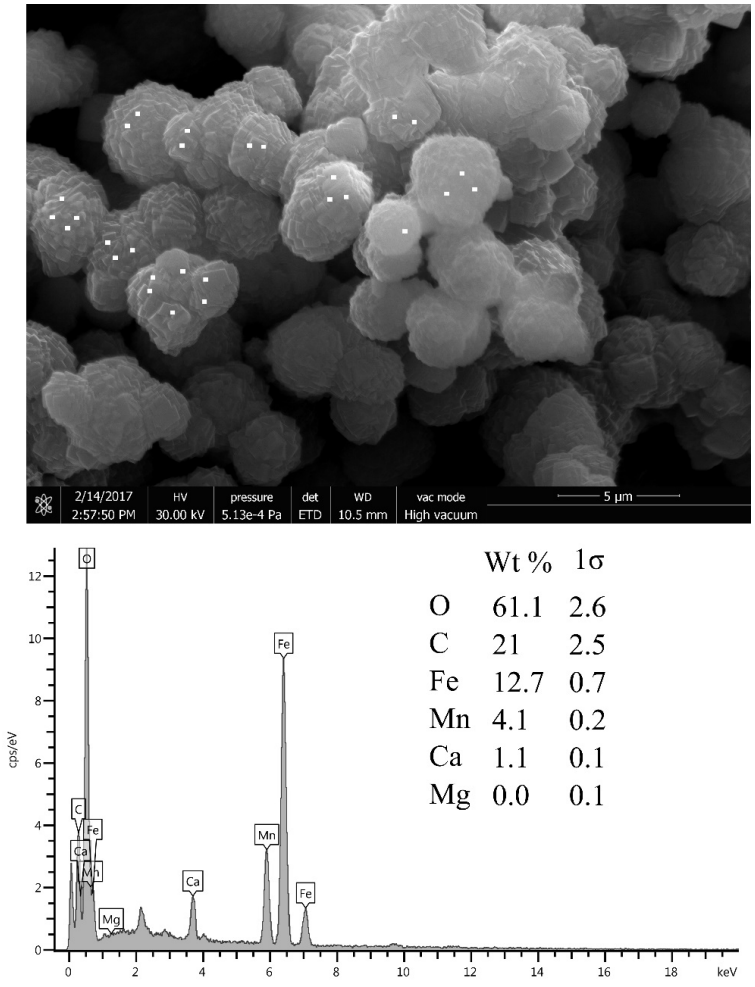


Figure A.14: BSE image and average EDS spectra from multiple point analyses (white dots) on siderite precipitate from experiment 1aF , with initial concentrations of Fe 10 mmol, Mn 5 mmol, Ca 5 mmol and Mg 5mmol, in freshwater conditions with no NaCl. No discernible uptake of Mg.

1.4.1.2 Brackish (1a)

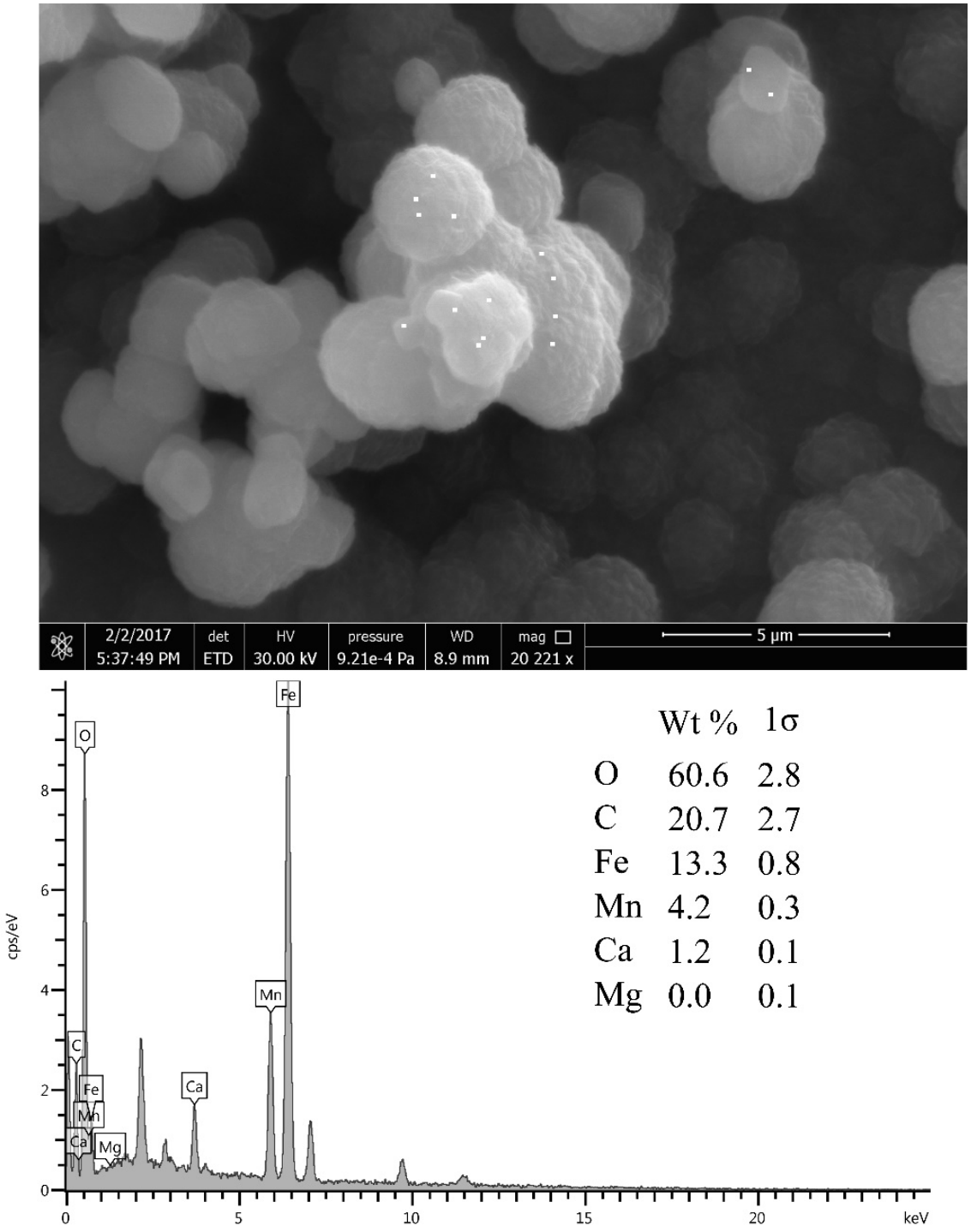


Figure A.15: BSE image and average EDS spectra from multiple point analyses (white dots) on siderite precipitate from experiment 1a , with initial concentrations of Fe 10 mmol, Mn 5 mmol, Ca 5 mmol and Mg 5mmol, in brackish conditions with 475 mmol NaCl. No discernible uptake of Mg.

1.4.1.3 Marine (1aFLFRp)

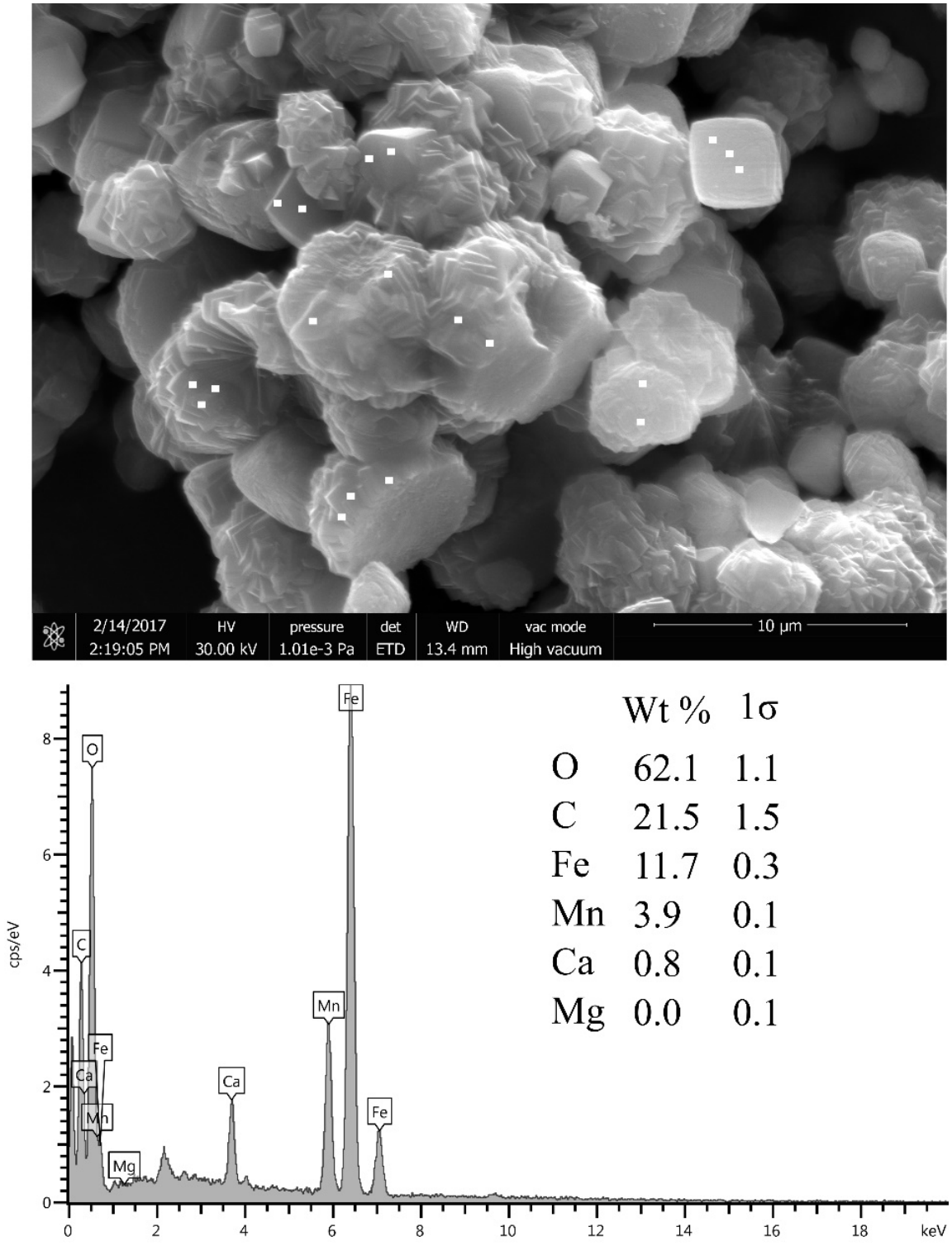


Figure A.16: BSE image and average EDS spectra from multiple point analyses (white dots) on siderite precipitate from experiment 1aFLFRp , with initial concentrations of Fe 1 mmol, Mn 0.5 mmol, Ca 0.5 mmol and Mg 0.5 mmol, in marine conditions with 700 mmol NaCl. No discernible uptake of Mg.

1.4.2 Experiment 3aF/3a

1.4.2.1 Fresh (3aF)

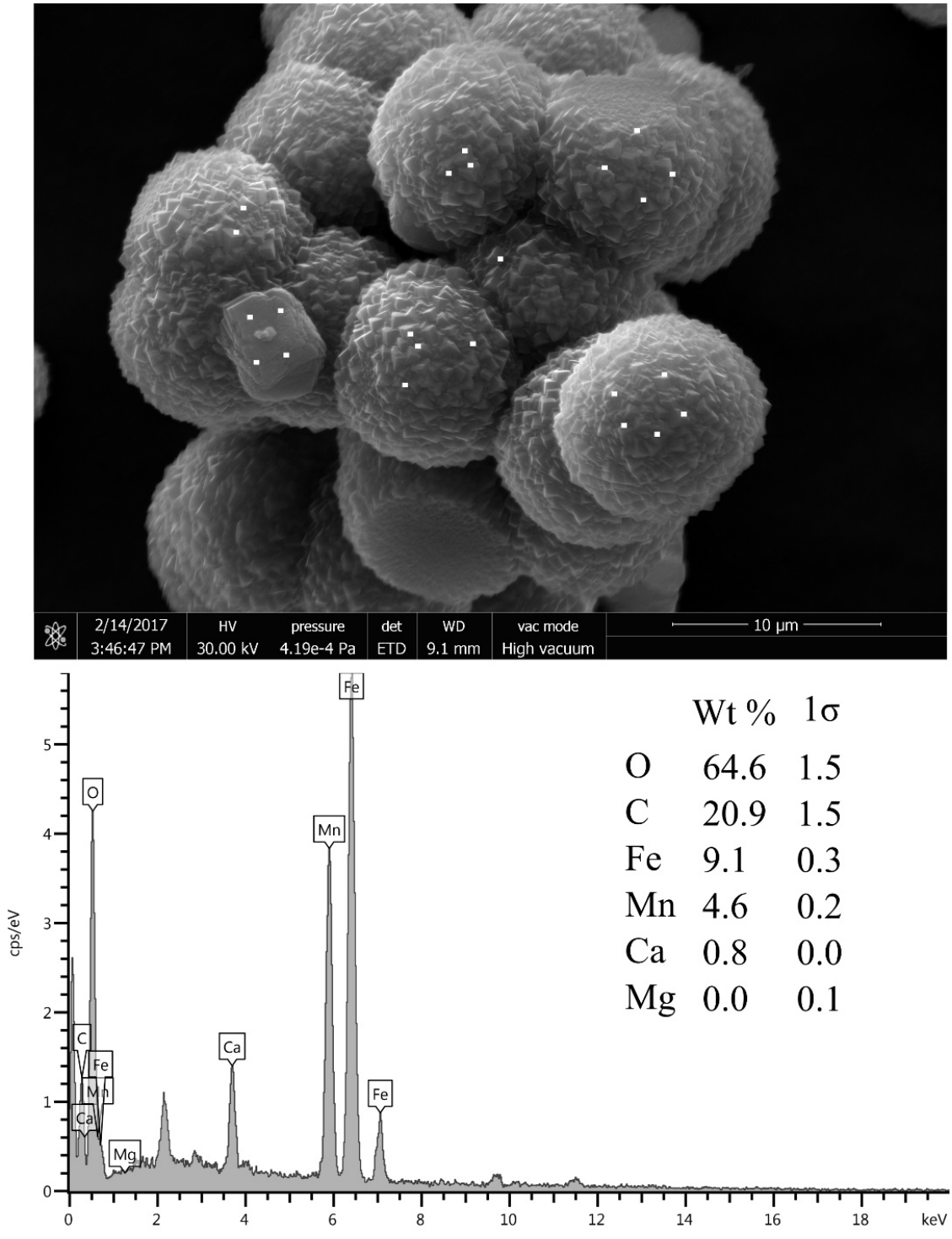


Figure A.17: BSE image and average EDS spectra from multiple point analyses (white dots) on siderite precipitate from experiment 3aF , with initial concentrations of Fe 10 mmol, Mn 10 mmol, Ca 5 mmol and Mg 5mmol, in freshwater conditions with no NaCl. No discernible uptake of Mg.

1.4.2.2 Brackish (3a)

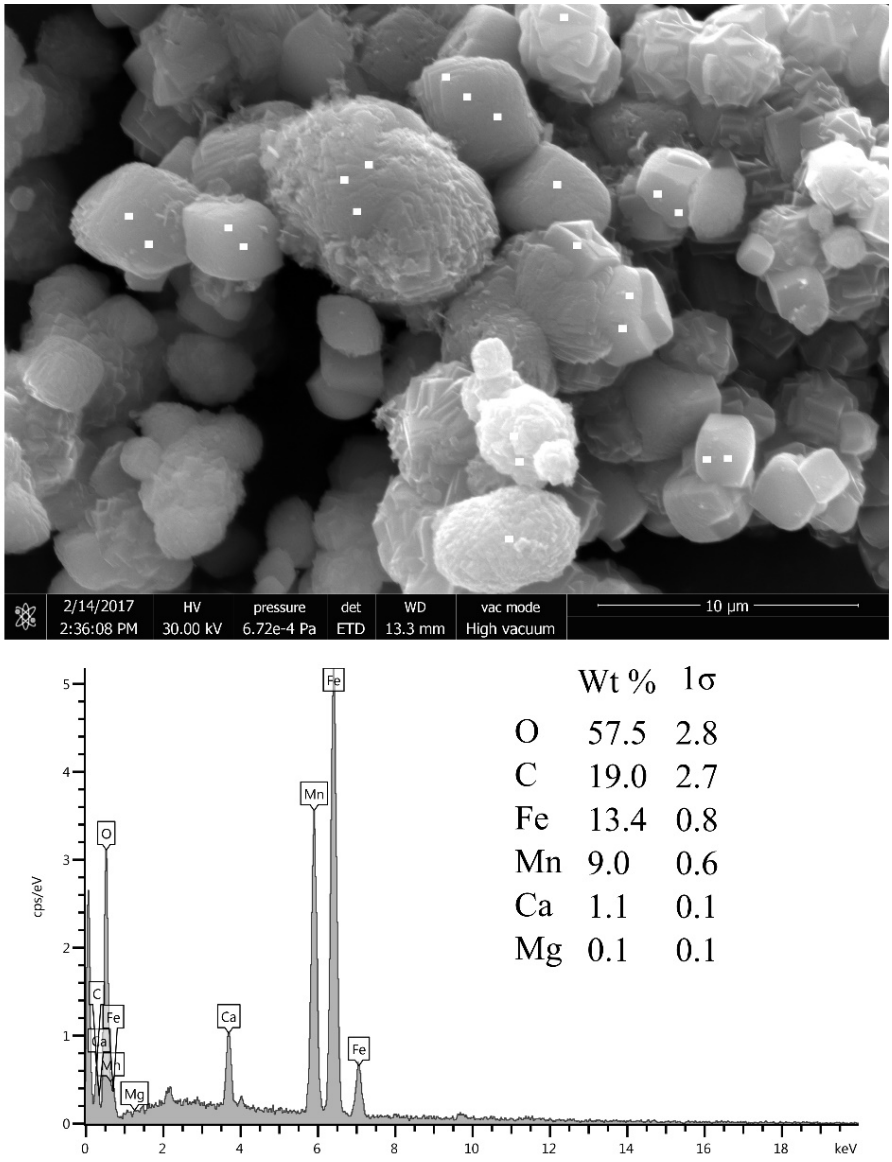


Figure A.18: BSE image and average EDS spectra from multiple point analyses (white dots) on siderite precipitate from experiment 3a, with initial concentrations of Fe 10 mmol, Mn 10 mmol, Ca 5 mmol and Mg 5mmol, and 475 mmol NaCl to simulate brackish conditions.

1.5 Data files

The data for Chapter 2 is available within the spreadsheet in supplementary materials named **AppendixA_1_1_Chapter2_ExperimentalSiderite** and includes data from nucleation and growth experiments.

Appendix B

Data presented here is applicable to Chapter 3.

1.1 Data files

The data for Chapter 3 is available within the spreadsheet in supplementary materials named **AppendixB_1_1_Chapter3_CarbonIsotopeStratigraphy** and includes:

- Composite carbon isotope record
- Data from individual boreholes.

1.2 Rock-Eval

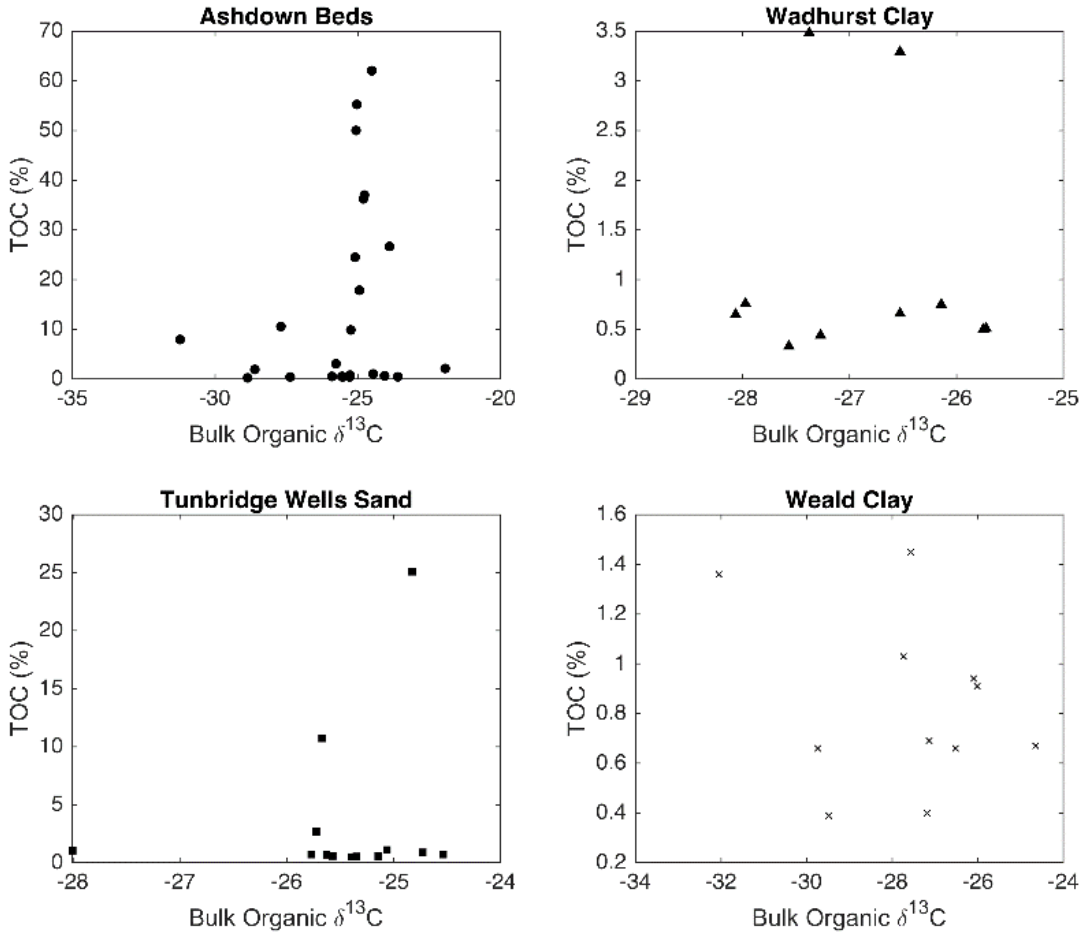


Figure B.19:Carbon Isotope compositions vs TOC within formation of the Wealden Supergroup. The values are generally scattered.

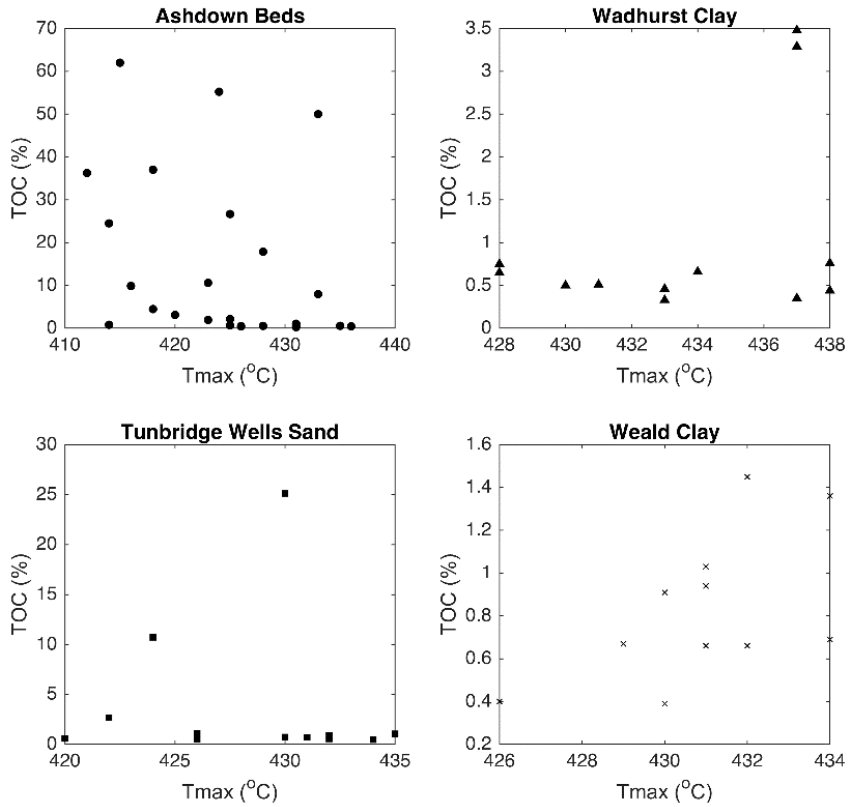


Figure B.20: Tmax vs TOC within formation of the Wealden Supergroup. The values are generally scattered.

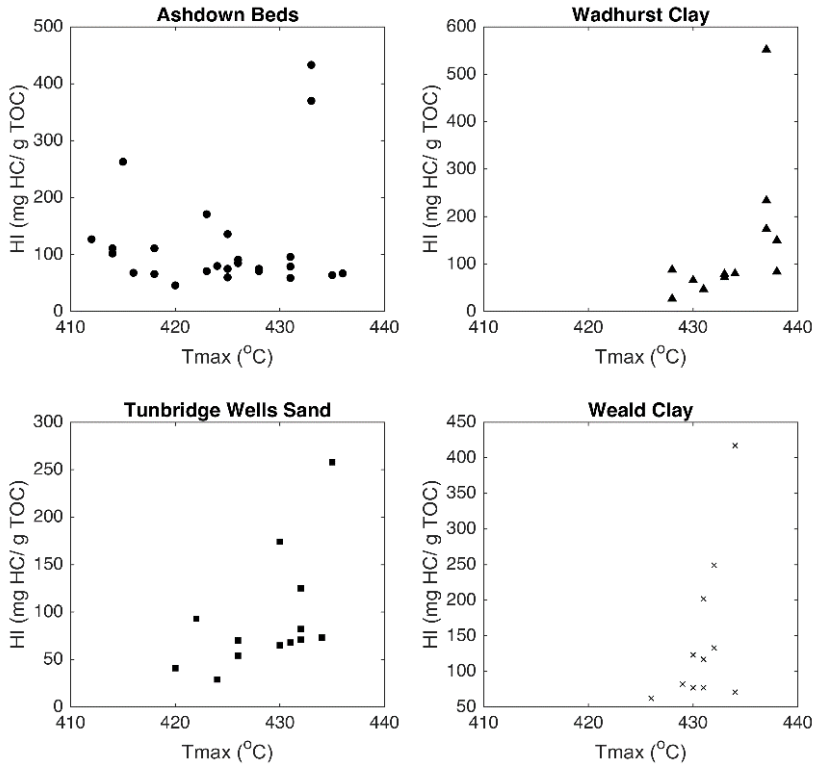


Figure B.21: Tmax vs HI within formation of the Wealden Supergroup. The values are generally scattered.

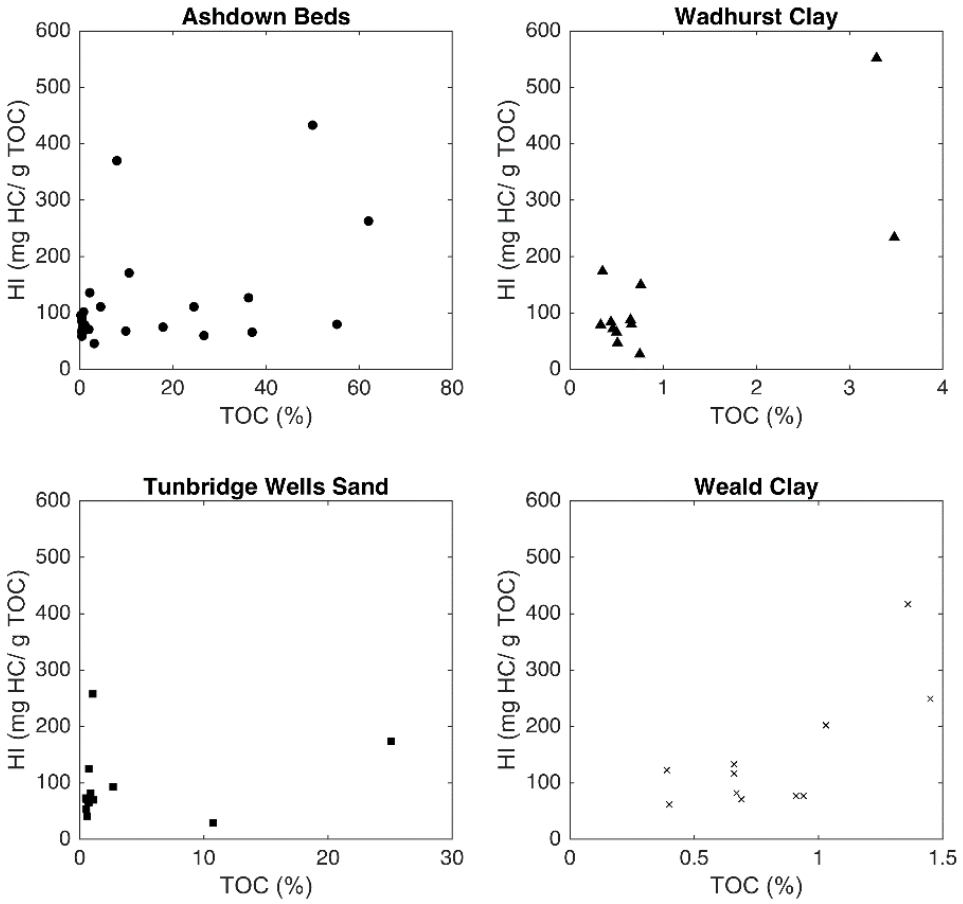


Figure B.22: HI vs TOC within formation of the Wealden Supergroup. The values are generally scattered.

Appendix C

Data presented here is applicable to Chapter 4.

1.1 Data files

The data for Chapter 4 is available within the spreadsheet in supplementary materials named '**AppendixC_1_1_Chapter4_SphaerosideriteCharacterisation'** and includes:

- XRD data from sphaerosiderites and bulk samples
- Elemental transects and R^2 values from transects

1.2 Formation scale cation relationships

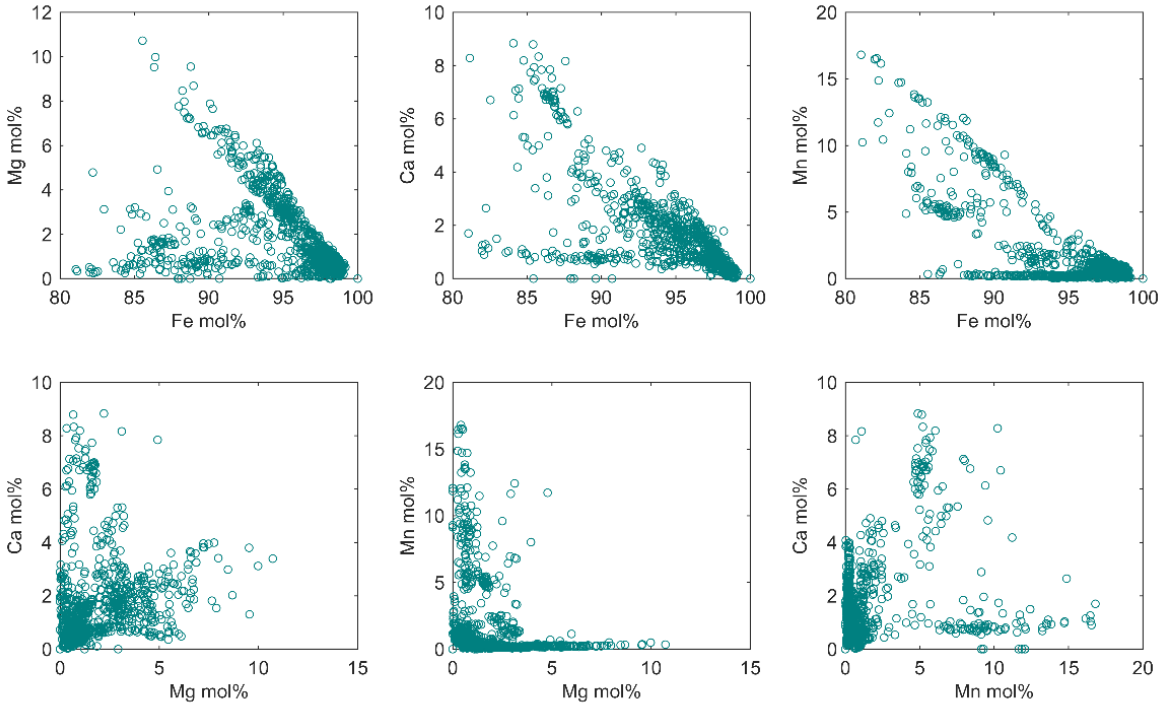


Figure C.23: Cation concentrations and their relationships in Ashdown Formation (Spheres = 17). R^2 values are Fe-Mg 0.13, Fe-Ca 0.54, Fe-Mn 0.41, Mg-Ca 0.01, Mg-Mn 0.04, Mn-Ca 0.14.

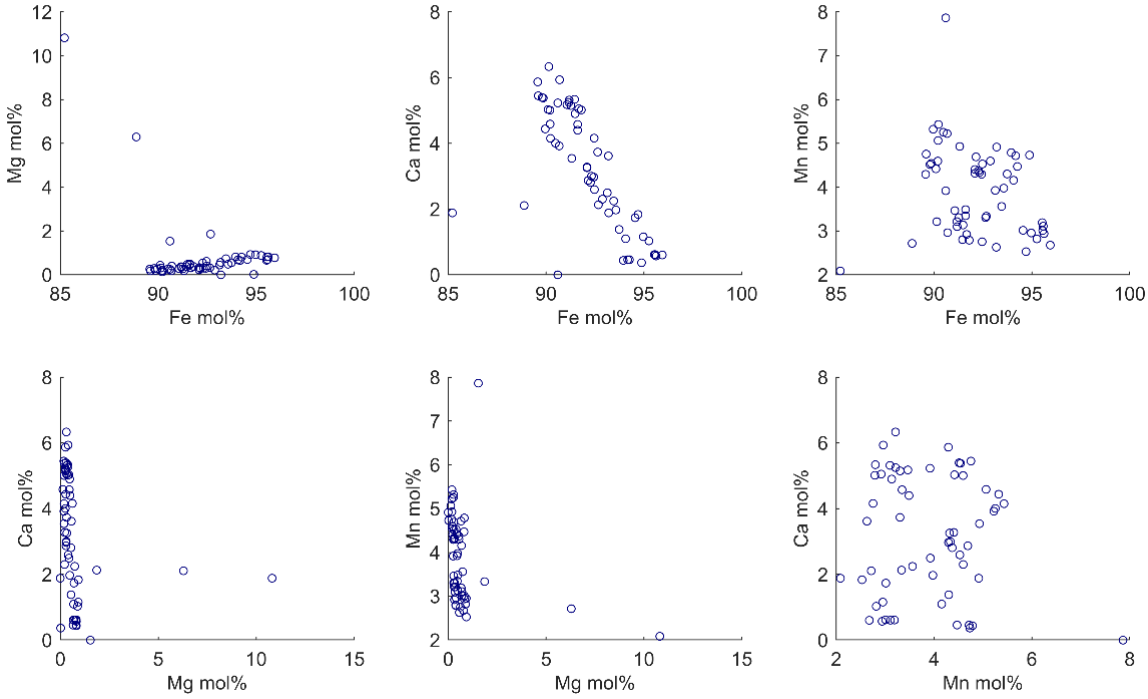


Figure C.24: Cation concentrations and their relationships in the Wadhurst Clay Formation (Spheres =3). R^2 values are Fe-Mg 0.14, Fe-Ca 0.45, Fe-Mn 0.04, Mg-Ca 0.06, Mg-Mn 0.09, Mn-Ca 0.004.

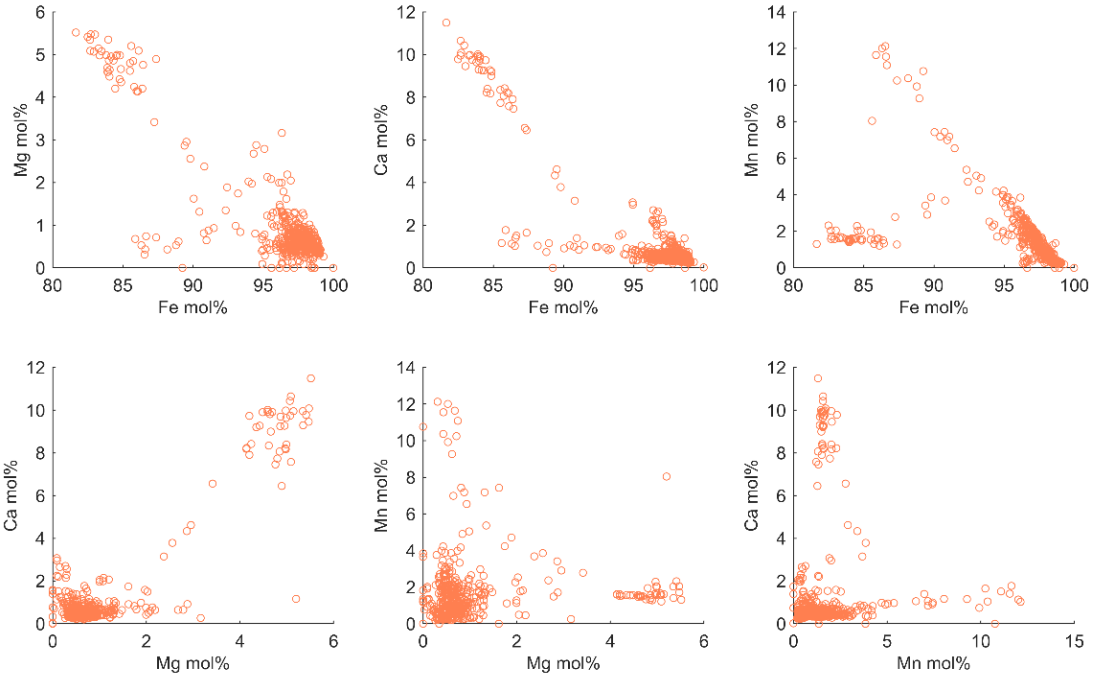


Figure C.25: Cation concentrations and their relationships in the Tunbridge Wells Sand Formation (Spheres = 7). R^2 values are Fe-Mg 0.76, Fe-Ca 0.79, Fe-Mn 0.23, Mg-Ca 0.82, Mg-Mn 0.004, Mn-Ca 0.002.

Sample	Fe mol%	FeMg	FeCa	FeMn	MgCa	MgMn	CaMn
67188F_2	89.7	0.174	-0.695	-0.758	-0.233	-0.117	0.212
66949F	98.4	-0.09	-0.497	-0.253	-0.058	-0.178	0.097
FC09	94	-0.911	-0.625	-0.465	0.329	0.495	0.145
FC011	94.1	-0.817	-0.119	-0.555	-0.008	0.451	0.05
FC05	92.7	-0.931	-0.701	-0.212	0.443	0.248	0.046
67084C	96.7	-0.062	0.001	-0.732	0.03	-0.065	-0.092
67095C	85.4	-0.516	-0.672	0.223	0.908	-0.869	-0.784
67092C	97.3	-0.132	-0.377	-0.701	-0.109	0.054	0.077
67087C	98.7	-0.752	-0.191	-0.01	-0.001	0.026	-0.197
66971F	97.1	-0.744	-0.965	0.186	0.576	0.222	-0.199
67175F	87.7	0.001	-0.112	-0.88	-0.035	-0.055	-0.01
67068W	97.1	-0.022	-0.084	-0.388	0	-0.091	-0.204
67078C	97.1	0.001	-0.089	-0.414	0.088	-0.364	-0.189
66962F	98.3	-0.385	-0.605	-0.109	0.088	-0.056	-0.003
67204F	91.2	-0.09	-0.637	-0.656	0.126	-0.015	0.114
67192F	96.7	0.011	-0.795	-0.608	-0.238	0.027	0.224
67198F	86.5	0.032	-0.791	-0.34	-0.206	-0.237	0.153
66963F	96.2	-0.66	-0.116	-0.954	0.018	0.47	0.078
67086C	95.9	-0.076	-0.561	-0.948	0.238	0.003	0.403
67101C	92.2	-0.159	-0.463	-0.04	-0.054	-0.094	-0.004
67081C_2	97.8	-0.626	-0.079	-0.833	-0.032	0.426	0.003
67081C_1	97.8	-0.038	-0.249	-0.414	-0.404	0.294	-0.076
67086C_2	96.3	-0.765	-0.695	-0.936	0.434	0.528	0.661
67086C_1	96.6	0	0.006	-0.94	-0.074	-0.007	-0.069
66951F_2	98.1	-0.108	-0.702	-0.303	-0.021	-0.167	0.318
66951F_1	98.5	-0.63	-0.426	0.093	0.041	-0.218	-0.238
67057W	97.1	0.088	-0.753	-0.77	-0.295	-0.071	0.329
66934F	96.3	-0.83	-0.17	-0.192	0.005	0.107	-0.024
67178F	98	-0.499	-0.834	-0.355	0.156	0	0.442
66955F	97.2	-0.85	-0.922	0.088	0.625	-0.053	-0.192

Table C.1: R^2 values between cations from elemental transects. Fe-Ca, and Fe-Mn are usually anti correlated, although the strength of correlation varies. Fe-Mg correlations are variable in strength and direction. Mg-Ca, Mg-Mn correlations are variable in strength and direction. Ca-Mn correlations are variable in strength and direction.

Appendix D

Data presented here is applicable to Chapter 5.

1.1 Data files

The data for Chapter 5 is available within the spreadsheet in supplementary materials named **AppendixD_1_1_Chapter5_WealdenPalaeohydrology** and includes:

- Average δ^{18}Osiderite in sphaerosiderite horizons
- Meteoric Sphaerosiderite Lines
- SIMS carbon and oxygen isotope compositions
- IRMS and Clumped data from ETH
- Calculated Groundwaters

1.2 FC9 SIMS transect

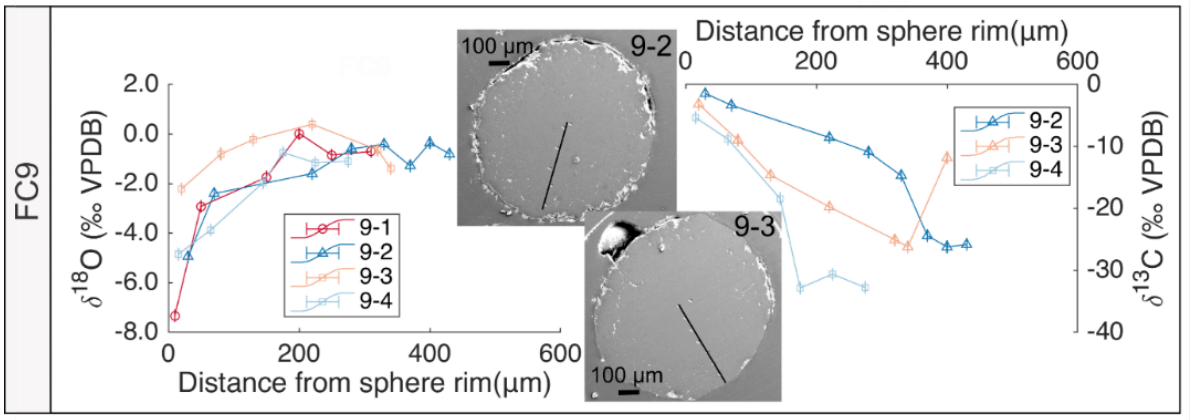


Figure D.26: Stable isotope transects and representative Backscatter Images from FC9 , from Fairlight Clays (Ashdown Formation) from Robinson et al (2010). Bulk $\delta^{18}O_{siderite}$ of these horizons were previously published in Robinson et al, (2010).

1.3 Temperatures from Farnsworth, *pers comm*, (2019)

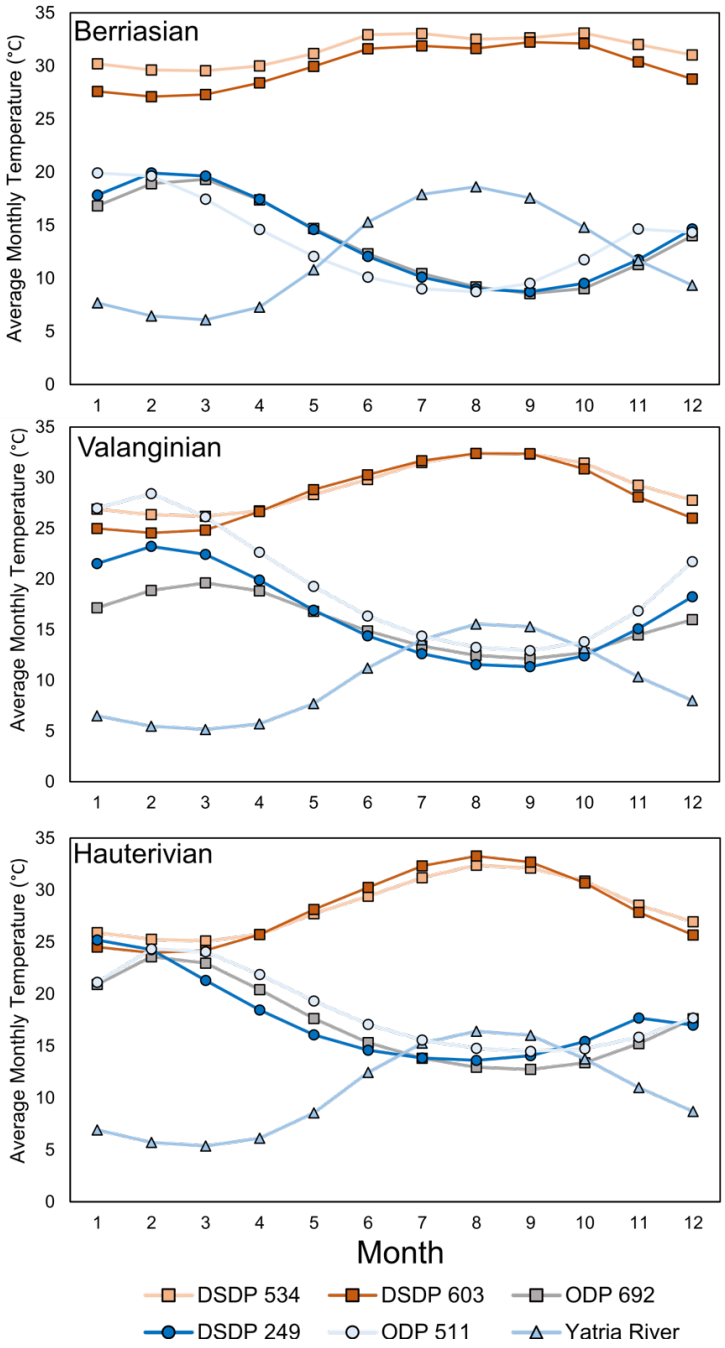


Figure D.27: Model parameters for 6 sites on which published data exists, annually for Berriasian, Valanginian and Hauterivian. DSDP 534 (palaeolatitude during the Valanginian: 18ºN) and DSDP 603(palaeolatitude during the Valanginian: 24ºN) are low latitudes, ODP 692(palaeolatitude during the Valanginian: 54ºS), DSDP 249(palaeolatitude during the Valanginian: 54ºS), ODP 511(palaeolatitude during the Valanginian: 51ºS) and Yatria river (palaeolatitude during the Valanginian: 51ºN) are high latitudes.